Controls on Reservoir Quality in the Lower Triassic Montney Formation

by

Noga Vaisblat

A thesis submitted in partial fulfillment of the requirements for the degree of

Doctor of Philosophy

Department of Earth and Atmospheric Sciences

University of Alberta

Abstract

The Lower Triassic Montney Formation is a world class hydrocarbons reservoir in Alberta and British Columbia. Although commonly described as a shale, it is a siltstone over most of its subcrop, for which predictive models for reservoir quality properties such as porosity and permeability, geomechanical properties, and water saturation are generally lacking. Reservoir properties are generally functions of rock fabric, rock composition and diagenetic processes, which in turn depend on sediment provenance, depositional environment, burial history of the rock, and paleo fluid-flow. This study is aimed to identify the compositional controls on reservoir quality properties in the Montney siltstone and their relationship to the lithostratigraphy. In addition, we compare controls on reservoir quality of the siltstone to those found for shale formation.

Variations of Young's Modulus, Poisson's Ratio, and relative brittleness from well logs were compared against indentation measurements of the four long cores and against rock composition in all wells. Young's modulus, brittleness, and hardness showed similar trends in each well, whereas Poisson's ratio demonstrated a trend with depth opposite to all other elastic parameters. Statistical analysis indicated that clay content, and to a lesser extent organic matter content, had the strongest control on elastic moduli in the Montney Formation, reducing Young's modulus, brittleness, and hardness, but increasing Poisson's ratio.

Clay content is the most significant parameter affecting the mechanical properties of the Montney Formation, an observation consistent with several other fine-grained reservoirs. An increase in clay content leads to an increase in dynamic Poisson's Ratio and a decrease in dynamic Young's Modulus values in all the formations examined in this study. In addition, water saturation and the number of bedding planes are positively correlated with a decrease in rock brittleness in the Montney Formation.

Quartz content exerts a positive control on both porosity and permeability, related to strengthening of the rock framework and reduced porosity loss due to compaction. Elevated

clay content is also associated with higher porosity and permeability, possibly in part because of an association with quartz, but also because clays may shelter interconnected primary porosity that promotes permeability. Organic matter content is negatively correlated to porosity and permeability despite the presence of organic matter porosity, because relict oil (now pyrobitumen) plugs primary pore space and because other pore types contribute more to the total pore volume of the rock.

Sedimentological analysis identified 16 lithofacies across the basin, with depositional environments ranging from tidal flat to offshore sediments. No clear distinctions were found between petrophysical or geomechanical properties of different lithofacies in each well. More importantly, the same lithofacies commonly displays significantly different geomechanical or petrophysical properties in each of the wells. We attribute the weak influence of depositional environments on the sediment to the size and compositional homogeneity of detrital material that entered the basin, and to massive cementation at shallow burial depth that further homogenized the rock and eliminated any compositional differences between lithofacies.

Water saturation is calculated for eight wells in the Pouce Coupe field of the Montney Formation. We use the software GAMLS$^{©}$ to perform a probabilistic multi-variate cluster analysis of well-log data that identifies rock types endmembers (electroclasses) and assigns matrix and fluids properties to them. A matrix and fluids mass-balance is performed, accounting for the assigned fluids properties and rock composition. Our model is computed and calibrated against well-logs and core data. Results show that modeled mineralogy and computed total water saturation fit core measurements in the model well and the validation well and are consistent with previously published data for the Montney Formation. The probabilistic model allows for better estimations of hydrocarbons reserves and permits more credible decision-making when targeting low S_w reservoir zones.

Preface

This thesis is an original work by Noga Vaisblat, who participated in a project funded by a consortium of oil companies and NSERC (Natural Sciences and Engineering Research Council of Canada). Vaisblat was primarily responsible for all work presented in this thesis, including sample cutting and processing, data analysis, creating figures and writing. Main coauthors include Dr. Nicholas B. Harris, Dr. Rick Chalaturnyk, and Dr. Eric V. Eslinger. Dr. Harris is the supervisory author of this thesis and the associated manuscripts (see below) and was also involved with data acquisition and interpretations. Dr. Rick Chalaturnyk provided funding for the project, and Dr. Eslinger provided the platform for petrophysical analysis and modeling (GAMLS), assisted with petrophysical interpretations and advised about clay minerals diagenesis.

Chapter 2 describes diagenesis and its relationship to reservoir quality in the Montney Formation. The manuscript of this chapter is in preparation for publication. Coauthors include Dr. Harris who was involved with data acquisition and interpretations and provided guideless and feedback to the scientific writing, Dr. Rick Chalaturnyk provided funding for the project, and Dr. Korhan Ayranci who conducted core description and lithofacies identification, Dr. Matthew Power who provided QEMSCAN analyses, Dr. Federico Krause and Dr. Chris DeBuhr who assisted with SEM-CL imaging, and Dr. David L. Bish who provided the facilities and assisted in quantitative XRD analyses interpretations. Drs. Vincent Crombez, Tristan Euzen, and Sebastien Rohais were involved in the writing of chapter 2, provided data and assisted with interpretations.

Chapter 3 of this thesis was published as a conference paper to Asia Pacific Unconventional Resources Technology Conference held in Brisbane, Australia, 18-19 November, 2019, as Noga Vaisblat, Alireza Rangriz Shokri, Korhan Ayranci, Nick Harris, and Rick J. Chalaturnyk, "Significance of Rock Compositional Control on Geomechanical Properties and Hydraulic Fracturing of the Montney Formation, Western Canadian Basin". This manuscript will be

submitted to a journal in the future. Chapter 3 describes the geomechanical properties of the Montney Formation siltstone, examines their compositional (mineralogy and organic matter) controls, and their relationship with depositional environment. The chapter also includes a comparison between the geomechanical properties of the Montney siltstone and clay-rich mudrock formations (shales). Coauthors include Dr. Harris who was involved with data acquisition and interpretations and provided guideless and feedback to the scientific writing, Dr. Rick Chalaturnyk provided funding for the project, Dr. Rangriz Shokri who conducted modeling of hydraulic fracturing, Dr. Korhan Ayranci who conducted core description and lithofacies identification, Dr. Matthew Power who provided QEMSCAN analyses, and Dr. David L. Bish who provided the facilities and assisted in quantitative XRD analyses interpretations.

Chapter 4 describes and interprets petrophysical characteristics of the Montney Formations, examines their compositional (mineralogy and organic matter) controls, and their relationship with depositional environment. The chapter also includes a comparison between the petrophysical properties of the Montney siltstone and clay-rich mudrock formations (shales). The manuscript of this chapter is in preparation for publication. Coauthors include Dr. Harris who was involved with data acquisition and interpretations and provided guideless and feedback to the scientific writing, Dr. Rick Chalaturnyk provided funding for the project, Dr. Korhan Ayranci who conducted core description and lithofacies identification, Dr. Matthew Power who provided QEMSCAN analyses, Dr. David L. Bish who provided the facilities and assisted in quantitative XRD analyses interpretations, and Corey Twemlow and Nik Minion who provided porosity and permeability analysis.

Chapter 5 describes a predictive model for water saturation in the Montney Formation. The manuscript of this chapter is in preparation for publication. Coauthors include Dr. Eslinger who provided the platform for the petrophysical analysis and modeling (GAMLS) and assisted with petrophysical interpretations, Dr. Harris who was involved with data acquisition and

So much of the terrain is unknown, but none of it is unknowable.

(If she wakes, Michael Koryta, 2019)

Acknowledgements

Boy what a journey it has been! Eight hectic years of being a student, a teacher, a mom, a wife, a friend (order constantly rotated). So many new experiences, so much more knowledge, so much growing up. All of this could not have happened without the love of my wonderful, lovely, (and cheeky) Mica and Yuval, and without the support of my husband Gal, who is a stable anchor to our family. Above all, my love, thank you for letting me be me.

A debt of gratitude I owe to these three-

To Dr. Nick Harris, my supervisor, who is the best mentor a student could ask for. Thank you, Nick for your support and encouragement. Thank you for the patience that went into editing each abstract and manuscript, and for helping me establish connections all over the world, open doors wherever possible and giving me every opportunity to promote my research. Thank you for trusting me to teach your class and for helping me figure out what king of a teacher I want to be. Mostly, Dr. Harris, thank you for your concern for me and my family's wellbeing.

To Dr. Rick Chalaturnyk, who welcomed me into the RG^2 research group and the world of geomechanical engineering. Thank you, Dr. Rick for the opportunity to expand my horizons in new directions (and do really cool stuff) and for introducing me to the wonderful RG^2 team. What a privilege it is to be part of your research group.

To the late Dr. Eric Eslinger, who taught me most of what I know about well-logs analysis, a good bit of what I know about mineralogy, and about all one can do when both fields are combined. Thank you, Eric for always being in the background, supporting and making sure I am on track. We lost not only a great scientist, but a terrific person and a good friend. You are missed dearly.

A special thanks is due to Dr. Brian Jones who provided advice and guidance. His door was always open, and in more than one occasion he brought perspective back to where it was badly needed.

Table of Contents

Table of Tables

Table of Figures

Chapter 4:

Chapter 5:

Chapter 1 - Introduction

1.1 Overview

Evaluation of reservoir quality is a critical element in assessing the economic viability of developing and producing hydrocarbon plays. In conventional reservoirs, reservoir quality is determined primarily by the petrophysical properties of the rock (porosity and permeability). In unconventional reservoirs, reservoir quality depends also on its geomechanical properties, as production relies on successful hydraulic stimulation. Water saturation is also critical in the assessment of any reservoir type, both because it affects hydrocarbons reserves and because it influences relative permeability of hydrocarbons.

Reservoir quality parameters (porosity, permeability and geomechanical properties) are functions of rock fabric, mineralogy and diagenetic processes, which in turn depend on sediment provenance, depositional processes and environment, burial history and paleo-fluid flow. Lithofacies are manifestations of different depositional environments and commonly have unique compositions and grain size distributions, and thus different initial porosity and permeability (Morad et al., 2010). Initial porosity and permeability affect compaction rate, and control fluid-flow through the rock. These fluids can alter pore water chemistry and initiate diagenetic processes such as dissolution or cement precipitation. Therefore, different lithofacies in a formation may be associated with different diagenetic pathways and eventually, different reservoir quality properties.

Diagenetic models for silt-rich mudstones (siltstone) reservoirs, unlike sandstone and clay-rich mudstones (shale) reservoirs, are poorly developed, and the factors affecting reservoir quality in siltstones, including links between reservoir quality and depositional and diagenetic history are not yet well understood. The Lower Triassic Montney Formation of the Western Canadian Sedimentary Basin, a world-class unconventional resource of gas, gas condensate and oil, is a silt-rich mudstone (siltstone) over most of its subcrop. The availability

1

of long cores across much of the Montney play provides an outstanding opportunity to document diagenetic processes and to study links between diagenesis and reservoir quality.

This thesis presents a comprehensive study of controls on reservoir quality in the Montney Formation and contrasts its characteristics and properties with those of finer grained shale reservoir formations. The study examines the relationships between reservoir quality parameters (porosity, permeability, and geomechanical properties), the depositional environment of the rock (lithofacies; macro- rand microscale rock fabric), rock composition, grain size, and diagenesis, accounting for sediment provenance, burial history, and paleoclimate. Finally, a method for computing water saturation using well-logs mineralogical data is presented.

This thesis addresses the following questions:

(1) What diagenetic processes were/are active in the Montney Formation and how do they affect the mineralogical composition of the siltstone?

(2) Are diagenetic processes in the siltstone related to rock fabric (lithofacies)?

(3) How did compaction, cementation, and secondary porosity development influence the petrophysical properties of the siltstone?

(4) How did compaction and cementation affect the geomechanical properties of the siltstone?

(5) What is the fundamental difference in the control over reservoir quality (porosity, permeability, and geomechanical properties) between silt-rich mudstones (siltstones) and finer grained clay-rich mudstones (shales)?

(6) If diagenesis control rock composition, can rock composition be used to predict water saturation for the Montney siltstone using matrix-fluid mass balance approach (GAMLS MFBG)?

1.2 Overview (Geological Background)

The Montney Formation subcrops over an area of 130,000 km^2 in central and southwestern Alberta and northeastern British Columbia (Fig. 1.1). The formation was deposited on the western margin of Pangea during the Induan and Olenekian stages of the Lower Triassic (Davies et al., 1997; Utting et al., 2005; Henderson et al. 2018), in a fore-arc to retro-foreland setting (Blakey, 2014; Golding et al., 2016; Rohais et al., 2018). Paleogeographic reconstructions suggest that during the Lower Triassic the basin was rotated approximately 30° clockwise from its current position, and positioned at 30° North (Golonka et al., 1994; Davies et al., 1997; Blakey, 2014). Hot and periodically arid climate with seasonal monsoons prevailed in the region (Davies, 1997; Golonka and Ford, 2000; Preto et al., 2010; Sun et al., 2012; Zonneveld and Moslow, 2018).

The Montney Formation was deposited in a westward-dipping and deepening basin. Depositional environments include shoreface facies, near-shore facies, off-shore successions, and submarine fans (e.g. Davies et al., 1997, 2018; Zonneveld et al., 2011; Playter, 2013; Crombez et al., 2016; Euzen et al., 2018; Moslow et al., 2018; Zonneveld and Moslow, 2018). The Laurentian continental margin to the east, containing a wide variety of rock types, was the predominant source for the sediments with a smaller contribution from the Innuitian orogenic wedge to the north (Ross et al., 1997; Beranek et al., 2010; Golding et al., 2016), and a potential volcanic sediment source to the west (Edwards et al., 1994; Crombez et al., 2017; Rohais et al., 2018).

The Montney Formation is subdivided into Upper and Lower Montney siltstone members, separated in eastern and southeastern areas of the subcrop by the Dolomitic Coquina Middle Member. The Middle Member thins and becomes less distinguishable from the Upper and Lower siltstone members to the west (Davies et al., 1997; Dixon, 2000; Moslow, 2000; Zonneveld and Moslow, 2018). The Permian-Triassic unconformity bounds the Montney

3
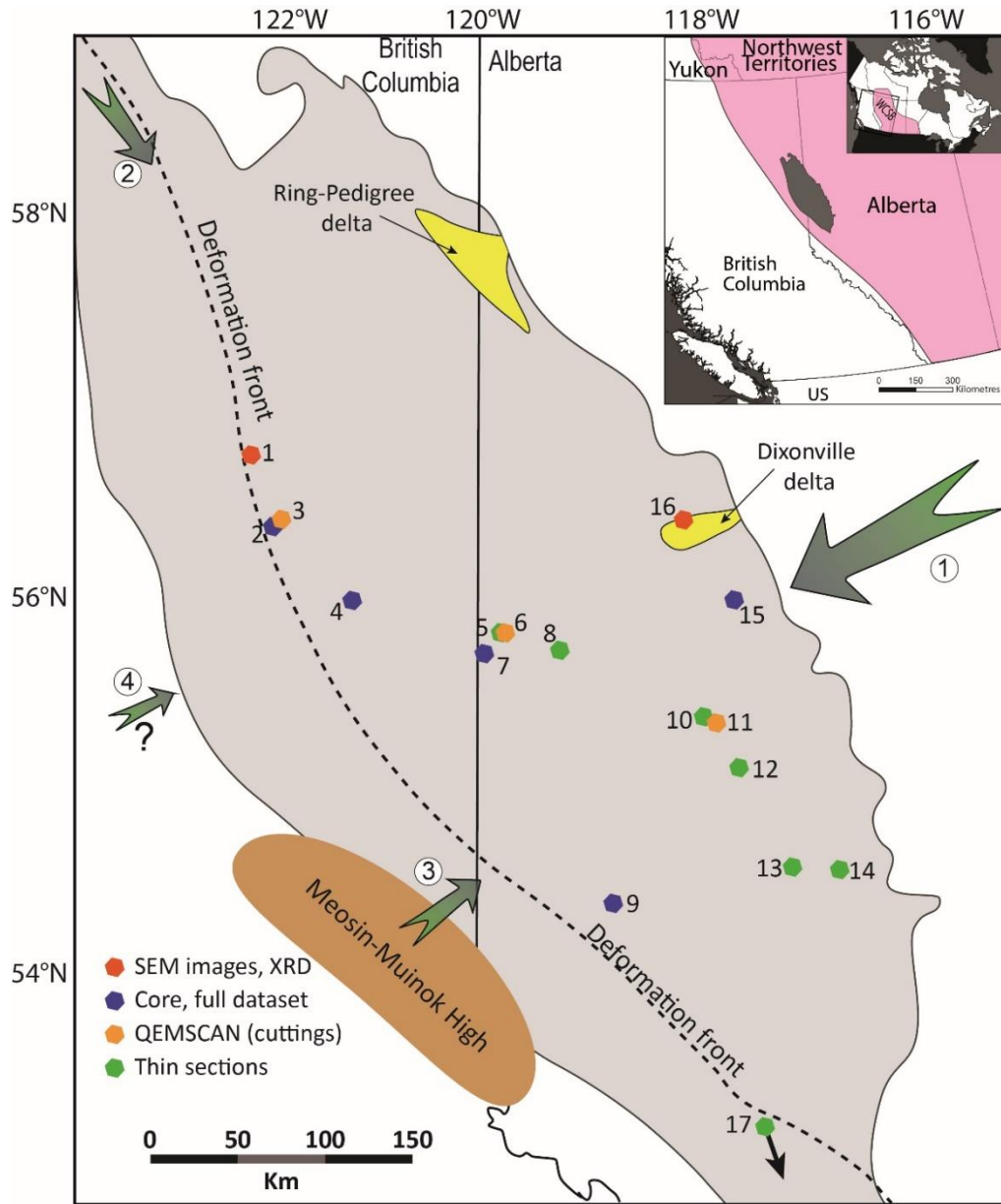
Fig. 1.1: The Montney Formation in Alberta and British Columbia. Insert shows the location of the Montney Formation in the Western Canada Sedimentary basin. Green Arrows show inferred directions of sediments transport into the basin. Arrow size indicates the relative importance of the sediment source. Most of the sediments composing the Montney Formation were sourced from the northwestern Margin of Laurentia, positioned to the east (arrow 1). Smaller amounts of sediment came from the Inuitian orogenic wedge and the Yukon-Tanana accretionary terrain to the north (arrow 2), and from the Meosin-Muinok High to the southwest (arrow 3). A potential minor western sediment source (arrow 4) was also postulated. Most of the updip section of the Formation was eroded, but two deltas (The Dixonville delta and the Ring-Pedigree delta) are preserved in the sedimentary record. Hexagons show location of study wells. Color-coding relates to the dataset obtained from the wells. Map modified after Zonneveld and Moslow (2018).

Formation at its base. The Coplin and sub-Jurassic unconformities, formed during the Late Cretaceous Laramide Orogeny, bound the formation from above in the eastern part of the basin (Fig.2) (Gibson and Edwards, 1990; Edwards et al., 1994; Davies et al., 1997; Moslow, 2000) and reduce its thickness to < 1m in central Alberta. In the western part of the basin (northwestern Alberta and British-Columbia), where the Coplin unconformity cuts through younger intervals, the Montney Formation retains its full thickness, reaching over 350 m, and is overlain by the Doig Formation.
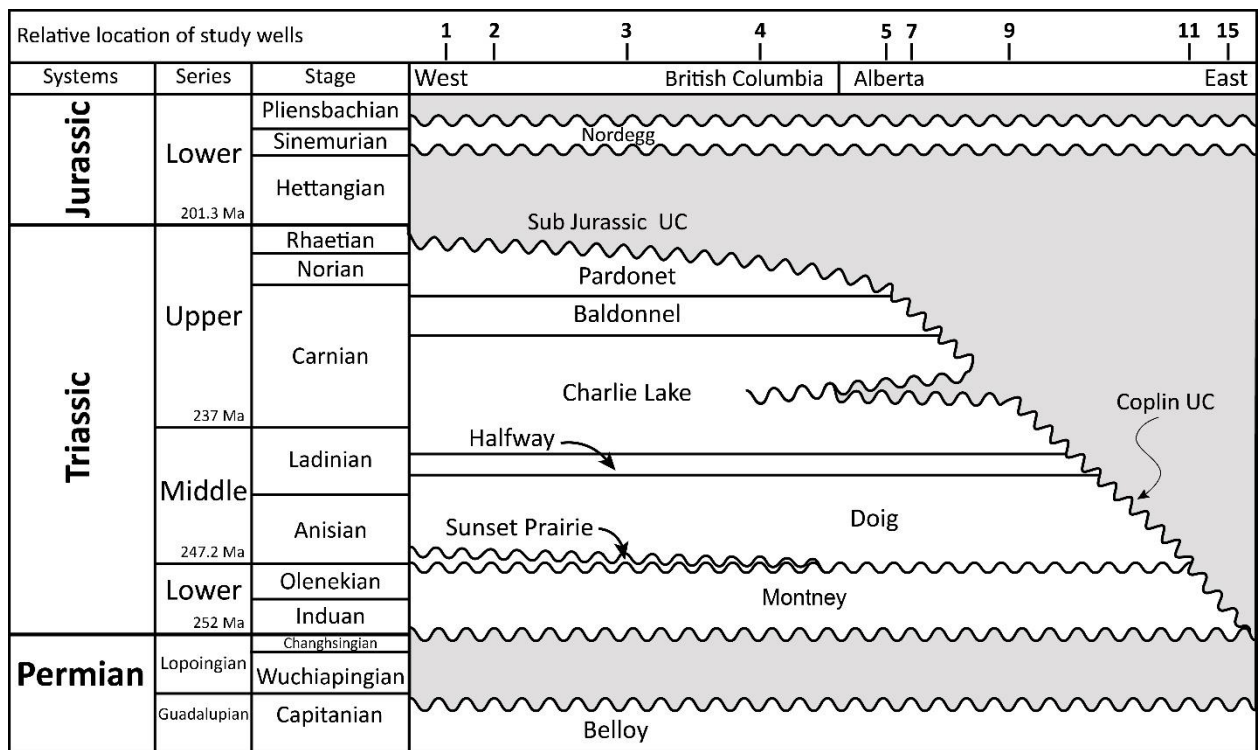
Fig. 2.1: A stratigraphic chart for the Lower Triassic Montney Formation. The location of wells where mineralogy data was obtained for is marked at the top of the chart. UC is unconformity. Ages after Golding et al., 2016.

Burial history analysis indicates that from the time of deposition to the end of the Jurassic (~ 100 million years), the formation was never buried deeper than 1000 m (Ness, 2001; Ducros et al., 2017; Rohais et al., 2018). The Laramide Orogeny, beginning in the Early

Cretaceous, triggered rapid subsidence and initiated high sedimentation rates in the WCSB. The Montney Formation reached its maximum burial depth and hence maximum temperatures at the culmination of this event (ca. 57.8 Ma) (Willett et al., 1997; Ness, 2001; Ducros et al., 2017; Rohais et al., 2018). From the end of the Paleocene to present, the basin has undergone continuous erosion and uplift.

In its present configuration, the Montney Formation exhibits several northeast - southwest trends. The formation deepens from less than 1 km along the eastern subcrop to > 4 Km depth near the Rock Mountains deformation front. Corrected present day bottom-hole temperatures increase from <50°C in the northeast to > 100 °C in the southwest (BC Oil and Gas Commission, 2012), with only the southwestern edge of the formation reaching temperatures >90°C. Thermal maturity ranges from R_o=0.59% in the shallow buried northeastern section to R_o>2% in the deeply buried section to the southwest (Riediger et al., 1990; Sanei et al., 2015; Romero-Sarmiento et al., 2016; Crombez et al., 2017).

1.3 Organization of the thesis

The thesis is composed of four chapters, each focusing on a different aspect of reservoir quality. Chapter 2 describes and interprets the diagenetic evolution of the Montney Formation siltstone and presents the first quantitative analysis of cement volumes in this formation. Diagenesis is also discussed in relation to the burial history (Ness, 2011; Ducrous, 2017) and the climatic and oceanic condition at the time of deposition. Finally, this chapter investigates the relationship between lithofacies, diagenetic events and cement volumes.

Chapters 3 and 4 of the thesis examine the geomechanical and petrophysical properties of the Montney Formation through well-log and core analysis. Relationships between rock composition and fabric (lithofacies) and reservoir quality properties of the rock are discussed and explained in light of the diagenetic history of the rock. In addition, chapters 2 and 3 investigate the main differences between the petrophysical and geomechanical properties of

6

the silt-rich mudstone (siltstone) and several clay-rich mudstone (shale) formations and suggest possible mechanism controlling these differences.

Chapter 5 describes a predictive model for water saturation in the Montney Formation. This chapter focuses on the relationship between rock composition (in particular clay minerals and organic matter), rock petrophysical properties (porosity and permeability), and water saturation, and incorporates insights and models developed in the previous chapters.

1.4 Reference

BC oil and gas commission, 2012. Montney Formation play atlas for NEBC.

Beranek, L.P., Mortensen, J.K., Orchard, M.J., and Ullrich, T., 2010. Provenance of North American Triassic strata from west-central and southeastern Yukon: correlations with coeval strata in the Western Canada Sedimentary Basin and Canadian Arctic Islands. Canadian Journal of Earth Sciences 47, 53-73. https://doi.org/10.1139/E09-065.

Blakey, R.C., 2014. Mesozoic paleogeography and tectonic history - western North America: Triassic tectonics and paleogeography, 245 Ma. http://deeptimemaps.com/north-american-key-time-slices-series. Last accessed july 20, 2019.

Crombez, V., Baudin, F., Rohais, S., Riquier, L., Euzen, T., Pauthier, S., Ducros, M., Caron, B. and Vaisblat, N., 2017. Basin scale distribution of organic matter in marine fine-grained sedimentary rocks: Insight from sequence stratigraphy and multi-proxies analysis in the Montney and Doig Formations. Marine and Petroleum Geology, 83: 382-401.

Crombez, V., Rohais, S., Baudin, F., and Euzen, T., 2016. Facies, well-log patterns, geometries and sequence stratigraphy of a wave-dominated margin: insight from the Montney Formation (Alberta, British Columbia, Canada). Bulletin of Canadian Petroleum Geology, 64(4), 516-537.

Davies, G.R., 1997. Aeolian sedimentation and bypass, Triassic of western Canada, Bulletin of Canadian Petroleum Geology 45(4), 624–642.

Davies, G.R., Watson, N., Moslow, T.F., and Maceachern, J.A., 2018. Regional subdivisions, sequences, correlations and facies relationships of the Lower Triassic Montney Formation, west-central Alberta to northeastern British Columbia, Canada - With emphasis on role of paleostructure. Bulletin of Canadian petroleum geology, 66(1), 23-92.

Davies, G.R., Moslow, T.F., and Sherwin, M.D., 1997. The Lower Triassic Montney Formation, west-central Alberta. Bulletin of Canadian Petroleum Geology, 45(4), 474-505.

Dixon, J., 2000. Regional lithostratigraphic units in the Triassic Montney formation of Western

Canada. Bulletin of Canadian Petroleum Geology, 48(1), 80–83.

Ducros, M., Sassi, W., Vially, R., Euzen, T., and Crombez, V., 2017. 2-D Basin modeling of the Western Canada Sedimentary Basin across the Montney-Doig System: Implications for hydrocarbon migration pathways and unconventional resources potential, in: AbuAli, M.A., Moretti, I., and Bolås, H.M.N. (Eds.), Petroleum Systems Analysis-Case Studies: American Association of Petroleum Geologists Bulletin Memoir, 114. pp. 117-134. https://doi.org/10.1306/13602027M1143703.

Edwards, D.E., Barclay, J.E., Gibson, D.W., Kvill, G.E., and Halton, E., 1994. Triassic strata of the Western Canada Sedimentary Basin, in: Mossop, G.D., and Shetsen, I. (Eds.), Geological Atlas of the Western Canada Sedimentary Basin. Canadian Society of Petroleum Geologists and Alberta Research Council, Calgary, pp. 259–275.

Euzen, T., Moslow, T.F., Crombez, V., and Rohais, S., 2018. Regional stratigraphic architecture of the spathian deposits in western Canada - Implications for the Montney resource play. Bulletin of Canadian Petroleum Geology. 66(1), 175-192.

Gibson, D.W., and Edwards, D.E., 1990. An overview of Triassic stratigraphy and depositional environments in the Rocky Mountain Foothills and Western Interior Plains , Peace River Arch area , northeastern British Columbia. Bulletin of Canadian Petroleum Geology, 38(1), 146-158.

Golding, M.L., Mortensen, J.K., Ferri, F., Zonneveld, J.-P., and Orchard, M.J., 2016. Determining the provenance of Triassic sedimentary rocks in northeastern British Columbia and western Alberta using detrital zircon geochronology, with implications for regional tectonics. Canadian Journal of Earth Sciences, 53(2), 140-155. https://doi.org/10.1139/cjes-2015-0082.

Golonka, J., and Ford, D., 2000. Pangean (Late Carboniferous–Middle Jurassic) paleoenvironment and lithofacies. Palaeogeography, Palaeoclimatology, Palaeoecology, 161(1-2), 1-34. https://doi.org/10.1016/S0031-0182(00)00115-2.

Golonka, J., Ross, M.I., and Scotese, C.R., 1994. Phanerozoic paleogeographic and paleoclimatic modeling maps, in: Embry, A.F., Beauchamp, B., and Glass, D.J. (Eds.), Pangea, Global Environments and Resources. Canadian Society of Petroleum Geologist, Calgary, 1-47.

Henderson, C.M., Golding, M.L., and Orchard, M.J., 2018. Conodont sequence biostratigraphy of the Lower Triassic Montney Formation. Bulletin of Canadian Petroleum Geology, 66(1), 7-22.

Morad, S., Al-Ramadan, K., Ketzer, J.M., and De Ros, L.F., 2010. The impact of diagenesis on the heterogeneity of sandstone reservoirs: A review of the role of depositional facies and

sequence stratigraphy. American Association of Petroleum Geologists Bulletin, 94(8), 1267–1309. https://doi.org/10.1306/04211009178.

Moslow, T.F., 2000. Reservoir architecture of a fine-grained turbidite system: Lower Triassic Montney Formation, Western Canada Sedimentary Basin, in: Weimer, P. (Ed.), Deep-Water Reservoirs of the World. SEPM Society for Sedimentary Geology, Houston, Texas, pp. 686-713. https://doi.org/10.5724/gcs.00.15.0686.

Moslow, T.F., Haverslew, B., and Henderson, C.M., 2018. Sedimentary facies, petrology, reservoir characteristics, conodont biostratigraphy and sequence stratigraphic framework of a continuous (395m) full diameter core of the lower Triassic Montney Fm, northeastern British Columbia. Bulletin of Canadian Petroleum Geology, 66(1), 259-287.

Ness, S.M., 2001. The application of basin analysis to the Triassic succession, Alberta Basin: an investigation of burial and thermal history and evolution of hydrocarbons in Triassic rocks. Ms.C. Thesis, Department of Geology and Gepophysics, University of Calgary, Calgary, Alberta, Canada.

Playter, T.L., 2013. Petrographic and x-ray microtomographic analysis of the Upper Montney Formation, Northeastern British Columbia, Canada. Ms.C. Thesis, Department of Earth and Atmospheric Sciences, University of Alberta, Edmonton, Alberta, Canada.

Preto, N., Kustatscher, E., and Wignall, P.B., 2010. Triassic climates - State of the art and perspectives. Palaeogeography, Palaeoclimatology, Palaeoecology, 290(1-4), 1-10. https://doi.org/10.1016/j.palaeo.2010.03.015.

Riediger, C.L., Fowler, M.G., Brooks, P.W., and Snowdon, L.R., 1990. Triassic oils and potential Mesozoic source rocks, Peace River Arch area, Western Canada Basin. Organic Geochemistry, 16(1-3), 295–305. https://doi.org/10.1016/0146-6380(90)90049-6.

Rohais, S., Crombez, V., Euzen, T., and Zonneveld, J.-P., 2018. Subsidence dynamics of the Montney Formation (Early triassic, western Canada sedimentary basin): Insights for its geodynamic setting and wider implications. Bulletin of Canadian Petroleum Geology, 66(1), 128-160.

Romero-Sarmiento, M.F., Euzen, T., Rohais, S., Jiang, C., and Littke, R., 2016. Artificial thermal maturation of source rocks at different thermal maturity levels: Application to the Triassic Montney and Doig formations in the Western Canada Sedimentary Basin. Organic Geochemistry, 97, 148-162. https://doi.org/10.1016/j.orggeochem.2016.05.002.

Ross, G.M., Gehrels, G.E., and Patchett, P.J., 1997. Provenance of Triassic strata in the Cordilleran miogeocline , western Canada. Bulletin of Canadian Petroleum Geology, 45(4), 461-473.

Sanei, H., Wood, J.M., Ardakani, O.H., Clarkson, C.R., and Jiang, C., 2015. Characterization

of organic matter fractions in an unconventional tight gas siltstone reservoir. International Journal of Coal Geology, 150-151, 296-305. https://doi.org/10.1016/j.coal.2015.04.004.

Sun, Y., Joachimski, M.M., Wignall, P.B., Chunbo, Y., Chen, Y., Jiang, H., Wang, L., Lai, X., and Yan, C., 2012. Lethally hot temperatures during the Early Triassic greenhouse. Science, 338, 366-370. https://doi.org/10.1126/science.1224126.

Utting, J., Zonneveld, J.-P., MacNaughton, R.B., and Fallas, K.M., 2005. Palynostratigraphy, lithostratigraphy and thermal maturity of the Lower Triassic Toad and Grayling, and Montney formations of western Canada, and comparisons with coeval rocks of the Sverdrup Basin, Nunavut. Bulletin of Canadian Petroleum Geology, 53(1), 5-24. https://doi.org/10.2113/53.1.5.

Willett, S.D., Issler, D.R., Beaumont, C., Donelick, R.A., and Grist, A.M., 1997. Inverse modeling of annealing of fission tracks in apatite; 2, Application to the thermal history of the Peace River Arch region, Western Canada sedimentary basin. American Journal of Science, 297(10), 970-1011. https://doi.org/10.2475/ajs.297.10.970.

Zonneveld, J.-P., and Moslow, T.F., 2018. Palaeogeographic setting, lithostratigraphy, and sedimentary framework of the Lower Triassic Montney Formation of western Alberta and northeastern British Columbia. Bulletin of Canadian Petroleum Geology, 66(1), 93-127.

Zonneveld, J.-P., Golding, M.L., Moslow, T.F., Orchard, M.J., Playter, T.L., and Wilson, N., 2011. Depositional framework of the Lower Triassic Montey Formation, West-central Alberta and Northeastern British Columbia, in: Geoconvention. CSPG CSEG CWLS, Calgary, AB, Canada, pp. 1-4.

Chapter 2 - Compositional and diagenetic evolution of a siltstone, with implications for reservoir quality; an example from the Lower Triassic Montney Formation in western Canada

Noga Vaisblat, Nicholas B. Harris, Korhan Ayranci, Matthew Power, Chris DeBhur, David L. Bish, Rick Chalaturnyk, Federico Krause, Vincent Crombez, Tristan Euzen, Sebastien Rohais (Manuscript in preparation)

Abstract

Diagenetic models for silt-rich mudstone (siltstone) are less well developed than those for sandstone and clay-rich mudstone. In addition, the influences of diagenetic processes on reservoir quality in siltstone formations are poorly understood. Here we examine the roles of depositional facies, detrital composition, and diagenetic processes in the compositional evolution and reservoir quality of the Lower Triassic Montney Formation, a prominent siltstone dominated reservoir in western Canada with very large reserves of oil, gas-liquids and natural gas. We applied high-resolution, advanced petrographic methods including FEG-SEM (SE, BSE, EDX and SEM-CL), XRD, and QEMSCAN technologies, as well as He-pycnometry on samples from 17 different locations that represent a range of depths and thermal maturities. Cross-cutting and overgrowth relationships and volumes of authigenic phases demonstrate massive precipitation of quartz, feldspar, dolomite, calcite and anhydrite cements at shallow burial depths, leading to compositional homogeneity among different lithofacies. Unlike clay-rich mudstone, siltstones preserve relatively high porosity and permeability at shallow burial depth, which allow for relatively high rates of fluid flow through the rock, possibly driven by reflux of concentrated seawater in nearshore saltpans. In contrast to sandstones, deep burial diagenesis played a relatively minor role in the compositional

11

evolution of the Montney Formation siltstone and is expressed in the form of pressure solutions and minor amounts of fibrous illite precipitation.

2.1 Introduction

With the development of unconventional reservoirs over the past several decades, much attention has been focused on understanding mudstones diagenetic evolution (for example Nadeau et al., 2005; Laughrey et al., 2011; Milliken and Olson, 2017; Roberts and Elmore, 2018). Mudstones are defined as rocks composed predominantly of clay and silt size grains (< 62.5 μm) (Aplin et al., 1999; Flemming, 2000; Macquaker and Adams, 2003; Lazar et al., 2015). Several schemes are available for classifying these fine-grained sediments (Shepard, 1954; Prejup, 1988; Flemming, 2000; Macquaker and Adams, 2003; Lazar et al., 2015), but grain size variations are rarely discussed when mudstone diagenesis is studied. In particular, no distinction is made between, silt-dominates and clay-dominated mudrocks, although their diagenetic histories may be substantially different. Yet, mechanical and chemical diagenesis are the main factors that influence porosity and permeability development of reservoirs following deposition, both in turn influenced by the grain size and sorting of the deposited sediment.

In this paper, we investigate the diagenesis of the silt rich mudstone (siltstone) composing the Lower Triassic Montney Formation, and compare our findings with diagenetic studies of clay rich mudstones (shales). With estimated reserves of 450 TCF of gas, 14,520 MMB of gas liquids, and 1125 MMB of oil (National Energy Board, Government of Canada, 2013), the Montney Formation is a major host of hydrocarbons reservoir in the Western Canadian Sedimentary Basin (WCSB) and one of the most important siltstone hydrocarbon reservoirs in the world.

We examine the relationships between reservoir quality, the lithostratigraphic framework of the formation, the detrital and authigenic components in the rock, and the presence and distribution of organic matter. Because porosity and permeability in this reservoir are

functions of these relationships, a thorough and complete understanding of the temporal and geographic variability in these components is key to understanding the paragenesis and development of this reservoir. The sedimentary and diagenetic models developed in this study are critically important because they provide the information that will facilitate the interpretation and understanding of siltstone reservoirs elsewhere in the world.

2.2 Geological setting

The Montney Formation covers over 130,000 km^2 in central and southwestern Alberta and northeastern British Columbia (Fig. 2.1). The formation was deposited on the western margin of Pangea during the Lower Triassic (Induan and Olenekian) (Davies et al., 1997; Utting et al., 2005; Zonneveld et al., 2010; Henderson et al., 2018), in a back-arc to foreland setting (Ferri and Zonneveld, 2008; Golding et al., 2016; Rohais et al., 2018). Paleogeographic reconstructions suggest that the basin was rotated approximately 30° clockwise from its current position, and positioned at 30° North (Golonka et al., 1994; Davies et al., 1997; Blakey, 2014). Hot, periodically arid climate with seasonal monsoons prevailed in region during the Lower Triassic (Davies, 1997; Golonka and Ford, 2000; Preto et al., 2010; Sun et al., 2012; Zonneveld and Moslow, 2018).

Extensive sedimentological studies of the Montney Formation describe deposition in a westward-dipping and deepening basin. Depositional environments varied, and sediments include shoreface facies, near-shore facies, off-shore successions, and submarine fans (e.g. Davies et al., 1997, 2018; Zonneveld et al., 2011; Playter, 2013; Crombez et al., 2016; Euzen et al., 2018; Moslow et al., 2018; Zonneveld and Moslow, 2018). Sediments comprising the Montney Formation were predominantly derived from the northwestern Laurentian continental margin to the east of the basin, with a smaller contribution from the Inuitian orogenic wedge and the Yukon-Tanana accretionary terrain to the north of the basin (Fig. 2.1) (Ross et al., 1997; Beranek et al., 2010; Golding et al., 2016). The Meosin-Muinok high to southwest of the basin (Fig. 2.1) was another potential sediment source, although it not clear whether this
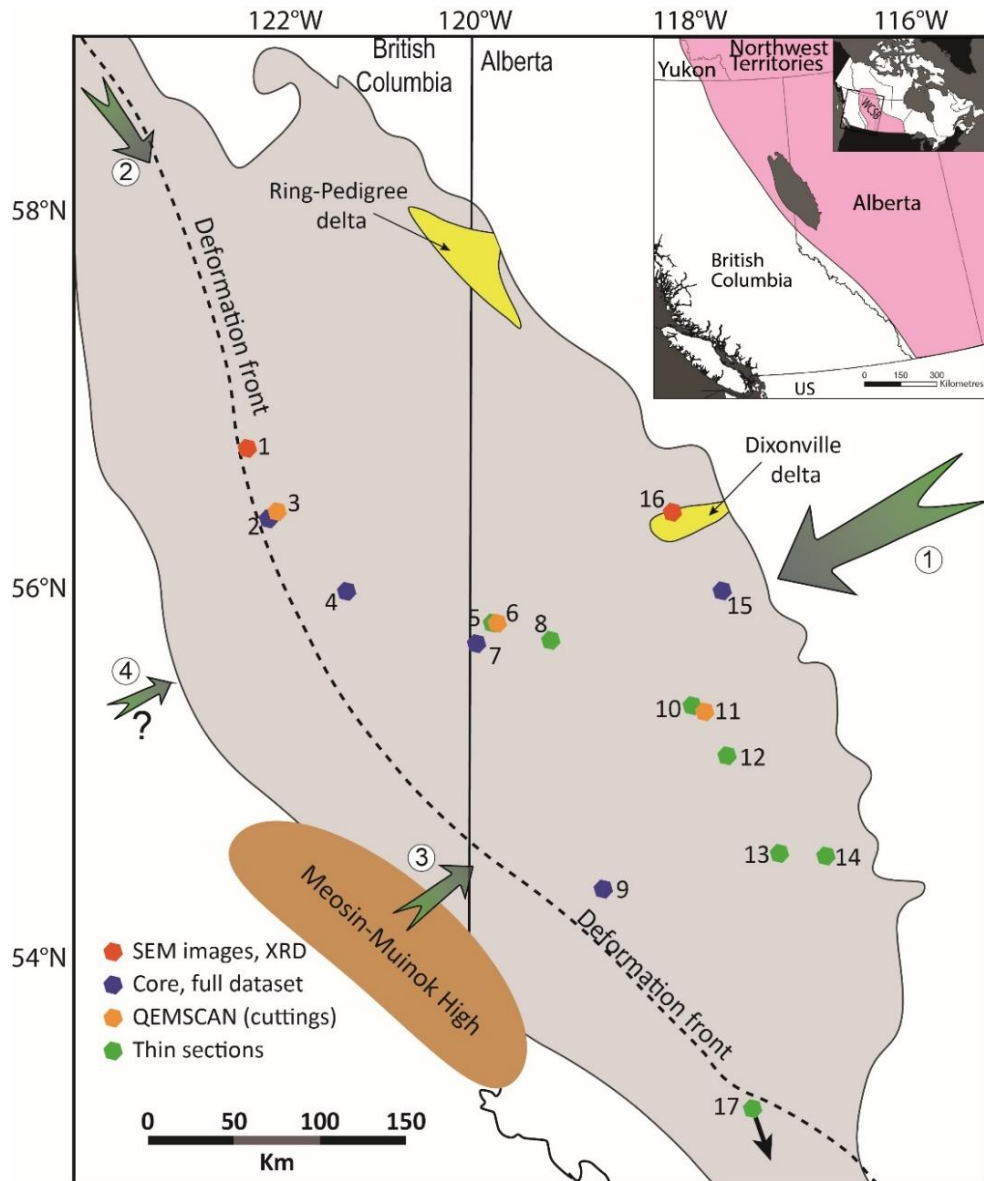
Fig. 2.1: A map of the Montney Formation in Alberta and British Columbia. Insert shows the location of the Montney Formation in the Western Canada Sedimentary basin. Green Arrows show inferred directions of sediments transport into the basin. Arrow size indicates the relative importance of the sediment source. Most of the sediments were sourced from the northwestern Margin of Laurentia, positioned to the east (arrow 1). Smaller amounts of sediment came from the Inuitian orogenic wedge and the Yukon-Tanana accretionary terrain to the north (arrow 2), and from the Meosin-Muinok High to the southwest (arrow 3). A potential minor western sediment source (arrow 4) was also postulated. Most of the updip section of the Formation was eroded, but two deltas are preserved (yellow). Hexagons show location of study wells. Color-coding relates to the dataset obtained from the wells (see table 1 for more details). Full dataset includes core description, SEM and SEM-CL imaging, thin section analysis, QEMSCAN analysis on rock chips, porosity, and TOC. Map modified after Zonneveld and Moslow (2018).

high existed later than the Griesbachian (Early Induan) (Zonneveld and Moslow, 2014, 2018). Finally, it is possible that a portion of the sediments in the Montney Formation was sourced from accretionary terrains postulated to of the sediments in the Montney Formation was sourced from accretionary terrains postulated to be positioned to the west of the basin at Lower Triassic time (Zonneveld and Moslow, 2018 and reference therein) (Fig. 2.1).

The Montney Formation is subdivided into Upper and Lower Montney siltstone members, separated in the east and southeast by the Dolomitic Coquina Middle Member. The Middle Member becomes thinner and less distinguishable from the Upper and Lower siltstone members westwards (Davies et al., 1997; Dixon, 2000; Moslow, 2000; Zonneveld and Moslow, 2018). The Permian-Triassic unconformity bounds the Montney Formation at its base. The Coplin and sub-Jurassic unconformities, formed during the Late Cretaceous Laramide
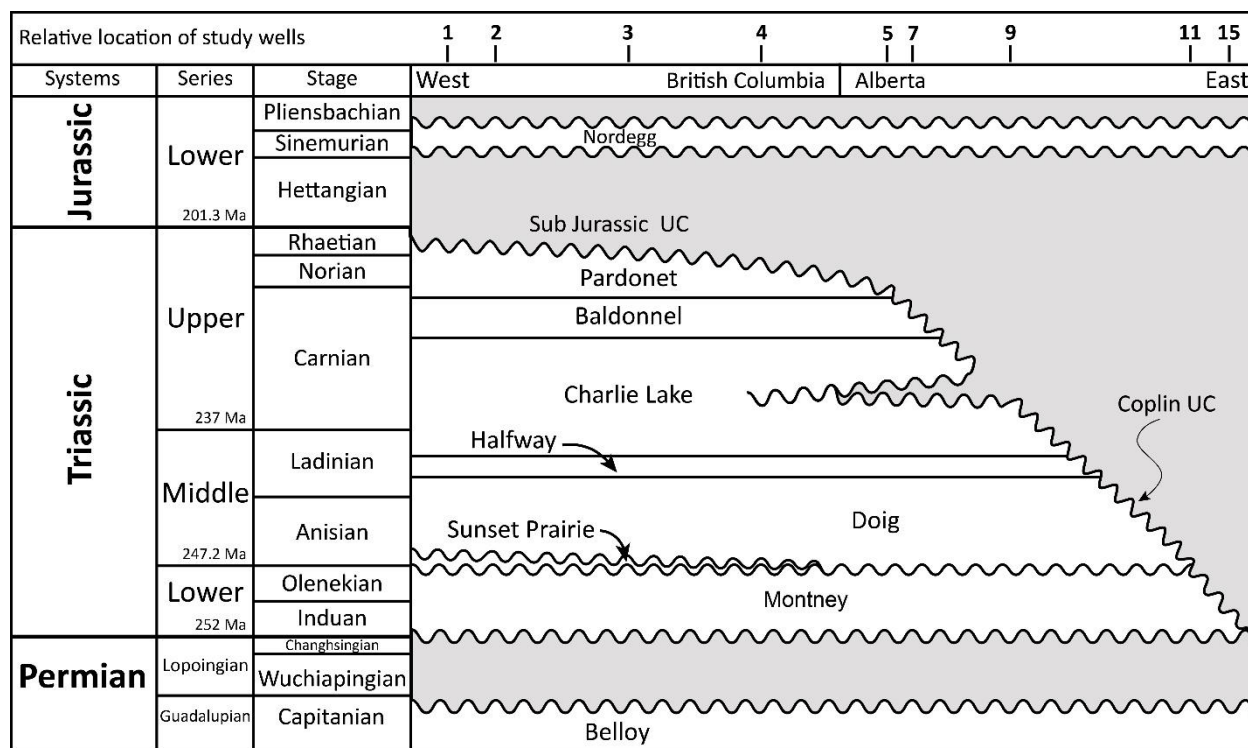
Fig. 2.2: A chronostratigraphic chart for the Lower Triassic Montney Formation. The location of wells where mineralogy data was obtained for is marked at the top of the chart. UC is unconformity. Ages after Golding et al., 2016.

Orogeny, bound the formation from above in the eastern part of the basin (Fig. 2.2) (Gibson and Edwards, 1990; Edwards et al., 1994; Davies et al., 1997; Moslow, 2000) and reduce its thickness to < 1m in central Alberta. In the western section of the basin (northwestern Alberta and British-Columbia) where the Coplin unconformity cuts through younger intervals, the Montney Formation retains its full thickness, reaching over 350 m, and is overlain by the Sunset Prairie Formation (Furlong et al., 2018) or the Doig Formation.

Burial history analysis indicates that from the time of deposition to the end of the Jurassic (a time span of ~ 100 million years), the formation was never buried deeper than 1000 m (Ness, 2001; Ducros et al., 2017; Rohais et al., 2018). The Laramide Orogeny, beginning in the Early Cretaceous, triggered rapid subsidence and initiated high sedimentation rates in the WCSB. The Montney Formation reached its maximum burial depth and hence maximum temperatures at the culmination of this event (ca. 57.8 Ma) (Willett et al., 1997; Ness, 2001; Ducros et al., 2017; Rohais et al., 2018). From the end of the Paleocene to present, the basin has undergone continuous erosion and uplift.

In its present configuration, the Montney Formation exhibits several northeast - southwest trends. The formation shallows to the northeast from > 4 Km depth near the deformation front in the west to less than 1 Km along the eastern subcrop. Corrected present day bottom-hole temperatures increase from <50°C in the northeast to > 100 °C in the southwest (BC Oil and Gas Commission, 2012), with only the southwestern edge of the formation reaching temperatures >90°C. Thermal maturity ranges from R_o=0.59% in the shallow buried northeastern section to R_o>2% in the deeply buried section to the southwest (Riediger et al., 1990; Ibrahimbas and Riediger, 2004; Sanei et al., 2015; Crombez, 2016; Romero-Sarmiento et al., 2016; Wood and Sanei, 2016; Crombez et al., 2017). Those northeast-southwest trends are locally disturbed by syndepositional tectonism or paleotopography inherited from the pre-Triassic basin structure (Davies et al., 1997, 2018; Moslow and Davies, 1997; Zonneveld and Moslow, 2014, 2018; Moslow et al., 2018; Rohais et al., 2018).

2.3 Methodology

2.3.1 Materials and sampling

Our analyses are based on a combination of drill cuttings samples and core samples, selected to represent a range of grain sizes and depositional facies. Table 2.1 summarizes all sample types, sampling intervals, and analyses obtained for each of the study wells. Where possible, sample splits for all analysis were taken from the same set of samples. Four long cores were selected for extensive analyses, based on the availability of cores intersecting all or most of the Montney Formation interval. Two cores represent distal and deeply buried section of the basin (wells 2 and 4); one well was selected to represent more proximal, deeply buried section of the basin (well 9), and the last well was selected to represent a proximal section of the basin that is buried to a shallow depth. Additional thin sections (9) and core/outcrop samples (18) from thirteen other locations were examined to provide comprehensive coverage of the formation. The locations for all sampled wells in this study are presented in Fig. 2.1.

2.3.2 Core description

Detailed sedimentological descriptions were obtained for four cores (total length of 615 m, excluding a total of 51.5 m of missing core sections), recording sedimentary features as small as 1 cm to inform the suite of lithofacies present. Lithofacies were identified and distinguished on the basis of: (1) lithology, (2) grain size, (3) physical sedimentary structures, (4) trace fossil assemblages, and (5) bioturbation intensity (BI).

The lithological classification scheme was adopted from the Macquaker and Adams (2003) mudstones classification. According to this classification, mudstones are defined as sedimentary rocks comprised of at least 50% grains that are silt-size or smaller, and a rock is described based on its sedimentary structures and all components that form more than

Table 2.1: Data set summary

Well #	Well location	Sample type	depth range (m)	Core description	SEM/ SEM-CL	Thin sections	Quantitative XRD	QEMSCAN	Matrix porosity	TOC
1	d-48-A/94-B-9	Core chips	1963 - 2068		15[c]					
2	16-17-083-25w6m	Core samples	2396 - 2364	available	31	6	4	70 (2-16)[d,e]	37 (2-19)[e]	45 (2-19)[e,f]
3	12-36-83-25W6	Cuttings	1855 - 2380					98 (5-20)		98 (5-20)[g]
4	16-29-079-20W6	Core samples	2616 - 2793	available	4	11	9	62 (1-5)	62 (1-6)	43 (2-11)[f]
5	14-14-76-12W6	Cuttings	2175 - 2545					55 (5-10)		25 (5)[g]
6	06-27-076-12W6	Thin section	2462.5 - 2447.3			2				
7	06-03-079-13W6	Pseudocuttings[b]	1930.5 - 2244.4					297 (1)	109 (1-6)	75 (1-8)
8	103/08-19-075-08W6	Thin section	2226			1				
9	05-24-63-6W6	Core samples	3272 - 3388	available	7	15	2	40 (2-3)	50 (0.5-5)	40 (2-3)[f]
10	16-10-073-26W5	Thin section	1793.2 - 1794.5			2				
11	06-33-072-25W5	Cuttings	1590 - 1740					28 (5)		30 (5)[g]
12	102/07-20-70-24W5	Thin section	1744.75			1				
13	07-01-065-22W5	Thin section	1960.5			1				
14	04-36-064-19W5	Thin section	1889.75			1				
15	103/05-20-079-22W5	Core samples	860 - 933	available	15	26[h]	9	66 (1-2)	37 (1-3)	25 (1-6)[f]
16	15-23-086-01W6	Core samples	881		3		3			
17	Norquay lookout[a]	Thin section	3.9			1				

[a]For sampling details see Crombez et al. (2016).

[b]Crushed and homogenized 1 m intervals.

[c]Number of samples analysed.

[d]Sampling interval for the specific analysis, meters.

[e]Large distance between samples due to missing core.

[f]TOC in wt%, obtained from Leco TOC analysis.

[g]TOC in wt%, obtained from RockEval analysis.

[h]Thin sections were also exhamined under table-top CL microscope.

10% of the rock volume. A rock can be dominated by a component (>90%), rich in a component (50-90%) or bearing a component (10-50%).

Lithofacies were grouped into two groups based on their present-day apparent grain size distribution as measured by QEMSCAN analysis (see below). Present-day apparent grain size includes the detrital grain and cement overgrowths if present. Thus, the present-day apparent grain size reflects both the water energy at the environment of deposition and the degree of cementation surrounding the detrital grains.

2.3.3 Petrography

Petrographic observations were obtained from thin sections and SEM analysis. Grain size in most of samples is coarse silt size or smaller (<63 μm), rendering a point count via standard optical microscopy unreliable. Therefore, quantitative data was collected from Scanning Electron microscopy (SEM) images, and thin section analysis focused on identifying coarse diagenetic phases (calcite, dolomite, and anhydrite cements). Samples for thin sections were selected to represent all lithofacies described in the four long cores. Thin sections were polished to 30 μm and half of each thin section was stained with alizarin red and potassium ferricyanide to facilitate carbonate minerals identification. We examined 73 thin sections under an Axio Zeiss Scope.A1 optical microscope equipped with a CITL Mk5 cold-cathode cathodoluminescence unit.

We used SEM analysis to study minerals morphology, distinguish between detrital grains and cements, constrain the paragenetic sequence based on overgrowths and cross-cutting relationships between minerals and define the timing of cementation relative to compaction. Petrographic analysis was also used to identify grain- or cement-supported fabrics and to distinguish mobilized hydrocarbons from depositional macerals.

Both the freshly exposed surface of broken core chips and polished or ion-milled surfaces were examined. Polished samples were ion-milled with a Fischione Model 1060 SEM Mill at the University of Alberta. All samples were coated with gold or carbon prior to SEM

investigation. SEM and energy dispersive X-ray spectroscopy (EDS) analysis was carried out on a JEOL 6301F Field Emission SEM (FE-SEM) or a Zeiss EVO LS15 EP-SEM, with an accelerating voltage of 20 kV, at the University of Alberta.

To evaluate cementation volumes and detrital quartz grain size, 16 ion-milled samples were analyzed with a FEI Quanta 250 FEG SEM equipped with a GATAN MonoCL4 detector (SEM-CL) and a Bruker Quantax EDX at the University of Calgary. For each of these samples, three (1000X magnification) or four (750X magnification) areas were randomly selected perpendicular to bedding and secondary-electron, back-scattered electron, and cathodoluminescence images were recorded, along with energy-dispersive spectra. A 437-point grid was used for point counting on each image. EDS elemental maps were used to identify the mineral at each of the grid points, and SEM-CL images were used for separating detrital from authigenic phases. Errors associated with point count analysis were calculated following the method described in Van Der Plas and Tobi (1965). Detrital grain size was determined by measuring the longest axis of detrital quartz grains, and sphericity ratio was obtained by dividing the short axis by the length of the perpendicular, long axis at mid height.

2.3.4 Mineral composition and grain size

In addition to the point count analysis described above, mineralogical composition for a large number of samples was obtained through QEMSCAN analysis. Quantitative x-ray diffraction (XRD) analysis was conducted on a small sample subset to verify QEMSCAN analysis results.

All 178 drill cutting samples (wells 3, 5, and 11), together with 238 core chips samples collected in constant intervals (wells 2, 4, 9, and 15) and 297 pseudocutting samples (well 7) were selected for mineralogical analysis. A ~5 g sub-sample was randomly separated from each drill cuttings sample and sent for analysis. From each core samples, a small (~ 2 cm^2), visually representative chip was cut perpendicular to bedding and analyzed. For well 7, a continuous sliver was cut along the entire length of the core and divided into 1-m intervals.

Each interval was then crushed and mixed to generate pseudo-cuttings and a random subsample from each section (~50 g) was sent for QEMSCAN analysis.

Quantitative mineralogical composition, including clay minerals, average mineral size for each of the mineralogical phases identified, average grain size for feldspars and macroporosity values (pores >5 μm) were determined by QEMSCAN analysis at SGS Canada laboratories in Burnaby, BC, Canada. Repeatability of QEMSCAN measurements is very high (commonly <2% difference between repeated measurements of the same sample (Power, pers. Com.). The main limitation of the QEMSCAN method is that the minimal grain/mineral size reported is limited by the pixel size selected for analysis, 4.8 μm in this study. However, clay minerals in this study were commonly aggregated into clumps rather than single laths, and we found that a pixel size of 4.8 μm is sufficient for appropriate description of the rock.

Mineral size reported from QEMSCAN analysis is an average calculated from the horizontal intercept lengths of mineral crystals within a sample. However, if crystals of the same mineralogical phase are adjoining, QEMSCAN analysis might report those grains as a single large particle. For this reason, grain size results from QEMSCAN analysis that are larger than the 85th percentile (P_{85}) were considered outliers.

To obtain grain size (as opposed to particle size) from QEMSCAN analysis, the mineral phase under interest is isolated from the dataset and touching particles are separated. Then, particles are grouped into size-bins by the length of their apparent long axis. Results are reported as percent area of the mineral in each size-bin. We obtained grain size from both K-feldspar and Na-feldspar and calculated the weighted average grain size for each sample based on the relative abundances of the two feldspar. Grain size was not obtained for quartz grains because we were unable to sufficiently separate touching grains. To overcome this obstacle, we manually measured the average quartz grain size on SEM images of 17 samples. We then compared the results with the average grain sizes obtained from QEMSCAN analysis of feldspars. This investigation revealed that the average quartz (measured manually) deviated ±5 μm from the average feldspar grain size obtained from QEMSCAN analysis. Since

this deviation is close to the minimal detection limit of the QEMSCAN, we find the weighted average of feldspar grain size sufficient for describing grain size distribution in our samples.

Grain size analysis in sedimentary rocks is commonly performed using an optical microscope and reported in 0.25 phi (φ) intervals (Folk and Ward, 1957; Saner et al., 1996; Wang et al., 2002). In our study, a larger bin width (~1φ) was selected to avoid data skewing due to pixel size (4.8 μm). Bin sizes are very fine silt (4.8-7.8 μm), fine silt (7.8-15.6 μm), medium silt (15.6-31 μm), coarse silt (31-63 μm), very fine sand (63-125 μm), and fine sand (125-250 μm). Particles with clay compositions are considered to be clay-size. It is important to note that although an effort is made for separating touching grains, it is possible that not all such contacts are identified, particularly where grains are touching along a flat contact. Similar to the mineral size analysis, inclusion of touching grains in the dataset will slightly skew the results towards coarser grain size, and the minimum mineral size reported is limited to 4.8 μm. It is difficult to assess the error associated with measuring grain size using this method, but the error is largest where associated with measuring grains that are close to the pixel size (i.e. grains with diameter close to 5 μm).   Present-day grain size frequency distribution properties were calculated with the geometric formulas suggested by Folk and Ward (1957).

In addition to QEMSCAN analysis, 26 samples were selected for quantitative bulk composition and clay mineral XRD examination. Six samples were analyzed at the James Hutton Institute, Aberdeen, Scotland. X-ray diffraction patterns were recorded with a Panalytical Xpert Pro instrument using Ni-filtered CuKα radiation and an Xcelerator position-sensitive detector, counting for 100 seconds per 0.0167° step between 3-70°2θ. The clay fraction (<2μm) was separated by timed sedimentation in water, prepared as oriented mounts on glass and scanned between 3-45°2θ in the air-dried state and after glycolation. The remaining samples were analyzed at the Mineralogy Facility at the Indiana University in Bloomington. X-ray diffraction patterns were recorded with a Bruker D8 Advance X-Ray Powder Diffractometer, using CuKα radiation and a Si(Li) energy-dispersive detector, counting

for 2 seconds per 0.02° step between 2-70°2θ. Clay fraction (<2μm) was separated by timed sedimentation in water, and concentrates were prepared as randomly oriented mounts on zero-background quartz plates and scanned between 2-20°2θ in the air-dried state and after glycolation.

2.3.5 Porosity

Residual (present day) porosity in the siltstone is a product of mechanical diagenesis, chemical diagenesis, and organic matter diagenesis. Estimates of residual porosity assists in assessing the portion of original porosity lost due to each of the diagenetic processes. QEMSCAN analysis provided macroporosity values (>4.8 μm) and include open pores and pores occluded with organic matter. QEMSCAN macroporosity values are reported for all drill cutting, pseudocutting and core samples analyzed. Point count analysis provided values for primary porosity, secondary porosity, and porosity filled with organic matter for 17 samples. In addition, matrix porosity was measured using a Quantachrome Pentapyc analyzer 5200e at Trican (now AGAT) laboratories in Calgary Alberta (136 samples from wells 2, 4 and 15), Core laboratories in Calgary, Alberta (109 samples, well 7), or Terratek, in Salt Lake City, Utah (50 samples, well 3). Matrix porosity can identify any pore larger than the Helium atom radius (1.4 Å) and is thus considered microporosity.

2.3.6 Organic Matter

Organic matter is filling a portion of the pores in the siltstone. It is thus important to account for this phase when evaluating the porosity evolution in the siltstone. Drill cutting samples (153) were analyzed for total organic content (TOC) using a RockEval VI pyrolysis at IFPEN, France. Details of this analysis are described in Crombez et al. (2016). In addition, 153 core samples and 109 pseudocutting samples were analyzed for TOC using the LECO-TOC method at Geomark Laboratories, Humble, Texas. Samples from wells 2, 4, and 9 were extracted from gas-producing wells and did not require cleaning prior to testing. Samples

from well 15 (an oil-producing well) were cleaned prior to testing in a Dean-Stark device using a mixture of acetone (30 wt%), methanol (23 wt%), and chloroform (47 wt%).

2.4 Results

2.4.1 Core Description

Fourteen lithofacies were identified in the four long cores (Table 2.2, Fig. 2.3). Lithology and physical sedimentary structures were the main criteria used to characterize these facies, but in the upper parts of the formation, (sections that were reassigned to the Sunset Prairie Formation (Furlong et al., 2018), ichnological characteristics were important in defining different lithofacies. Core descriptions for the four wells are provided in appendix 1.

All lithofacies described in this study but one (lithofacies D, a mudstone, comprising 0.2% of the total core length examined) are either silt-dominated or silt-rich mudstones. In the distal downdip wells 2 and 4, the most abundant lithofacies are the laminated siltstone (lithofacies G/H) and the Massive siliceous clayey siltstone (lithofacies J), containing 86% silt-size grains, respectively. Other important lithofacies in the distal wells are the faintly laminated calcareous siltstone (lithofacies F, 83% silt), and the Interbedded siliceous-mudstone and calcareous- siltstone (lithofacies P, 87% silt). The bioturbated, calcareous, sandy siltstone (lithofacies M/N, 73% silt) is found only at the uppermost section of the two distal cores and is part of the newly defined Sunset Prairie Formation (Furlong et al., 2018). Lithofacies G/H (laminated siltstone), and lithofacies J (Massive siliceous clayey siltstone) were also identified in the section identified as the Sunset Prairie Formation, but are not exclusive tothis unit, and in fact comprise much of the Montney Formation (Table 2.3).

In the deeply buried proximal (to the Meosin Muinok High; Fig. 1) well 9, the most abundant lithofacies are the massive sandy siltstone (lithofacies B). The average silt and sand content in this lithofacies are 76% and 19%, respectively, but both grain size classes experience large variations (47-87% for silt 6-47% for sand). Another important lithofacies

in well 9 is the Massive siliceous clayey siltstone (lithofacies J, 86% silt) and the Hummocky to ripple cross-stratified sandy siltstone (lithofacies O, 82% silt).

In the proximal, shallow buried, updip well 15, the dominated lithofacies is Interlaminated siltstone and sandstone (lithofacies A). This lithofacies also has a wide range of silt and sand content. Silt content varies between 31 and 87% with an average of 65%, and sand content varies between 9 and 40% (2 samples have higher sand content of 62 and 53%) and an average of 23%. Dolomitic siltstone (lithofacies E) is the second major lithofacies in well 15. This highly dolomitized lithofacies contains 78 to 98% silt grains (average of 84%), and up to 3% sand grains (average of 2%).

Table 2.2: A summary of all lithofacies characteristics in four Montney core.

Facies	Lithology	Rock type classification [a]	Sedimentary structures	Trace fossil Assemblage	Bioturbation intensity	Average composition			% core2 [d] Distal, deeply buried	% core 4 Distal, deeply buried	% core 9 Proximal, deeply buried	% core 15 Proximal, shallowly buried	% all
						% Clay	% Silt	% Sand					
A	Interlaminated siltstone and sandstone	Sand bearing, silt rich to sand and clay-bearing, silt rich mudstone	Dominant flaser and lenticular bedding, current ripples, rare climbing ripples, mud rip-up clasts and soft sediment deformation	*Thalassinoides, Conichnus, Planolites*, and escape structures	0-2	11.9 (4.5)[b]	65.0 (10.3)	23.1 (11.1)			10.6	53.1	16.8
B	Massive sandy siltstone	Silt-rich to sand-bearing, silt rich mudstone	Rare soft sediment deformation, flame structures, carbonate nodules, mud rip-up clasts, and high-angle cross bedding	N/A	0	5.1 (2.5)	76.0 (11.0)	19.0 (10.7)			37.7	12.0	13.1
C	Bioturbated clay-rich siltstone	Sand and clay-bearing, silt rich mudstone	Horizontal parallel to wavy lamination	*Thalassinoides, Palaeophycus, Planolites*, and *Scolicia* (?)	3-5	15.0[c]	69.0	17.0			0.03	2.0	0.5
D	Mudstone	Silt-bearing, clay-rich mudstone	Horizontal parallel lamination	N/A	0	No data						0.6	0.2
E	Dolomitic siltstone	Dolomite cement-dominated to dolomite cement-rich, silt-dominated to sand and clay-bearing, silt-rich mudstone	Low-high angle bedding, and rare rip-up clasts/ dolomitic breccia	N/A	0	7.2 (3.4)	75.2 (13.3)	17.6 (12.7)				22.4	5.9
F	Faintly laminated calcareous siltstone	Calcite cement-bearing, clay-bearing, silt-rich mudstone	Horizontal parallel lamination, carbonaceous grains, and rare shell debris	Biodeformation structures	0-1	14.6 (4.0)	83.3 (6.8)	2.1 (5.0)	16.5			9.8	6.6
G/H	Laminated siltstone	Silt-dominated to clay-bearing, silt-rich mudstone	Horizontal parallel lamination, rare wavy bedding, current ripples, rare amalgamated current ripples, soft sediment deformation, and presence of dolomite beds	Biodeformation structures, Planolites, laminae disruption and escape structures	0-1	11.8 (3.3)	85.9 (3.2)	2.3 (2.7)	58.4	61.5	10.4		31.1
I	Horizontal to irregularly laminated calcareous siltstone	Calcite cement-bearing, clay-bearing, silt-rich mudstone	Horizontal parallel and wavy lamination, and rare current ripples	Bio-deformation structures	3-5	12.4 (2.9)	85.9 (3.7)	1.7 (0.8)	2.3	2.9			1.2
J	Massive siliceous clayey siltstone	Silica cement-bearing, silt-dominated mudstone to clay-bearing, silt-rich mudstone	Rare dolomite beds	N/A	0	12.5 (3.4)	86.0 (2.9)	1.5 (1.3)	9.2	21.3	20.7		12.6
K	Massive calcareous clayey siltstone	Calcite cement-bearing, clay-bearing, silt-rich mudstone	Rare siltstone beds and lamination	N/A	0	14.9 (4.9)	82.7 (1.8)	2.5 (3.1)	0.8	3.7			1.0
L	Siliceous phosphatic siltstone	Silica cement-bearing, clay-bearing, silt-rich mudstone with phosphate nodules	mm-scale silica-rich lens-shaped structures, and phosphate nodules	Biodeformation structures	0-3	14.9 (2.6)	83.7 (2.6)	1.4 (1.0)	2.8	5.2			1.9
M/N	Bioturbated, calcareous, sandy siltstone	Calcite cement-bearing, sand-bearing, silt-rich mudstone	Rare mud rip-up clasts and phosphate nodules	*Phycosiphon, Teichichnus, Rosselia Cylindrichnus, Planolites, Skolithos, Asterosoma, Palaeophycus, Thalassinoides*, rare *Scolicia, Arenicolithes*, and *Arthicnus*	5-6	5.5 (1.4)	72.7 (1.2)	22.3 (1.2)	2.6	5.3			1.8
O	Hummocky to ripple cross-stratified sandy siltstone	Silt rich to sand-bearing, clay-bearing, silt-rich mudstone	Hummocky cross-stratification, current ripples, climbing ripples, mud rip-up clasts, rare loading structures and soft sediment deformation	Rare *Planolithes*	0-1	6.0 (2.8)	82.0 (2.3)	12.0 (3.5)			20.5		5.4
P	Interbedded siliceous-mudstone and calcareous- siltstone	Silica and calcite cement-bearing silt rich to clay-bearing, silt-rich mudstone	Soft sediment deformation, normal grading, shell debris, mud drapes, mud rip-up clasts, mud escape structures, current ripples, carbonate nodules, rare horizontal parallel lamination, and wavy lamination	N/A	0	10.6 (1.3)	87.2 (1.2)	2.2 (0.5)	7.5				1.8

[a] After Macquaker and Adams, 2003.

[b] Standard deviation 1σ.

[c] One sample.

[d] Facies % of core, normalize to exclude missing core sections.
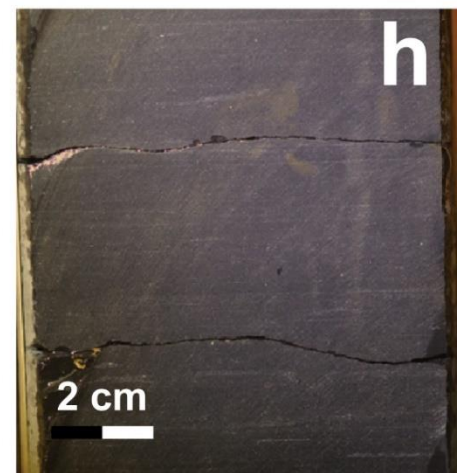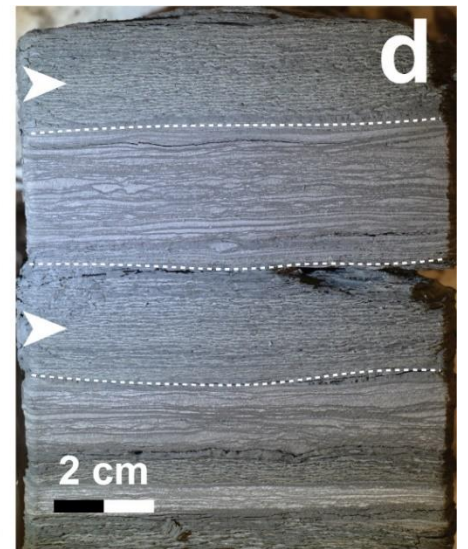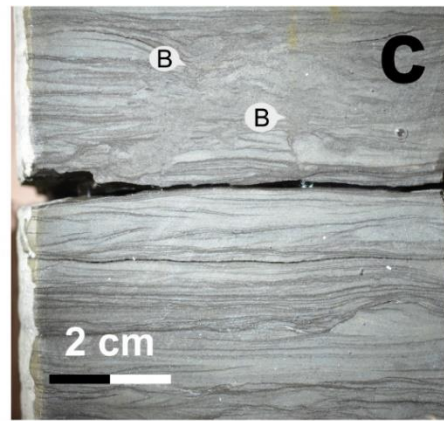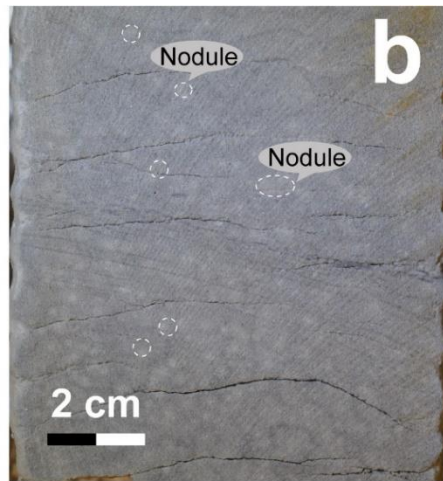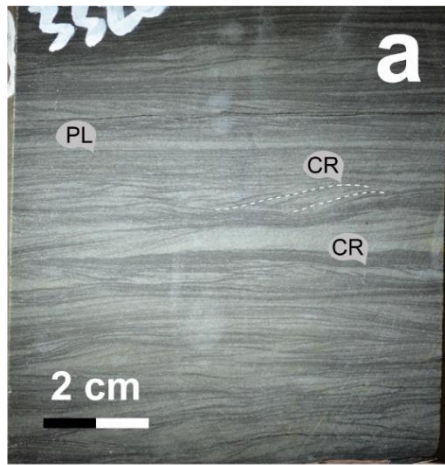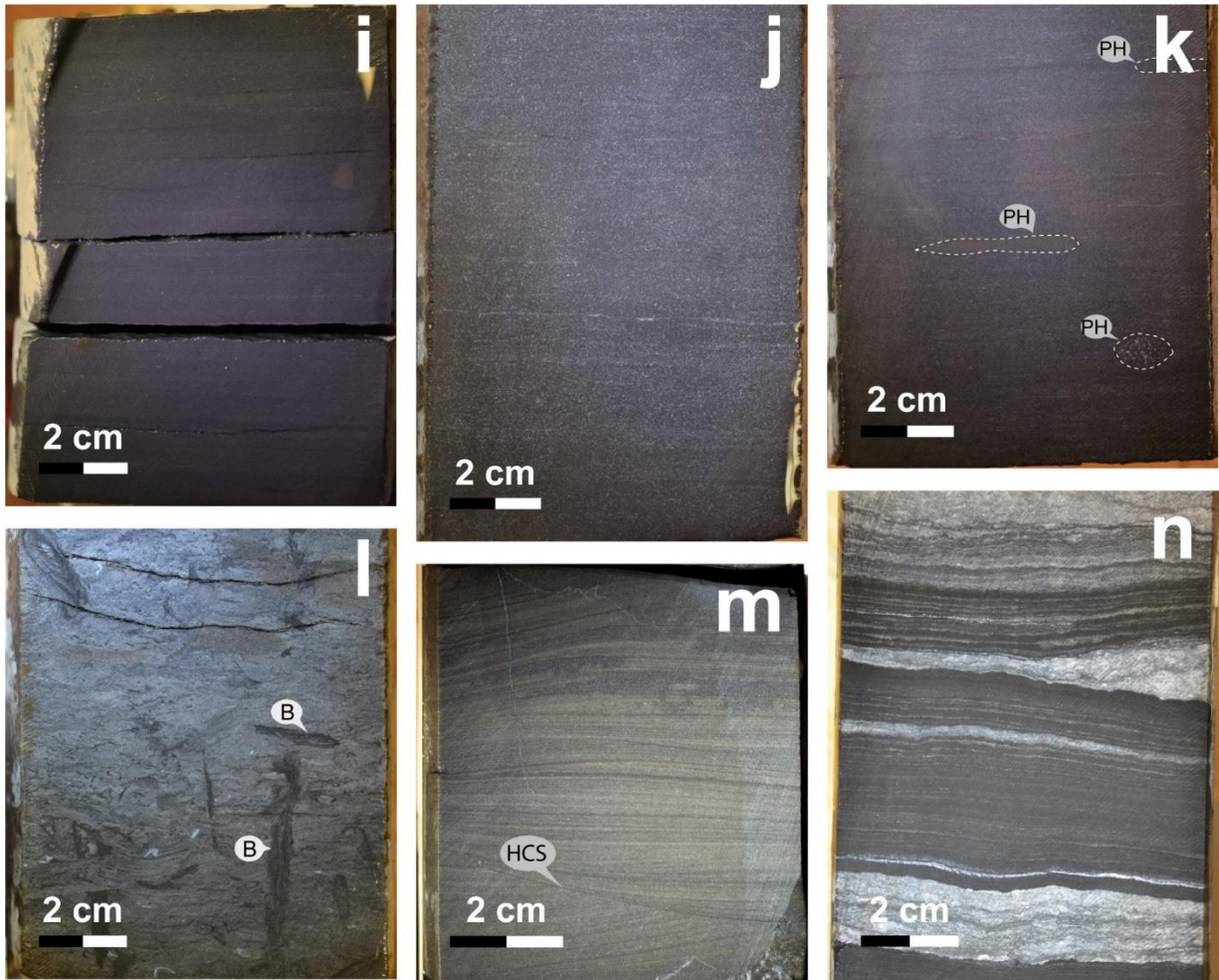
Fig. 2.3: Representative photograph of lithofacies identified in the four Montney Formation cores. (a) Lithofacies A - interlaminated siltstone and sandstone with current ripples. (b) Lithofacies B - massive to convolute bedded Massive sandy siltstone with carbonate concentration (in white). (c) Lithofacies C - bioturbated clay-rich siltstone. (d) Lithofacies D - mudstone with Horizontal parallel lamination (sections where lithofacies D is present are marked by arrows). (e) Lithofacies E - dolomitic siltstone. (f) Lithofacies F - faintly laminated calcareous siltstone. Arrows point to faint laminations). (g) Lithofacies G/H - laminated siltstone. (h) Lithofacies I - horizontal to irregularly laminated calcareous siltstone. (i) Lithofacies J - massive siliceous clayey siltstone. (j) Lithofacies K - massive siliceous clayey siltstone. (k) Lithofacies l - siliceous phosphatic siltstone with phosphate nodules (highlighted in white). (l) Lithofacies M/N - bioturbated, calcareous, sandy siltstone. (m) Lithofacies O - hummocky to ripple cross-stratified sandy siltstone. (n) Lithofacies P - interbedded siliceous-mudstone and calcareous- siltstone. CR - current ripple, PL- planar lamination, B - burrow, PH - phosphate, HCS - hummocky cross stratification.

2.4.2 Grain size distribution

Grain size distribution is reported according to the method proposed by Folk and Ward, 1957. Fig. 2.4 shows the average and range of cumulative grain size distribution for each lithofacies. The graphic statistical variables (Folk and Ward, 1957) calculated for each sample from the graphs in Fig. 2.4 and averages for each lithofacies are presented in Table 2.3.
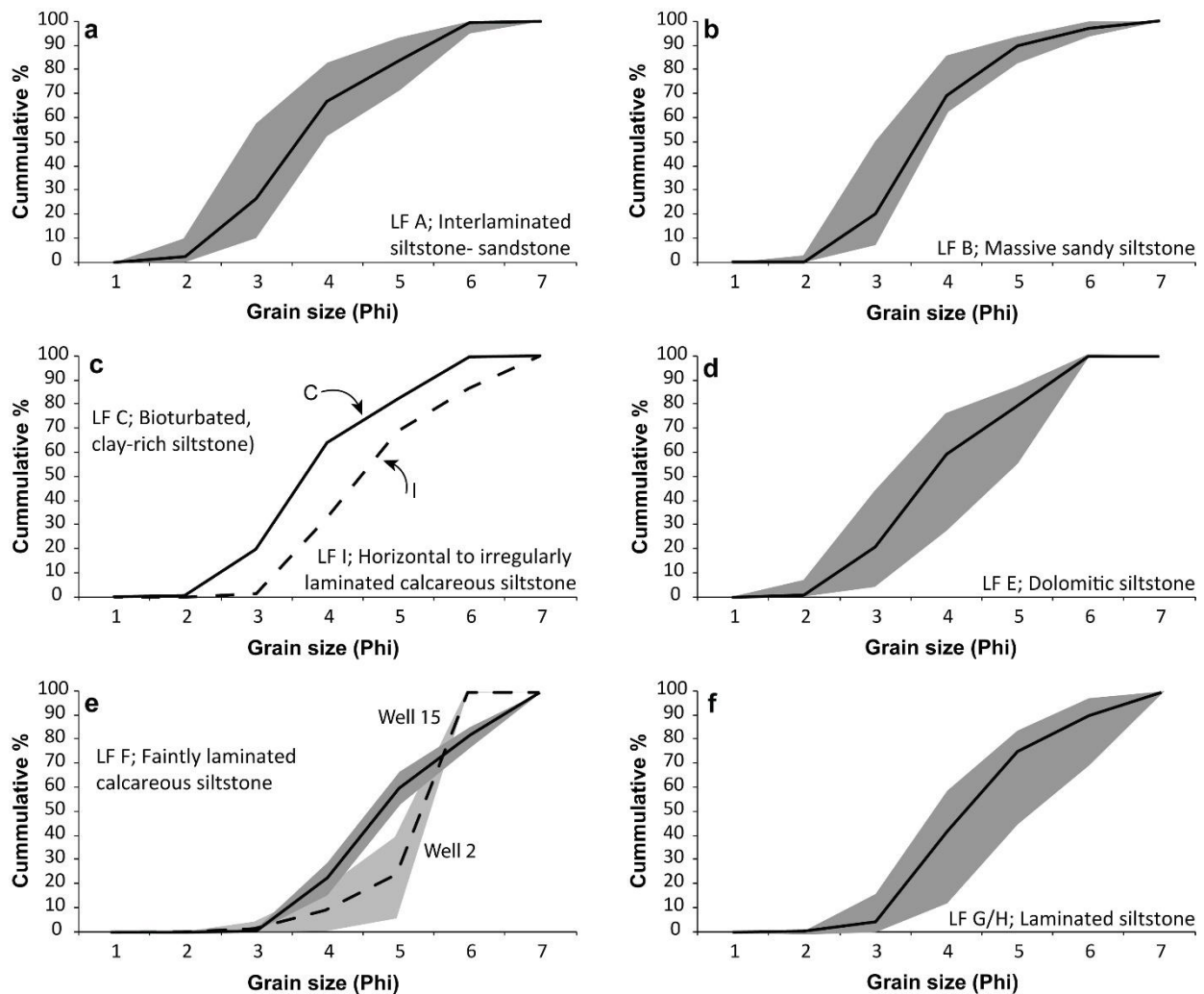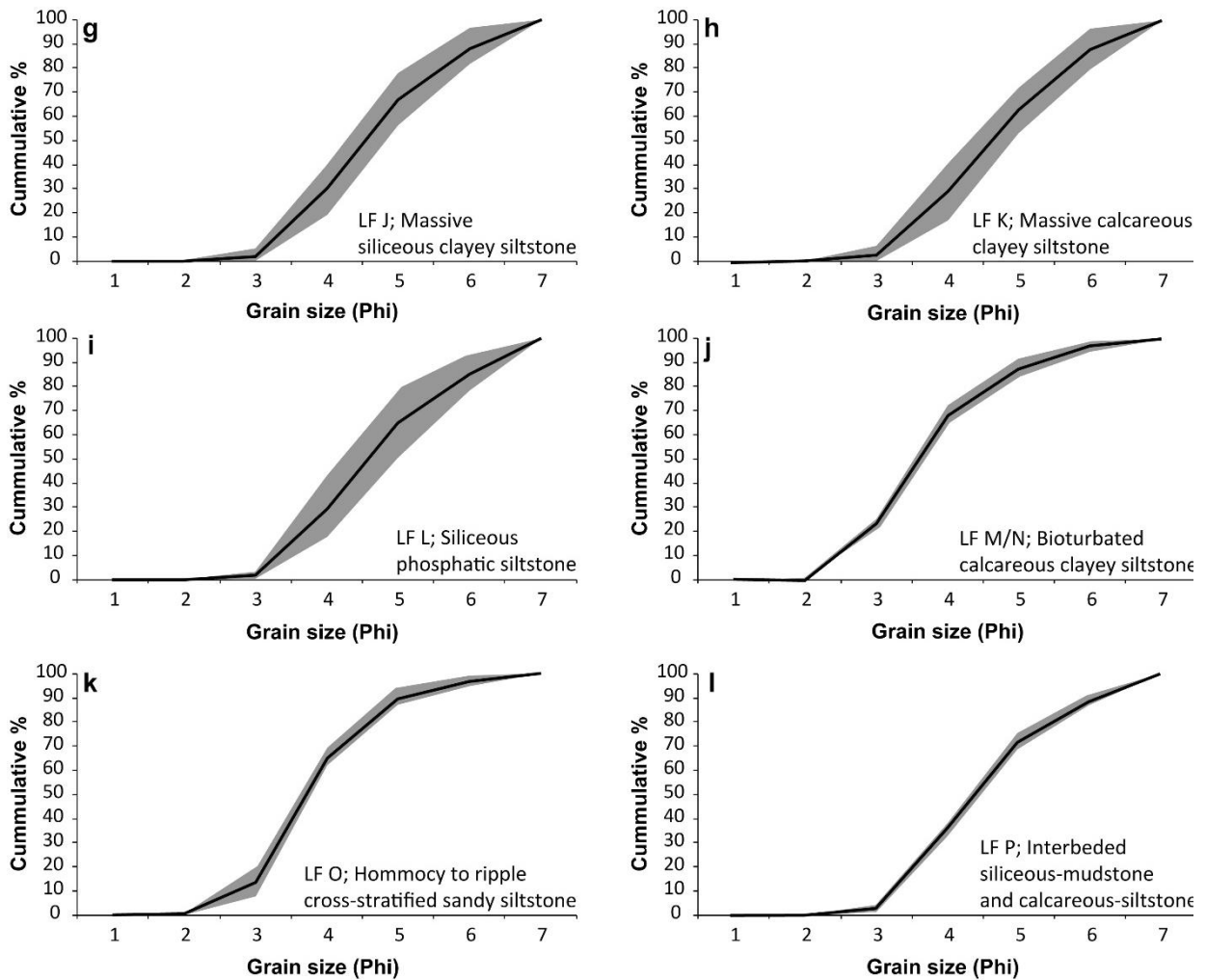
Fig. 2.4: Cumulative grain size distribution in phi (φ) units, for all lithofacies identified in the study. Black line is the average cumulative grain size for the lithofacies. Gray area shows grain size range for all samples taken from the lithofacies. No samples were obtained from lithofacies D (mudstone). Lithofacies F (faintly laminated calcareous siltstone) is the only lithofacies where a significant difference in grain size distribution exists between samples taken from different cores.

Group	Group I						Group II		Group III						
Lithofacies	A	B	C	E	M/N	O	G/H	I	F (total)	F (Well 2)	F (Well 15)	J	K	L	P
Mode (µm)	42.55	49.65	44.21	44.39	44.64	52.33	37.72	35.66	48.38	36.72	69.74	36.77	35.76	37.02	36.02
	(5.6)[d]	(4.70)	--	(12.35)	(3.29)	(3.07)	(3.45)	(1.48)	(19.66)	(2.62)	(19.42)	(2.99)	(0.45)	(3.84)	(0.97)
Mean[a]	4.14	4.12	4.28	4.44	4.10	4.25	4.95	5.01	5.19	5.08	5.37	4.98	4.92	4.96	4.92
	(0.25)	(0.25)	--	(0.52)	(0.07)	(0.06)	(0.30)	(0.01)	(0.40)	(0.19)	(0.62)	(0.14)	(0.20)	(0.21)	(0.07)
σ1[b]	1.11	0.94	1.10	1.03	1.04	0.93	0.87	0.92	0.82	0.86	0.75	0.80	0.82	0.74	0.82
	(0.11)	(0.10)	--	(0.18)	(0.08)	(0.06)	(0.26)	(0.03)	(0.26)	(0.23)	(0.30)	(0.19)	(0.25)	(0.10)	(0.06)
Skeweness c	0.21	0.14	0.21	0.14	0.14	0.23	-0.08	-0.08	-0.25	-0.25	-0.24	-0.25	-0.23	-0.49	-0.26
	(0.05)	(0.31)	--	(0.16)	(0.06)	(0.03)	(0.40)	(0.02)	(0.26)	(0.28)	(0.27)	(0.53)	(0.46)	(0.23)	(0.10)

[a] $$Graphic\ mean = \frac{\phi16 + \phi50 + \phi84}{3}$$

[b] $$Graphic\ standard\ deviation = \frac{\phi84 - \phi16}{4} + \frac{\phi95 - \phi5}{6.6}$$

[c] $$Inclussive\ graphic\ skewness = \frac{\phi16 + \phi84 - 2\phi50}{2(\phi84 - \phi16)} + \frac{\phi5 + \phi95 - 2\phi50}{2(\phi95 - \phi5)}$$

[d] *Standard deviation*

In addition, samples were grouped into larger grain-size bins: sand (> 63 µm), silt (4.8 - 63 µm) and clay (<4.8 µm). Samples were plotted on a ternary diagram, and the classification of Macquaker and Adams (2003) was applied to identify the rock type of each lithofacies (Table 2.3, Fig. 2.5). Based on a combination of the Folk and Ward, (1957) classification and the Macquaker and Adams (2003) classification, lithofacies were divided into three groups (Table 2.4, Fig. 2.5). Group one lithofacies somewhat coarser than other lithofacies and most samples in this group contain >10% sand size grains. Samples in these lithofacies are poorly to moderately sorted (0.5 < σ1 < 1.5) with a positively skewed grain size distribution (tail of fine grains). Group two lithofacies are all siltstones with up to 10% sand content. Samples in these lithofacies are moderately sorted (0.5 < σ1 < 1) and have a nearly symmetrical grain size distribution (Skewedness ~ 0). Group three lithofacies are all fine grained, with <5% sand size grains. These lithofacies are all moderately sorted (0.5 < σ1 < 1) with a negatively skewed grain size distribution (tail of coarse grains). Lithofacies F (faintly laminated calcareous siltstone) showed somewhat different grain size distribution in samples taken from well 2 and well 5. Although the mode in samples taken from these two wells is different, (36.72 µm for well 2 and 69.74 µm for well 15), graphic statistical variables are not

significantly different for samples from either of the two wells, or for the combined dataset of all samples (Table 2.3). It is worth noting that consideration of the error associated with the graphic statistical parameters do not change classification of any of the lithofacies.
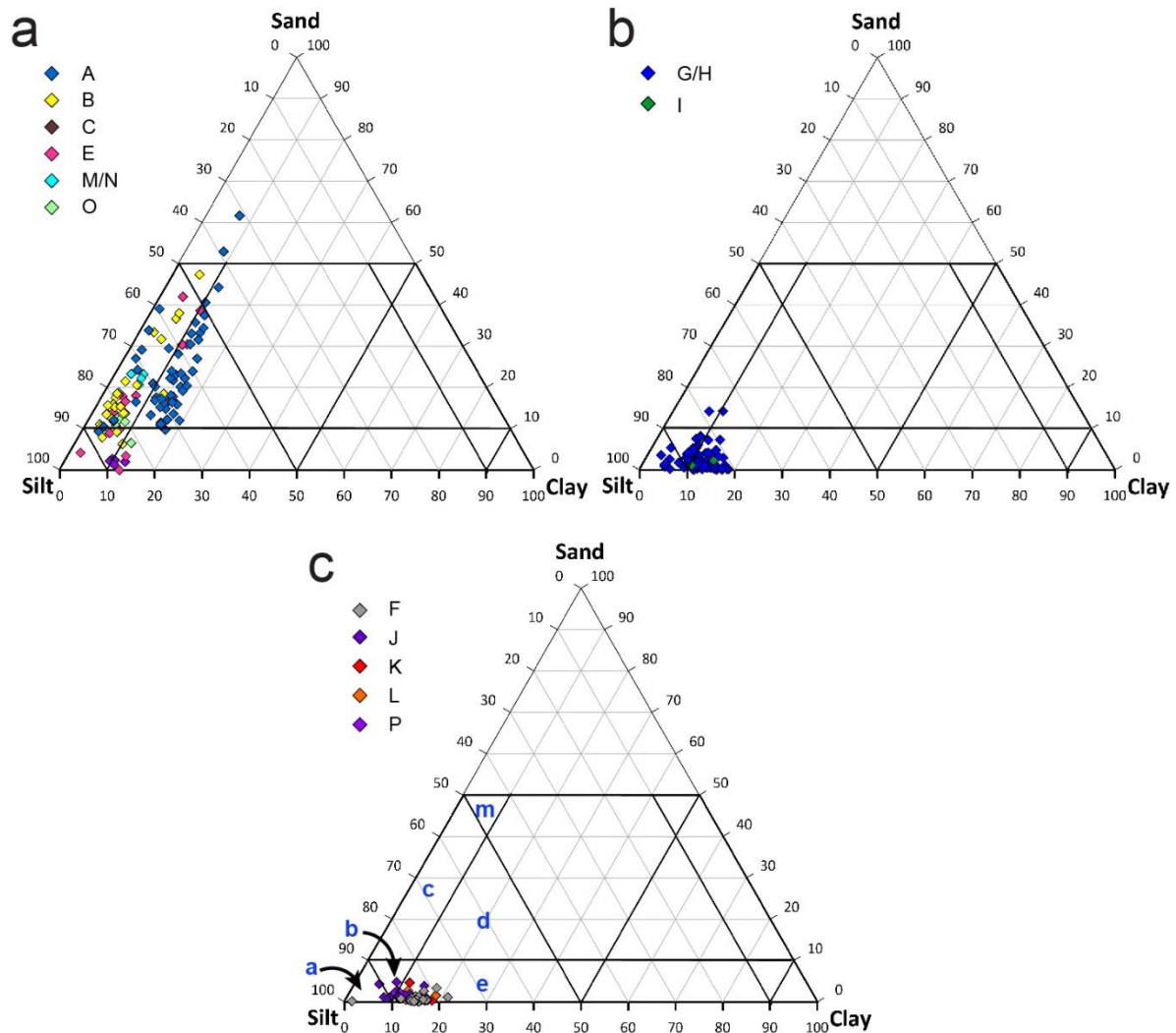
Fig. 2.5: Grain size distribution of all 14 lithofacies identified in wells 2, 4, 9, and 15. (a) Group one, mixed siltstone-sandstone lithologies (sand commonly >10%). Samples in this group have clear sedimentary structures (b) Group two, siltstone with up to 10% sand. Samples in this group are commonly laminated. (c) Group three, siltstone with up to 5% sand. With the exception of lithofacies P, samples in this group are massive in appearance. Letters (blue) mark the classification fields denoted by Macquaker and Adams (2003), where [a] is silt-dominated mudstone, [b] silt-rich mudstone, [c] sand-bearing, silt-rich mudstone, [d] sand and clay-bearing, silt-rich mudstone, [e] clay-bearing, silt-rich mudstone, and [m] sand and silt-bearing mudstone.

2.4.3 Detrital grain assemblage

Total mineral composition obtained from QEMSCAN analysis for all wells is provided in Fig. 2.6. Detrital minerals were identified through SEM-CL analysis and quantified by point count analysis on SEM-CL images (Table 2.4). Detrital quartz occurs as angular to subangular grains (Fig. 2.7a, i-l) and constitutes an average of 25.5% of bulk rock composition, equivalent to 71.3% of total quartz (Table 2.4). Detrital chert grains (2.7% of bulk composition and 7.4% of total quartz) are identified by mottled blue-red luminescence pattern, and a microporous texture of silica particles containing abundant porosity and inclusions (Fig. 2.7b, c). Rare collapsed agglutinated foraminifera, identified by a prominent midline, are present (Fig. 2.7d).

Detrital feldspar grains are angular to subangular (Fig. 2.8). K-feldspar and Na-feldspar average 6.9% and 6.1% of bulk samples, 67.7% and 66.0% of total feldspar, respectively. Under the optical microscope, feldspar grains are commonly weathered along cleavage planes. SEM imaging identified variable degrees of dissolution in detrital grains of both feldspars.

All micas and most clays in the siltstone are of detrital origin. Micas include muscovite and biotite. Chlorite was recognized in both QEMSCAN and XRD analyses and was identified in SEM analysis as detrital material of metamorphic origin based on appearance and relatively coarse grain size (Fig. 2.9a) (also noted by Zonneveld and Moslow, 2018; Moslow et al., 2018), and similar in morphology to other mica grains. Mica grains are subangular to subrounded, and many are bent, displaced along cleavage planes, and have splayed edges (Fig. 2.9a). Mica-like chlorite is susceptible to dissolution and breakage along cleavage planes (Fig. 2.9b). Based on QEMSCAN analysis, muscovite shows the highest concentrations of all micas (up to 7.5 wt%), chlorite has a maximum concentration of 4.2 wt%, and biotite is present only in minor amounts (<1.5 wt%).
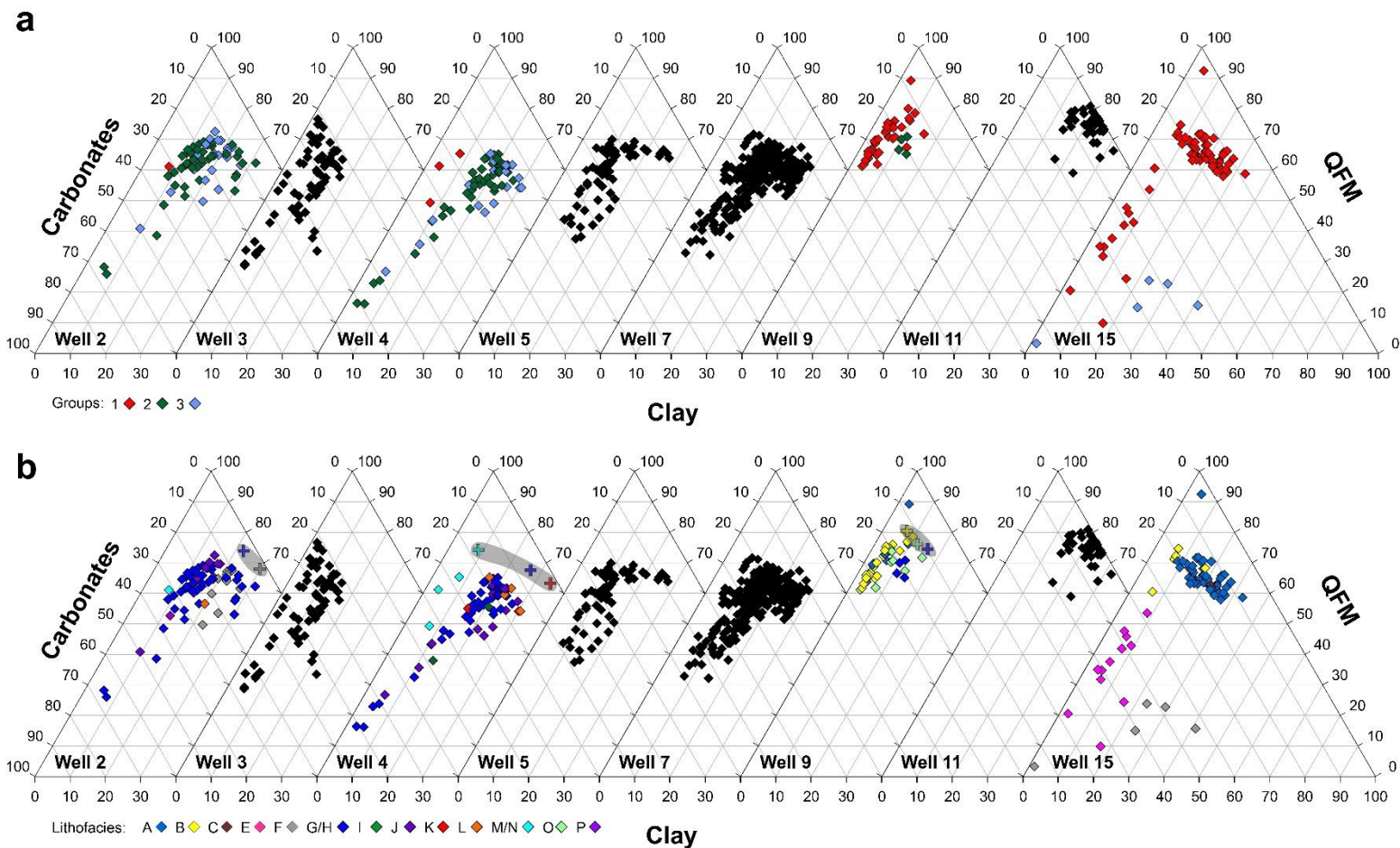
Fig. 2.6: QEMSCAN analysis results in wt%. QFM is the sum of quartz, K-feldspar, Na-feldspar and micaceous minerals. Clay minerals include MLIS and kaolinite, and carbonate minerals include calcite, dolomite and Fe-rich dolomite. Compositional variations between samples of different groups (a) and different lithofacies (b) are presented for the four Montney cores logged. Note the large variations in the content of carbonate minerals between samples in all wells. Plus symbols in (b) are calculated detrital composition for several lithofacies. With the exception of well 15, lithofacies from group one have the lowest clay content. With the exception of well 15, different lithofacies and different lithofacies groups are compositionally indistinct from one another.

34

Mixed layer illite-smectite (MLIS) clays are present as clay coats (Fig. 2.9c) or as aggregate grains between detrital grains (Fig. 2.9d). MLIS is present in all the samples examined, but concentrations determined by QEMSCAN analysis generally vary across the basin from just under 1 wt% to over 30 wt%. Point count analysis results (Table 2.4) are somewhat lower than the QEMSCAN reported concentrations, with average total clay content of 3% and a maximum of 7%. XRD analysis of glycolated clay mounts established a maximum of 5% expandable layers for MLIS throughout most of the basin. Only in three samples (well 16 from the Dixonville Delta) does MLIS show higher expandability of 20%.

Dolomite occurs predominantly as a rounded to well-rounded detrital grains, surrounded by rhombohedral overgrowths. These detrital dolomite grains are identified by their bright luminescence, weathered (cloudy) appearance in thin sections (Fig. 2.10a), and the presence of dissolution pits (Fig. 2.10b) which are commonly <1.5 µm in diameter. In several samples from cores 15 and core 9, larger dissolution pits (>5 µm) were identified (Fig. 2.10d). Total dolomite concentration averages at 17.5% of bulk composition. However, only a third of the dolomite in the Montney is of detrital origin (Table 2.4; 5.4% of bulk composition and 32.2% of total dolomite on average); the remaining fraction is diagenetic in origin.

Detrital grains of different minerals may vary in size. However, since detrital quartz is the least susceptible for dissolution in our samples, we used it as a proxy for detrital grain size. Detrital quartz grain size was measured on SEM-CL images for samples from wells 2, 4, and 9. Average detrital quartz grain size in individual samples ranges from 0.5 to 96 µm, but most of the grains measured (P_{15}-P_{85}) show a much narrower range of 5-40 µm. Well 2 has smaller detrital quartz grains (average 12.7 µm) than wells 4 and 9 in which detrital quartz grain size is similar and averages ~24 µm. The sphericity index (short grain axis / long grain axis) is 0.5±0.2 for all three wells, indicating a majority of elongated detrital quartz grains.

Table 2.4: Point count analysis results

	Well	2					4						9					
	Sample	3E	4P	12E	16O	16I	2AE	2H	3AJ	4V	5AD	5V	1C	2AQ	3B	4F	5K	5N
	Depth (m)	2281.0	2289.0	2431.1	2480.9	2487.0	2621.0	2644.0	2653.0	2703.0	2731.0	2739.0	3278.0	3289.1	3340.0	3364.0	3379.0	3376.0
	Lithofacies	G/H	G/H	G/H	F	F	M/N	G/H	G/H	K	G/H	G/H	B	B	O	B	G/H	B
Detrital	Qz detrital	27.2 (2.5) [a]	22.3 (2.3)	26.2 (2.4)	27.9 (2.5)	19.3 (2.2)	27.3 (2.5)	22.2 (2.3)	16.7 (2.1)	9.2 (1.6)	22.1 (2.3)	27.3 (2.5)	27.6 (2.5)	38.1 (2.7)	26.3 (2.4)	31.9 (2.6)	32.3 (2.6)	29.3 (2.5)
	Chert	1.1 (0.6)	2.1 (0.8)	4.4 (1.1)	4.4 (1.1)	2.0 (0.8)	3.3 (1.0)	4.9 (1.2)	2.4 (0.9)	0.0 (0.0)	1.0 (0.5)	3.3 (1.0)	4.2 (1.1)	2.0 (0.8)	2.4 (0.8)	3.4 (1.0)	2.9 (0.9)	2.3 (0.8)
	K-feldspar detrital	5.8 (1.3)	5.5 (1.3)	3.7 (1.0)	3.7 (1.0)	4.3 (1.1)	5.1 (1.2)	5.8 (1.3)	8.6 (1.5)	1.9 (0.8)	13.3 (1.9)	7.0 (1.4)	9.8 (1.6)	10.0 (1.7)	9.7 (1.6)	9.9 (1.6)	8.8 (1.6)	4.3 (1.1)
	Na-feldspar detrital	4.6 (1.2)	5.8 (1.3)	6.4 (1.4)	7.0 (1.4)	5.2 (1.2)	5.0 (1.2)	8.5 (1.5)	5.4 (1.3)	3.8 (1.1)	8.8 (1.6)	9.0 (1.6)	7.0 (1.4)	6.2 (1.3)	5.7 (1.3)	4.9 (1.2)	5.8 (1.3)	4.5 (1.1)
	Dolomite detrital	2.6 (0.9)	3.0 (0.9)	2.3 (0.8)	1.2 (0.6)	4.4 (1.1)	16.9 (2.1)	5.9 (1.3)	4.2 (1.1)	8.3 (1.5)	2.5 (0.9)	3.4 (1.0)	7.7 (1.5)	4.6 (1.2)	7.2 (1.4)	5.4 (1.3)	6.1 (1.3)	6.2 (1.3)
	Clay	2.9 (0.9)	5.1 (1.2)	5.6 (1.3)	2.4 (0.8)	7.3 (1.4)	2.6 (0.9)	5.6 (1.3)	2.3 (0.8)	1.3 (0.6)	6.8 (1.4)	4.9 (1.2)	1.0 (0.5)	0.5 (0.4)	0.1 (0.2)	0.8 (0.5)	2.2 (0.8)	0.3 (0.3)
	Mica	7.1 (1.4)	7.8 (1.5)	14.1 (1.9)	18.0 (2.1)	16.5 (2.0)	3.9 (1.1)	7.0 (1.4)	4.2 (1.1)	2.9 (0.9)	6.7 (1.4)	12.9 (1.9)	3.4 (1.0)	5.2 (1.2)	2.9 (0.9)	3.5 (1.0)	7.1 (1.4)	2.6 (0.9)
	Heavy minerals	0.3 (0.3)	0.7 (0.5)	0.5 (0.4)	0.0 (0.0)	0.4 (0.4)	0.2 (0.2)	0.9 (0.5)	0.2 (0.3)	0.3 (0.3)	0.6 (0.4)	0.5 (0.4)	0.5 (0.4)	0.3 (0.3)	0.7 (0.5)	0.2 (0.2)	0.1 (0.2)	0.2 (0.2)
Authigenic	Qz cement (1st generation)	5.1 (1.2)	3.2 (1.0)	3.1 (1.0)	5.6 (1.3)	5.1 (1.2)	3.3 (1.0)	2.8 (0.9)	2.5 (0.9)	1.9 (0.7)	5.4 (1.2)	6.0 (1.3)	6.0 (1.3)	5.1 (1.2)	7.9 (1.5)	8.7 (1.6)	6.7 (1.4)	9.3 (1.6)
	Qz cement (2nd generation)	1.9 (0.7)	3.2 (1.0)	2.8 (0.9)	4.2 (1.1)	2.7 (0.9)	2.4 (0.8)	1.0 (0.6)	3.7 (1.0)	1.7 (0.7)	3.5 (1.0)	1.5 (0.7)	0.8 (0.5)	1.5 (0.7)	2.0 (0.8)	2.9 (0.9)	1.7 (0.7)	1.5 (0.7)
	K-feldspar cement	7.0 (1.4)	5.4 (1.2)	2.4 (0.9)	2.2 (0.8)	1.4 (0.6)	1.3 (0.6)	1.5 (0.7)	1.4 (0.7)	1.4 (0.7)	2.3 (0.8)	3.8 (1.1)	4.2 (1.1)	4.6 (1.2)	6.2 (1.3)	4.6 (1.2)	3.1 (1.0)	2.5 (0.9)
	Na-feldspar cement	2.4 (0.9)	2.3 (0.8)	1.9 (0.8)	1.4 (0.7)	1.4 (0.7)	0.8 (0.5)	1.8 (0.7)	1.7 (0.7)	0.9 (0.5)	1.3 (0.6)	0.1 (0.2)	2.7 (0.9)	3.2 (1.0)	3.0 (0.9)	2.6 (0.9)	1.5 (0.7)	2.0 (0.8)
	Na-feldspar albitization	1.0 (0.5)	1.0 (0.6)	1.1 (0.6)	0.8 (0.5)	1.1 (0.6)	0.2 (0.3)	0.0 (0.0)	1.4 (0.7)	0.3 (0.3)	1.2 (0.6)	2.7 (0.9)	2.7 (0.9)	3.4 (1.0)	2.7 (0.9)	0.2 (0.3)	0.8 (0.5)	1.9 (0.7)
	Dolomite cement	1.2 (0.6)	2.1 (0.8)	2.6 (0.9)	2.7 (0.9)	6.9 (1.4)	11.3 (1.7)	3.2 (1.0)	1.9 (0.7)	4.0 (1.1)	0.1 (0.2)	0.7 (0.5)	7.1 (1.4)	1.4 (0.6)	7.2 (1.4)	4.0 (1.1)	7.3 (1.4)	14.4 (1.9)
	Fe-dolomite	6.5 (1.4)	6.8 (1.4)	3.5 (1.0)	3.5 (1.0)	10.3 (1.7)	0.6 (0.4)	12.6 (1.8)	8.4 (1.5)	23.9 (2.4)	4.6 (1.2)	3.5 (1.0)	6.1 (1.3)	3.7 (1.0)	7.3 (1.4)	9.7 (1.6)	4.0 (1.1)	12.7 (1.8)
	Calcite (1st generation)	5.1 (1.2)	6.9 (1.4)	0.9 (0.5)	3.0 (0.9)	2.7 (0.9)	0.0 (0.0)	2.0 (0.8)	2.6 (0.9)	3.3 (1.0)	2.1 (0.8)	1.6 (0.7)	0.0 (0.0)	0.0 (0.0)	0.0 (0.0)	0.0 (0.0)	0.0 (0.0)	0.0 (0.0)
	Calcite (2nd generation)	7.1 (1.4)	3.5 (1.0)	4.3 (1.1)	1.1 (0.6)	1.2 (0.6)	3.9 (1.1)	2.9 (0.9)	25.1 (2.4)	26.0 (2.4)	4.2 (1.1)	2.0 (0.8)	0.0 (0.0)	0.0 (0.0)	0.0 (0.0)	0.0 (0.0)	0.0 (0.0)	0.0 (0.0)
	Anhydrite	0.0 (0.0)	0.0 (0.0)	0.0 (0.0)	0.0 (0.0)	0.0 (0.0)	0.0 (0.0)	0.0 (0.0)	0.0 (0.0)	0.0 (0.0)	0.0 (0.0)	0.0 (0.0)	2.3 (0.8)	1.5 (0.7)	4.1 (1.1)	3.0 (0.9)	0.0 (0.0)	1.6 (0.7)
	Halite	0.2 (0.2)	0.0 (0.0)	0.0 (0.0)	0.0 (0.0)	0.2 (0.2)	0.0 (0.0)	0.0 (0.0)	0.0 (0.0)	0.0 (0.0)	0.0 (0.0)	0.0 (0.0)	0.0 (0.0)	0.0 (0.0)	0.0 (0.0)	0.0 (0.0)	0.0 (0.0)	0.0 (0.0)
	Pyrite	1.3 (0.6)	1.9 (0.8)	2.3 (0.8)	1.7 (0.7)	2.5 (0.9)	1.1 (0.6)	0.7 (0.5)	0.5 (0.4)	0.6 (0.4)	1.8 (0.7)	0.9 (0.5)	0.6 (0.4)	0.8 (0.5)	0.4 (0.3)	0.7 (0.5)	2.4 (0.8)	0.6 (0.4)
	Phosphate	1.3 (0.6)	0.0 (0.0)	0.0 (0.0)	0.5 (0.4)	0.2 (0.3)	1.4 (0.6)	0.7 (0.5)	0.1 (0.2)	0.7 (0.5)	1.0 (0.5)	0.5 (0.4)	0.8 (0.5)	3.2 (1.0)	0.9 (0.5)	1.0 (0.5)	0.5 (0.4)	0.9 (0.5)
porosity	Primary porosity	0.0 (0.0)	3.2 (1.0)	0.0 (0.0)	2.3 (0.8)	1.3 (0.6)	2.2 (0.8)	2.6 (0.9)	2.7 (0.9)	2.3 (0.8)	2.3 (0.8)	3.7 (1.0)	1.9 (0.8)	1.6 (0.7)	0.9 (0.5)	0.9 (0.5)	2.5 (0.9)	1.5 (0.7)
	Organic matter-filled porosity	7.0 (1.4)	5.8 (1.3)	8.8 (1.6)	4.0 (1.1)	1.1 (0.6)	5.6 (1.3)	5.1 (1.2)	1.3 (0.6)	2.7 (0.9)	4.9 (1.2)	3.2 (1.0)	1.6 (0.7)	1.5 (0.7)	0.6 (0.4)	0.8 (0.5)	1.4 (0.6)	0.6 (0.4)
	Secondary porosity	0.1 (0.2)	0.2 (0.3)	0.1 (0.2)	0.0 (0.0)	0.1 (0.2)	0.4 (0.3)	0.3 (0.3)	0.5 (0.4)	0.2 (0.3)	0.3 (0.3)	0.0 (0.0)	0.3 (0.3)	0.1 (0.2)	0.0 (0.0)	0.0 (0.0)	0.7 (0.5)	0.3 (0.3)
unknown	Unknown	1.4 (0.7)	2.2 (0.8)	3.1 (1.0)	2.3 (0.8)	2.3 (0.8)	1.4 (0.7)	1.9 (0.7)	2.1 (0.8)	2.4 (0.8)	3.1 (1.0)	1.5 (0.7)	1.8 (0.7)	1.4 (0.7)	1.7 (0.7)	1.1 (0.6)	2.2 (0.8)	0.5 (0.4)
	Total	100.0	100.0	100.0	100.0	100.0	100.0	100.0	100.0	100.0	100.0	100.0	100.0	100.0	100.0	100.0	100.0	100.0

		2					4						9					
	IGV$_m^c$ (Vol %)	46.0	44.3	32.6	32.2	37.1	33.8	36.9	51.9	69.6	33.5	27.6	33.9	28.1	40.6	38.8	31.1	47.9
φ^b=60% — COPL % [d]		25.9	28.2	40.7	41.0	36.4	39.6	36.6	16.9	--	39.9	39.9	39.5	44.4	32.6	34.7	42.0	23.6
	CEPL % [e]	34.1	29.3	19.3	17.7	22.7	18.8	21.5	40.4	--	18.6	18.6	19.2	14.6	26.8	24.8	16.2	35.0

[a] standard deviation, 2σ.   [c] Intergranular volume.
[b] Initial porosity.   [d] % of initial porosity lost due to compaction.   [e] % of initial porosity lost due to cemntation.
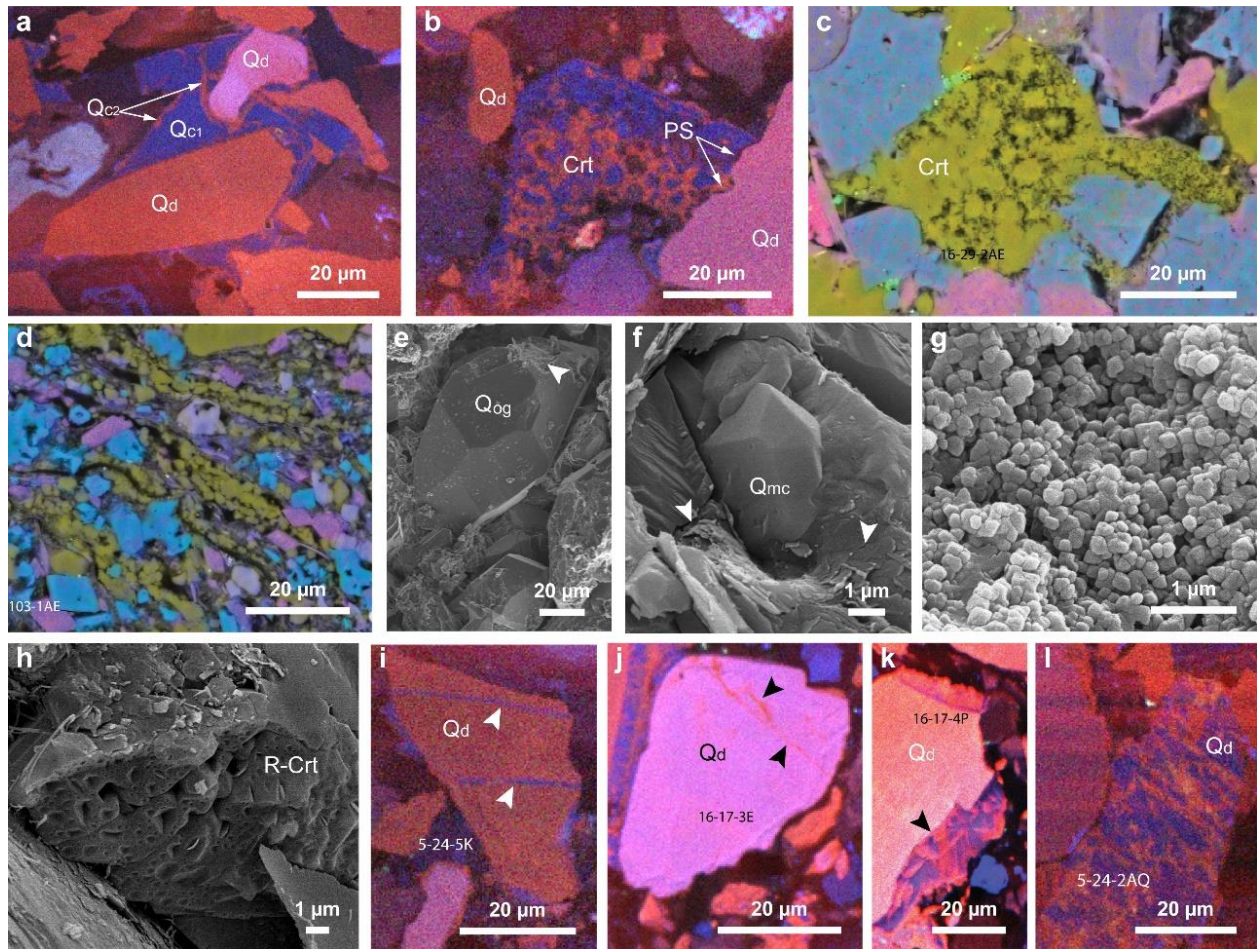
Fig. 2.7: Quartz in the Montney Formation (a) SEM CL image of detrital quartz grains (Qd), blue luminescent early quartz cement (Qc1), and red luminescent late quartz cement (Qc2); Sample 3B, well 9, 3340 m. (b) SEM-CL image of a chert fragment (Crt) with spongy texture and mottled blue and red luminescence. Note concave-convex contact of pressure solution (PS) between chert fragment and adjacent detrital quartz grain; sample 2H, well 4, 2664m. (c) SEM-EDS image of chert (Crt) with spongy texture and abundant porosity. Sample 2AE, well 4, 2621 m. (d) SEM-EDS image of agglutinated foraminifera. Sample 1AE, well 15, 864.9 m. (e) SEM-SE image of massive quartz cement overgrowth (Qog). Note clay coats inhibiting quartz cementation (white arrow), sample 1S, well 15, 876.9 m. (f) SEM-SE image of euhedral microcrystalline quartz cement (Qmc). Note lack of cement adjacent grains, where detrital clay coats are present (white arrow). (g) SEM-SE of Silica nanospheres, sample 20A, well 2, 2530 m.(h) SEM-SE image of recrystallized chert (R-Crt). Incomplete transformation of chert to quartz created holes on the face of a quartz crystal, sample 10, well 1, 2028m. (i) SEM-CL image of a fractured detrital quartz grain. Fractures are filled with blue-luminescing cement. Sample 5K, well 9, 3379 m. (j) SEM-CL image of a fractured detrital quartz grain. Fractures are filled with red-luminescing cement. Sample 3E, well 2, 2281 m. (k) SEM-CL image of fractured blue-luminescing cement. Fractures are filled with red-luminescing cement. Sample 4P, well 2, 2289 m. (l) Shattered detrital quartz cement. Many fractures are filled with red-luminescing cement. Shattered grains are rare. Sample 2AQ, well 9, 3289 m.
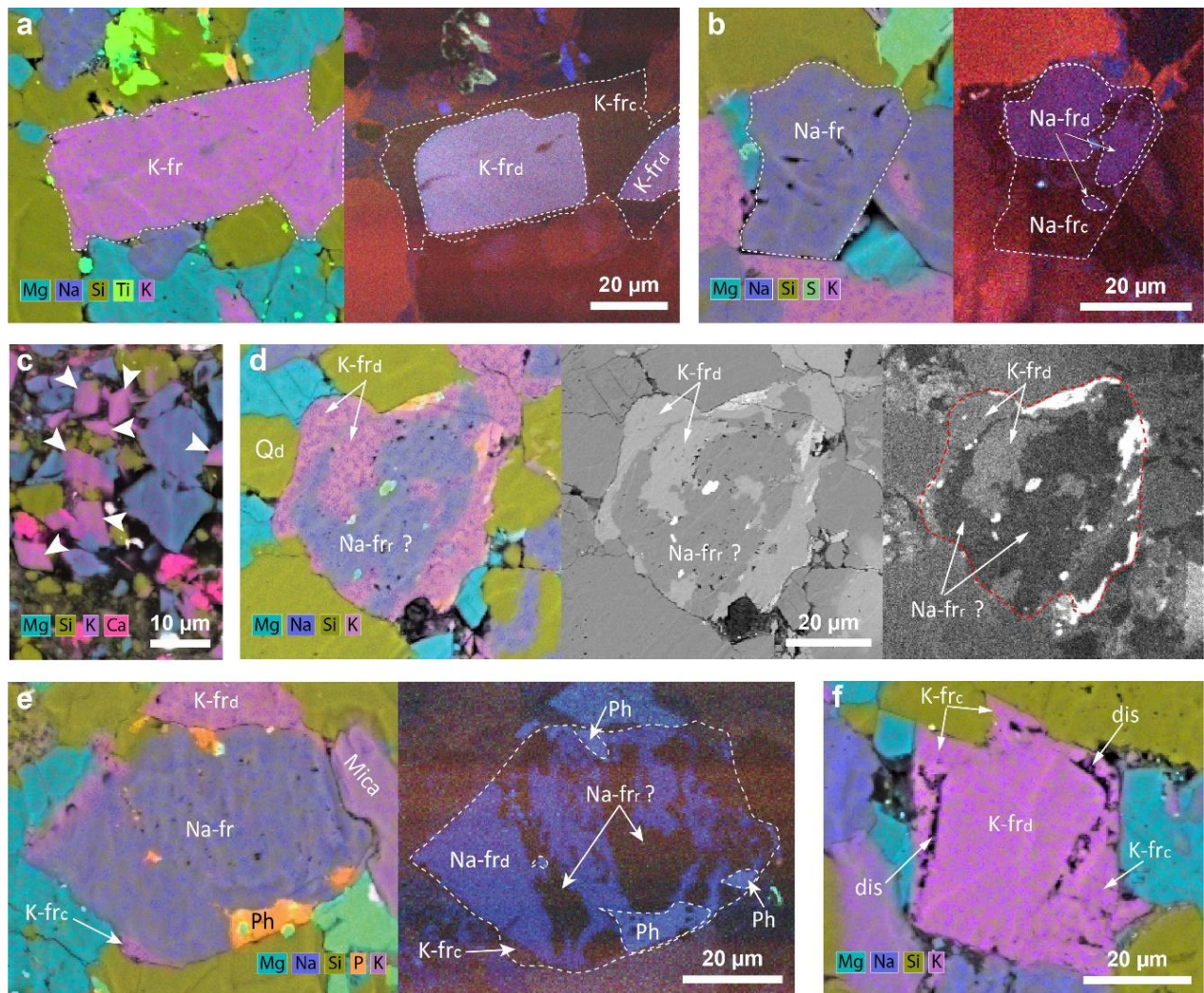
Fig. 2.8: Feldspars in the Montney Formation. (a) SEM-EDS image (left) and SEM-CL image (right) of highly luminescent detrital K-feldspar (K-frd) surrounded by a rim of non-luminescent K-feldspar cement (K-frc), sample 4F, well 9, 3364m. (h) SEB-SE image of K-feldspar and quartz overgrowth, sample 1S, well 15, 878.5 m. (b) SEM-EDS image (left) and SEM-CL image (right) showing detrital Na-feldspar (Na-frd) and Na feldspar cement (Na-frc). Note the straight edges of the cement, sample 4F, well 9, 3364m. (c) SEM-EDS image showing discrete euhedral K-feldspar crystals (white arrows), sample 1AE, well 15, 864.9m. (d) SEM-EDS image (left), SEM BSC (center), and SEM-CL image (right) of luminescent detrital K-feldspar (K-frd) and non-luminescent authigenic Na-feldspar replacing the detrital grain (Na-frr), sample 2AQ, well 4, 3289.05 m. (e) SEM-EDS image (left) and SEM-CL image (right) of highly luminescent detrital Na-feldspar (Na-frd) and non-luminescent authigenic Na-feldspar replacing the detrital grain (Na-frr). Note K-feldspar cement (K-frc) overgrowing Na-feldspar, sample 1C, well 9, 3278m. (f) SEM-EDS image of dissolution at the boundary between detrital grain and cement rim of K-feldspar, sample 1C, well 9, 3278m.
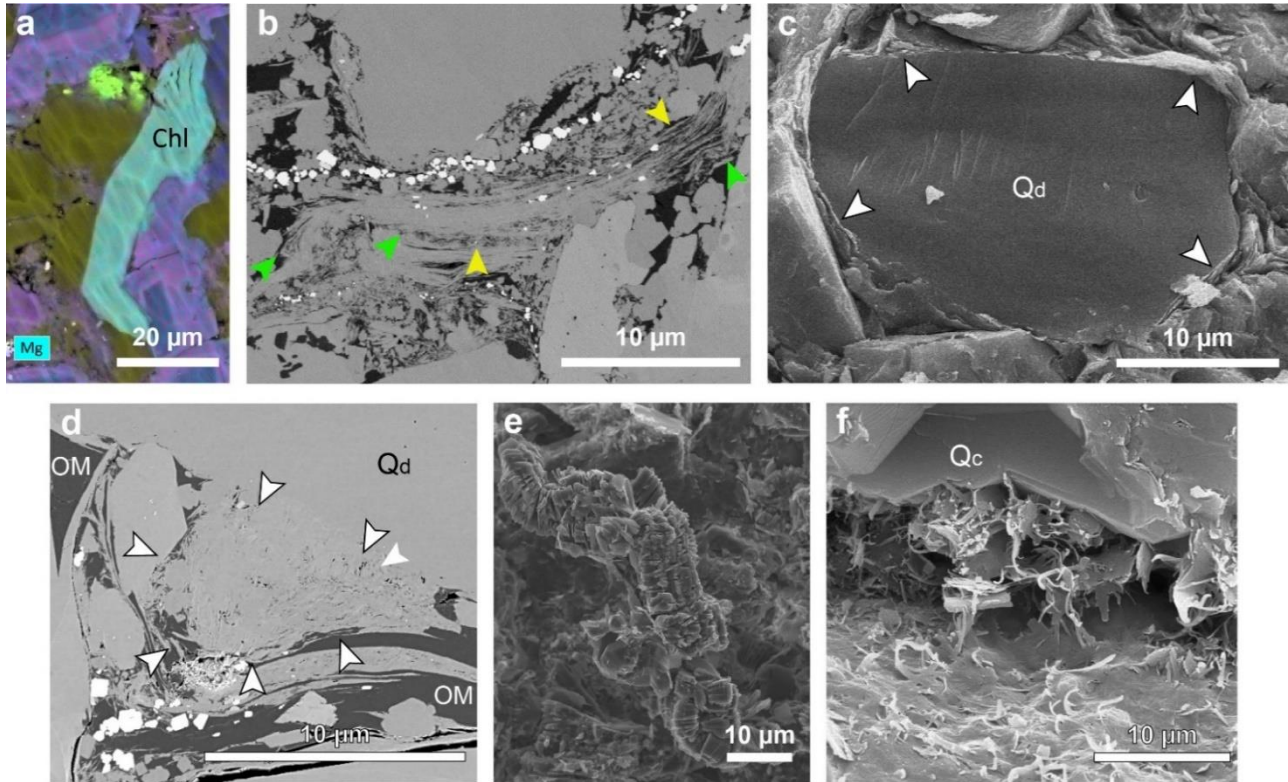
Fig. 2.9: Mica and clay minerals in the Montney Formation. (a) SEM-EDS image of chlorite (Mg-rich mica). Note split grain edges, sample 16I, well 2, 2487m. (b) SEM-BS image of deformed (green arrow) and dissolved (yellow arrow) mica grain, sample 10D, well 2, 2396 m. (c) SEM-SE image of detrital clay coats around a detrital quartz grain, sample, 7C, well 2, 2342.1 m. (d) SEM-BS image of a clay clump (white arrows) between detrital grains. White minerals are pyrite; sample 9P, well 2, 2366.25 m. (e) SEM-SE image of authigenic pore lining kaolinite, sample A, well 16, 875.55 m. (f) SEM-SE image of pore bridging fibrous illite, developing on detrital clay, sample 1, well 1, 2006 m.

2.4.4 Authigenic phases

Authigenic minerals were identified through thin section, SEM and SEM-CL analyses. Cement volumes were calculated from point count analysis of SEM-CL images (Table 2.4).

2.4.4.1 Quartz

Two generations of authigenic quartz are present (Fig. 2.7a). The first and more abundant generation exhibits blue cathodoluminescence and comprises an average of 5.1% of mineral volume, and 14.2% of total quartz. The second generation of quartz cement is identified by

bright red cathodoluminescence and forms thin rims surrounding the blue quartz cement or detrital quartz grains. Red luminescent quartz cement averages 2.3% of bulk composition and 7.0% of total quartz. Fractured quartz grains are uncommon, are mostly linear, and usually around 1 μm in width. Fractures are filled with either blue or red quartz cement (Fig. 2.7 I, j). Rarely, a complicated network of red cement fills fractures developed in blue cement (Fig. 2.7k) or shattered detrital quartz grains (Fig. 2.7l).

SEM images of freshly broken surfaces show that quartz cement forms overgrowths (Fig. 7e), euhedral microcrystalline cement (Fig. 2.7f), and silica nanospheres (Fig. 2.7g) (terminology adopted from Longman et al., 2019). Development of quartz overgrowths was inhibited to some degree by detrital clay coating (Fig. 7h), and in many cases overgrowth surfaces are speckled with angular holes <1μm (Fig. 2.7i). Silica nanospheres are a minor phase, locally appearing as grain coats, which are too thin to identify in polished samples.

2.4.4.2 Feldspars

Authigenic feldspars have dark cathodoluminescence under SEM-CL (Fig. 2.8). Both K-feldspars and albite form a single overgrowth generation (Fig. 2.8a, b), and K-feldspar also forms discrete euhedral crystals (Fig. 2.8c). Feldspar cement (overgrowth or discrete euhedral crystals) constitute 32.3% and 21.4% of total K-feldspar and total albite, respectively. K-feldspar cement overgrows detrital grains of both feldspar types (Fig. 2.8a, e), whereas albite cement overgrows only detrital Na-feldspar (Fig. 2.8b). A low-luminescing albite appears to replace both K-feldspar (Fig. 2.8d) and Na-feldspar (Fig. 2.8e). We note that these grains might also be interpreted as plutonic detrital grains with low luminescence albite. However, we favor the interpretation of albitization due to the nonlinear morphology of the low-luminescing albite and its association with porosity that is potentially secondary (Milliken, 1989). Replacive albite accounts on average for 13.5% of total Na-feldspar.
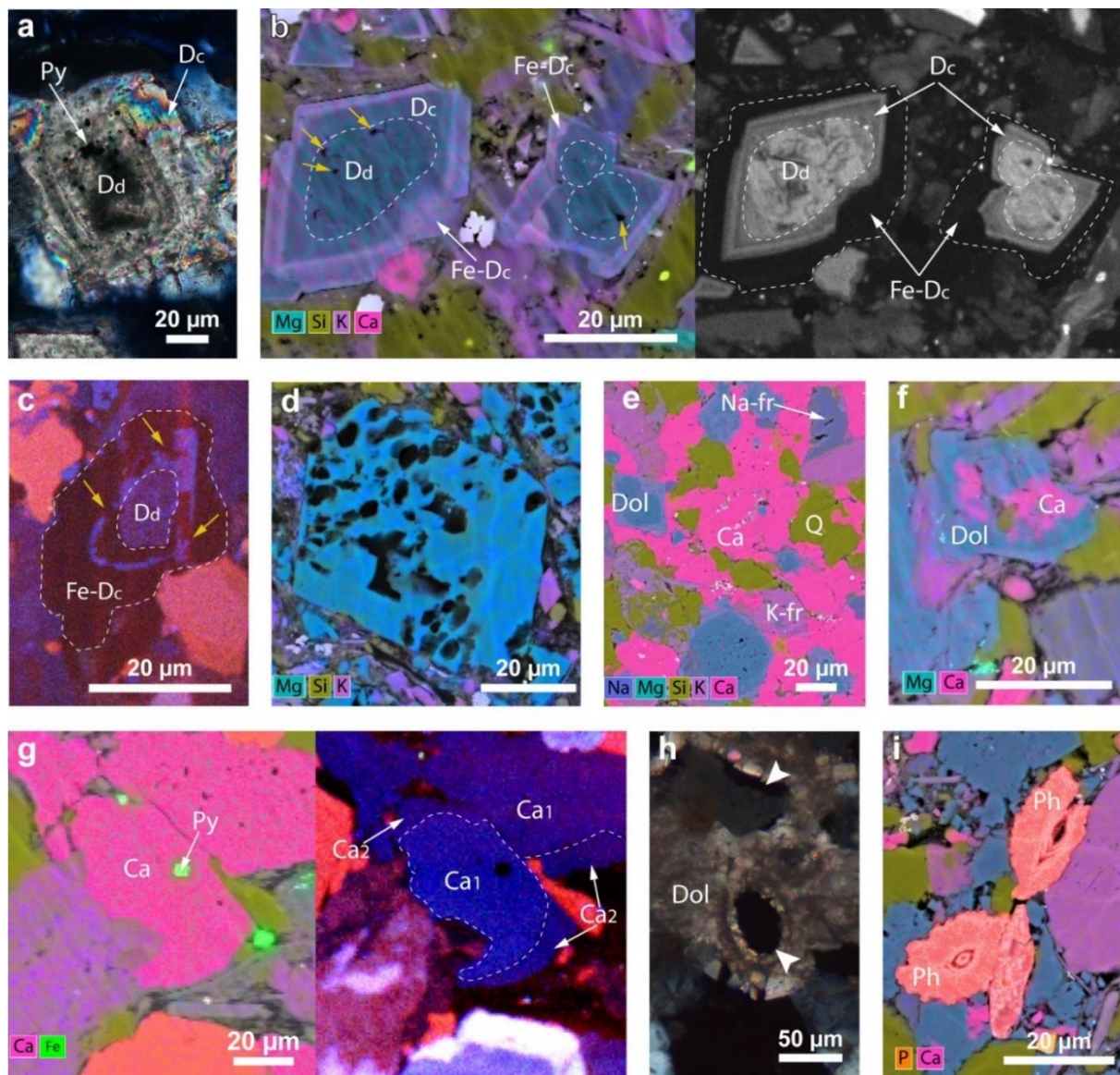
Fig 2.10: Carbonate minerals. Thin section photomicrograph showing euhedral dolomite cement (Dc) surrounding a detrital dolomite (Dd) core. Note pyrite (Py) inclusions in the dolomite cement, sample 1AC, well 15, 867 m. (b) SEM-EDS (left) and SEM-CL (blue channel, right) of detrital dolomite (Dd), surrounded by dolomite cement (Dc) and Fe-rich dolomite cement (Fe-Dc). Small dissolution pits (yellow arrows) are present in the detrital dolomite, sample 16I, well 2, 2487 m. (c) SEM-CL image showing detrital dolomite and cement. Outer rim is composed of non- luminescent Fe-dolomite. Fe-dolomite cement is replacing earlier dolomite cement with bright blue luminescence (yellow arrows), sample 3AJ, well 4, 2653 m. (d) Large dissolution vuggs in dolomite (in both detrital well and cement), sample 1AE, well 15, 864.9 m. (e) Poikilotopic calcite cement in SEM-EDS image. Sample 3AJ, well 4, 2653 m.(f) SEM-EDS image showing calcite filling pores left by dissolution of detrital dolomite, sample 3E, well 2, 2281 m. (g) SEM-EDS (left) and SEM-CL (right) showing two generations of calcite. The first calcite cement generation (Ca$_1$) contains euhedral pyrite inclusions and has bright luminescence. The second calcite cement generation (Ca$_2$) crystallized around Ca$_1$, has darker, more muted blue luminescence pattern than Ca$_1$. (h) Moldic porosity in dolomite cement, sample 170803, well 13, 1960.5 m. (i) Phosphate replacing fossils, sample 2AE, well 4, 2621 m.

Extensive dissolution of K-feldspar cement is a minor phenomenon in the Montney Formation but is important locally. Dissolution occurs mainly along the boundary between the detrital grain and the cement rim (Fig. 2.8l) and is most common in Well 15, and to a lesser degree in Well 9.

2.4.4.3 Dolomite

At least four generations of dolomite cement were identified under CL and SEM-CL microscope (Fig. 2.10a, b). Absence of evidence for dissolution of authigenic dolomite, and sharp transitions between cement generations suggest continuous cementation with rapidly changing fluid composition. The last dolomite generation is an iron-rich dolomite (Fe ~ 5 wt%, based on QEMSCAN analysis), easily identified by the brighter BSE signal and quenched cathodoluminescence (Fig. 2.10b). In some samples, iron-rich dolomite replaces earlier dolomite cements (Fig. 2.10c), and occasionally detrital dolomites.

Authigenic dolomite amounts to 12.1% of rock volume, and 67.8% of total dolomite. In most samples, more than 30% of the dolomite is Fe-rich, but in most samples (P_{15}-P_{85}) Fe-rich dolomite concentration is < 7 wt%. Dissolution pits in detrital dolomite are either empty or filled with authigenic pyrite, phosphate, and rarely quartz and K-feldspar (Fig. 2.10a, b).

2.4.4.4 Calcite

Most calcite occurs as pore-filling poikilotopic cement (Fig. 2.10e) and to a much lesser extent as a replacive phase after detrital dolomite (Fig. 2.10f). Two generations of poikilotopic calcite were identified (Fig. 2.10g), indicated by different intensities of blue cathodoluminescence. The first calcite cement generation (37.1% of total calcite) contains euhedral pyrite inclusions. The second calcite cement generation (62.3% of total calcite) has the same CL pattern as the calcite that replaces dolomite. Point count analysis establishes that dolomite replacing calcite accounts for < 1% of total calcite in the Montney Formation (Table 2.4). Moldic porosity and associated dolomitic and potentially phosphatic infill cements

of shells and other bioclasts (Fig. 2.10h, i) are evidence of dissolution and/or replacement of the primary aragonite or calcite.

2.4.4.5 Clay minerals

Kaolinite is present in significant amounts (P_{85}>2.5%) only in wells 11 and 15. Samples from wells 15 and 16 also contain abundant authigenic kaolinite crystals and vermiform kaolinite that fills open pores (Fig. 2.9e). Authigenic fibrous illite is pore-bridging and pore-lining, nucleating on detrital clays (Fig. 2.9f), mica grains, and rarely on kaolinite. Fibrous illite is variably distributed between all intervals and is completely absent from some samples. In addition, fibrous illite crystal growth is not uniform, with fiber lengths varying from several micrometers in some samples to less than one micrometer in others. In the quantitative data from the QEMSCAN analysis, fibrous illite is grouped together with MLIS clays.

2.4.4.6 Pyrite, anhydrite, and phosphate

Pyrite occurs in a range of forms and associations including framboids and euhedral crystals (Fig. 2.11a), as inclusions in a variety of cements (calcite, dolomite, feldspar and chert), in open pore space, within patched of organic matter, and between sheets of mica grains. All pyrite identified is interpreted to be authigenic, although it is possible that some of the pyrite is of detrital origin, based on the presence of clay coats on framboids (Fig. 2.11b).

All anhydrite is authigenic and forms bedding-parallel poikilotopic cement (Fig. 2.11c) or is concentrated in nodules. It was not possible to distinguish different cement generations using SEM-CL due to the non-luminescent nature of anhydrite and lack of morphological differences between possible cement generations. Phosphate occurs as phosphatized shell and shell debris (Fig. 2.10i), phosphatic nodules (Fig. 2.11d), grain coatings, or pore-filling cement. In addition, phosphate is also present as inclusions in dolomite and anhydrite
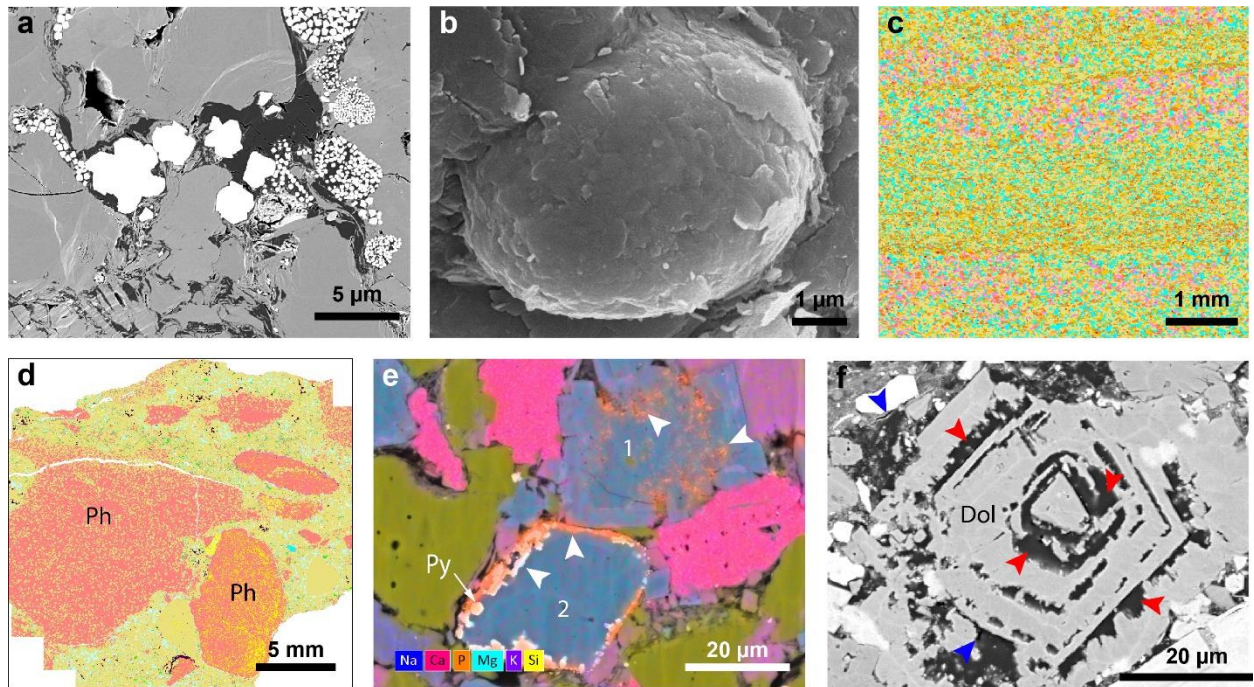
Fig. 2.11: Organic matter and minor mineral phases in the Montney Formation. (a) BS-SEM image of pyrite framboids and pyrite crystals within the siltstone matrix. Note abundant organic matter (dark gray) plugging pores. Sample,3A, well 2, 2285 m. (b) SE-SEM image of a pyrite framboids coated in detrital clay. Clay coats suggest pyrite framboids were transported from the original site of precipitation, sample 6, well 1, 1986 m. (c) QEMSCAN image of bedding -parallel anhydrite (pink color), sample 3B, well 9, 3340 m. (d) QEMSCAN image showing phosphatic nodules (pink), sample 170940, well 10, 1794.5 m. (e) EDS- SEM image showing (1) phospahte incorporated into dolomite (white arrow), and (2) phosphate precipitating at the boundary of a dolomite grain (white arrow), together with pyrite (white crystals) ,sample 3E, well 2, 2281 m. (f) BSE-SEM image showing organic matter (red arrows) filling secondary porosity in dolomite. Blue arrows point to pores which show darker on BSE images. Sample 1AE, core 15, 864.9 m.

cements (Fig. 2.11e). Although we considered all phosphate in our samples as authigenic, it is possible that some of the phosphate, particularly phosphate composing shells and shell fragments is primary.

2.4.4.7 Organic matter:

Total organic carbon content averages at 1.2 wt%, with minimum and maximum values of 0.05 and 4 wt%, respectively. Organic matter content generally increases with depth, and decreases eastwards, towards the shallow basin. No primary (depositional) macerals were

44

identified in this study, based on morphology, thus the organic matter in our samples appears to be of secondary origin (i.e. bitumen or pyrobitumen). Organic matter fills interparticle porosity between detrital and authigenic particles (Fig. 2.11a), as well as intraparticle porosity in mica, pyrite, feldspars and dolomites (Fig. 2.11f).

2.4.5 Porosity, compaction, and Intergranular Volume (IGV)

Matrix porosity from helium pycnometry ranges from 0.6 to 27.1%. The error reported for these measurements is under 6% for all samples, and most commonly under 1.5%. Porosity reported from QEMSCAN analysis varies between 0.2 and 22.7%. In contrast, open porosity (primary and secondary porosity) estimated through point count analysis (Table 2.4) varies between 0.1 and 3.7%. No clear depth trends were observed with any type of porosity measurement. Matrix porosity and QEMSCAN macroporosity values are presented in Fig. 2.12. Matrix porosity (which includes microporosity) is consistently greater than QEMSCAN porosity (macroporosity only). Porosity measured by point counting is equal to or less than porosity measured by QEMSCAN. This may indicate that a large fraction of the pores consists of micropores, smaller than 4.8 µm, although we note that the QEMSCAN macroporosity data also include large (> 4.8 um) pores filled with organic matter. Secondary porosity (porosity generated through framework grain dissolution (Siebert et al., 1984; Harris, 1989) averages 4.2% of total porosity and only 0.2% of bulk rock volume.

Evidence for mechanical compaction is present at the microscopic scale in the form of bent or broken mica grains where layers have separated (Fig. 2.9a, b), clay clumps that deform around detrital grain (Fig. 2.9c), and fractured detrital grains (Fig. 2.7i-l). Intergranular volume (IGV) is a direct measure of mechanical compaction, accounting for the total space between detrital grains, which decreases with increasing compaction. Commonly, IGV is used for assessing the degree of compaction of sandstones, where it is calculated by combining residual pore volume, cement volume, and matrix components (Houseknecht, 1987; Wilson and McBrige, 1988; Ehrenberg, 1989; Lundegard, 1992; Paxton et al., 2002).
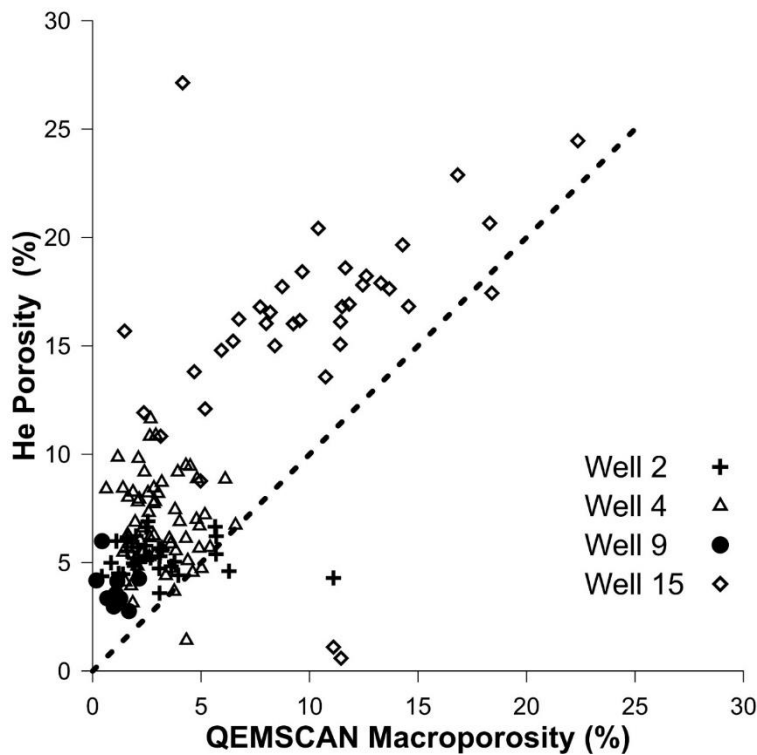
Fig. 2.12: Macroporosity values obtained from QEMSCAN analysis (pores > 4.8) and matrix porosity (pores > 0.31 Å). Matrix porosity is consistently higher than porosity measured through QEMSCAN analysis indicating that a large fraction of the pores in the samples consists of micropores, smaller than 4.8 μm.

Recently, Milliken and Olson (2017) introduced a modified term, IGV_m that is moreappropriate for calculating intergranular volume of mudrocks. IGV_m include the residual primary porosity, cements, and pore-filling secondary organic matter.

The IGV_m values obtained from point count analysis vary greatly between samples and range from 27.6 to 69.4% (Table 2.4). For samples from well 2, lithofacies G/H has IGV_m values of 32.5 - 46.0%, whereas lithofacies F has somewhat lower IGV_m values of 32.2 - 37.1%. For well 4, lithofacies K has the highest IGV_m value of 69.4%. The intergrannular volume of lithofacies G/H and M/N in this well ranges between 27.6 and 51.9%. In well 9, Lithofacies B has IGV_m values of 28.1 to 47.6%, Lithofacies O has IGV_m value of 40.6%, and lithofacies G/H has IGV_m value of 31.1%.

Lithofacies K (massive calcareous clayey siltstone) has the highest IGV_m volume (69.4%), when considering all wells in the data set. Lithofacies G/H (laminated siltstone) has the largest ranges of IGV_m values (27.6 - 51.9%), followed by lithofacies B (massive sandy siltstone) with a somewhat smaller IGV_m range (28.1 - 47.6%). Lithofacies F (faintly laminated calcareous

siltstone) has an intermediate range of IGV_m values (32.2 - 37.1%). Lithofacies M/N (bioturbated, calcareous, sandy siltstone) and lithofacies O (hummocky to ripple cross-stratified sandy siltstone), with one sample each, have IGV_m values of 33.8%, and 40.6%, respectively. With the exception of the sample from lithofacies K, samples from group one (on average, the coarsest grained samples) have the highest IGV_m values, whereas samples from groups two and three have similar IGV_m values. However, it is important to bear in mind that the reported IGV_m ranges may be heavily influenced by the limited number of samples associated with each lithofacies (Table 2.4).

Evidence for chemical compaction (pressure-solution) is recorded in a large number of samples and affects mostly silicate minerals. For the most part, pressure-solution only penetrates cement rims of silicate minerals (Fig. 2.11a), and in fewer cases non-cemented detrital quartz grains (Fig. 2.11b) As overgrowths are commonly of variable thickness, even around a single grain, it is difficult to quantitatively assess the amount of material removed through chemical compaction.

2.4.6 Relative timing of diagenetic events

The Montney Formation has a wide range of burial depths and organic matter maturities, but there are few systematic differences in the nature of the diagenetic phases with depth. Based on petrographic evidence (cement overgrowths and crosscutting relationship between authigenic phases or dissolution events), we divided all diagenetic processes into pre-burial diagenesis and post burial diagenesis. The paragenetic sequence for the formation is presented in Fig. 2.13 and described below.

2.4.6.1 Pre-burial diagenetic events

Early or pre-burial diagenesis occurs at or very close to the sediment-water interface. Preburial diagenetic processes include dissolution of unstable aragonite/calcite shells (Fig. 2.10h), phosphatization of bioclasts (Fig. 2.10i), phosphatic nodules (Fig. 2.11d) growth, and phosphatic grain coats growth (Fig. 2.11e).

2.4.6.2 Post-burial diagenetic events

Post-burial diagenetic events are characterized by mechanical compaction and massive cementation of carbonate and silicate minerals. The first cements to precipitate were the two generations of quartz (Fig. 2.7a), one generation of K-feldspar (Fig. 2.8a), one generation of Na-feldspar (Fig. 2.8b), and several generations of dolomite with a final Fe-rich dolomite cement (Fig. 2.10b). All these cements are localized around different detrital grains. Since no crosscutting relationships were identified between the cements, we suggest they effectively precipitated contemporaneously.

Two generations of poikilotopic calcite cement were identified, both precipitated around earlier authigenic phases (quartz, feldspars and dolomite), (Fig. 2.10e). The first generation of calcite cement contains pyrite inclusions (Fig. 2.10g) and thus postdates the formation of at least some of the pyrite. Calcite that replaces dolomite (Fig. 2.10g) shares similar luminescence with the second generation of calcite cement, suggesting that both precipitated from a single fluid and are contemporaneous.

Much like calcite cement, anhydrite is poikilotopic, engulfing early authigenic phases (quartz, feldspar, and dolomite), (Fig. 2.11c). None of our SEM-CL samples contained both anhydrite and calcite, and we were unable to constrain the relative temporal relationship between these two phases. However, as both calcite and anhydrite cements engulf and thus postdate quartz, feldspar and dolomite cements, we interpret them as approximately contemporaneous.

Pressure solution penetrates cement rims of quartz and feldspars and were thus developed after these cements precipitated (Fig. 2.14). However, we were not able to confirm the temporal relationship between pressure solution and calcite and anhydrite cements.
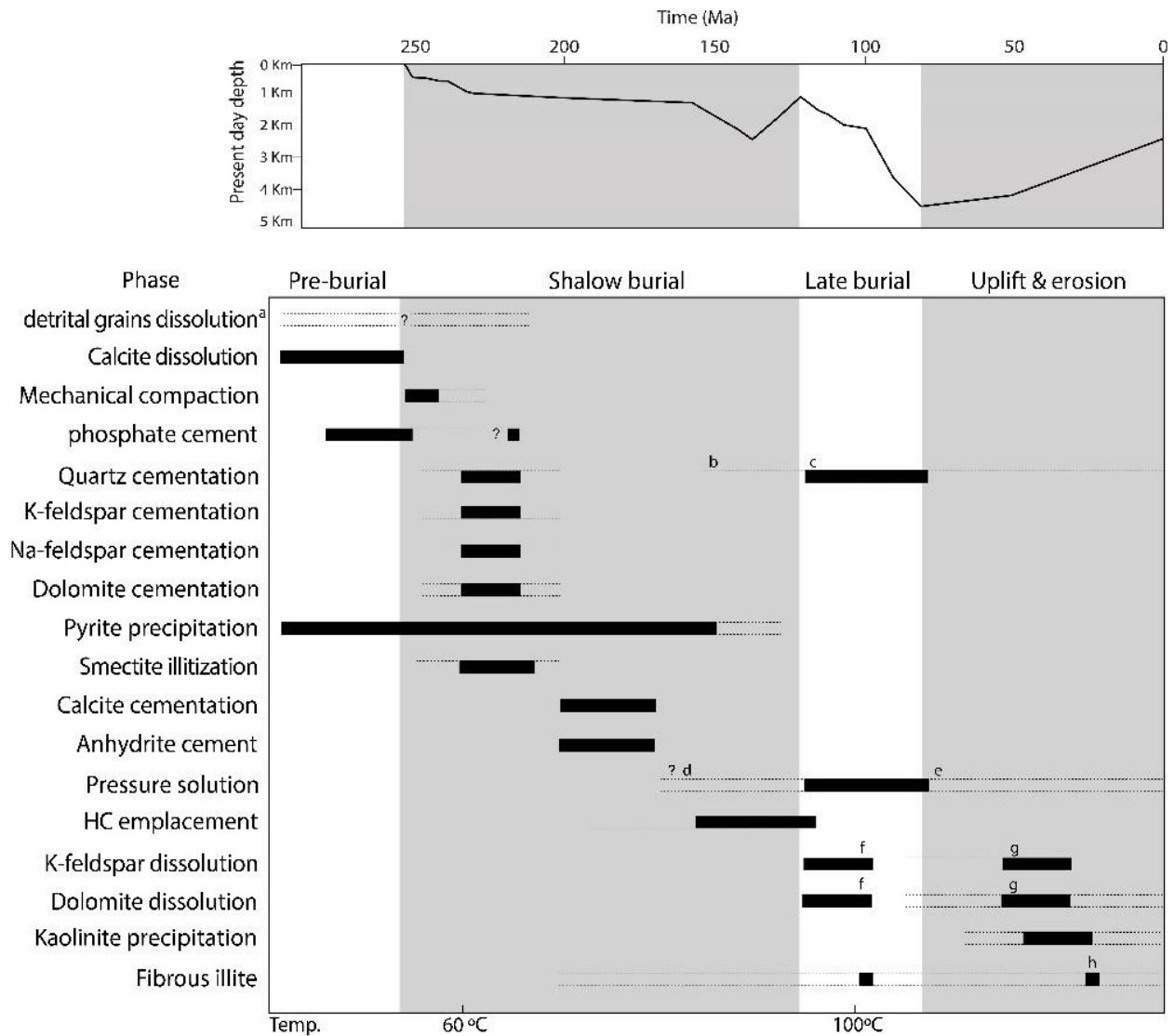
Fig. 2.13: Paragenetic sequence for the Montney Formation. Burial diagram adopted from well C-70-B/93-P-9 of Ducros et al. (2017). (a) Detrital component slightly dissolved on seabed include dolomite, feldspars and chert (b) Process continues in the deep section of the basin when temperatures are currently 100°C or higher (c) Albitization (d) Process developed only in the shallow section of the basin.

Pyrite is present as inclusions in different cements (calcite, dolomite, feldspar and chert), in open pore space (Fig. 2.7b), within patches of organic matter (Fig. 2.9b, d; Fig. 2.11a), and between sheets of mica grains. This indicates that pyrite formation was a recurring or continuous process that began shortly after deposition and ended, at the earliest, with the formation of the last of these cements although crystal growth in open pores could have continued for much longer.

Residual hydrocarbons (bitumen and pyrobitumen) plug a large portion of the original inter and intragranular pores and infills secondary porosity that developed in cemented grains (Fig. 2.11a, f). This suggests that hydrocarbon emplacement postdated cementation of feldspars, quartz, dolomite, calcite and anhydrite and that grain dissolution either predates or is contemporaneous with the emplacement organic matter. In samples where secondary porosity is not filled with organic matter (Fig. 2.8f), this temporal relationship is less well constrained. Micropores developed in some of the organic matter in wells where organic matter is mature or over-mature postdates organic matter emplacement.

As suggested by the preservation of their delicate structure and their pore filling and/ or pore bridging nature, the last phases to crystalize in the Montney Formation are fibrous illite (Fig. 2.9f) and kaolinite clays (Fig. 2.9d), especially in the shallowly buried eastern wells (well 15 and well 16). Fibrous illite locally overgrows kaolinite, indicating that illite precipitation postdates this of kaolinite. The elative timing of hydrocarbons emplacement with respect to precipitation of authigenic illite is not clear.

2.4.6.3 Unconstrained diagenetic events

The timing of minor dissolution identified in detrital chert (Fig. 2.7b), feldspars (Fig. 2.8b) and dolomite grains (Fig. 2.10b) is not well constrained. This dissolution is restricted to detrital grains and does not occur in any of the cement overgrowths. Partial dissolution of detrital grains may be associated with pre-burial transport and weathering processes, but it could also be a post-depositional event. Overall, no clear petrographic evidence was found to

determine the accurate timing of small-scale detrital grain dissolution. Similarly, we were not able to constrain the timing of albitization of detrital K-feldspar (Fig. 2.8d) and Na-feldspar grains (Fig. 2.8e). Finally, the relative timing of hydrocarbons migration/generation with respect to clay minerals precipitation is not entirely clear.
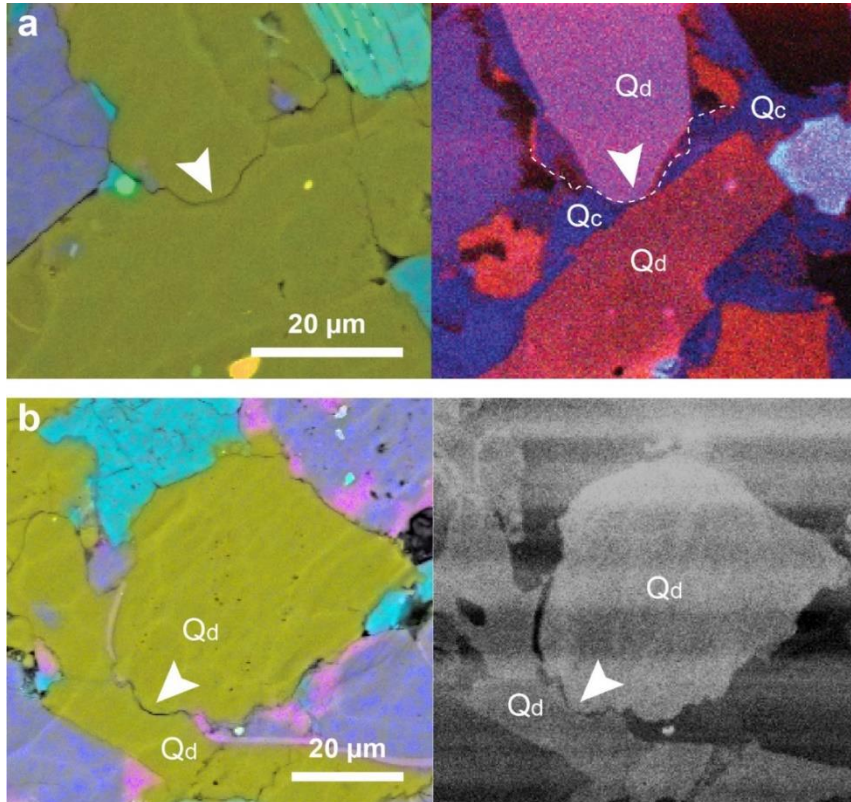
Fig. 2.14: Pressure solution in Montney samples. (a) SEM-EDS image (left) and SEM-CL image (right) of pressure solutions (white arrow) between a detrital quartz grain (Qd) and quartz cement (Qc). Sample 5N, well 9, 3376m. (b) SEM-EDS image (left) showing quartz grains with morphology that resembles pressure solution (white arrow). SEM-CL image (right) confirms pressure solution between two detrital quartz grains (Qd). Sample 2AQ, well 9, 3289 m.

2.5 Discussion

2.5.1 Grain size, sorting, and sediment transport mechanism

Grain size and sorting are key parameters that can provide information about sedimentation mechanisms and energy levels of the transporting medium (commonly wind or water) at the site of deposition. The mean grain size of samples from group one averages at 4.2 φ (54 μm) whereas mean grain size of samples from groups two and three averages at 5.0 φ (31 μm). The mode (most abundant grain size) varies over a narrow range, between 4.4 - 4.8 φ (36.7 and 46.3 μm).

Few studies have examined the grain size in the Montney Formation in detail through optical microscopy. Davies et al. (1997) reported that grain size varied between 3 and 4.6 φ (40 to 120 μm) with a majority of the samples falling between 3.5 and 4 φ (62.5 - 88 μm). Barber (2002) and Sanei et al. (2016) on the other hand, report grain size distributions and modes that are similar to our results. The graphic standard deviation (1σ, Table 2.2) calculated from grain size data indicates that our siltstone samples are moderately to poorly sorted, whereas other studies describe the Montney siltstone as moderately to well-sorted (Davies et al., 1997; Barber, 2002; Sanei et al., 2016). Different grain size distribution (Davies et al., 1997) and sorting patterns (Davies et al., 1997; Barber, 2002) probably stem from the fact that these studies almost exclusively examined reservoir facies within the Montney such as shoreface and turbidites which tend to be better sorted, whereas this study includes a wider range of lithofacies. Sampling location was not reported by Sanei et al. (2016), making comparison to our results difficult.

Our interpretation is similar to this of Davies et al. (1997) and Barber (2002). We suggested that grain size distribution points towards a mixed traction and suspension aeolian transport mechanism (Tsoar and Pye, 1987; Bullard and Livingstone, 2009; Nickling and Neumann, 2009) and that the Montney siltstone are similar to other loess deposits (e.g. Mason et al., 2003; Sun et al., 2006; Prins and Vriend, 2007; Crouvi et al., 2008; Nottebaum et al.,

2015). Zonneveld and Moslow (2014; 2018) suggested more complex transport processes, involving wind-blown material accumulation in fluvial channels of ephemeral rivers that drained into the basin during flash floods. The authors, however, agreed that aeolian processes contributed significantly to sediment accumulation in the Montney Formation siltstone.

2.5.2 Depth and time constraints for diagenetic processes

Compaction and cementation act in combination to reduce the depositional porosity of the rock. However, while mechanical compaction acts to reduce the intergranular volume, cementation can lead to its preservation if it occurs before maximum compaction was achieved. To evaluate the depth of cements precipitation it is necessary to consider the final volume of cement and the porosity of the sediment at the time of deposition.

Once formed and unless dissolution occurs, cement volume remains unchanged with continuing burial. In the Montney Formation, there is little evidence for cement dissolution, other than through pressure solution. From SEM-CL analysis, we established that chemical compaction affected mostly overgrowths and was rarely documented to influence detrital grains. Although it is difficult to quantify the effect of pressure solution, it is reasonable to assume that chemical compaction made only a minor contribution to porosity reduction in the formation. If the depositional porosity of the rock is known, one can use the present IGV_m volume of a sample to assess at what depth the rock was cemented, and compaction ceased. Minimum IGV_m value (27.6%, sample 5V, well 4) can be used as a lower limit to the depositional porosity of the sediment, and maximum IGV_m value (69.4%, sample 4V, well 4) can be used as the upper limit of sediment porosity at the time of deposition.

Information on the depositional porosity of silt-size sediments is scarce. Hedberg (1926) and Chilingarian (1983) estimated initial porosities for siltstones to be between 50 and 80%. Scuderi et al. (2015) measured porosity of 45% in a siltstone sample taken from an outcrop of the Marcellus Formation in the vicinity Newton Hamilton, Pennsylvania. Sample description

was not provided, but since the Marcellus Formation in this area is overmature (%Ro>2.0; U.S. Department of Energy, 2017) the rock has been compacted prior to its exhumation and the reported porosity of 45% cannot be considered as the depositional porosity of the sample.

In addition, a compilation of porosities for silt-rich sediments (silt-size grains content of 60 to 90%) between 0 and 1700 m was obtained by the Ocean Drilling Program and reported by Kominz et al. (2011). In this dataset, depositional porosity of silt-rich sediment varies between 40 and 95%. However, within a few tens of meters porosity in most measurements is reduced to about 60%. We thus selected 60% as the depositional porosity for the Montney siltstone, similar to values of 53 to 57% assumed by Ness (2001) in a basin modeling study of several Montney wells. In the Kominz et al. (2011) dataset, porosity for silt-rich sediments is well constrained (more than one measurement in similar depths) up to a depth of 1200 m. We used this compaction curve (black curve, Fig. 2.15) to determine the maximum depth at which cementation occurred in our samples.

Intergranular volume in our dataset ranges from 27.6 to 69.5%, but the IGV_m of most samples (14 of 17 samples) is between 31.1 and 51.9. All the samples were retrieved from depths larger than 2280 m (Table 2.4), but the IGV_m values of the samples suggest that compaction ceased at a much shallower depth, ranging from 150 to 1100 m. Green arrows in Fig. 2.15 indicate the cementation depths of three samples with IGV value of 52% (Fig. 2.15a), 40% (Fig. 2.15b) and 27.6% (Fig. 2.15c). Samples with IGV_m > 60% could not be placed on the compaction curve. An IGV_m value that is higher than the depositional porosity of the rock suggests that some of the cement precipitated in pores previously occupied by detrital grains. However, we were not able to confirm framework grain dissolution in samples with high IGV_m.

Depositional porosity of clean, well-sorted sands is approximately 45% (Paxton et al., 2002). Sandstones reach maximum compaction at about 2 to 2.5 Km, at which point porosity stabilizes at 26% and is not reduced further with burial (Paxton et al., 2002) (Fig. 2.15). The silt-rich sediment of the Montney Formation is moderately to poorly sorted (Table 2.3), and

it is possible that its initial porosity is lower than 60% and closer to that of sands. In this case, the siltstone compaction curve should move closer to the sandstone compaction curve (Fig. 2.15), which would result in shallower cementation depth for most of our samples. If depositional porosity was closer to 45%, this would also indicate that samples with IGV_m values larger than 45% have experienced some degree of detrital material dissolution.

In addition to estimating the depth of cementation, it is also possible to assess if porosity loss was influenced more by compaction or by cementation. The portion of the original porosity lost due to compaction (compactional porosity loss, COPL) and the portion of the original porosity lost due to cementation (cementational porosity loss, CEPL) are calculated using equations 1 and 2 (Ehranberg, 1989):

$$(1)\ COPL = \emptyset_i - \frac{((100 - \emptyset_i) * IGV_m)}{100 - IGV_m}$$

$$(2)\ CEPL = (\emptyset_i - COPL) * \frac{C_m}{IGV_m}$$

Where $\emptyset_i$ is the depositional porosity of the sediment, and C_m is the combined volume of cement and secondary organic matter (bitumen) in primary pores (Milliken and Olson, 2017). Assuming a depositional porosity of 60% in calculating COPL and CEPL, cementation was responsible for more porosity loss than compaction (CEPL > COPL; Table 2.4) in samples that were cemented at a very shallow depth (<300 m) and thus have preserved IGV_m values larger than 44%. Heavily cemented samples are not unique to a single well, a single lithofacies, or a particular member of the formation, making it difficult to identify a control for cementation in these samples.

Compaction was responsible for most of the porosity loss in the majority of the samples (COPL > CEPL). These samples were cemented at a larger depth (300 - 1100 m) and thus record smaller IGV_m values (27.6 - 40.6%). This suggests that the initial compaction rate of the siltstone was very high, and only samples that were cemented within the top 300 m of
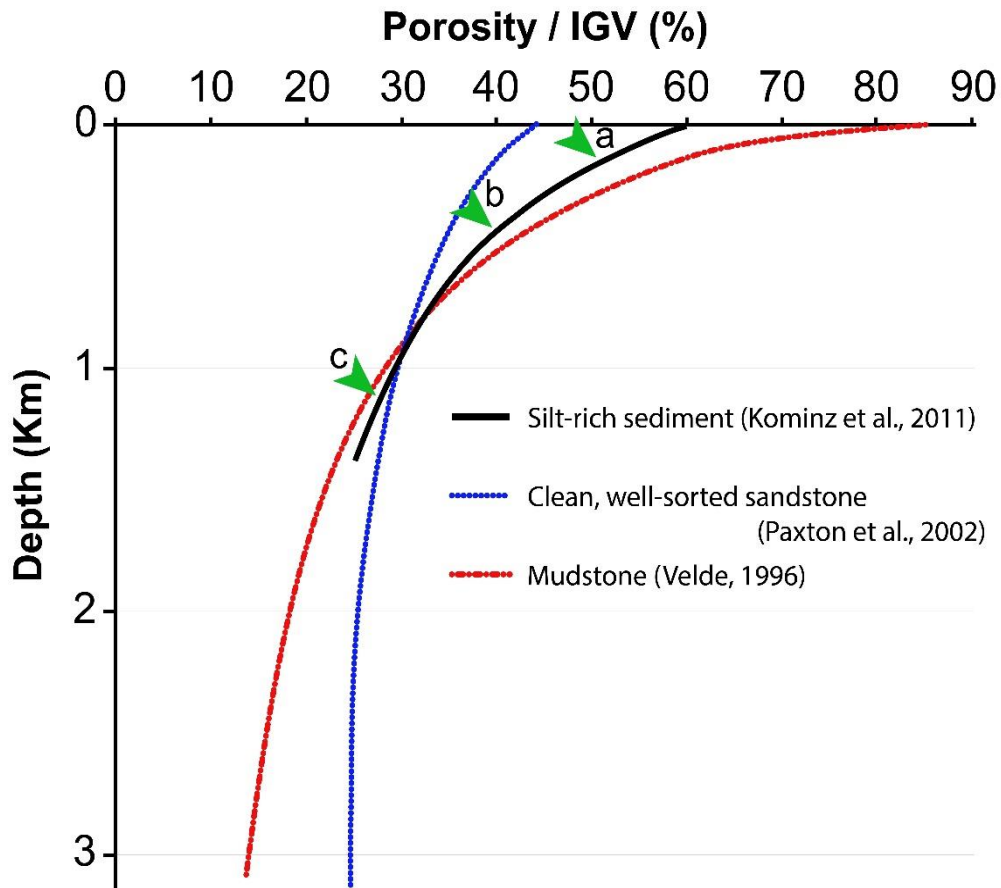
Fig. 2.15: Porosity/ IGV depth plot for silt-rich sediment (black line), clean, well-sorted sandstone (blue line), and shale (red line). The rate of mechanical compaction is the main control over porosity reduction with depth, but cement halts compaction. If cement is present, the IGV value can indicates the depth of cementation.

Green arrows show the cementation depths of three samples from the Montney siltstone. (a) sample depth is 2653 m, but an IGV of 52% indicates cementation occurred at ~150 m depth (sample 3AJ, well 4). (b) sample depth is 3278 m, but an IGV of 40% indicates cementation occurred at 500 m depth (sample 1C, well 9). (c) sample depth is 2739 m, but an IGV of 27.6% indicates cementation occurred at 1000 m depth (Sample 5V, well 4). Samples with IGV > 60% (initial porosity) could not be placed on the compaction graph. Such high IGV value suggests that a portion of the detrital grains was dissolved or that the initial porosity is larger than 60%.

the interval retained high IGV_m values. However, most samples with lower IGV_m values were also cemented at a relatively shallow depth (< 1100 m).

Reworked clasts containing dolomite cement (Davies et al., 2018) and low dolomite formation temperatures (<60°C) identified from fluid inclusion analyses (Davies et al., 1997)

further support our interpretation of cements precipitation at shallow burial depths. Large volumes of cements together with indications for shallow cements precipitation suggest the existence of an open pore network that allowed space for mineral precipitation and enabled massive fluid flow through the rock. These fluids, which would have been seawater, possibly mixed with some fraction of hydrothermal fluids (Liseroudi et al. 2020), advected the solutes responsible for the massive precipitation of quartz, feldspars, calcite, dolomite, ferroan-dolomite, pyrite, and anhydrite cements that account for over 30% of the rock mass in the Montney siltstone (Table 2.4). Ness (2001) and Ducros et al. (2017) demonstrated through basin modeling that the Montney experienced slow burial for 100 million years following deposition, reaching a burial depth of about 1,500 m at the end of the Jurassic. Given this, we propose that shallow burial cementation occurred during this time period (Fig. 2.13).

2.5.3 Preburial and shallow burial diagenetic processes

In order to understand the processes controlling dissolution and cementation at the sediment-water interface and during very shallow burial, one needs to consider the environmental conditions under which the Montney siltstone was deposited. Early Triassic oceans were hot, acidic, and at least intermittently oxygen-depleted. Worldwide ocean acidification began at the end of the Permian and extended into the Middle Triassic, caused by increased atmospheric CO_2 concentrations that originated from the Siberian Traps volcanic eruptions (Sobolev et al., 2011; Zonneveld, 2011; Clarkson et al., 2015).

Elevated atmospheric CO_2 was also responsible for elevated surface ocean temperatures, which exceeded 32°C near the equator (Sun et al., 2012) and 26°C at 30°N latitude (Kiehl and Shields, 2005). Models show that elevated ocean surface temperatures did not significantly diminish with depth, leading to arrested oceanic circulation and widespread deep water anoxia (Kiehl and Shields, 2005). Anoxic or dysoxic bottom water conditions are proposed for the time of the Montney siltstone deposition, based on the presence of sulfide pseudomorphs of pollen grains and spores, the paucity of trace fossils, and concentration of trace elements that

are sensitive to redox conditions (U, V and Mo) (Zonneveld et al., 2010; Crombez et al., 2017). Under acidic and reducing conditions, the saturation limits in ocean water are high for alkaline elements such as sodium, potassium and calcium, as well as magnesium and iron (Tribovillard et al., 2006; Caracciolo et al., 2014).

2.5.3.1 Calcite dissolution:

The lack of detrital calcite in the Montney Formation can be attributed to global oceanic acidification during the early Triassic (Sobolev et al., 2011; Zonneveld, 2011; Clarkson et al., 2015) and elevation of the calcite compensation depth (CCD) to the shallow marine settings (Playter, 2013). Other options for calcite dissolution include acids released by decaying organic matter (Wallmann et al., 2008) or the presence of unstable aragonitic precursors. Dissolution processes may also have led to the small dissolution pits observed in many of the detrital minerals (mainly feldspars, dolomite, and chert), although these features may also be related to grain weathering during sediment transport.

2.5.3.2 Feldspars and dolomite cementation

We suggest that shortly after deposition pH stabilized through mineral dissolution that released alkali elements into the pore water. Mineral dissolution was partly derived by the acidic ocean water, and partially by acids released through oxidation of organic matter (Wallmann et al., 2008). The increased alkalinity is manifested through the precipitation of feldspars and dolomite cements, as well pyrite and iron-rich dolomite, indicating a decrease in the solubility of the dissolved alkali elements (Tribovillard et al., 2006; Caraccido et al., 2014). Without isotopic data, and potentially even with such information, establishing the source for different types of cements is speculative.

Dolomitization models that explain sources of calcium and magnesium ions required for dolomite precipitation and mechanism that drive the circulation of water carrying these cations through the rock may apply to the Montney Formation. Summaries of such models are provided by Warren (2000) and Machel (2004). Even with hypersaline brines that are

saturated with calcium and magnesium, over 70 volumes of water are required for precipitating one volume of dolomite (Warren, 2000). Moving such large volumes of water demands that the rock maintain high porosity and high permeability, indicating that dolomite precipitation is a shallow burial process.

The evaporative-brine refluxing model (Saller and Henderson, 1998 and reference therein; Machel, 2004) may be a suitable model for dolomite precipitation in the Montney Formation is. The evaporative-brine refluxing model was proposed originally by Adams and Rhodes (1960) and documented worldwide in ancient and modern settings and in both platforms and in ramps (Saller and Henderson, 1998; Warren, 2000; Machel, 2004) and is consistent with our interpretation of shallow burial dolomitization. According to this model, dense hypersaline brines, saturated with calcium and magnesium form in lagoons through evaporation. Gravitational flow drives the brines downward through the underlying rock where dolomite precipitates due to retrograde solubility (Warren, 2000; Jones and Xiao, 2005)

The evaporative-brine refluxing model requires that an evaporative lagoon exists on the margins of the basin. The updip portion of the Montney Formation was eroded during the Late Cretaceous Laramide Orogeny (Edwards et al., 1994; Davies et al., 1997, Moslow, 2000), but arid climate has been inferred for the area during the Triassic based on the presence of aeolian dunes, regionally extensive anhydrite, palynomorphs and reworked anhydrite nodules in the Montney Formation and the age equivalent Sulphur Mountain Formation (Zonneveld and Moslow, 2018 and reference therein).

In addition to increased flux of calcium and magnesium, evaporated seawater also contains elevated concentration of sodium and potassium. We propose that the dolomitizing fluids carried with them sufficient sodium to precipitate Na-feldspar cements. In accordance to the models suggested by Kalsbeek (1991) and González-Acebrón et al., (2010) It is possible that this sodium flux is also responsible for the albitization observed in our sample. Increased potassium concentrations in evaporated seawater, together with potassium

59

released by albitization of K-feldspar (Fig. 2.8d) also provided solutes for the precipitation of K-feldspar cement.

2.5.3.3 Quartz:

The precipitation of large volumes of quartz cement is commonly considered to be triggered by temperature dependent reactions that occur during deep burial (for example: McBride, 1989; Walderhaug, 1994; Giles et al., 2000). However, IGV values in our Montney Formation data set indicate shallow cementation. Total quartz cement concentration (first and second generation varies between 3.5 and 11.6%, with an average of 7.4% (Table 2.4). Shallow (1-2 Km) quartz cementation of such volumes is documented in reservoirs world-wide (Fisher et al., 2000; Giles et al., 2000; Hartmann et al., 2000) and attributed to feldspar dissolution, reprecipitation of dissolved siliceous skeletal grains, pressure solution, and precipitation from silica-saturated meteoric water (McBride, 1989 and reference therein; Giles et al., 2000; Worden and Morad, 2000 and reference therein).

The solubility of silica in water is very low (Williams et al., 1985 and reference therein), and improbably high volumes of water would be required to supply enough silica to precipitate the volumes of quartz in the Montney (Worden and Morad, 2000). In addition, there is no indication of silica influx from neighboring mudrocks in the form of increased quartz cementation towards the top or bottom edges of the formation. Therefore, an internal silica source for quartz cement is favored. We suggest that several internal sources combined to provide silica for the two generations of quartz cement.

Some silica was provided through in-situ dissolution and/or recrystallization of chert. Dissolution of chert grains is readily identified through SEM imaging (Fig. 2.7c), and evidence for chert recrystallization is in the form of seemingly intact, euhedral quartz grains that retained some of the mottled luminescence texture of chert (Fig. 2.7b). Angular holes identified on the surface of quartz overgrowth (Fig. 2.7h) may support this interpretation. Hattori et al. (2003) suggested that a similar morphology of quartz in the Miocene Kunimi

60

Formation in Japan reflects incomplete recrystallization of chert to quartz, leaving the crystal surfaces irregular and uneven. Alternatively, the angular cavities in chert grains and dissolution porosity in chert may reflect decalcification of the chert (tripolitic chert; Manger, 2014). Our petrographic analysis showed that detrital chert recrystallization cannot account by itself for the amount of quartz cement in the samples.

The silt-size quartz grains themselves may have been another potential source for the quartz cement. The structure of all quartz crystals terminates in a thin layer (~100 nm) of amorphous silica (Cecil, 2004) composed of either siloxane (Si-O-Si) or silanol (Si-OH) groups (Vansant et al., 1995). Amorphous silica is much more soluble than quartz (Aase at al., 1996) and can become an important source for silica (Cecil, 2004). Experiments on mechanically abraded quartz grains demonstrated that the lattice structure of quartz is distorted to a depth of at least 15 μm, rendering the outer section of the grain metastable and relatively soluble (Cecil, 2004 and references therein). These experiments suggest that silt-size quartz grains deposited by aeolian processes, particularly very small grains (2-3 microns) are highly reactive and can be easily dissolved.

Another fraction of the quartz cement is sourced from biogenic silica. Reports of biogenic silica in the Montney Formation are rare. Zelazny et al. (2018) hypothesized that chert in the time-equivalent Sulphur Mountain Formation in Alberta resulted from concentrations of radiolarian and/or sponge spicules. In addition, Wust et al. (2018) suggested that biogenic silica is an important component in at least 2 intervals within the Montney Formation in AB, based on Al/Si ratios and results from principal component analysis. In mudrocks, aluminum is commonly associated with detrital clay minerals (Tribovillard et al., 2006). A positive correlation between silicon and aluminum indicates the presence of detrital quartz, whereas excess of silicon relative to aluminum indicates the presence of biogenic silica (Tribovillard et al., 2006; Ross and Bustin, 2009). In the Montney Formation, both aluminum and silicon concentrations are affected by the presence of large amounts of quartz and feldspars cements

and authigenic clays, and in this case, increased ratio between silicon and aluminum can nor be easily used to indicate the presence of biogenic silica.

Our petrographic observations suggest that a small amount of biogenic silica is preserved in the Montney Formation in the form of silica nanospheres (Fig. 2.7g), interpreted to be the product of bacterial activity (Al Rajaibi et al., 2015; Milliken and Olson, 2017; Longman et al., 2019), and possible remnants of agglutinated foraminifera (Fig. 2.7d). Silica nanosphere cement is difficult to identify in polished Montney samples, but examination of freshly exposed surfaces under the SEM indicate that it is a minor type of silica cement in the Formation. It is possible, however, that some of the biogenic silica was dissolved and incorporated into one of the quartz cements generations.

Finally, some of the quartz cement originated from pressure solution (Fig. 2.7b, Fig. 2.14). In classic models, pressure solution is associated with high temperatures during deep burial (Walderhaug, 1994; Bloch et al., 2002). Other studies (summarized by Makowitz and Milliken, 2003) suggest that fractures in quartz grains that are close to the dissolving edge enhance quartz dissolution rate at grains contact. Since microfractures can develop in grains over a range of effective stresses, starting at depth of only a few meters (Wong, 1990; Makowitz and Milliken, 2003), the presence of microfractured quartz grains does not necessarily indicate deep burial.

Microfractures in quartz grains are present in our samples (Fig. 2.7 i-l), all of which are filled with quartz cement. The presence of different generations of cements in the microfractures indicates that at least two different microfractures systems exist in the samples. The first (blue) quartz cement filling microfractures may have formed during shallow burial, while the second (red) quartz cement fills microfractures that may have formed during deep burial, associated with pressure solutions. However, our data do not provide definitive constraints on the timing and conditions of the late quartz cementation event.

Quartz cement volumes vary over a wide range (2 to 11 wt%) for grain sizes < 20 μm. Coarser grain sizes are related to higher cement volumes (5-12 wt%) (Fig. 2.16a). This

implies that detrital grain size a is not the main factors controlling quartz cement volume. We propose that that the main control on quartz cementation is the abundance of detrital clay coatings on detrital quartz grains (Fig. 2.7c, 2.9c), which can inhibit quartz cementation by blocking potential nucleation cites (Heald and Larese, 1974; Wilson, 1992). Group one samples have the lowest amount of clay and high quartz cement volume, and samples from group three have higher clay concentration but similarly high quartz cement volume. (Fig. 2.16b). This comparison demonstrates that higher clay concentration in the matrix does not equate more extensive clay coats on detrital grains. (Needham et al., 2005) demonstrated that clay cots can be generated through digestive processes of worms. Lithofacies in group one have the highest bioturbation index (Table 2.2) and thus the highest probability to have clay coats and lower quartz cement volume.

2.5.3.4 Pyrite

Pyrite framboids form under euxinic conditions, either in the water column or below the water-sediment interface (Wilkin et al., 1996; Wilkin and Barnes, 1997; Wignall and Newton, 1998). Berner (1984) and Wilkin et al. (1996) demonstrated that framboids growing in the euxinic water column are generally <6 μm and are more uniform in size than framboids growing in the sediment, whereas crystalline pyrite is thought to develop only within the sediment itself. The wide size variation in pyrite framboids observed in our samples, together with the presence of crystalline pyrite suggest that pyrite precipitation occurred mostly within the sediment rather than in the water column.

2.5.3.5 Calcite and anhydrite cementation

The source for calcite cement in the Montney is not clear but has been postulated to be derived from carbonate dissolution in the underlying Permian strata (Nassichuk, 2000), possibly due to hydrothermal fluid involvement (Liseroudi et al., 2020).

Through petrographic observations, we were able to identify only one generation of anhydrite cement. Liseroudi et al. (2020) identified report two generations of anhydrite in
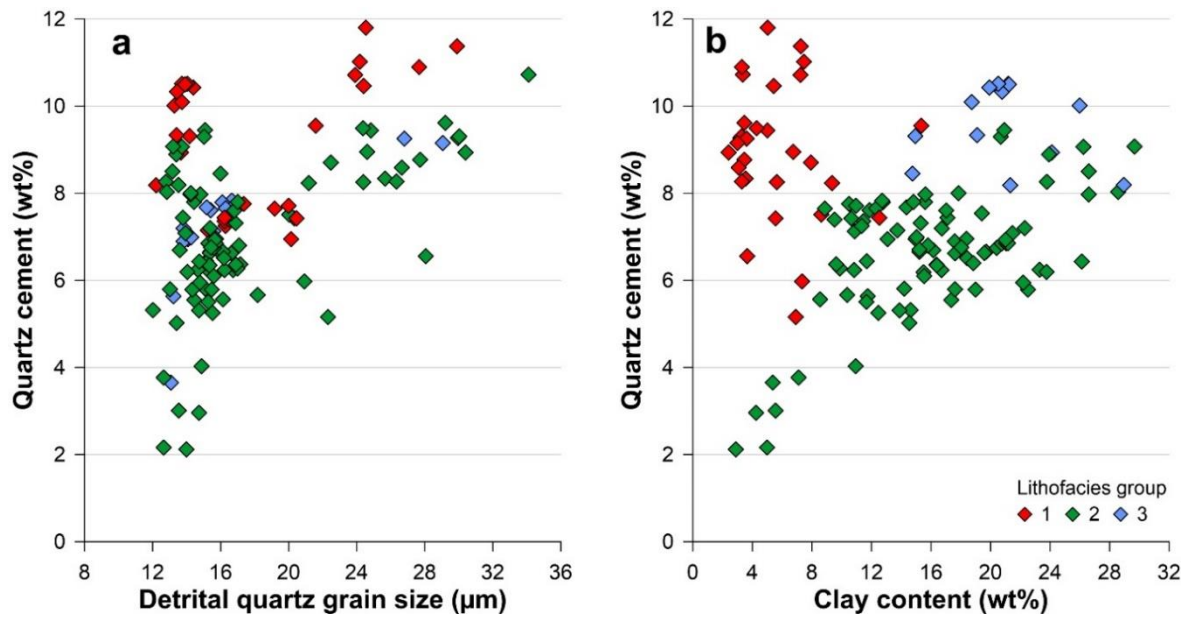
Fig. 2.16: Quartz cement volume, detrital quartz grain size and clay content for the three lithofacies groups in wells 2, 4, and 9. Cement volumes were calculated from QEMSCAN analysis results based on the average cement content of each mineral per facies, obtained from point count analysis (Table 4). (a) quartz cement. Note a wide range of cement volume at grain size < 20 μm, and higher cement volumes at coarser grain sizes, suggesting detrital grain size is not the main factor controlling quartz cement volumes. (b) Clay content and quartz cement. Samples from lithofacies group one have the lowest amount of clay and high quartz cement volume, and samples from lithofacies group three have higher clay concentration but similarly high quartz cement volume, demonstrating that higher clay concentration in the matrix does not equate more extensive clay coats on detrital grains. Lithofacies in group one have the highest bioturbation index and thus the highest probability to have clay coats generated through bioturbation. Respectively, samples from this group have the lowest volume of quartz cement.

the Montney Formation through isotopic analysis. Similar to our observations, Davies et al. (1997) and Liseroudi et al. (2020) attributed all of the anhydrite cementation to early diagenesis (shallow diagenesis in this study). Based on sulfur and oxygen isotopic compositions, Liseroudi et al. (2020) suggested that the first anhydrite cement precipitated directly from Triassic seawater, whereas the later generation shows compositional similarities to underlying Devonian evaporites.

2.5.3.6 Illitization and albitization:

Compositional variations of MLIS clays in the Montney Formation provide additional information about the diagenetic evolution of the siltstone. Our QEMSCAN analysis results indicate that the major clay species in the Montney Formation is MLIS (70-98% of total clay content), and quantitative XRD analysis determined MLIS composition to be illite (95)/ smectite (5) with insignificant swelling potential throughout most of the basin. Reports of swelling clays in the Montney are limited to the Ring-Border and Dixonville fields (Fig. 2.1) at the northeastern margin of the formation (Edwards et al., 1994; Zonneveld and Moslow, 2014, 2018). Quantitative XRD analysis of three samples taken from the Dixonville field (well 16, Fig. 2.1) confirmed the presence of MLIS with approximately 20% swelling layers (illite (80)/ smectite (20)). SEM examination of freshly exposed surfaces indicated that all the clays in those samples (other than kaolinite) have a detrital morphology and although they might be chemically altered from a detrital precursor, they did not precipitate *in situ*.

The occurrence of slightly swelling clays geographically near and at similar burial depth to occurrences of non-swelling clays indicates that reduction of swelling potential of the clays in the Montney does not result from high temperatures (>90 ^{o}C), as is shown for smectite illitization in the Gulf of Mexico (Hower et al., 1976; Boles and Franks, 1979). As it is unlikely that the Ring-Border and Dixonville deltas (Fig. 2.1) had a different sediment source than the rest of the formation, a different model for smectite illitization is required. We suggest that smectite illitization in the Montney Formation was a time-dependent, low temperature reaction, taking place at temperatures of 60-80°C, over extended period of time (10^8 years), and requiring high enough permeability to allow large volumes of water to interact with the rock (Buatier, 1992; Kirsimäe et al., 1999; Moore, 2000).

We propose that partially illitized detrital MLIS clays were deposited as dispersed material between other matrix components. The MLIS clays were further illitized to their current composition [illite (95)/ smectite (5)] over 100 million years following deposition, as the

Montney was slowly buried to a maximum depth of ~1500 m. Prolonged shallow burial maintained high porosity and permeability in the siltstone, allowing large volumes of fluid to pass through the formation and interact with the available MLIS.

The illitization of smectite consumes potassium. In some cases, local K-feldspar dissolution is considered as the source of potassium for the time-dependent reaction (Moore, 2000), but in other cases a source external to the formation is contemplated (Van De Kamp, 2008). Illitization of smectite and albitization (replacement of K-feldspar by Na-feldspar) are two processes that involve concurrent exchange of alkali elements and are commonly linked (Hower et al., 1976; Morad and Aldahan, 1987; Saigal et al., 1988; Aagaard et al., 1990). Potassium released by the albitization reaction becomes available for illitization of MLIS clays. Although we have documented some post-burial K-feldspar and mica dissolution in our samples, albitization of K-feldspar is interpreted to provide most of the potassium for the illitization of smectite. Mass balance calculations based on point count results (appendix 2) show that albitization would have released sufficient potassium to illitize all MLIS clays in the Montney to their present-day composition.

For the most part, clays in the Montney Formation are dispersed within the matrix of hard grains. The slightly swelling clays [illite (80)/ smectite (20)] in the Dixonville and Ring Border deltas however were deposited mostly in several cm thick beds. It is possible that the lower permeability of these beds restricted fluid flow and thus potassium supply and led to the preservation of some swelling potential in these clays.

The process of illitization of smectite also would have released large amounts of silica (Hower et al., 1976; Boles and Franks, 1979) which may have contributed to the first generation of quartz cement. Mass balance calculations (appendix 2) show that smectite illitization would have contributed 5-20% of the silica composing the first quartz cement generation.

2.5.3.7 Organic matter

Whether organic matter in the Montney is primary (i.e. present in the siltstone at the time of deposition) or is a result of hydrocarbons migration is still debated. Movement of liquid hydrocarbon within the siltstone is recorded by flow structure preserved in solid pyrobitumen (Chalmers and Bustin, 2012; Akai and Wood 2014; Sanei et al 2015; Wood et al., 2015; Wood et al., 2018), but these observations have no bearing on the source of the liquid hydrocarbons.

Some oil-to-source correlation studies concluded that oil migrated into the Montney from the overlying Doig, Nordegg, and the Exshaw Formations (Riediger, 1990; Chatellier et al., 2018; Feng et al., 2016) but others suggest that at least some hydrocarbons were generated in the western section of the Montney Formation (Feng et al., 2016; Feng, personal communication). However, depositional macerals have never been reported from this deeply buried wester section of the formation, possibly because of the high maturity that makes it is extremely difficult to distinguish pyrobitumen from kerogen, if the latter is present in the rock (Lewan and Kotarba, 2014).

The presence of depositional macerals and remnant generation potential are also disputed. Sanei et al. (2015) and Wood et al. (2018) noted the absence of primary macerals from their samples, which varied in maturity (Ro% 0.93 to 2.08), and Sanei et al. (2015) indicated that less than 10% of samples examined still have some generation potential. On the other hand, Romero-Sarmiento et al. (2016) established the presence of vitrinite and liptinite in immature Montney samples and there are several reports of good to very good generation potential for samples with immature and early mature organic matter from the Montney (Ibrahimbas and Riediger, 2004; Ejezie, 2007; Chalmers and Bustin 2012; Feng et al., 2016; Chatellier et al., 2018) that indicate the presence of non-spent organic matter.

We did not identify any depositional macerals in our samples, and all the organic matter is considered secondary in origin (i.e. migrated hydrocarbons). The massive cementation documented in our study require that large volumes of water bearing solutes flow through

the siltstone, and it is difficult to envision that marine organic matter will be preserved under such conditions. It is possible that primary organic matter was preserved in very fine-grained intervals, where flow was drastically restricted.

2.5.4 Late shallow burial diagenesis (eastern subcrop)

Late diagenesis in the eastern section of the Montney Formation, particularly in areas closer to the subcrop edge (wells 15 and 16, Fig. 2.1) is characterized by meteoric water influence at shallow depth. The effect of meteoric water is evident by the precipitation of kaolinite (Fig. 2.9e) and massive overgrowths of quartz (Fig. 2.7e) and K-feldspar, together with extensive dissolution of dolomite (Fig. 2.10d). We lack quantitative data to assess the degree of cement development for the shallow Montney wells (wells 15 and 16), but QEMSCAN data show an increase in kaolinite for wells 11 and 15, demonstrating the effect of meteoric water on the erosional edge of the subcrop. Similar observations were reported for the subcrop edge of the Brent Formation of the North Sea (Osborne et al., 1994).

2.5.6 Composition and grain size dependency of lithofacies

The diagenetic pathway of a rock may be linked to its depositional environment through variation in grain size and detrital composition. Grain size and composition dictate both the initial porosity and permeability of a rock (Morad et al., 2010) and its compaction rate, thus controlling available pore space for cementation and fluid-flow. Here we examine the relationships between lithofacies in the Montney Formation, grain size and detrital mineralogical composition. In addition, we consider the effect of diagenetic processes on the overall mineralogical composition of the lithofacies.

Bulk rock compositions and calculated average detrital composition for seven lithofacies from three cores are presented in Fig. 2.6b. Detrital composition was calculated by subtracting the percentage of cement (obtained from point count analysis) from the total content of each phase (obtained from QEMSCAN analysis). For example, lithofacies F in well two has an average of 39.2 wt% of quartz. Point count analyses (Table 2.4) demonstrated that 28.8% of

the quartz in this facies is authigenic, while 71.2% of the quartz is detrital. The detrital quartz content for lithofacies F in well 2 is therefore 27.9 wt%.

The main difference in present-day mineralogical composition and calculated detrital composition between the study wells pertains to carbonate mineral content, and to a lesser extent quartz and feldspar content (Fig. 2.6). Present day composition (detrital grains and cements) are similar between lithofacies, and only in the easternmost core (well 15) are lithofacies compositionally distinct from one another.

The relative homogeneity of rock composition is explained in part by small compositional differences between lithofacies (Fig. 2.6b), suggesting that the detrital material that entered the basin was fairly homogeneous. In addition, our point count analysis, the total volume of shallow diagenesis cements accounts for more than 30% of present day rock volume (Table 2.4).The large volumes of cements precipitated during shallow burial diagenesis overcame the small compositional differences in detrital grain composition between the different lithofacies in the rock and led to compositional homogeneity of the Montney siltstone.

2.5.7 Implications of diagenesis for reservoir quality

As reservoir quality is determined mainly by porosity and relative permeability, it is important to consider how diagenetic processes influenced those properties. Locally (primarily in areas near the erosional edge of the formation), dissolution can be an important porosity-generating mechanism, but dissolution is generally a minor phenomenon in the Montney Formation and will not be discussed further.

Cementation and compaction acted together to reduced porosity and permeability in the Montney Formation. Ghanizadeh et al. (2015) and Sanei et al. (2016), referring mainly to carbonate cement, showed that heavily cemented Montney samples have a higher proportion of small pores and lower permeabilities than uncemented samples. They qualitatively attributed large volumes of carbonate cementation to larger grain size, explaining that coarser intervals retained higher porosity and permeability and allowed for higher paleo fluid flow that

led to the precipitation of larger volumes of cement. It is worth noting that both Ghanizadeh et al. (2015) and Sanei et al. (2016) referred to present day apparent grain size, which includes detrital grains and potentially their corresponding cement overgrowths rather than the detrital grains present at the time of dolomite cement precipitation.

We examined the relationship between detrital quartz grain size (calculated using the equation presented in Fig. 2.17) and cements volume in three wells in the study area. Cement volumes were calculated from QEMSCAN analyses for each lithofacies in each well based on the relative percentage of each cement, obtained from point-count analyses. For example, point count analyses results show that dolomite cement is 53% of the total dolomite for lithofacies G/H in well 2 (Table 2.4). Therefore, 53% of the dolomite identified in QEMSCAN analysis for all samples of lithofacies G/H in well 2 was considered authigenic. Results of these calculations are presented in Fig. 2.17a, b. It is evident that no correlation exists between detrital quartz grain size and either total cement volume or calcite cement volume in our samples. In fact, most samples from group one, which are the coarser samples, have little to no calcite cement.

Our observations support the findings of Chalmers and Bustin (2012) that calcite cement is responsible for much of the porosity destruction in the Montney Formation. In addition, we recognize that organic matter emplacement dramatically reduced porosity in the Montney Formation and agree with the conclusion of Wood et al. (2015) that there is no statistically significant correlation between porosity and TOC on a regional scale.
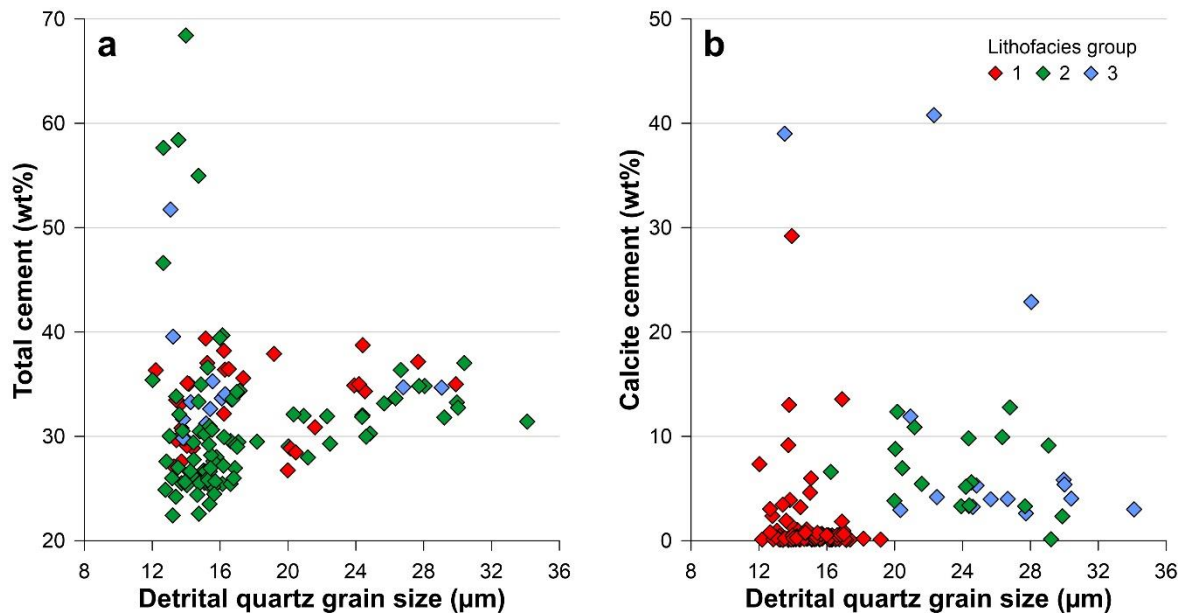
Fig. 2.17 Detrital quartz grain size and cement volumes for the three lithofacies groups in wells 2, 4, and 9. Cement volumes were calculated from QEMSCAN analysis results based on the average cement content of each mineral per facies, obtained from point count analysis (Table 4). Note that a clear distinction between samples from different groups exist in none of the graphs. (a) Total cement volume includes quartz, feldspar, dolomite, calcite, anhydrite, pyrite, halite and phosphate. No correlation exists between detrital quartz grain size and dolomite cement or total cement volume. (b) No correlation exists between detrital quartz grain size and calcite cement. Most samples from group one which have the largest grain size, have the lowest amount of calcite cement.

2.6 Are siltstones unique?

The Montney Formation has been referred to for many years as a 'shale' in publications and by industry (e.g. Keneti and Wong, 2010; Norton et al., 2010; Davey, 2012; Nieto et al., 2013), even though it has long been recognized as composed mainly of silt-sized grains (e.g. Polt and Krause, 1997; Krause et al., 2012, Vaisblat et al., 2017). Mechanical diagenesis of clastic sediments is strongly influenced by grain size and shape, as they control compaction rates (Chilingarian1983; Aplin and Macquaker, 2011, and references therein). A comparison of compaction curves for sandstones, siltstones and mudstones (Fig. 2.15) demonstrates that

71

with increasing grain size the compaction rate in the upper 1.5 Km diminishes. At depth > 1Km, a siltstone retains higher porosity and permeability than the finer grained mudstone.

Grain size influences chemical diagenesis in addition to compaction. Finer grained rocks provide larger surface area of detrital minerals per unit volume, increasing the amount of nucleation sites for cementation and can lead to larger cement volume (Ben Baccar et al., 1993; Walderhaug, 1994, 1996; Lander and Walderhaug, 1999). On the other hand, experiments demonstrated that that quartz cement crystallization rate decreases considerably when euhedral faces develop, which happens faster when the detrital core is smaller (Lander et al., 2008). Our observations suggest that the large surface area available for cementation in the Montney siltstone, combined with slower initial compaction rate (compared to clay rich mudstones) and a prolonged shallow burial allowed for sufficient fluid flow to overcomes slower cementation rates. Depending on the burial history, it is possible that siltstones may be more prone to early massive cementation relative to sandstones and mudstones.

Compared to other well-described fine-grained sediments (Fig. 2.18), the Montney Formation siltstone contains equal or lower amounts of clay and carbonate minerals and higher amounts of quartz and feldspars (with the exception of the Barnett and Woodford mudstones, where much of the silica is not of detrital origin (Milliken et al., 2007; Dong and Harris, 2020). It is important to note that almost all of the studies of mudstone diagenesis do not report grain size distribution, making the comparison between the Montney siltstone and other mudrocks difficult. However, it is possible to compare the abundance of hard grains (quartz and feldspar) and soft, malleable components (clays) between the two mudstones types. This comparison shows that the Montney siltstone contains lower concentration of clays and higher concentration of hard grains relative to most mudrocks described in Fig. 2.18.

Combining mineralogical differences with petrographic observation of mudrocks and siltstones illustrate that the fundamental difference between mudrocks and siltstones is the rock framework. Where mudrocks are matrix supported, with silt grains 'floating' within a clay-rich matrix, the Montney siltstone has a hard, cement-supported framework.
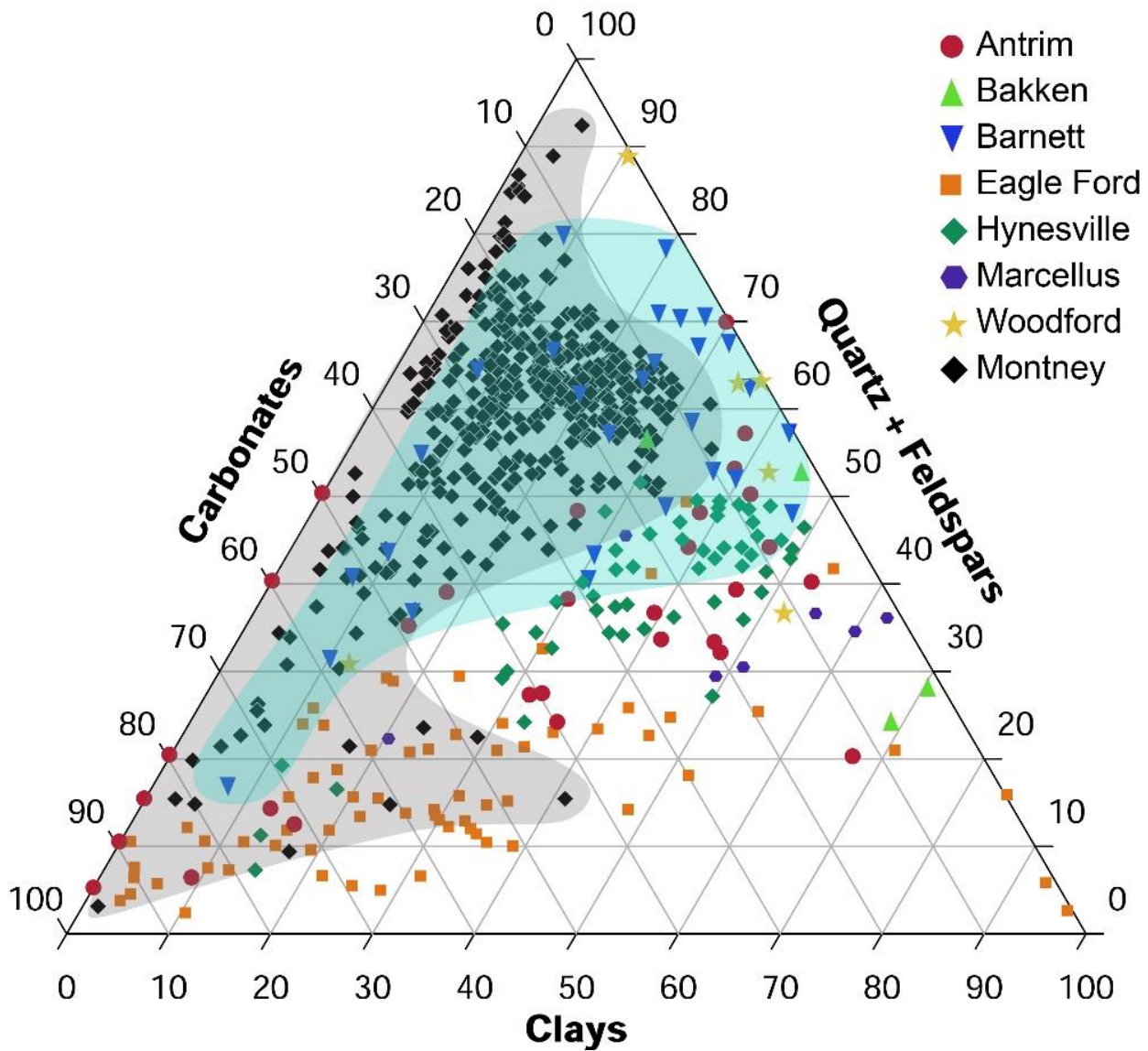
Fig. 2.18: Mineralogical composition of the Montney Formation (black diamonds, gray envelope) compared to various shale formations (after Chermak and Schreiber, 2014). The Montney Formation is most similar to the Barnett (blue rectangles, till envelope), but contains similar or lower clay concentrations, and for the most part less carbonate minerals than other shales.

2.7 Conclusions

We examined the effect of diagenetic processes on the composition and reservoir quality of the Lower Triassic Montney Formation siltstone and demonstrate that:

(1) Most of the diagenetic processes occurred during shallow burial (less than 1000 m).

(2) In the Montney Formation, and possibly in other siltstones, deep burial diagenesis plays only a minor role in the compositional evolution of the rock and appears to be confined to pressure solution and the precipitation of a late, secondary quartz cement phase.

(3) The limited grain size variation in the siltstone suggests aeolian transport for much of the sediment. Because of the limited variability of grain size and the relatively homogeneous detrital composition, depositional environment had little influence of the deposited sediment.

(4) Precipitation of massive amounts of cements at shallow burial depth (11-1100 m) further homogenized rock composition and eliminated compositional variability between the different lithofacies in the rock.

(5) Meteoric water influx in the shallow area of the Montney generated secondary porosity, but also led to kaolinite and quartz precipitation.

(6) Clay rich mudrocks (shales) and silt rich mudrocks (siltstones) differ fundamentally in terms of rock frameworks. Clay rich mudrocks are matrix supported whereas the Montney siltstone has a hard, cement-supported framework.

2.9 Reference

Aagaard, P., Egeberg, P.K., Saigal, G.C., Morad, S., and Bjorlykke, K., 1990. Diagenetic albitization of detrital K-feldspars in Jurassic, Lower Cretaceous and Tertiary clastic reservoir rocks from offshore Norway; II, Formation water chemistry and kinetic considerations. Journal of Sedimentary Research, 60(4), 575-581.

Aase, N.E., Bjørkum, P.A., and Nadeau, P.H., 1996. The Effect of grain-coating microquartz on preservation of reservoir porosity. American Association of Petroleum Geologists Bulletin, 80(10), 1654-1673.

Adams, J.E. and Rhodes, M.L., 1960. Dolomitization by Seepage Refluxion. American Association of Petroleum Geologists Bulletin, 44(12), 1912-1920.

Akai, T., and Wood, J.M., 2014, Petrophysical analysis of a tight siltstone reservoir: Montney Formation, Western Canada. the 20th Formation Evaluation Symposium of Japan, P. 1-4.

Al Rajaibi, I.M., Hollis, C., and Macquaker, J.H., 2015. Origin and variability of a terminal Proterozoic primary silica precipitate, Athel Silicilyte, South Oman Salt Basin, Sultanate of Oman. Sedimentology, 62(3), 793-825. https://doi.org/10.1111/sed.12173.

Aplin, A.C., and Macquaker, J.H., 2011. Mudstone diversity: Origin and implications for source, seal, and reservoir properties in petroleum systems. American Association of Petroleum Geologists Bulletin, 95(12), 2031-2059. https://doi.org/10.1306/03281110162.

Aplin, A.C., Fleet, A.J. and Macquaker, J.H,1999. Muds and mudstones: Physical and fluid-flow properties, Geological Society of London, Special Publications 158, 1-8.

Barber, L.M., 2002. Sedimentology, Diagenesis and reservoir characterization of the Montney Formation at Sturgeon Lake South 'F' Pool West-Central Alberta, M.Sc. thesis, Department of geology and geophysics, University of Calgary, Calgary, Alberta, Canada.

BC oil and gas commission, 2012. Montney Formation play atlas for NEBC.

Ben Baccar, M., Fritz, B., and Made, B., 1993. Diagenetic albitization of K-feldspar and plagioclase in sandstone reservoirs: thermodynamic and kinetic modeling. Journal of Sedimentary Research, 63(6), 1100-1109. https://doi.org/10.1306/D4267CB2-2B26-11D7-8648000102C1865D.

Beranek, L.P., Mortensen, J.K., Orchard, M.J., and Ullrich, T., 2010. Provenance of North American Triassic strata from west-central and southeastern Yukon: correlations with coeval strata in the Western Canada Sedimentary Basin and Canadian Arctic Islands. Canadian Journal of Earth Sciences 47, 53-73. https://doi.org/10.1139/E09-065.

Berner, R.A., 1984. Sedimentary pyrite formation: An update. Geochimica et Cosmochimica Acta, 48(4), 605-615. https://doi.org/10.1016/0016-7037(84)90089-9.

Blakey, R.C., 2014. Mesozoic paleogeography and tectonic history - western North America: Triassic tectonics and paleogeography, 245 Ma. http://deeptimemaps.com/north-american-key-time-slices-series. Last accessed july 20, 2019.

Bloch, S., Lander, R.H., and Bonnell, L., 2002. Anomalously high porosity and permeability in deeply buried sandstone reservoirs: Origin and predictability. American Association of Petroleum Geologists Bulletin, 86(2), 301-328.

Boles, J.R., and Franks, S.G., 1979. Clay diagenesis in Wilcox sandstones of Southwest Texas; implications of smectite diagenesis on sandstone cementation. Journal of Sedimentary Research, 49(1), 55-70.

Buatier, M.D., 1992. Smectite-Illite transition in Barbados accretionary wedge sediments: TEM and AEM evidence for dissolution/crystallization at low temperature. Clays and Clay Minerals, 40(1), 65-80. https://doi.org/10.1346/CCMN.1992.0400108.

Caracciolo, L., Arribas, J., Ingersoll, R.V., and Critelli, S., 2014. The diagenetic destruction of porosity in plutoniclastic petrofacies: The Miocene Diligencia and Eocene Maniobra formations, Orocopia Mountains, southern California, USA. Geological Scoiety of London speciasl publication, 386, 49–62. https://doi.org/10.1144/SP386.9.

Cecil, C.B., 2004. Eolian dust and the origin of sedimentary chert. Open-File Report 2004-1098: US Geological Survey, 2004. Last accessed March 31, 2020.

Chalmers, G.R., and Bustin, M.R., 2012. Geological evaluation of Halfway–Doig–Montney hybrid gas shale–tight gas reservoir, northeastern British Columbia. Journal of Marine and Petroleum Geology, 38(1), 53-72.

Chatellier, J.Y., Simpson,K., Perez, R., and Tribobillard, N., 2018. Geochemically focused integrated approach to reveal reservoir characteristics linked to better Montney productivity potential. Bulletin of Canadian Petroleum Geology, 66(2), 516-551.

Chilingarian G.V., 1983. Compactional Diagenesis. In: Parker A., Sellwood B.W. (Eds.), Sediment diagenesis. NATO ASI Series (Series C: Mathematical and Physical Sciences), vol 115. Springer, Dordrecht.

Clarkson, M.O., Kasemann, S.A., Wood, R.A., Lenton, T.M., Daines, S.J., Richoz, S., Ohnemueller, F., Meixner, A., Poulton, S.W., and Tipper, E.T., 2015. Ocean acidification and the Permo-Triassic mass extinction. Science, 348(6231), 229-232. https://doi.org/10.1126/science.aaa0193.

Crombez, V., 2016 P´etrofaci`es, s´edimentologie et architecture stratigraphique des roches riches en mati`ere organique: ´etude multi-approches des formations Montney et Doig (Trias inferieur et moyen, Alberta - Colombie Britannique, Canada). PhD. Thesis, Sciences de la Terre. Universit´e Pierre et Marie Curie, Paris, France.

Crombez, V., Baudin, F., Rohais, S., Riquier, L., Euzen, T., Pauthier, S., Ducros, M., Caron, B. and Vaisblat, N., 2017. Basin scale distribution of organic matter in marine fine-grained sedimentary rocks: Insight from sequence stratigraphy and multi-proxies analysis in the Montney and Doig Formations. Marine and Petroleum Geology, 83: 382-401.

Crombez, V., Rohais, S., Baudin, F., and Euzen, T., 2016. Facies, well-log patterns, geometries and sequence stratigraphy of a wave-dominated margin: insight from the Montney Formation (Alberta, British Columbia, Canada). Bulletin of Canadian Petroleum Geology, 64(4), 516-537.

Davey, H., 2012. Geomechanical characterization of the Montney shale, northwest Alberta and northeast British Columbia, Canada. M.Sc. Thesis, Department of Geology and Geological Engineering, Colorado School of Mines, Golden, Colorado, USA.

Davies, G.R., 1997. Aeolian sedimentation and bypass, Triassic of western Canada, Bulletin of Canadian Petroleum Geology 45(4), 624–642.

Davies, G.R., Watson, N., Moslow, T.F., and Maceachern, J.A., 2018. Regional subdivisions, sequences, correlations and facies relationships of the Lower Triassic Montney Formation, west-central Alberta to northeastern British Columbia, Canada - With emphasis on role of paleostructure. Bulletin of Canadian petroleum geology, 66(1), 23-92.

Davies, G.R., Moslow, T.F., and Sherwin, M.D., 1997. The Lower Triassic Montney Formation, west-central Alberta. Bulletin of Canadian Petroleum Geology, 45(4), 474-505.

Dixon, J., 2000. Regional lithostratigraphic units in the Triassic Montney formation of Western Canada. Bulletin of Canadian Petroleum Geology, 48(1), 80–83.

Dong, T., Harris, N.B., Knapp, L.J., McMillan, J.M., and Bish, D.L., 2018. The effect of thermal maturity on geomechanical properties in shale reservoirs: An example from the Upper Devonian Duvernay Formation, Western Canada Sedimentary Basin. Marine and Petroleum Geology, 97, 137-153.

Ducros, M., Sassi, W., Vially, R., Euzen, T., and Crombez, V., 2017. 2-D Basin modeling of the Western Canada Sedimentary Basin across the Montney-Doig System: Implications for hydrocarbon migration pathways and unconventional resources potential, in: AbuAli, M.A., Moretti, I., and Bolås, H.M.N. (Eds.), Petroleum Systems Analysis-Case Studies: American Association of Petroleum Geologists Bulletin Memoir, 114. pp. 117-134. https://doi.org/10.1306/13602027M1143703.

Edwards, D.E., Barclay, J.E., Gibson, D.W., Kvill, G.E., and Halton, E., 1994. Triassic strata of the Western Canada Sedimentary Basin, in: Mossop, G.D., and Shetsen, I. (Eds.), Geological Atlas of the Western Canada Sedimentary Basin. Canadian Society of Petroleum Geologists and Alberta Research Council, Calgary, pp. 259–275.

Ehrenberg, S.N., 1989. Assessing the relative importance of compaction processes and cementation to reduction of porosity in sandstones: Reply. American Association of Petroleum Geologists Bulletin, 73(10), 1274-1276. https://doi.org/10.1306/44b4aa23-170a-11d7-8645000102c1865d.

Ejezie, N., 2007, Triassic oil families and possible source rocks, Peace River Embayment area, Alberta, Canada, Ms.C. Thesis, Department of Geology and Geophysics, University of Calgary, Calgary, Alberta, Canada.

Elphinstone, R. and Gorter, J.D., 1991. As the worm turns: implications of bioturbation on source rocks of the Horn Valley Siltstone. Bureau of Mineral Resources, Geology and Geophysics, Bulletin 236(3), 17-332.

Euzen, T., Moslow, T.F., Crombez, V., and Rohais, S., 2018. Regional stratigraphic architecture of the spathian deposits in western Canada - Implications for the Montney resource play. Bulletin of Canadian Petroleum Geology. 66(1), 175-192.

Feng, W., Chen, Z., and Jiang, C., 2016. Oil and source correlations of Triassic Montney Formation in WCSB: Implication to shale gas resource potential in: GeoConvention. CSPG CSEG CWLS, Calgary, AB, Canada, p. 1.

Ferri, F., and Zonneveld, J.-P., 2008. Were Triassic rocks of the Western Canada Sedimentary Basin deposited in a foreland. Canadian Society of Petroleum Geologists Reservoir, 35(10), 12-14.

Fisher, Q.J., Knipe, R.J., and Worden, R.H., 2000. Microstructures of deformed and non-deformed sandstones from the North Sea: implications for the origins of quartz cement in sandstones. Special Publication-International Association of Sedimentologists, 29, 129-146.

Flemming, B.W., 2000. A revised textural classification of gravel-free muddy sediments on the basis of ternary diagrams. Continental shelf research, 20(10-11), 1125-1137.

Folk, R.L., and Ward, W.C., 1957. Brazos River bar [Texas]; a study in the significance of grain size parameters. Journal of Sedimentary Research, 27(1), 3-26.

Furlong, C.M., Gingras, M.K., Moslow, T.F., and Zonneveld, J.-P., 2018. The Sunset Prairie Formation: designation of a new Middle Triassic formation between the Lower Triassic Montney Formation and Middle Triassic Doig Formation in the Western Canada Sedimentary Basin, northeast British Columbia. Bulletin of Canadian Petroleum Geology, 66(1), 193-214.

Ghanizadeh, A., Clarkson, C.R., Aquino, S., Ardakani, O.H., and Sanei, H., 2015. Petrophysical and geomechanical characteristics of Canadian tight oil and liquid-rich gas reservoirs: I. Pore network and permeability characterization. Fuel, 153, 664-681.

https://doi.org/10.1016/j.fuel.2015.03.020

Gibson, D.W., and Edwards, D.E., 1990. An overview of Triassic stratigraphy and depositional environments in the Rocky Mountain Foothills and Western Interior Plains , Peace River Arch area , northeastern British Columbia. Bulletin of Canadian Petroleum Geology, 38(1), 146-158.

Giles, M.R., Indrelid, S.L., Beynon, G.V., Amthor, J., Worden, R.H., and Morad, S., 2000. The origin of large-scale quartz cementation: evidence from large data sets and coupled heat-fluid mass transport modelling. Special Publication-International Association of Sedimentologists, 29, 21-38.

Golding, M.L., Mortensen, J.K., Ferri, F., Zonneveld, J.-P., and Orchard, M.J., 2016. Determining the provenance of Triassic sedimentary rocks in northeastern British Columbia and western Alberta using detrital zircon geochronology, with implications for regional tectonics. Canadian Journal of Earth Sciences, 53(2), 140-155. https://doi.org/10.1139/cjes-2015-0082.

Golonka, J., and Ford, D., 2000. Pangean (Late Carboniferous–Middle Jurassic) paleoenvironment and lithofacies. Palaeogeography, Palaeoclimatology, Palaeoecology, 161(1-2), 1-34. https://doi.org/10.1016/S0031-0182(00)00115-2.

Golonka, J., Ross, M.I., and Scotese, C.R., 1994. Phanerozoic paleogeographic and paleoclimatic modeling maps, in: Embry, A.F., Beauchamp, B., and Glass, D.J. (Eds.), Pangea, Global Environments and Resources. Canadian Society of Petroleum Geologist, Calgary, 1-47.

González-Acebrón, L., Arribas, J., and Mas, R., 2010. Role of sandstone provenance in the diagenetic albitization of feldspars: A case study of the Jurassic Tera Group sandstones (Cameros Basin, NE Spain). Sedimentary Geology, 229(1-2), 53-63.

Hancock, N.J., and Taylor, A.M., 1978. Clay mineral diagenesis and oil generation in the Middle Jurassic Brent Sand Formation, Journal of the Geological Society of London, 135, 69-72.

Harris, N.B., 1989. Diagenetic quartzarenite and destruction of secondary porosity: An example from the Middle Jurassic Brent sandstone of northwest Europe. Geology 17(4), 361. https://doi.org/10.1130/0091-7613(1989)017<0361:DQADOS>2.3.CO;2.

Hartmann, B.H., Juhász-Bodnár, K., Ramseyer, K., and Matter, A., 2000. Polyphased quartz cementation and its sources: a case study from the Upper Palaeozoic Haushi Group sandstones, Sultanate of Oman. Special Publication-International Association of Sedimentologists,29, 253-270.

Hattori, I., Umeda, M., and Yamamoto, H., 2003. From chalcedonic chert to quartz chert; diagenesis of chert hosted in a Miocene volcanic-sedimentary succession, central Japan.

Journal of Sedimentary Research, 66(1), 163-174.

Heald, M.T., and Larese, R.E., 1974. Influence of coatings on quartz cementation. Journal of Sedimentary Research. 44(4), 1269-1274.

Hedberg, H.D., 1926. The Effect of gravitational compaction on the structure of sedimentary rocks. American Association of Petroleum Geologists Bulletin, 10(11), 1035-1072.

Henderson, C.M., Golding, M.L., and Orchard, M.J., 2018. Conodont sequence biostratigraphy of the Lower Triassic Montney Formation. Bulletin of Canadian Petroleum Geology, 66(1), 7-22.

Houseknecht, D.W., 1987. Assessing the relative importance of compaction processes and cementation to reduction of porosity in sandstones. American Association of Petroleum Geologists Bulletin, 71(6), 633-642. https://doi.org/10.1306/44B4AA23-170A-11D7-8645000102C1865D.

Hower, J., Eslinger, E.V., Hower, M.E., and Perry, E.A., 1976. Mechanism of burial metamorphism of argillaceous sediment: 1. Mineralogical and chemical evidence. Geological Society of America Bulletin, 87(5), 725.

Ibrahimbas, A., and Riediger, C., 2004. Hydrocarbon source rock potential as determined by RockEval 6/TOC pyrolysis, N.E. B.C. and N.W. Alberta. Resource Development and Geoscience Branch, Summary of Activities 2004, 7-18.

Jingli, Y., Xiuqin, D., Yande, Z. Tianyou, H., Meijuan, C., and Jinlian, P., 2013, Characteristics of tight oil in Triassic Yanchang Formation, Ordos Basin. Petroleum Exploration and Development, 40(2), 15-158.

Kalsbeek, F., 1992. Large-scale albitisation of siltstones on Qeqertakavsak island, northeast Disko Bugt, West Greenland. Chemical geology, 95(3-4), 213-233.

Keneti, A., and Wong, R.C.K., 2010. Investigation of anisotropic behavior of Montney shale under indirect tensile strength test, in: Canadian Unconventional Resources and International Petroleum Conference. Society of Petroleum Engineers, Calgary, AB, Canada, p. 9. https://doi.org/10.2118/138104-MS.

Kiehl, J.T., and Shields, C.A., 2005. Climate simulation of the latest Permian: Implications for mass extinction. Geology 33(9), 757. https://doi.org/10.1130/G21654.1.

Kirsimäe, K., Jøgensen, P., and Kalm, V., 1999. Low-temperature diagenetic illite-smectite in Lower Cambrian clays in North Estonia. Clay Minerals, 34(1), 151-163. https://doi.org/10.1180/000985599546000.

Kominz, M.A., Patterson, K., and Odette, D., 2011. Lithology dependence of porosity in slope and deep marine sediments. Journal of Sedimentary Research, 81(10), 730-742.

Krause, F.F., Wiseman, A.C., Williscroft, K.R., Solano, N., Morris, N.J., Meyer, R., and Marr, R., 2012. Petrographic and petrophysical comparison of the Montney Formation in the Sturgeon Lake South area. In Site, Canadian Well Logging Society Magazine, 31, 6-9.

Lai, J., Wang, G., Ran, Y., Zhou, Z., and Ciu, Y., 2016. Impact of diagenesis on the reservoir quality of tight oil sandstones: The case of Upper Triassic Yanchang Formation Chang 7 oil layers in Ordos Basin, China. Journal of Petroleum Science and Engineering, 145, 54-65.

Lander, R.H., Larese, R.E., and Bonnell, L.M., 2008. Toward more accurate quartz cement models: The importance of euhedral versus noneuhedral growth rates. American Association of Petroleum Geologists Bulletin, 92(11), 1537-1563.

Lander, R.H., and Walderhaug, O., 1999. Predicting porosity through simulating sandstone compaction and quartz cementation. American Association of Petroleum Geologists Bulletin, 83(3), 433449. https://doi.org/10.1306/00AA9BC4-1730-11D7-8645000102C1865D.

Laughrey, C.D., Ruble, T.E., Lemmens, H., Kostelnik, J., Butcher, A.R., Walker, G., and Knowles, W., 2011. Black shale diagenesis: insights from integrated high-definition analyses of post-mature Marcellus formation rocks, Northeastern Pennsylvania. *American Association of Petroleum Geologists* Search and Discovery Article #110150. http://www.searchanddiscovery.com/documents/2011/110150laughrey/ndx_laughrey.pdf. Last accessed March 31, 2020.

Lazar, O.R., Bohacs, K.M., Macquaker, J.H., Schieber, J., and Demko, T.M., 2015. Capturing key attributes of fine-grained sedimentary rocks in outcrops, cores, and thin sections: nomenclature and description guidelines. Journal of Sedimentary Research, 85(3), 230-246.

Lewan, M.D. and Kotarba, M.J., 2014. Thermal-maturity limit for primary thermogenic-gas generation from humic coals as determined by hydrous pyrolysis. American Association of Petroleum Geologists Bulletin, 98(12), 2581-2610. DOI: 10.1306/06021413204.

Liseroudi, M.H., Ardakani, O.H., Sanei, H., Pedersen, P.K., Stern, R.A., and Wood, J.M., 2020. Origin of sulfate-rich fluids in the early Triassic Montney Formation, Western Canadian Sedimentary Basin. Marine and Petroleum Geology, 104236. https://doi.org/10.1016/j.marpetgeo.2020.104236

Longman, M.W., Drake, W.R., Milliken, K.L., and Olson, T.M., 2019. A comparison of silica diagenesis in the Devonian Woodford shale (Central Basin Platform, West Texas) and Cretaceous Mowry shale (Powder River Basin, Wyoming), in: W. Camp, Milliken, K., Taylor, K., Fishman, N., Hackley, P., and Macquaker, J. (Eds.), Mudstone Diagenesis: Research

Perspectives for Shale Hydrocarbon Reservoirs, Seals, and Source Rocks: American Asociation of Petroleum Geologists Memoir 121, 49-68. https://doi.org/10.1306/13672210M12163.

Lundegard, P.D., 1992. Sandstone porosity loss; a "big picture" view of the importance of compaction, Journal of Sedimentary Research, 62(2), 250-260.

Machel, H.G., 2004. Concepts and models of dolomitization: a critical reappraisal. Geological Society, London, Special Publications, 235(1), 7-63.

Macquaker, J.H., and Adams, A.E., 2003. Maximizing information from fine-grained sedimentary rocks: An inclusive nomenclature for mudstones. Journal of Sedimentary Research, 73(5), 735-744.

Makowitz, A., and Milliken, K.L., 2003. Quantification of brittle deformation in burial compaction, Frio and Mount Simon Formation sandstones. Journal of Sedimentary Research, 73(6), 1007-1021.

Manger, W.L., 2014. Tripolitic chert development in the Mississippian lime: New insights from SEM. In Mississippian Lime Play Forum. 20 February, Oklahoma City, OK, USA,

McBride, E.F., 1989. Quartz cement in sandstones: A review. Earth-Science Reviews, 26(1-3), 69-112.

Meunier, A., and Velde, B., 2004. Illite: Origins, evolution, and metamorphism. Springer, Berlin.

Milliken, K.L., 1989. Petrography and composition of authigenic feldspars, Oligocene Frio Formation, south Texas. Journal of Sedimentary Research, 59(3), 361-374.

Milliken, K.L., and Olson, T., 2017. Silica diagenesis, porosity evolution, and mechanical behavior in siliceous mudstones, Mowry Shale (Cretaceous), Rocky Mountains, U.S.A.. Journal of Sedimentary Research, 87(4): 366-387. doi: https://doi.org/10.2110/jsr.2017.24.

Milliken, K., Choh, S.J., Papazis, P., and Schieber, J., 2007. "Cherty" stringers in the Barnett Shale are agglutinated foraminifera. Sedimentary Geology, 198(3-4), 221-232.

Moore, D.M., 2000. Diagenesis of the Purington Shale in the Illinois Basin and implications for the diagenetic state of sedimentary rocks of shallow Paleozoic basins. Journal of Geology, 108(5), 553-567. https://doi.org/10.1086/314423.

Morad, S., Al-Ramadan, K., Ketzer, J.M., and De Ros, L.F., 2010. The impact of diagenesis on the heterogeneity of sandstone reservoirs: A review of the role of depositional facies and sequence stratigraphy. American Association of Petroleum Geologists Bulletin, 94(8), 1267–1309. https://doi.org/10.1306/04211009178.

Morad, S., and Aldahan, A.A., 1987. Diagenetic replacement of feldspars by quartz in

sandstones. Journal of Sedimentary Research, 57(3), 488-493. https://doi.org/10.1306/212F8B70-2B24-11D7-8648000102C1865D

Moslow, T.F., 2000. Reservoir architecture of a fine-grained turbidite system: Lower Triassic Montney Formation, Western Canada Sedimentary Basin, in: Weimer, P. (Ed.), Deep-Water Reservoirs of the World. SEPM Society for Sedimentary Geology, Houston, Texas, pp. 686-713. https://doi.org/10.5724/gcs.00.15.0686.

Moslow, T.F., Haverslew, B., and Henderson, C.M., 2018. Sedimentary facies, petrology, reservoir characteristics, conodont biostratigraphy and sequence stratigraphic framework of a continuous (395m) full diameter core of the lower Triassic Montney Fm, northeastern British Columbia. Bulletin of Canadian Petroleum Geology, 66(1), 259-287.

Moslow, T.F., and Davies, G.R., 1997. Turbidite reservoir facies in the Lower Triassic Montney Formation, west-central Alberta. Bulletin of Canadian Petroleum Geology, 45(4), 507-536.

Nadeau, P.H., Bjørkum, P.A., and Walderhaug, O., 2005. Petroleum system analysis: Impact of shale diagenesis on reservoir fluid pressure, hydrocarbon migration, and biodegradation risks. In Geological Society, London, Petroleum Geology Conference series, 6(1), 1267-1274.

Nassichuk, B.R., 2000. Sedimentology, diagenesis and reservoir development of the lower Triassic Montney formation, northeastern British Columbia. , Ms.C. Thesis, Department of Earth and Ocean Sciences, University of British Columbia, Vancouver, British Columbia, Canada.

National energy board, 2013. Canada's energy future 2013 energy supply and demand projections to 2035. https://www.cer-rec.gc.ca/nrg/ntgrtd/ftr/2013/2013nrgftr-eng.pdf. Last accessed March 31, 2020.

Needham, S.J., Worden, R.H., and McIlroy, D., 2005. Experimental production of clay rims by macrobiotic sediment ingestion and excretion processes. Journal of Sedimentary Research, 75(6), 1028-1037.

Ness, S.M., 2001. The application of basin analysis to the Triassic succession, Alberta Basin: an investigation of burial and thermal history and evolution of hydrocarbons in Triassic rocks. Ms.C. Thesis, Department of Geology and Gepophysics, University of Calgary, Calgary, Alberta, Canada.

Nieto, J., Batlai, B., and Delbecq, F., 2013. Seismic lithology prediction : A Montney Shale Gas case study. CSEG Recorder, 38(2), 34-41.

Niu, B., and Ishida, H., 2000. Different rates of smectite illitization in mudstones and sandstones from the Niigata Basin, Japan. Clay Minerals, 35(1), 163-173. https://doi.org/10.1180/000985500546558.

Norton, M., Hovdebo, W., Cho, D., Jones, M., and Maxwell, S., 2010. Surface seismic to microseismic : An integrated case study from exploration to completion in the Montney shale of NE British Columbia, Canada, in: Society of Exploration Geophysicists Annual Meeting. Denver, Colorado, p. 5.

Osborne, M., Haszeldine, R.S., and Fallick, A.E., 1994. Variation in kaolinite morphology with growth temperature in isotopically mixed pore-fluids, Brent Group, UK North Sea. Clay Minerals, 29(4), 591-608. https://doi.org/10.1180/claymin.1994.029.4.15.

Paxton, S.T., Szabo, J.O., Ajdukiewicz, J.M., and Klimentidis, R.E., 2002. Construction of an intergranular volume compaction curve for evaluating and predicting compaction and porosity loss in rigid-grain sandstone reservoirs. American Association of Petroleum Geologists Bulletin, 86(12), 2047-2067.

Pejrup, M., 1988. The triangular diagram used for classification of estuarine sediments: a new approach. In: Boer, P.L., van Gelder, A., and Nio, S.D. (Eds.), Tide-influenced sedimentary environments and facies. Reidel, Dordrech p. 530.

Playter, T.L., 2013. Petrographic and x-ray microtomographic analysis of the Upper Montney Formation, Northeastern British Columbia, Canada. Ms.C. Thesis, Department of Earth and Atmospheric Sciences, University of Alberta, Edmonton, Alberta, Canada.

Polt, R.H., and Krause, F.F., 1997. New discovery in the Montney Formation: "Sturgeon Lake South, Triassic F-Pool", a shoreface sandstone reservoir. Canadian Society of Petroleum Geologists and Society for Sedimentary Geology (SEPM) Joint Convention, Core Conference, pp. 237-255.

Preto, N., Kustatscher, E., and Wignall, P.B., 2010. Triassic climates - State of the art and perspectives. Palaeogeography, Palaeoclimatology, Palaeoecology, 290(1-4), 1-10. https://doi.org/10.1016/j.palaeo.2010.03.015.

Qiu, Z., Tao, H., Zou, C., Wang, H., Ji, H., and Zhou, S., 2016. Lithofacies and organic geochemistry of the Middle Permian Lucaogou Formation in the Jimusar Sag of the Junggar Basin, NW China. Journal of Petroleum Science and Engineering, 140, 97-107.

Riediger, C.L., Fowler, M.G., Brooks, P.W., and Snowdon, L.R., 1990. Triassic oils and potential Mesozoic source rocks, Peace River Arch area, Western Canada Basin. Organic Geochemistry, 16(1-3), 295–305. https://doi.org/10.1016/0146-6380(90)90049-6.

Roberts, J.M., and Elmore, R.D., 2018. A diagenetic study of the Woodford Shale in the southeastern Anadarko Basin, Oklahoma, USA: Evidence for hydrothermal alteration in mineralized fractures. Interpretation, 6(1), SC1-SC13.

Rohais, S., Crombez, V., Euzen, T., and Zonneveld, J.-P., 2018. Subsidence dynamics of the Montney Formation (Early Triassic, western Canada sedimentary basin): Insights for its

geodynamic setting and wider implications. Bulletin of Canadian Petroleum Geology, 66(1), 128-160.

Romero-Sarmiento, M.F., Euzen, T., Rohais, S., Jiang, C., and Littke, R., 2016. Artificial thermal maturation of source rocks at different thermal maturity levels: Application to the Triassic Montney and Doig formations in the Western Canada Sedimentary Basin. Organic Geochemistry, 97, 148-162. https://doi.org/10.1016/j.orggeochem.2016.05.002.

Ross, G.M., Gehrels, G.E., and Patchett, P.J., 1997. Provenance of Triassic strata in the Cordilleran miogeocline , western Canada. Bulletin of Canadian Petroleum Geology, 45(4), 461-473.

Saigal, G.C., Morad, S., Bjorlykke, K., Egeberg, P.K., and Aagaard, P., 1988. Diagenetic albitization of detrital K-feldspar in Jurassic, Lower Cretaceous, and Tertiary clastic reservoir rocks from offshore Norway, I. Textures and origin. Journal of Sedimentary Research, 58(6), 1003-1013.

Saller, A.H., and Henderson, N., 1998. Distribution of porosity and permeability in platform dolomites: Insight from the Permian of west Texas. American Association of Petroleum Geologists Bulletin, 82(8), 1528-1550.

Sanei, H., Haeri-Ardakani, O., Ghanizadeh, A., Clarkson, C.R., and Wood, J.M., 2016. Simple petrographic grain size analysis of siltstone reservoir rocks: An example from the Montney tight gas reservoir (Western Canada). Fuel 166, 253-257. https://doi.org/10.1016/j.fuel.2015.10.103.

Sanei, H., Wood, J.M., Ardakani, O.H., Clarkson, C.R., and Jiang, C., 2015. Characterization of organic matter fractions in an unconventional tight gas siltstone reservoir. International Journal of Coal Geology, 150-151, 296-305. https://doi.org/10.1016/j.coal.2015.04.004.

Saner, S., Cagatay, M.N., and Sanounah, A.A., 1996. Relationships between shale content and grain-size parameters in the Safaniya Sandstone reservoir, NE Saudi Arabia. Journal of Petroleum Geology, 19(3), 305-320.

Scuderi, M.M., Kitajima, H., Carpenter, B.M., Saffer, D.M., and Marone, C., 2015. Evolution of permeability across the transition from brittle failure to cataclastic flow in porous siltstone. Geochemistry, Geophysics, Geosystems, 16(9), 2980-2993.

Shepard, F.P., 1954. Nomenclature based on sand-silt-clay ratios. Journal of sedimentary Research, 24(3), 151-158.

Siebert, R.M., Moncure, G.K., and Lahann, R.W., 1984. A Theory of framework grain dissolution in sandstones, in: McDonald, D.A., and Surdam, R.C. (Eds.), Clastic Diagenesis. The American Association of Petroleum Geologists, Tulsa, pp. 163-176. https://doi.org/10.1306/M37435.

Sobolev, S. V., Sobolev, A. V., Kuzmin, D. V., Krivolutskaya, N.A., Petrunin, A.G., Arndt, N.T., Radko, V.A., and Vasiliev, Y.R., 2011. Linking mantle plumes, large igneous provinces and environmental catastrophes. Nature, 477, 312-316. https://doi.org/10.1038/nature10385.

Sun, Y., Joachimski, M.M., Wignall, P.B., Chunbo, Y., Chen, Y., Jiang, H., Wang, L., Lai, X., and Yan, C., 2012. Lethally hot temperatures during the Early Triassic greenhouse. Science, 338, 366-370. https://doi.org/10.1126/science.1224126.

Tribovillard, N., Algeo, T.J., Lyons, T., and Riboulleau, A., 2006. Trace metals as paleoredox and paleoproductivity proxies: An update. Chemical Geology, 232(1-2), 12-32. https://doi.org/10.1016/j.chemgeo.2006.02.012.

U.S. energy Information administration, 2017. Marcellus shale play Geology Review. https://www.eia.gov/maps/pdf/MarcellusPlayUpdate_Jan2017.pdf. Last accessed March 31. 2020.

Utting, J., Zonneveld, J.-P., MacNaughton, R.B., and Fallas, K.M., 2005. Palynostratigraphy, lithostratigraphy and thermal maturity of the Lower Triassic Toad and Grayling, and Montney formations of western Canada, and comparisons with coeval rocks of the Sverdrup Basin, Nunavut. Bulletin of Canadian Petroleum Geology, 53(1), 5-24. https://doi.org/10.2113/53.1.5.

Vaisblat, N., Harris, N.B., DeBhur, C., Euzen, T., Gasparrini, M., Crombez, V., Rohais, S., Krause, F. and Ayranci, K. 2017. Diagenetic model for the deep Montney Formation, Northeastern British Columbia. Geoscience BC Report 2017-1, p. 37-48. http://www.geosciencebc.com/i/pdf/SummaryofActivities2016/SoA2016_Vaisblat.pdf.

Van de Kamp, P.C., 2008. Smectite-illite-muscovite transformations, quartz dissolution, and silica release in shales. Clays and Clay Minerals, 56(1), 66-81.

Van der Plas, L., and Tobi, A.C., 1965. A chart for judging the reliability of point counting results. American Journal of Science, 263(1), 87-90.

Vansant, E.F., Van Der Voort, P., and Vrancken, K.C., 1995. Characterization and chemical modification of the silica surface. Amsterdam, Elsevier (chapter 1).

Velde, B., 1996. Compaction trends of clay-rich deep sea sediments. Marine Geology, 133(3-4), 193-201.

Walderhaug, O., 1996. Kinetic modeling of quartz cementation and porosity loss in deeply buried sandstone reservoirs. American Association of Petroleum Geologists Bulletin, 80(5), 731-745.

Walderhaug, O., 1994. Temperatures of quartz cementation in Jurassic sandstones from the Norwegian continental shelf; evidence from fluid inclusions. Journal of Sedimentary

Research, 64(2a), 311-323. https://doi.org/10.1306/D4267D89-2B26-11D7-8648000102C1865D.

Wallmann, K., Aloisi, G., Haeckel, M., Tishchenko, P., Pavlova, G., Greinert, J., Kutterolf, S., and Eisenhauer, A., 2008. Silicate weathering in anoxic marine sediments. Geochimica et Cosmochimica Acta, 72(12), 2895-2918.

Wang, X., Dong, Z., Zhang, J., Qu, J., and Zhao, A., 2003. Grain size characteristics of dune sands in the central Taklimakan Sand Sea. Sedimentary Geology, 161(1-2), 1-14.

Warren, J., 2000. Dolomite: occurrence, evolution and economically important associations. Earth-Science Reviews, 52(1-3), 1-81.

Wignall, P.B., and Newton, R., 1998. Pyrite framboid diameter as a measure of oxygen deficiency in ancient mudrocks. American Journal of Science, 298(7), 537-552. https://doi.org/10.2475/ajs.298.7.537.

Wilkin, R.T., and Barnes, H.L., 1997. Formation processes of framboidal pyrite. Geochimica et Cosmochimica Acta, 61(2), 323-339. https://doi.org/10.1016/S0016-7037(96)00320-1.

Wilkin, R.T., Barnes, H.L., and Brantley, S.L., 1996. The size distribution of framboidal pyrite in modern sediments: An indicator of redox conditions. Geochimica et Cosmochimica Acta, 60(20), 3897–3912. https://doi.org/10.1016/0016-7037(96)00209-8.

Willett, S.D., Issler, D.R., Beaumont, C., Donelick, R.A., and Grist, A.M., 1997. Inverse modeling of annealing of fission tracks in apatite; 2, Application to the thermal history of the Peace River Arch region, Western Canada sedimentary basin. American Journal of Science, 297(10), 970-1011. https://doi.org/10.2475/ajs.297.10.970.

Williams, L.A., Parks, G.A., and Crerar, D.A., 1985. Silica diagenesis; I, Solubility controls. Journal of Sedimentary Research, 55(3), 301-311.

Wilson, M.D., 1992. Inherited grain-rimming clays in sandstones from eolian and shelf environments: their origin and control on reservoir properties. Origin Diagenesis and Petrophysics of Clay Minerals in Sandstones SEPM Special Publication No. 47, 209-225.

Wilson, J.C., and McBridge, E.F., 1988. Compaction and porosity evolution of Pliocene sandstones, Ventura Basin, California. American Association of Petroleum Geologists Bulletin, 72(6), 664-681.

Wong, T.-F., 1990, Mechanical compaction and brittle–ductile transition in porous sandstones, in Knipe, R.J., and Rutter, E.H. (Eds.), Deformation Mechanisms, Rheology, and Tectonics: Geological Society of London, Special Publication 54, p. 111–122.

Wood, J.M., Sanei, H., Haeri-Ardakani, O., Curtis, M.E., and Akai, T., 2018. Organic petrography and scanning electron microscopy imaging of a thermal maturity series from

the Montney tight-gas and hydrocarbon liquids fairway. Bulletin of Canadian Petroleum Geology, 66(2), 499-515. https://doi.org/10.1038/ncomms13614.

Wood, J.M., and Sanei, H., 2016. Secondary migration and leakage of methane from a major tight-gas system. Nature Communications, 7, 13614.

Wood, J.M., Sanei, H., Curtis, M.E., and Clarkson, C.R., 2015. Solid bitumen as a determinant of reservoir quality in an unconventional tight gas siltstone play. International Journal of Coal Geology, 150-151, 287–295. https://doi.org/10.1016/j.coal.2015.03.015.

Worden, R., and Morad, S. (Eds.), 2000. Quartz cementation in sandstones, Malden, MA: Blackwell Science.

Wüst, R.A., Tu, S., Nassichuk, B., Bozarth, T., Tucker, J., and Cui, A., 2018. Chemostratigraphy, petrography, and SEM investigations of the Lower Triassic Montney Formation in Alberta: Implications for a new and revised diagenetic and depositional model. Bulletin of Canadian Petroleum Geology, 66(2), 436-471.

Zelazny, I.V., Gegolick, A., Zonneveld, J.-P., Playter, T., and Moslow, T.F., 2018. Sedimentology, stratigraphy and geochemistry of Sulphur Mountain (Montney equivalent) Formation outcrop in south central Rocky Mountains, Alberta, Canada. Bulletin of Canadian Petroleum Geology, 66(1), 288-317.

Zonneveld, J.-P., 2011. Suspending the rules: unraveling the ichnological signature of the Lower Triassic post-extinction recovery interval. Palaios 26(11), 677–681. https://doi.org/10.2307/41317453.

Zonneveld, J.-P., and Moslow, T.F., 2018. Palaeogeographic setting, lithostratigraphy, and sedimentary framework of the Lower Triassic Montney Formation of western Alberta and northeastern British Columbia. Bulletin of Canadian Petroleum Geology, 66(1), 93-127.

Zonneveld, J.-P., and Moslow, T.F., 2014. Perennial river deltas of the Montney Formation : Alberta and British Columbia subcrop edge, in: Geoconvention. CSPG CSEG CWLS, Calgary, AB, Canada, pp. 1-2.

Zonneveld, J.-P., Golding, M.L., Moslow, T.F., Orchard, M.J., Playter, T.L., and Wilson, N., 2011. Depositional framework of the Lower Triassic Montey Formation, West-central Alberta and Northeastern British Columbia, in: Geoconvention. CSPG CSEG CWLS, Calgary, AB, Canada, pp. 1-4.

Zonneveld, J.-P., Beatty, T.W., MacNaughton, R.B., Pemberton, S.G., Utting, J., and Henderson, C.M., 2010. Sedimentology and ichnology of the Lower Triassic Montney Formation in the Pedigree-Ring/Border-Kahntah River area, northwestern Alberta and northeastern British Columbia. Bulletin of Canadian Petroleum Geology, 58(2), 115–140. https://doi.org/10.2113/gscpgbull.58.2.115.

Chapter 3 - Significance of Rock Compositional Control on Geomechanical Properties and Hydraulic Fracturing of the Montney Formation, Western Canadian Basin

Noga Vaisblat, Alireza Rangiz Shokri, Korhan Ayranci, Nicholas B. Harris, Rick Chalaturnyk, Matthew Power, David L. Bish

All raw data used in this chapter as well as high resolution figures and tables are available at doi:10.20383/101.0229

Abstract

We present critical data sets and insights into geomechanical properties of the Montney Formation siltstone in the Western Canadian Sedimentary Basin, the largest unconventional hydrocarbons reservoir in western Canada. Our study included indentation measurements and log-derived elastic moduli, including Young's modulus, Poisson's ratio, and brittleness. Further, we explore the relationship between the aforementioned geomechanical properties, mineralogy, and rock fabric, and investigate the influence of lithology on hydraulic fracturing propagation.

We examined seven wells along a northwest-southeast transect. Lithofacies analysis was conducted on four long Montney cores (70 to 250 m long). Young's modulus, Poisson's ratio, and brittleness were calculated from dipole sonic and density logs. Hardness profiles of core samples, measured by a hand-held indentation device, were compared with rock composition from QEMSCAN (mineralogy) and LECO-TOC (organic matter). A coupled hydro-mechanical code, capable of explicit inclusion of lithofacies variation and bedding discontinuities, was employed to investigate the response of the siltstone to hydraulic fracture propagation in the Montney Formation.

The variations of Young's modulus, Poisson's ratio, and relative brittleness from well logs were compared against indentation measurements of the four long cores and against rock composition in all wells. Young's modulus, brittleness, and hardness showed similar trends in each well, whereas Poisson's ratio demonstrated a trend with depth opposite to all other elastic parameters. Statistical analysis indicated that clay content, and to a lesser extent organic matter content, had the strongest control on elastic moduli in the Montney Formation, reducing Young's modulus, brittleness, and hardness, but increasing Poisson's ratio.

Sedimentological analysis identified 14 lithofacies across the basin, deposited in environments ranging from tidal flat to offshore sediments. No clear distinctions were found between the geomechanical properties of different lithofacies in each well. More importantly, the same lithofacies commonly displays significantly different geomechanical properties in each of the wells. The analysis from coupled numerical simulations also confirmed that effective fracture propagation is not lithofacies-dependent and demonstrated that in the Montney Formation effective stress has greater influence on fracture propagation than lithological variation. We attribute the weak influence of depositional environments on the sediment to the size and compositional homogeneity of detrital material that entered the basin, and to massive cementation at shallow burial depth that further homogenized the rock and eliminated any compositional differences between lithofacies.

3.1 Introduction

Reservoir quality in conventional reservoirs is estimated primarily by petrophysical rock properties - porosity and permeability. In unconventional reservoirs, where economic production generally relies on successful hydraulic stimulations, reservoir quality also depends on the geomechanical properties of the rock. Hydraulic stimulation applies enough pressure on the rock to cause failure. Brittle rocks undergo failure by forming fractures, leading to dilation of the rock volume. Ductile rocks on the other hand undergo plastic deformation during failure, which leads to volume contraction and minimal fracture development.

Understanding the factors controlling the elastic properties of tight reservoirs is therefore key for effectively targeting horizons for hydraulic fracturing.

The elastic moduli - Young's Modulus and Poisson's Ratio are the principal parameters used for evaluating the potential for a successful hydraulic stimulation operation in low permeability reservoirs (Rickman et al., 2008). Brittle rocks have high Young's Modulus and low Poisson's Ratio, whereas ductile rocks usually have low Young's Modulus and high Poisson's Ratio (Rickman et al., 2008). Brittleness has also been related to rock composition, with certain minerals (quartz and carbonates) enhancing brittleness, and other (clays and organic matter) reducing it (Al-awadi et al., 2009; Jarvie et al., 2007; Rickman et al., 2008; Wang and Gale, 2009; Aoudia et al., 2010; Harris et al, 2011; Herwanger et al., 2015; Dong et al., 2017). Since composition is at least partially dictated by the depositional environment through water motion energy, elastic moduli have also been correlated with different stratigraphic intervals, rock fabric (lithofacies), or sea-level changes (Harris et al. 2011; Slatt and Abousleiman, 2011; Dong et al., 2017).

The Lower Triassic Montney Formation of the Western Canada Sedimentary Basin is one of the most important hydrocarbon reservoirs in Canada, with reserves of 450 TCF of gas, 14,520 MMB of natural gas liquids (NGL), and 1125 MMB of oil (National Energy Board, 2013). The Montney Formation is a unique play, in part a normally pressured conventional reservoir, and in part an overpressured unconventional reservoir, produced mostly from stimulated horizontal wells. The Montney is dominated by silt-size siliciclastic and carbonates grains, variable concentration of clay minerals (0-30 Wt.%), low concentration of organic matter (commonly < 3 wt.%) and high cements volume (quartz, calcite and dolomite) that comprise up to 30% of the rock (Davies et al., 1997; Barber, 2002; Derder, 2012; Playter, 2013; this study, chapter 2). Organic matter maturity increases with burial depth from the northeast (immature) to the southwest (overmature) (Riediger et al., 1990; Ibrahimbas and Riediger, 2004; Crombez et al., 2016; Romero-Sarmiento et al., 2016). Compositional variation, together with a wide range of thermal maturity make the Montney an instructive subject for

analyzing relationships between rock fabric, rock composition, and the geomechanical properties of siltstones.

In this paper, we investigate the spatial and vertical variations of the geomechanical properties of the Montney Formation and their correlation to mineralogy and lithology. We then compare our findings with those obtained for three other mudrocks with in order to identify differences and similarities in the controls on geomechanical behavior between the two different rock types.

3.2 Geological setting

The Montney Formation extends over 130,000 km^2 in central and southwestern Alberta and northeastern British Columbia (Fig. 3.1). The Formation was deposited in the Western Canada Sedimentary Basin (WCSB) on the western margin of Pangea during the Early Triassic (Induan and Olenekian stages), (Fig. 3.2). Geodynamic interpretations for the Lower Triassic WCSB have evolved over the years. The basin was originally interpreted as a passive margin (Monger and Price, 1979; Coney et al., 1980; Price, 1994; Monger and Price, 2002) and later as a back-arc basin (Edwards et al., 1994; Miall and Blakey, 2008; Zonneveld et al., 2010) or fore-arc basin (Blakey, 2014; Golding et al., 2015; Rohais et al., 2016). The most recent interpretation positions the Lower Triassic WCSB in a foreland basin setting (Rohais et al., 2018). Paleogeographic reconstructions suggest deposition in a westward deepening basin, positioned at approximately 30° N, and rotated 30° clockwise from its present-day location (Golonka et al., 1994; Davies et al., 1997; Blakey, 2014).

The Montney Formation was deposited in one second-order sequence comprised of three third-order sequences (Davies et al., 1997; Moslow and Davies, 1997; Orchard and Zonneveld, 2009; Crombez et al., 2016, 2017; Davies et al., 2018; Moslow et al., 2018; Proverbs et al., 2018; Zonneveld and Moslow, 2018). The Formation unconformably overlies the Permian Belloy Formation and underlies the Sunset Prairie Formation (Furlong et al., 2018), the Doig Formation or the Nordeeg Formation (Fig. 3.2), depending on location in the

basin. The contact between the Montney and overlying formations is locally conformable, but elsewhere unconformable where the Coplin and sub-Jurassic unconformities, formed during the Laramide Orogeny (Gibson and Edwards, 1990; Edwards et al., 1994; Davies et al., 1997; Moslow, 2000) (Fig. 3.2) mark the contact.

It is estimated that several hundred meters of sediments were eroded in west and central
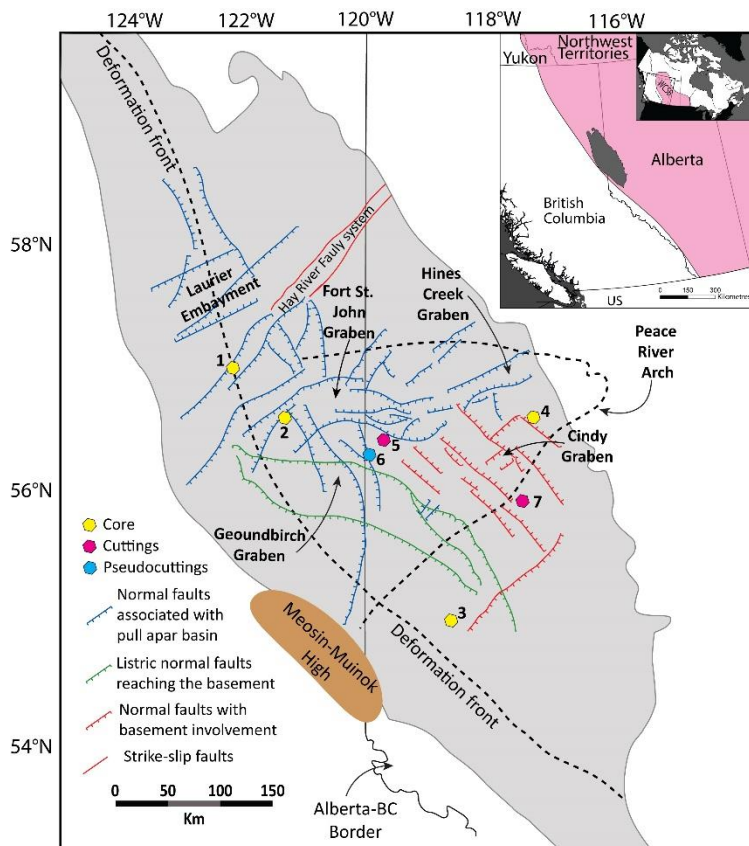
Fig. 3.1: A map showing the outline of the Montney Formation and major structural features in the Triassic strata in Alberta and British Columbia. Location of all study wells is indicated.

Insert: the location of the Montney Formation in the Western Canada Sedimentary Basin (pink).

Map modified after Zonneveld and Moslow, 2018. Structural features are taken from Furlong et al., 2018.

Alberta, while over 4000 m of sediments were removed close to the Rocky Mountains deformation front, where the unconformity cuts through younger intervals (Willett et al., 1997; Ness, 2001; Ducros et al., 2014, 2017; Rohais et al., 2018). This erosional event led to the thinning of the Formation to a 'zero edge' in the east, while leaving the westernmost section of the formation over 300 m thick.

The burial depth increases from under 800 m to over 2200 m from northeast to southwest with a corresponding increase in thermal maturity from $R_o=0.59\%$ to $R_o>2\%$ (Riediger et al.,
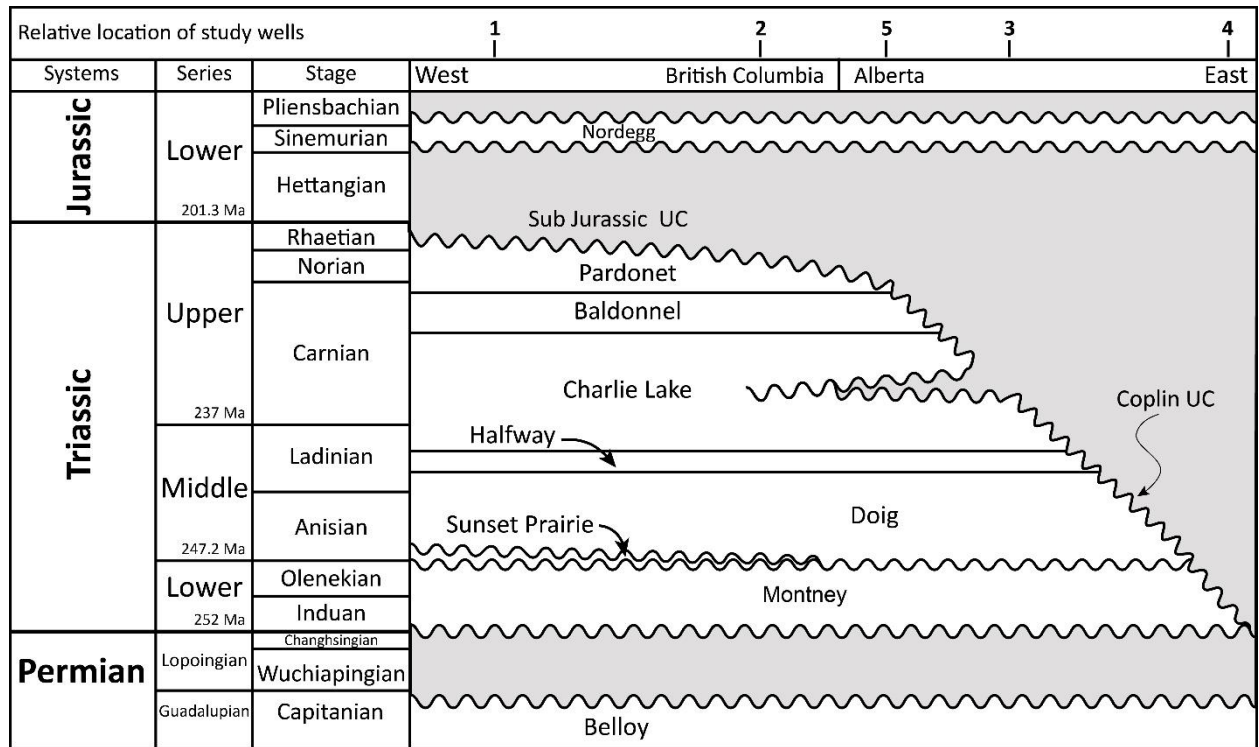
Fig. 3.2: Chronostratigraphic chart for the Triassic and Lower Jurassic of the subsurface in Alberta and British Columbia. The location of the study wells is marked at the top of the chart. UC is unconformity. Ages after Golding et al., 2016.

1990; Rokosh et al., 2012; Sanei et al., 2015; Romero-Sarmiento et al., 2016; Crombez, 2016; Crombez et al., 2016; Wood and Sanei, 2016). Formation pressure and pressure gradients in the Montney also increase from east to west. Pressure rises from 6000 kPa in the east to over 62,000 kPa in the west. The pressure gradient, which is normal in the eastern section of the Montney, departs from the hydrostatic pressure gradient (~10 kPa/m) into an overpressured regime (up to 17 kPa/m) in the western section of the formation (BC Oil and Gas Commission, 2012).

Sedimentological descriptions of the Montney Formation are available on both local and basinal scale (Davies et al., 1997; Nassichuk, 2000; LaMothe, 2008; Zonneveld et al., 2010; Zonneveld et al., 2011; Playter, 2013; Crombez, 2016; Crombez et al., 2016; Davies and Hume, 2016; Davies et al., 2018; Euzen et al., 2018; Moslow et al., 2018; Proverbs et al., 2018; Sanders et al., 2018; Zonneveld and Moslow, 2018). Interpretations of depositional

environments vary with location in the basin and range from deltaic and shoreface environments through inner and outer shelf environments to offshore environments. Studies suggest syndepositional reactivation of faults on a local scale and a possible existence of accretionary regime to the west (Davies et al., 1997; Zonneveld and Moslow, 2014; Crombez et al., 2016; Davies et al., 2018; Zonneveld and Moslow, 2018; Rohais et al., 2018; this study, chapter 2).

The Montney Formation is composed of sediments derived predominantly from the Canadian Shield, with a small but significant contribution of sediments from the Innuitian orogenic wedge to the north (Ross et al. 1997; Beranek et al., 2010; Golding et al., 2016), and potentially a minor input from a western source (Edwards et al., 1994; Golding et al., 2016; Rohais et al., 2018). Grain size varies from very fine sand to clay-size material, with a slight increase in grain size (to fine sand) toward the eastern margins (Gibson and Edwards, 1990; Edwards et al., 1994; Davies et al., 1997; Zonneveld et al., 2011; this study, chapter 2).

The detrital mineral assemblage consists of quartz, feldspars, micas, calcite, dolomite, iron-dolomite, mixed-layer illite smectite clays (MLIS), and pyrite, with minor amounts of apatite, barite, kaolinite, chlorite, and heavy minerals (Davies et al., 1997; Barber, 2002; Derder, 2012; Playter, 2013; Crombez, 2016; Vaisblat et al., 2017, chapter 2 this study). Rock composition is primarily determined by diagenetic processes, with extensive cements (mainly quartz, feldspar, dolomite, calcite and anhydrite) accounting that on average comprise one third of the rock volume (Davies et al., 1997; Vaisblat et al., 2017, chapter 2 this study).

3.3 Methodology

The data collected for this study is aimed at understanding the controls exerted by rock composition, rock fabric and sedimentological associations on the geomechanical behavior of the siltstone. Facies analysis of four long cores provided the sedimentological framework for

this study. Geomechanical parameters were calculated from well logs or measured on core samples. Rock composition (organic and inorganic) was measured on core samples and rock fabric (distribution of matrix, detrital grains and cements) was examined through SEM analysis. We then examined the variation of the geomechanical parameters with respect to lithofacies, composition, and rock morphology.

3.3.1 Materials and sampling

Our dataset includes seven wells drilled through the Montney Formation, located along a northwest-southeast cross-section (Fig. 3.1). Wells were selected based on the availability of cores and/or publicly available data intersecting all or most of the Montney Formation interval. Two cores were selected to represent distal and deeply buried section of the basin (wells 1 and 2), one well was selected to represent more proximal but still deeply buried section of the basin (well 3), and one well (well 4) was selected to represent a proximal section of the basin that is buried to a shallow depth. Data available for each well are summarized in Table 3.1. Samples, ten cm long, were collected in 1-3 m intervals from the back of the cores from wells 1-4. Data for well 5 was received directly from Birchcliff Energy, and data for wells 6 and7 were publicly available information obtained from the Alberta Energy Regulator (AER).

The data set also includes a suite of well logs for all wells, including gamma ray (GR), density (RHOB), neutron porosity (NPHI), compressional wave velocity (DTC), and shear wave velocity (DTS). Depth shift was performed for wells 1-5 using a stretch and squeeze method to match core GR curve to the wireline GR log curve.

Table 3.1: A summary of the dataset available for the study

Well #	Well location	core description	sample type	QEMSCAN	TOC	Well-Logs[f]
1	16-17-083-25w6m	available	Core samples	70[a] (2-16)[b,c]	45 (2-19)[d,b]	GR, RHOB, NPHI, DTC, DTS, core GR
2	16-29-079-20W6	available	Core samples	62 (1-5)	43 (2-11)[d]	GR, RHOB, NPHI, DTC, DTS, core GR
3	05-24-63-6W6	available	Core samples	40 (2-3)	40 (2-3)[d]	GR, RHOB, NPHI, DTC, DTS, core GR
4	103/05-20-079-22W5	available	Core samples	66	25 (1-6)[d]	GR, RHOB, NPHI, DTC, DTS, core GR
5	06-03-079-13W6		Pseudocuttings	297	75 (1-8)[d]	GR, RHOB, NPHI, DTC, DTS, core GR
6	14-14-76-12W6		cuttings	55	25 (5)[e]	GR, RHOB, NPHI, DTC
7	06-33-072-25W5		cuttings	28	30 (5)[e]	GR, RHOB, NPHI, DTC

[a]Number of samples analysed.
[b]sampling interval for the specific analysis, meters.
[c]Large distance between samples due to missing core.
[d]TOC in wt%, obtained from Leco TOC analysis.
[e]TOC in wt%, obtained from RockEval analysis.
[f]GR=Gamma Ray; RHOB=density; NPHI=neutron porosity; DTC=compressional sonic travel time; DTS=shear sonic travel time

3.3.2 Core description

We described sedimentological features in cores retrieved from wells 1-4 (total length of 635 m [2083 ft], excluding a total of 51.5 m [169 ft] of missing core sections) in order to identify lithofacies present in the Montney Formation. Information obtained through core description includes (1) lithology, (2) grain size, (3) physical sedimentary structures, (4) trace fossil assemblages, and (5) bioturbation intensity (BI). The lithological classification scheme was adopted from the Macquaker and Adams (2003) mudstones classification.

3.3.3 Mineralogical composition

Quantitative mineralogical composition was determined by QEMSCAN analysis at SGS Canada laboratories in Burnaby, BC, Canada. A small chip (~ 2 cm^2) was taken from the top of the 233 samples from cores 1-4 and sent for QEMSCAN analysis. For well 5, a continuous sliver of core was cut along the entire length of the core and divided into 301 1-m intervals. Each interval was then crushed and mixed to generate pseudo-cuttings, and a random subsample from each section (~50 g) was analyzed. Since no core was available, mineralogy for wells 6 and 7 was determined from cuttings samples. A total of 85 samples (~5 g each)

was collected in 5-10 m intervals. The repeatability of QEMSCAN measurements is very high, with results commonly being over 98% similar between repeated measurements of the same sample (Power, pers. Com.).

In addition to QEMSCAN analysis, 23 samples from cores 1-4 were selected for quantitative X-Ray diffraction (XRD) analysis of bulk and clay mineral composition. Six samples were analyzed at the James Hutton Institute, Aberdeen, Scotland, using a Panalytical Xpert Pro instrument using Ni filtered CuKα radiation and an Xcelerator position sensitive detector, counting for 100 seconds per 0.0167° step between 3-70°2θ. Clay fraction (<2μm) was separated by timed sedimentation, prepared as oriented mounts and scanned between 3-45°2θ in the air-dried state and after glycolation. All other samples were analyzed at the Mineralogy Facility at the Indiana University in Bloomington. XRD patterns were recorded using a Bruker D8 Advance X-Ray Powder Diffractometers from 2-70°2θ using Copper Kα radiation. Clay fraction (<2μm) was separated by timed sedimentation, prepared as randomly oriented mounts and scanned between 2-20°2θ in the air-dried state and after glycolation.

3.3.4 Organic Geochemical analysis

A total of 143 samples were selected from cores 1-4 for LECO-TOC analysis. A split from each sample was ground and homogenized. Well 4 was drilled in an oil-saturated zone, and samples from this core were cleaned in a Dean Stark apparatus, using a solution of ethanol (23 wt. %), acetone (30 wt. %) and chloroform (47 wt. %), prior to analysis. Organic carbon content was measured by LECO combustion analysis at GeoMark Research in Humble, TX. Seventy-seven random subsamples of the pseudo-cuttings sections from core 5 were also sent for LECO combustion analysis at GeoMark Research in Humble, TX. Organic carbon content for wells 6-7 was determined on 55 samples with Rock-Eval IV at IFP Energies Nouvelles, France. Analysis details and conditions are provided by Crombez et al. (2016).

3.3.5 Petrography

Scanning electron microscopy (SEM) and SEM-Cathodoluminescence (SEM-CL) imaging were used to examine the type and distribution of the organic matter and the detrital and authigenic phases, quantify cementation volumes, establish the relative timing of authigenic phases and describe the fabric of the samples. Both freshly broken core chips and mechanically polished or ion-milled samples were analyzed. Samples were ion-milled with a Fischione Model 1060 SEM Mill at the University of Alberta, Edmonton, and all samples were coated in gold or carbon prior to SEM investigation. SEM and energy dispersive x-ray spectroscopy (EDS) analysis was carried out on a JEOL 6301F Field Emission SEM (FE-SEM) or a Zeiss EVO LS15 EP-SEM, with an accelerating voltage of 20 kV, at the University of Alberta.

Cement volume quantification was carried out on 17 ion-milled samples examined with an FEI Quanta 250 FEG with a GATAN MonoCL4 detector (SEM-CL) at the University of Calgary. For each of the 17 samples, three (x1000 magnification) or four (x750 magnification) areas were randomly selected from sample cuts perpendicular to bedding, and scanned for secondary electrons, back scattered electron, EDS, and luminescence patterns. A 437 points grid was used for point counting on each image (>1300 points/sample). EDS maps were used for identifying mineralogical composition, while SEM-CL images were used to differentiate detrital grains from authigenic phases.

3.3.6 Shear wave velocity (DTS) prediction

Well-log suites for wells 6 and 7 did not include DTS (sonic shear waves) curve, which is essential for calculating the dynamic elastic moduli. For these wells, DTS curve was predicted through multivariate cluster analysis in GAMLS software. During a clustering run in GAMLS, predictions are automatically made for missing data using a multi-dimensional probabilistic interpolation. In essence, the code identifies the relationship between the DTS curve and all other curves (GR, RHOB, NPHI, DTC) in all wells in the clustering run, and applies this multi-

dimensional relationship to generate a synthetic DTS curve in the well where the curve is missing (E. Eslinger, pers. com.). To verify the model, DTS curve was omitted from a second well in the cluster run. The synthetic DTS curve generated for the second well was compared with the original log that was previously omitted (Fig. 3.3). The maximum deviation of the predicted DTS curve from the original DTS curve for the second well was 4.5% for the cluster run that includes well 6, and 8.5% for the cluster run that includes well 7.
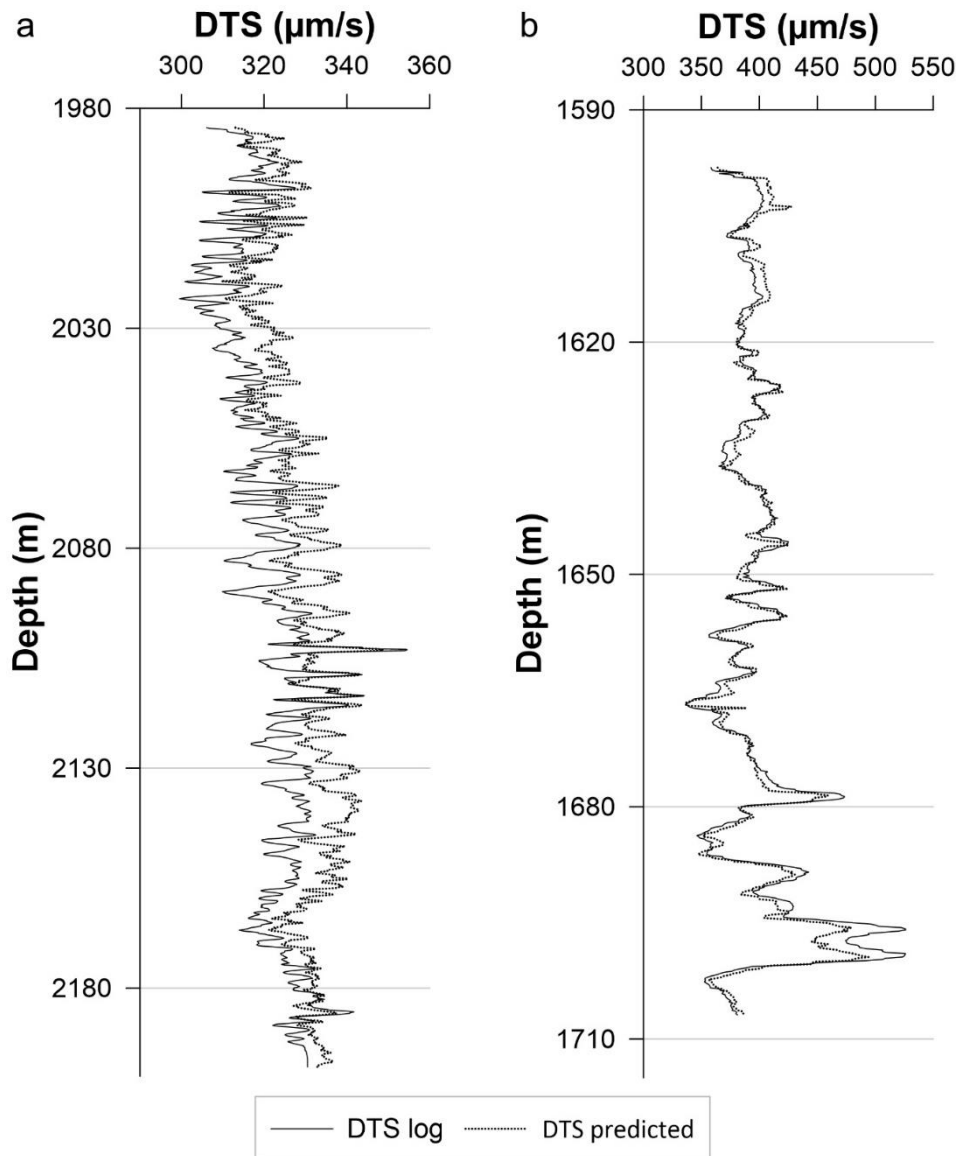
Fig. 3.3: Original shear wave travel time (DTS) and predicted shear wave travel time for well 10-33-078-12W6 (a) and well 13-30-71-25W5 (b). Those wells were used to verify the model predicting shear wave travel time for well 6 and 7, respectively.

3.3.7 Elastic properties, hardness, and brittleness index

Dynamic Young's Modulus (E_d) and dynamic Poisson's Ratio (v_d) were calculated from sonic and density well-logs, using equations introduced by Rickman et al. (2008), where ρ is bulk density, V_p is the P-wave sonic velocity, V_s is the S-wave sonic velocity.

$$(1) E_d = \frac{\rho V_s^2 (3V_p^2 - 4V_s^2)}{V_p^2 - V_s^2}$$

$$(2)\ v_d = \frac{V_p^2 - 2V_s^2}{2(V_p^2 - V_s^2)}$$

Rickman et al. (2008) proposed that formations with higher Young's Modulus and lower Poisson's Ratio exhibit a more brittle behavior, while samples with lower Young's Modulus and higher Poisson's Ratio exhibit a more ductile behavior.

In addition to the dynamic moduli, three different brittleness indicators are presented in this study, based on log response, mineralogical composition and hardness measurements. Sonic brittleness index (BI_{Sonic}) was calculated from log-derived dynamic Young's Modulus and dynamic Poisson's Ratio (Rickman et al., 2008), where E_{min} and E_{max} are the minimum and maximum dynamic Young's Modulus of the Montney Formation in each well, and v_{min} and v_{max} are the minimum and maximum values of dynamic Poisson's Ratio in each well through the formation interval. High BI_{Sonic} values indicate a more brittle (stiffer) rock, while lower BI_{Sonic} values indicate a more ductile rock.

$$(3) BI_{sonic} = \frac{1}{2}\left(\frac{E - E_{min}}{E_{max} - E_{min}} + \frac{v - v_{max}}{v_{min} - v_{max}}\right)$$

Various composition-based brittleness indices are available (Jarvie et al., 2007; Wang and Gale, 2009; Jin et al., 2014; Rybacki et al., 2016). Although their formulations are different and each index accounts for different mineralogical phases, all composition-based brittleness indices attempt to assess the fraction of the hard minerals in the rock, contributing to its overall brittleness.

We used the equation proposed by Rybacki et al. (2016) and modified by Moghadam et al. (2019) to calculate composition-based brittleness index (BI_{min}), where [Xi] is the volume %

of each component. We selected this equation because it takes into account more mineralogical phases than other existing composition-based brittleness index (Jarvie et al., 2007; Wang and Gale, 2009; Jin et al., 2014; Rybacki et al., 2016).

$$(4) BI_{min} = \frac{[Qtz]+[Fsp]+[Py]+0.5([Dol]+[Cal])}{[Qtz]+[Fsp]+[Py]+0.5([Dol]+[Cal])+[clay]+[TOC]+[por]}$$

Mineralogy is obtained from QEMSCAN analysis, TOC from Leco TOC or RockEval analyses, and porosity is estimated from the neutron porosity log. High BI_{min} values are indicative of a more brittle rock.

Hardness was estimated by an Equotip Bambino 2 hardness tester (wells 1-4) or an Equotip 550 Leeb hardness tester (well 5). Hardness testers are spring-loaded devices that release a metal ball to the surface of the sample that bounces back from the sample. Both impact velocity and the rebound velocity are recorded, and hardness is calculated from these velocities according to Eq.5:

(5) Hardness = (Rebound velocity/impact velocity)*1000.

Hardness is a qualitative measure of how susceptible the sample is to plastic deformation due to the force excreted on the surface by the dropping ball. Higher hardness values are associated with stiffer rock that is more resistant to deformation. Three hardness measurements were taken at each depth in 0.1-1 m intervals. Reported values are the average of all three measurements.

3.3.8 Hydraulic fracturing modeling

To assess the impacts of rock composition on hydraulic fracturing treatment, we studied fracture propagation in the Montney Formation using a three-dimensional distinct element code (3DEC from Itasca), acknowledged as a preferred discontinuum approach to numerically simulate hydraulic fracturing of naturally fractured shale plays (Cundall and Hart, 1992; Nagel et al., 2011; Rangriz Shokri et al., 2017). The size of the full hydro-mechanical model was 200m x 100m x 114m; the dimensions of inner domain were extended to reduce the boundary effects. The model outer boundaries were fixed in place using zero velocities. A summary of

input data is provided in Table 3.2. Details of the modelling approach is provided by Rangriz Shokri et al. (2019).

The sedimentological framework for the model is based on core description of the core retrieved from well 1 between the depths of 2400 and 2457 m (Fig. 3.8). The sedimentological analysis for this depth range includes 24 beds of 5 interbedded lithofacies. Following core to log depth adjustment the average values for dynamic Young's Modulus, dynamic Poisson's Ratio and density were calculated from downhole well-logs for each of the lithofacies in the section (Table 3.3). In addition, average values for dynamic Young's Modulus, dynamic Poisson's Ratio and density were calculated for the entire interval under investigation (Table 3.3). Conversion from dynamic to static Young's Modulus was done using publicly available moduli measurements for samples taken from well 1 (British-Columbia Oil and Gas Commission) (Fig. 3.5). A polynomial regression equation showed the best fit ($R^2=0.88$) between the dynamic and static Young's Modulus measurements (Fig. 3.4).

Two sets of simulations were carried out. In both simulations the model consisted of the same 24 beds; the order and thickness of the beds were maintained, and an identical gridding scheme were used. In the first set, each bed was assigned the average mechanical properties calculated for the lithofacies to which it is ascribed. In the second set all the beds were initialized with the average properties calculated for the entire interval (Table 3.3). In addition to the stimulation modeling sets, a series of grid sensitivity analysis was also performed. In our modeling runs, we began by simulating the opening of one discrete fracture from one stage of horizontal well. We then tested the influence of changing the depth of the injection point on fracture propagation.

Table 3.2: Summary of input data used in fully coupled hydro-mechanical simulations

Intact Rock Properties	Base Value	Outer Rock Properties	Base Value
Young's modulus	26.1 GPa	Young's modulus	26 GPa
Poisson's ratio	0.22	Poisson's ratio	0.22
Density	2615 kg/m^3	**Stresses/pressure** at 2427 m	
Joint Properties		Vertical stress	-62.14 MPa
Joint normal stiffness	23 GPa	Max. horizontal stress	-44.74 MPa
Joint shear stiffness	0.1*jkn	Min. horizontal stress	-32.31 MPa
Joint cohesion	1.53 MPa	Fluid pressure	23.81 MPa
Joint friction	27.6°	**Gradients**	
Joint tension	0-2.5 MPa	Vertical stress gradient	-25604 Pa/m
Initial joint aperture	0.0001 m	Min. horizontal stress gradient	-18435 Pa/m
Fluid Properties		Max. horizontal stress gradient	-13314 Pa/m
Fluid bulk modulus	3 MPa	Fluid pressure gradient	9810 Pa/m
Fluid density	1000 kg/m^3	**Simulation Parameters**	
Fluid viscosity	0.0015 Pa.s	Initially fractured radius	2 m
Model Parameters		Maximum allowable aperture	0.003 m
Depth to centre	2427 m	Injection location	centre (0,0,0)
Gravity	9.81 m/s^2	Injection rate	0.4 m3/s
Max. horizontal to vertical stress	0.72	Injection time	12 min
Min. horizontal to vertical stress	0.52	Crack flow injection	off
kH_max/kh_min ratio	1.4	Crack flow shut-in	off

Table 3.3: A summary of the values used in the hydraulic modeling for each lithofacies and the entire interval

Lithoacies	Description	Dynamic Poisson's Ratio	Dynamic Young's Modulus (GPa)	Static Young's Modulus (GPa)	Density (kg/m^3)
F	Faintly laminated calcareous siltstone	0.23[a] (0.01)[b]	46.76 (2.76)	23.37 (1.05)	2630.13 (23.10)
G/H	Laminated siltstone	0.21 (0.01)	52.38 (5.82)	26.3 (3.09)	2619.74 (32.62)
J	Massive siliceous clayey siltstone	0.21 (0.01)	52.73 (3.36)	26 (1.71)	2590.25 (35.75)
K	Massive calcareous clayey siltstone	0.21 (0.01)	54.6 (3.72)	27.04 (2.08)	2582.08 (23.11)
P	Interbedded siliceous mudstone and calcareous siltstone	0.23 (0.01)	55.27 (3.90)	27.46 (2.35)	2649.46 (19.57)
Full interval		0.22 (0.01)	52.55 (2.77)	26.09 (1.31)	2615.23 (23.38)

[a]Average value

[b]Standard deviation

Table 3.3: Average values of mechanical properties for each lithofacies and the full interval
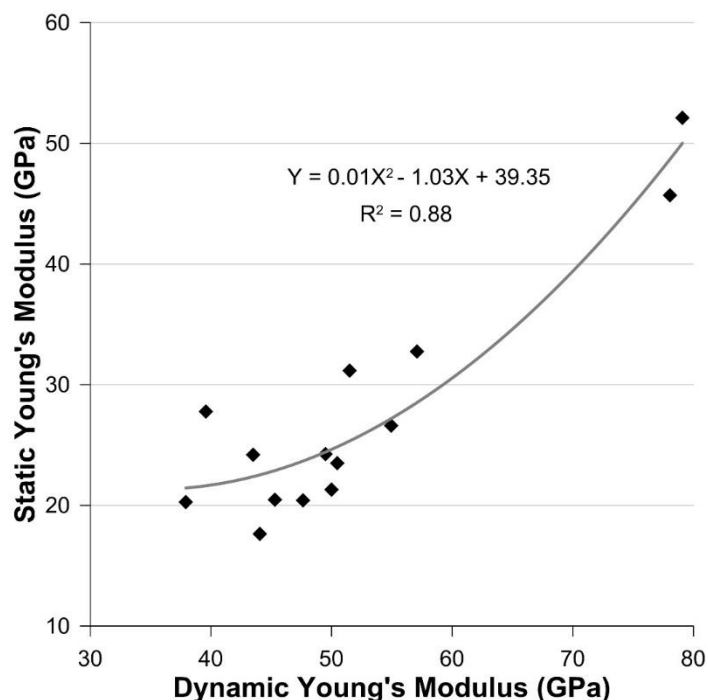
Fig. 3.4: Dynamic and static Young's Modulus for samples from well 1. Data obtained from publically available moduli measurements (British-Columbia Oil and Gas Commission). A polynomial regression equation showed the best fit ($R^2=0.88$) between the dynamic and static Young's Modulus measurements.

3.4 Results

3.4.1 Sedimentological analysis

Fourteen lithofacies were identified in the Montney Formation cores based on physical and ichnological sedimentary structures. Lithofacies distribution and characteristics are reported in Table 3.4. Seven of the 14 lithofacies identified (A, B, E, F, G/H, J, and O) comprise over 90% of all logged cores and the discussion in this paper will be limited to those seven lithofacies. Representative images of the seven major lithofacies are presented in Fig. 3.5. Core descriptions and vertical profiles for all wells are presented in Fig. 3.6 - 3.12. All the lithofacies are either silt-dominated or are either silt-dominated or silt-rich mudstones (Table 3.4)

In the deeply buried distal wells 1 and 2, lithofacies G/H (laminated siltstone) and lithofacies J (massive siliceous clayey siltstone) are the most abundant lithofacies, followed by lithofacies F (the faintly laminated calcareous siltstone). Lithofacies P (interbedded

siliceous-mudstone and calcareous- siltstone) and lithofacies M/N (bioturbated, calcareous, sandy siltstone; part of the newly defined Sunset Prairie Formation (Furlong et al., 2018)) are both locally important, but comprised less than 2% of the total core examined in this study and are thus not be discussed further.

In the deeply buried proximal well 9, the most important lithofacies are lithofacies B (massive sandy siltstone), lithofacies J (massive siliceous clayey siltstone), and lithofacies O (hummocky to ripple cross-stratified sandy siltstone). In the shallow buried proximal well 15, the dominated lithofacies is lithofacies A (interlaminated siltstone and sandstone), followed by lithofacies E (dolomitic siltstone).

Table 3.4: A summary of all major lithofacies characteristics in four Montney cores (wells 1-4)

Facies	Lithology	Rock type classification [a]	Sedimentary structures	Trace fossil Assemblage	Bioturbation intensity	Average composition			% core2 [c] (261 m)	% core 4 (185 m)	% core 9 (148 m)	% core 15 (51 m)	% all cores
						% Clay	% Silt	% Sand					
A	Interlaminated siltstone and sandstone alternation	Sand bearing, silt rich to sand and clay-bearing, silt rich mudstone	Dominant flaser and lenticular bedding, current ripples, rare climbing ripples, mud rip-up clasts and soft sediment deformation	*Thalassinoides, Conichnus, Planolites*, and escape structures	0-2	11.9 (4.5) [b]	65.0 (10.3)	23.1 (11.1)			10.6	53.1	16.8
B	Massive sandy siltstone	Silt-rich to sand-bearing, silt rich mudstone	Rare soft sediment deformation, flame structures, carbonate nodules, mud rip-up clasts, and high-angle cross bedding	N/A	0	5.1 (2.5)	76.0 (11.0)	19.0 (10.7)			37.7	12.0	13.1
E	Dolomitic siltstone	Dolomite cement-dominated to dolomite cement-rich, silt-dominated to sand and clay-bearing, silt-rich mudstone	Low-high angle bedding, and rare rip-up clasts/ dolomitic breccia	N/A	0	7.2 (3.4)	75.2 (13.3)	17.6 (12.7)				22.4	5.9
F	Faintly laminated calcareous siltstone	Calcite cement-bearing, clay-bearing, silt-rich mudstone	Horizontal parallel lamination, carbonaceous grains, and rare shell debris	Biodeformation structures	0-1	14.6 (4.0)	83.3 (6.8)	2.1 (5.0)	16.5			9.8	6.6
G/H	Laminated siltstone	Silt-dominated to clay-bearing, silt-rich mudstone	Horizontal parallel lamination, rare wavy bedding, current ripples, rare amalgamated current ripples, soft sediment deformation, and presence of dolomite beds	Biodeformation structures, Planolites, laminae disruption and escape structures	0-1	11.8 (3.3)	85.9 (3.2)	2.3 (2.7)	58.4	61.5	10.4		31.1
J	Massive siliceous clayey siltstone	Silica cement-bearing, silt-dominated mudstone to clay-bearing, silt-rich mudstone	Rare dolomite beds	N/A	0	12.5 (3.4)	86.0 (2.9)	1.5 (1.3)	9.2	21.3	20.7		12.6
O	Hummocky to ripple cross-straticatified sandy siltstone	Silt rich to sand-bearing, clay-bearing, silt-rich mudstone	Hummocky cross-stratification, current ripples, climbing ripples, mud rip-up clasts, rare loading structures and soft sediment deformation	Rare *Planolithes*	0-1	6.0 (2.8)	82.0 (2.3)	12.0 (3.5)			20.5		5.4

[a] After Macquaker and Adams, 2003.

[b] Standard deviation 1σ.

[c] Facies % of core, normalize to exclude missing core sections.

107

Fig. 3.5: Representative photographs of the major Montney Formation lithofacies: (a) lithofacies A, interlaminated siltstone and sandstone alternation. (b) Lithofacies B, massive sandy siltstone with carbonate concentration (in white). (c) lithofacies E, dolomitic siltstone. (d) lithofacies F, faintly laminated calcareous siltstone (arrows point to faint laminations). (e) lithofacies G/H, Laminated siltstone. (f) lithofacies J, massive, siliceous clayey mudstone, and (g) lithofacies O, hummocky to ripple cross-stratified sandy siltstone. CR - current ripple, HCS- Hummocky cross stratification.

Fig. 3.6: Well 1. Tracks from left to right are core description, vertical profiles of TOC, total clay content, QFM (quartz, feldspars and mica) and carbonate minerals (dolomite, Fe-dolomite, and calcite), dynamic Young's modulus (DYM), dynamic Poisson's Ratio (DPR), BI_{sonic}, hardness, Bi_{min,} and total hard and soft minerals concentrations.
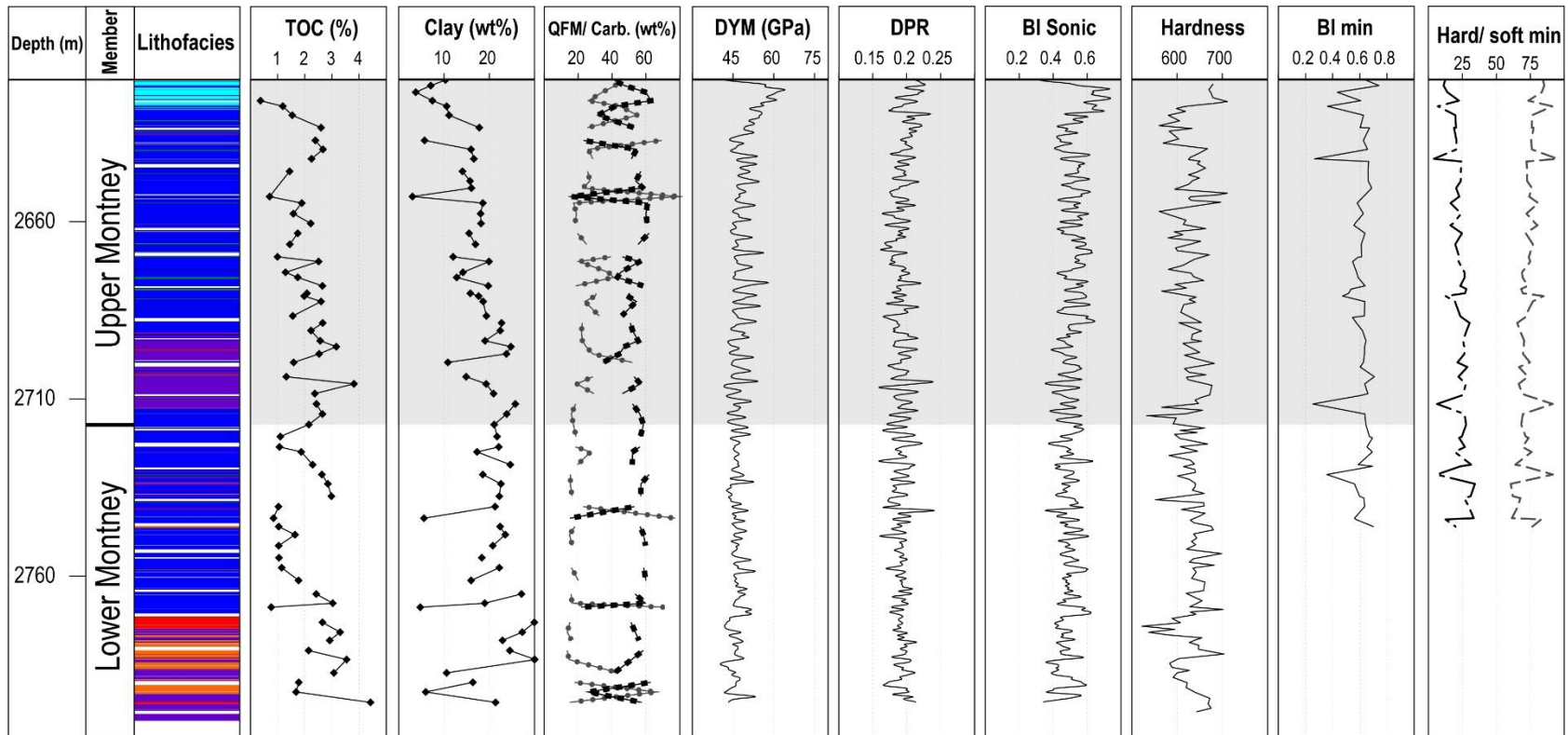
Fig. 3.7: Well 2. Tracks from left to right are core description, vertical profiles of TOC, total clay content, QFM (quartz, feldspars and mica) and carbonate minerals (dolomite, Fe-dolomite, and calcite), dynamic Young's modulus (DYM), dynamic Poisson's Ratio (DPR), BI_{sonic}, hardness, Bi_{min}, and total hard and soft minerals concentrations. See legend in Fig. 3.6.
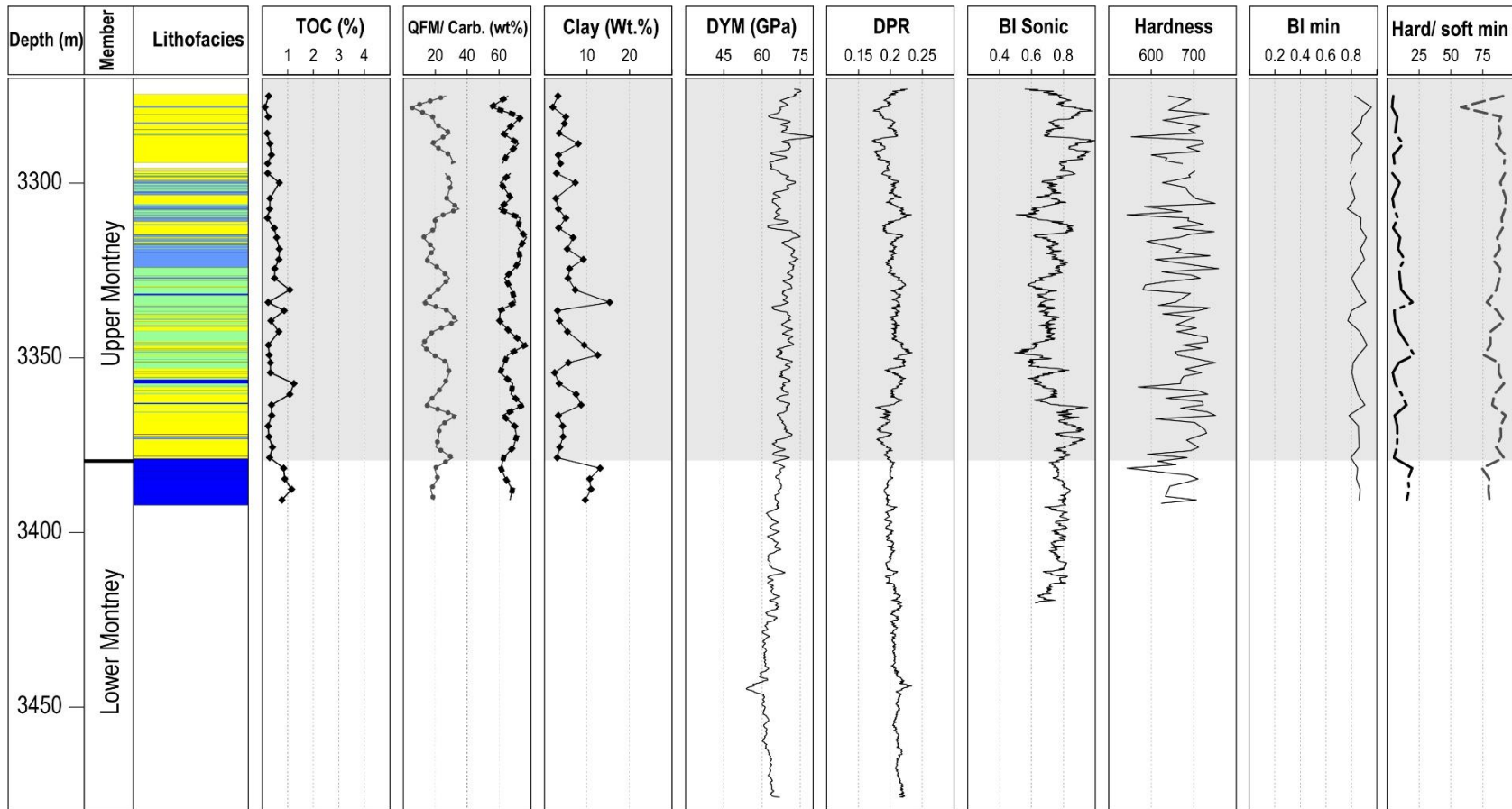
Fig. 3.8: Well 3. Tracks from left to right are core description, vertical profiles of TOC, total clay content, QFM (quartz, feldspars and mica) and carbonate minerals (dolomite, Fe-dolomite, and calcite), dynamic Young's modulus (DYM), dynamic Poisson's Ratio (DPR), BI_{sonic}, hardness, $Bi_{min,}$ and total hard and soft minerals concentrations. See legend in Fig. 3.6.
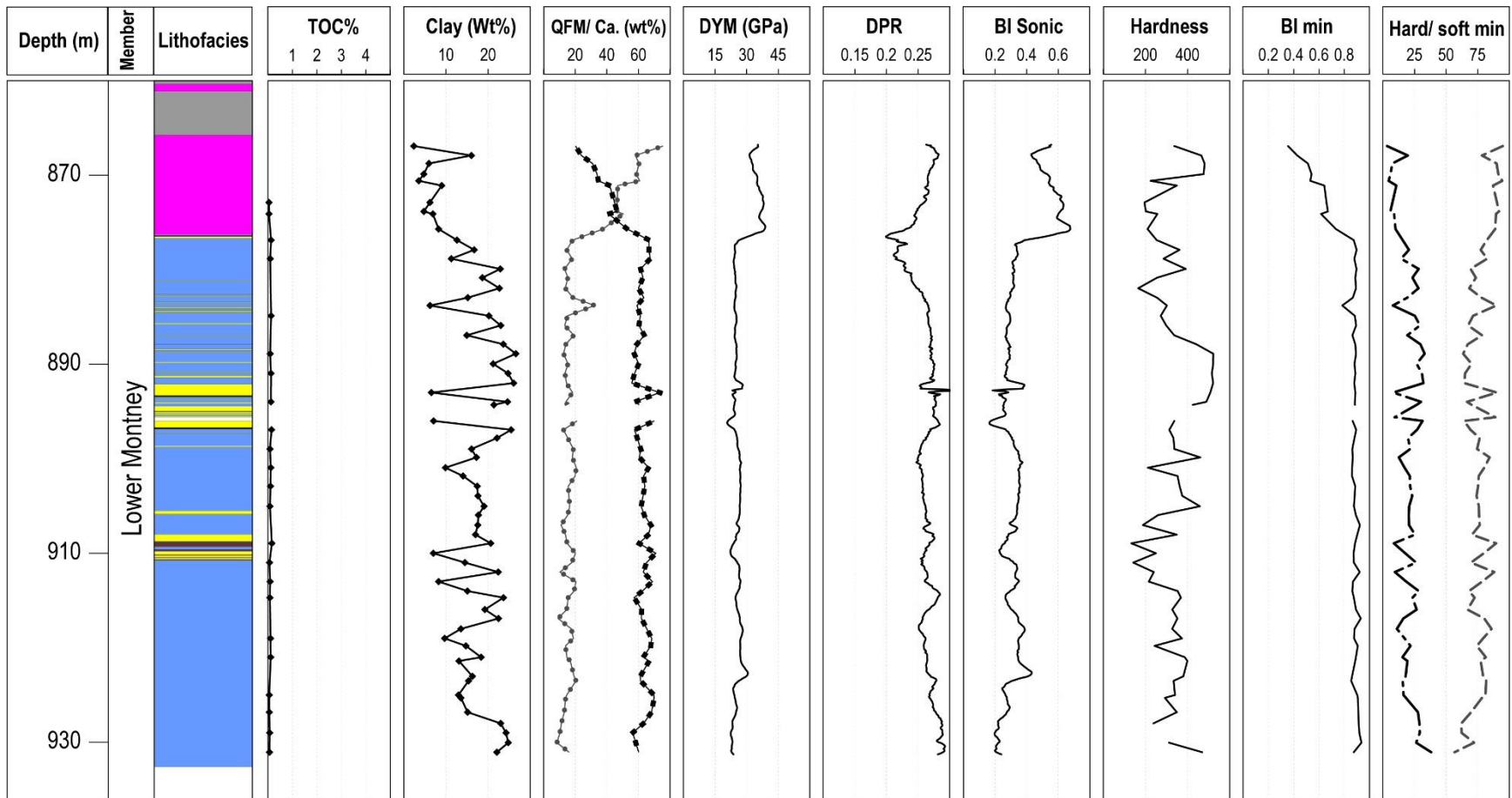
Fig. 3.9: Well 4. Tracks from left to right are core description, vertical profiles of TOC, total clay content, QFM (quartz, feldspars and mica) and carbonate minerals (dolomite, Fe-dolomite, and calcite), dynamic Young's modulus (DYM), dynamic Poisson's Ratio (DPR), BI$_{sonic}$, hardness, Bi$_{min}$, and total hard and soft minerals concentrations. See legend in Fig. 3.6.
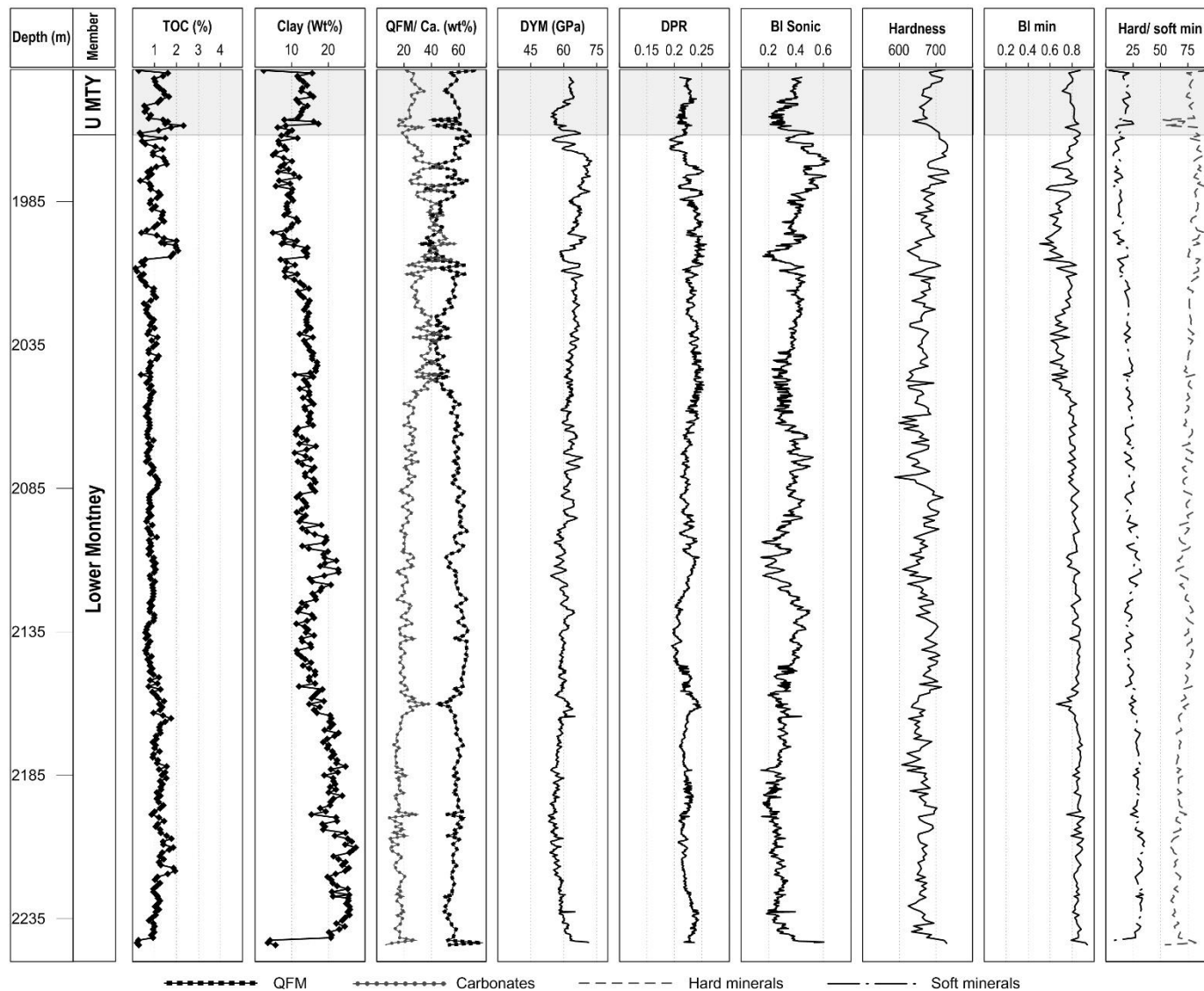
Fig. 3.10: Well 5. Tracks from left to right are vertical profiles of TOC, total clay content, QFM (quartz, feldspars and mica) and carbonate minerals (dolomite, Fe-dolomite, and calcite), dynamic Young's modulus (DYM), dynamic Poisson's Ratio (DPR), BI_{Sonic}, hardness and Bi_{min}, and total hard and soft minerals concentrations.

113
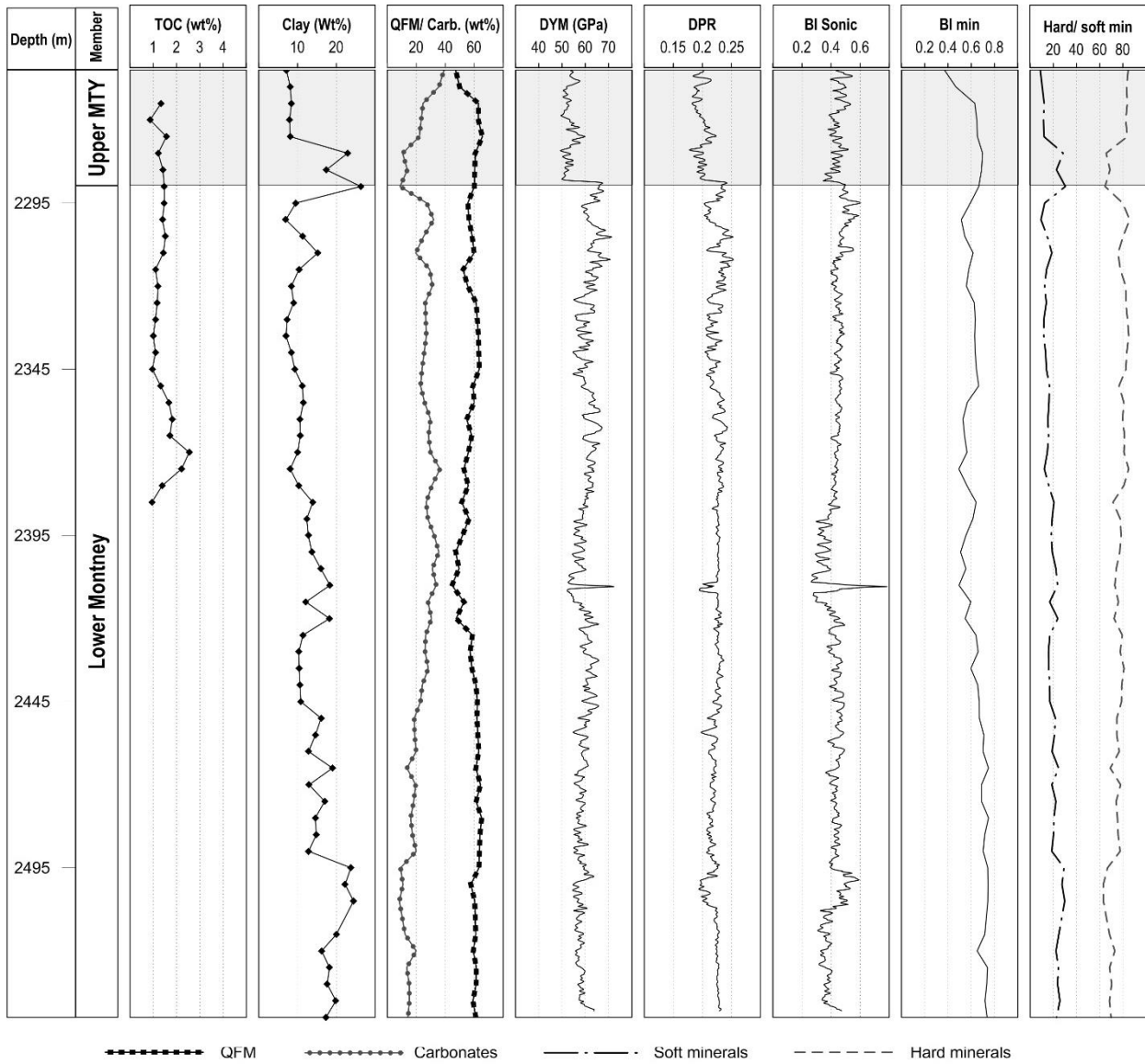
Fig. 3.11: Well 6. Tracks from left to right are vertical profiles of TOC, total clay content, QFM (quartz, feldspars and mica) and carbonate minerals (dolomite, Fe-dolomite, and calcite), dynamic Young's modulus (DYM), dynamic Poisson's Ratio (DPR), BI_{sonic}, hardness, Bi_{min}, and total hard and soft minerals concentrations.

114
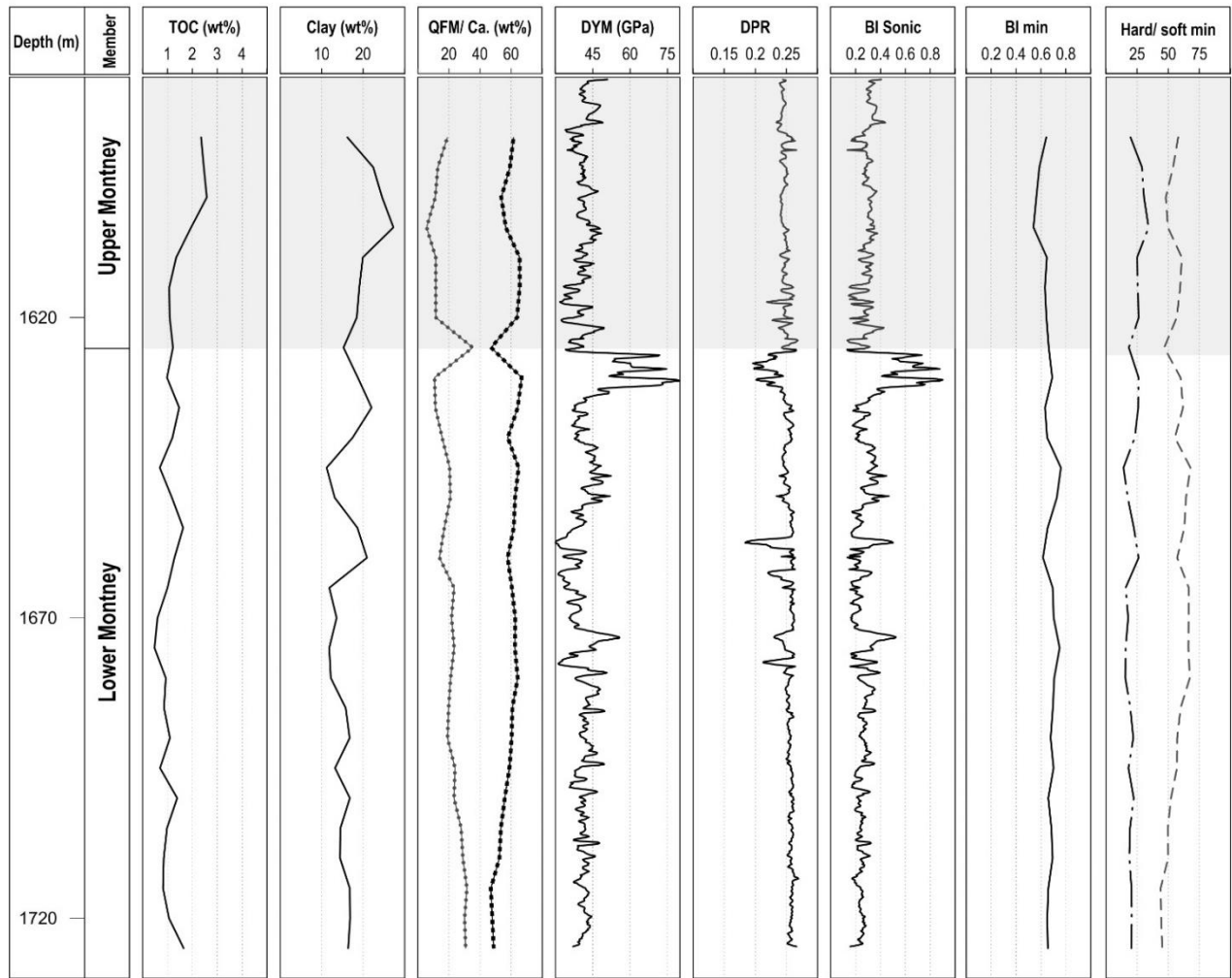
Fig. 3.12: Well 7. Tracks from left to right are vertical profiles of TOC, total clay content, QFM (quartz, feldspars and mica) and carbonate minerals (dolomite, Fe-dolomite, and calcite), dynamic Young's modulus (DYM), dynamic Poisson's Ratio (DPR), BI_{sonic}, hardness, Bi_{min}, and total hard and soft minerals concentrations.

3.4.2 Rock composition

Major mineralogical phases in the seven study wells include quartz, potassium and sodium feldspars, clay minerals (mixed-layer illite-smectite and kaolinite), calcite, dolomite, and iron-rich dolomite. Apatite and anhydrite are locally important. Table 3.5 summarizes the mineralogical composition for all seven wells, and Fig. 3.13 demonstrates that the compositional variation between wells are mostly due to differences in concentrations of carbonate mineral, and to a lesser extent differences in clay minerals abundance. In most cases, QFM (total Quartz-Feldspar-Mica) vertical profile (Fig. 3.6 - 3.12) varies antithetically to the total carbonate curve (dolomite, calcite, and Fe-rich dolomite), while total clay content varies largely in parallel to the QFM curve, although these relationships are somewhat less clear in the most proximal wells (wells 4 and 7).

Total organic carbon values for all samples ranges between 0.05 and 4.02 wt%, with an average of 1.10 wt%. Vertical TOC profiles for all wells are presented in Fig. 3.6 - 3.12. In well 1, TOC content decreases from the Upper to the Lower Montney (average of 1.9 and 1.0 wt%, respectively, for the two units), a pattern that was previously reported (Wood, 2013; Crombez, 2016; Crombez et al., 2017). The trend of decreasing TOC with depth is less clearly defined in well 2 and well 7 where both members of the Montney Formation are present (average of 2.2 and 1.8 wt% in the Upper Montney, and 1.85 and 1.0 wt% in the Lower Montney, respectively). Comparison to other wells in this data set is not possible because most or all of the Upper Montney section has been eroded (wells 5, 6, and 4), or because the Lower Montney interval was not cored (well 5). The most distal wells (1 and 2) in a depositional framework contain slightly higher amounts of organic carbon than more proximal wells.

Table 3.5: Average mineralogical composition (obtained from QEMSCAN analysis) and total organic carbon. Values are in wt%. Values in parentheses are standard deviation

well	n[a]	Quartz	K Feldspar	Plagioclase	Muscovite	Biotite	Chlorite	Kaolinite	Illite & MLIS	Calcite	Dolomite	Fe-Dolomite[b]	Fe Oxide & siderite	Pyrite	Sphalerite	Barite	Anhydrite	phosphate[c]	Heavy minerals[d]	n[e]	TOC[f]
Well 1	70	36.95 (5.51)	6.95 (2.81)	8.73 (2.46)	4.26 (1.35)	0.39 (0.31)	0.78 (0.63)	0.68 (0.26)	14.93 (5.63)	5.96 (4.36)	12.75 (7.41)	3.17 (4.65)	0.08 (0.15)	3.18 (1.15)	0.02 (0.04)	0.10 (0.07)	0.11 (0.06)	0.56 (1.49)	0.42 (0.08)	44	1.45 (0.79)
Well 2	65	29.46 (6.13)	8.27 (2.29)	8.98 (2.27)	4.16 (1.34)	0.18 (0.12)	0.50 (0.37)	0.61 (0.15)	16.58 (6.10)	7.94 (6.34)	14.71 (8.50)	5.37 (7.42)	0.07 (0.11)	2.11 (0.74)	0.03 (0.04)	0.03 (0.04)	0.10 (0.05)	0.43 (0.13)	0.48 (0.11)	44	2.00 (0.79)
Well 3	40	42.28 (4.36)	11.45 (2.75)	9.72 (2.15)	2.38 (1.14)	0.27 (0.25)	0.94 (0.40)	0.39 (0.14)	5.54 (3.18)	0.25 (0.08)	21.60 (6.60)	0.68 (0.71)	0.00 (0.00)	1.22 (0.78)	0.00 (0.00)	0.03 (0.03)	1.86 (5.56)	0.85 (0.50)	0.53 (0.19)	40	0.47 (0.30)
Well 4	74	41.95 (13.79)	7.24 (2.59)	2.33 (1.56)	3.01 (1.79)	0.06 (0.02)	0.15 (0.06)	2.05 (0.76)	14.18 (7.09)	3.30 (7.90)	19.36 (16.85)	2.19 (1.99)	0.00 (0.00)	2.30 (1.95)	0.00 (0.01)	0.03 (0.04)	0.30 (0.78)	1.17 (5.61)	0.37 (0.14)	28	0.19 (0.43)
Well 5	314	31.63 (6.25)	8.50 (1.78)	8.40 (2.13)	3.91 (1.25)	1.36 (0.66)	1.14 (0.63)	0.70 (0.24)	14.37 (5.57)	7.68 (7.79)	15.65 (5.28)	1.81 (1.07)	0.00 (0.00)	2.53 (0.99)	0.03 (0.27)	0.09 (0.23)	0.11 (0.07)	1.62 (6.51)	0.47 (0.09)	40	1.44 (0.82)
Well 6	74	36.99 (6.79)	7.70 (2.49)	6.34 (2.95)	2.53 (0.98)	0.60 (0.41)	1.08 (0.59)	1.16 (0.68)	11.51 (4.31)	2.92 (3.46)	22.28 (10.13)	1.02 (0.74)	0.31 (0.70)	3.17 (1.40)	0.00 (0.00)	0.13 (0.12)	0.95 (1.72)	0.95 (1.43)	0.36 (0.10)	37	1.07 (0.39)
Well 7	28	44.77 (6.30)	5.75 (1.76)	3.35 (1.26)	3.21 (1.14)	0.31 (0.17)	1.27 (1.03)	2.80 (1.95)	14.21 (2.49)	0.66 (1.11)	16.20 (8.01)	2.89 (2.80)	1.02 (1.95)	2.66 (1.12)	0.01 (0.02)	0.08 (0.06)	0.16 (0.15)	0.36 (0.18)	0.29 (0.05)	28	1.25 (0.54)

a. Number of samples analysed with QEMSCAN.
b. Fe concentration is 5-15%.
c. Apatite and monazite.
d. Heavy minerals inclue chromite, rutile & Ti-silicates, tourmaline, and zircon.
e. Number of samples analysed with LECO-TOC.
f. TOC values are obtained from Leco TOC analysis (wells 1-5) or RockEval analysis (wells 6-7).
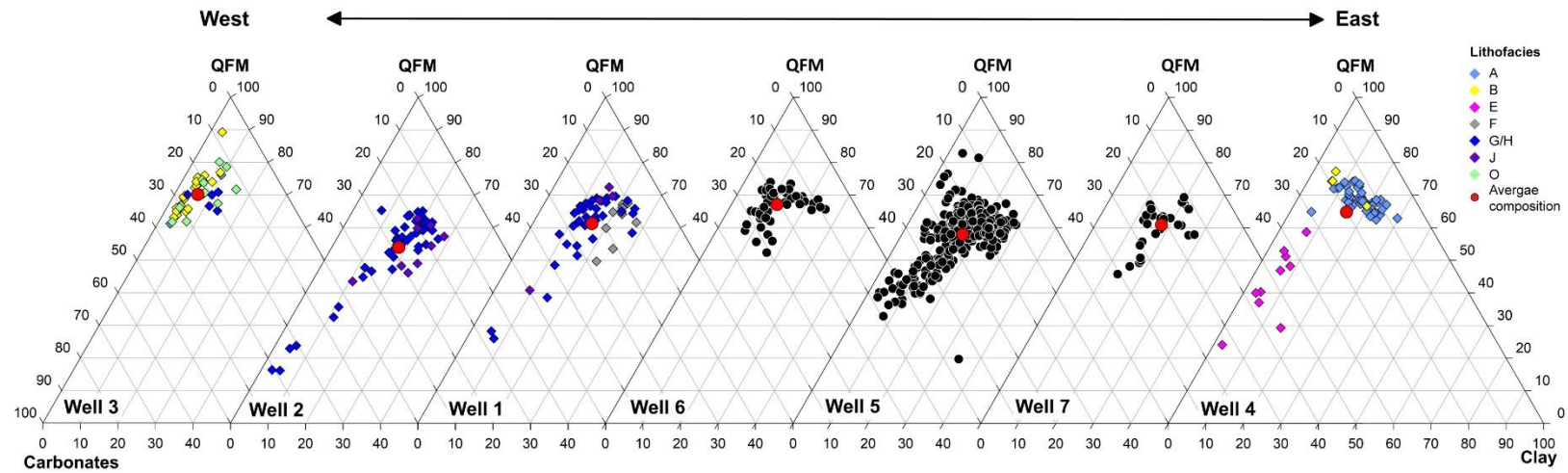
Fig. 3.13: Mineralogical composition of the seven study wells as obtained by QEMSCAN analysis of core samples (wells 1-5) and cuttings (wells 6-7). Wells are organized from deep/distal (west) to shallow/proximal (east), with the exception the shallow, western well 3 Light blue circles are the average composition of each well. For cores 1-4 lithological description was obtained. For these wells, mineralogical composition is presented by lithofacies. Note that it is impossible to distinguish one lithofacies from another solely based on their mineralogical composition. QFM: quartz, feldspar and mica. Feldspar minerals include Na-feldspar and K-feldspar, and mica minerals are muscovite, biotite and chlorite. Carbonates are calcite, dolomite, and Fe-rich dolomite, and clays include mixed layer Illite-smectite, illite, and kaolinite.

3.4.3 Scanning Electron Microscopy - Cathodoluminescence (SEM-CL)

Scanning electron microscopy on ion-milled surfaces revealed a cemented framework of hard grains, with readily visible grain-to-grain contacts and organic matter dispersed between the minerals (Fig. 3.14a). No differences were found in the distribution of organic matter in samples from different lithofacies and no depositional organic macerals were identified in any sample. An extensive diagenetic study of the Montney Formation (chapter 2 this study) found that massive shallow burial cementation affected the entire formation, including precipitation of quartz, feldspar, dolomite, and calcite cements (Fig. 3.14b) that comprise more 30% of the present-day rock volume. Deep burial diagenesis occurred during the Laramide orogenic event, when the siltstone was exposed to elevated temperatures. Deep burial diagenesis is characterized by hydrocarbon maturation, pressure solution (Fig. 3.14 a), and authigenic clay precipitation (fibrous illite in most of the Montney Formation, and kaolinite in the shallow regions). No significant differences were found between different lithofacies in either the character or magnitude of the diagenetic processes.

3.4.4 Hardness

Hardness values vary between 133 and 860 with a median value of 670; these values are similar or slightly lower than hardness measurements previously reported for the Montney Formation (Ghanizadeh et al., 2015b; Wust and Cui, 2018). Vertical profiles of hardness measurements (Fig. 3.6 - 3.12) show slight decreases with depth. Hardness measurement values somewhat increase from distal to proximal positions in the basin (medians of 640 and 668 for wells 1 and 3, respectively), but are the lowest in the most proximal well in the study (median of 337 for well 4) (Fig. 3.15). There is no clear effect of burial depth on the rock hardness values, and with the exception of well 2, where hardness values for the Lower Montney are slightly higher than those measured for Upper Montney (medians of 637 and 627, respectively), the Upper Montney member shows consistently higher hardness values (20-40 units) than the Lower Montney (fig. 3.10).
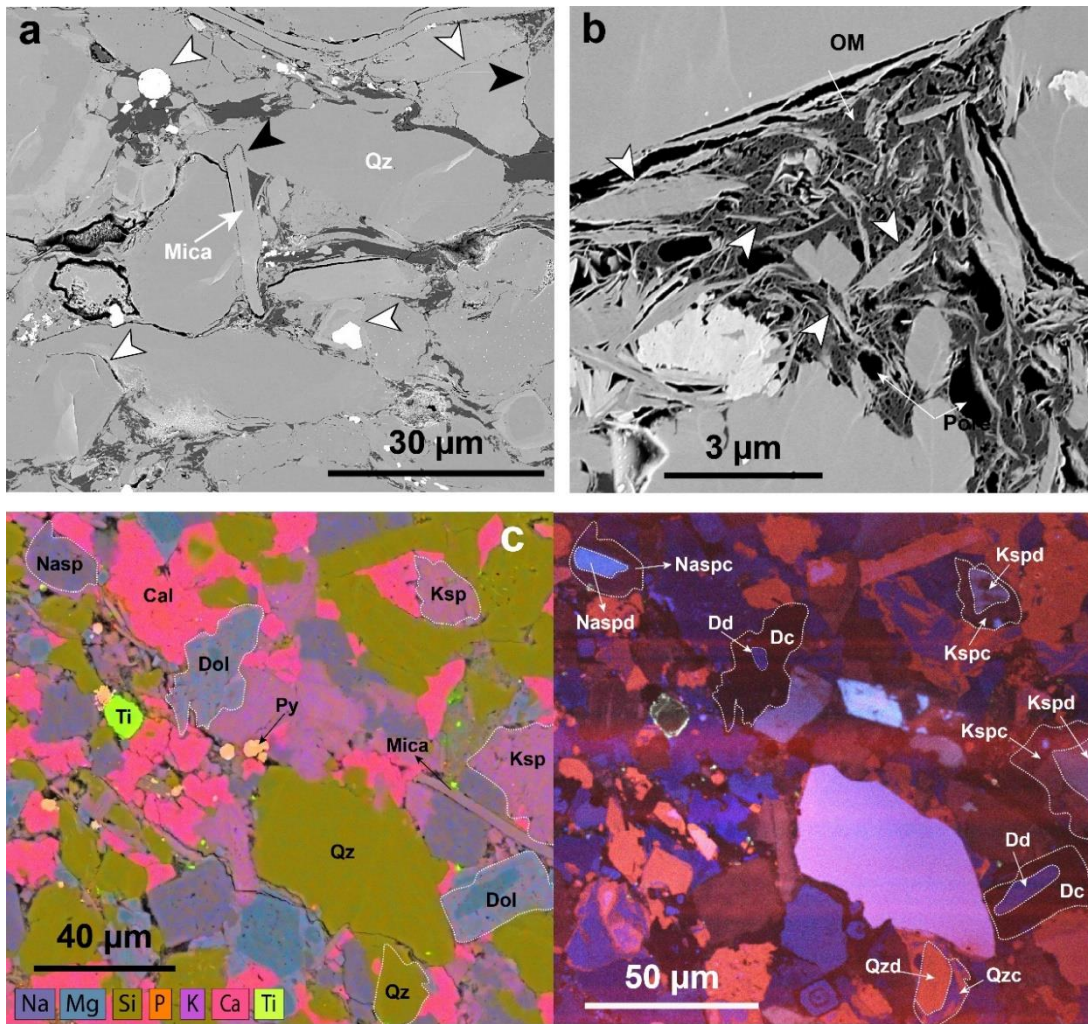
Fig. 3.14: (a) BS-SEM image of a typical Montney siltstone. Black is porosity, dark gray is OM, and in light gray are minerals. Framework grains contact (white arrows) and pressure solution contact (black arrows) are common. Note the Mica grain pressure solving into a quartz grain (Qz) in the middle of the image. Core 1, sample 9P, 2368.3 m. (b) Authigenic clays (white arrows) found together with pore-filling organic matter (OM, dark grey). Core 1, sample 12H, 2427.9 m. (c) SEM-EDS (left) and SEM-CL (right) of the same sample, showing detrital grains and authigenic cements. Nasp is Na-feldspar, Ksp is K-feldspar, Qz is quartz, Dol is dolomite, Cal is calcite, Py is pyrite, and Ti is titanite. On the SEM-CL image (right), d suffix (?) is for detrital grain, while c suffix is for cement. Core 2, sample 3AJ, 2653 m.
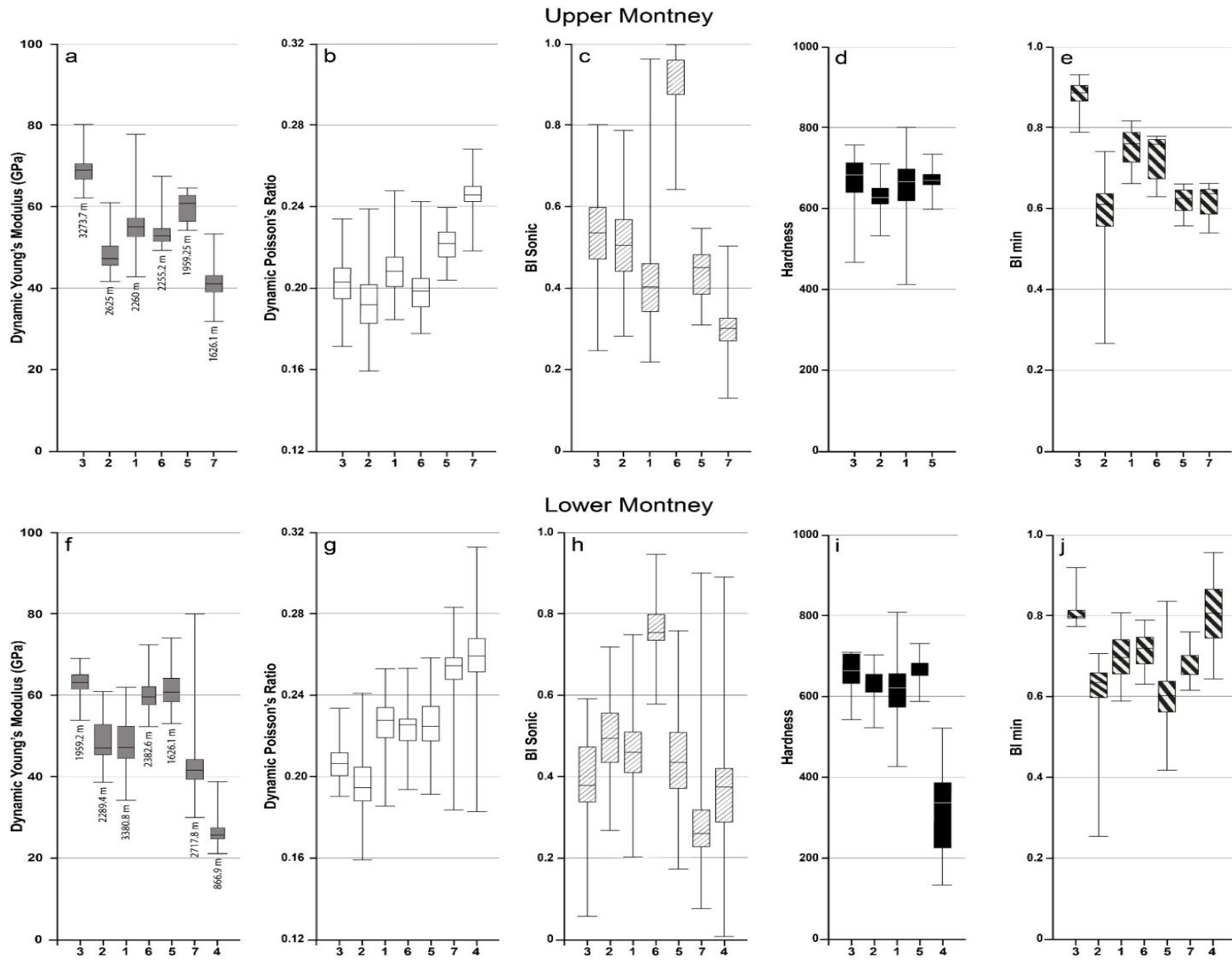
Fig. 3.15: Range and mean values for all study wells on a west-east (proximal/ shallow- distal/ deep) cross section for the Upper and Lower Montney Members (a,f) dynamic Young's Modulus (b,g) dynamic Poisson's Ratio (c, h) BI$_{Sonic}$ (d, i) hardness (e, j) Bi$_{min}$.

3.4.5 Mineral Brittleness Index (BI_{min})

The Mineral Brittleness Index varies over a large range (0.1-0.92) in the study wells. BI_{min} curves (Fig. 3.6 - 3.12) increase somewhat with depth in all but the most distal well (well 1), where BI_{min} decreases with depth. BI_{min} vertical profiles behave somewhat similarly to the Hardness, dynamic young's Modulus, and Sonic Brittleness index, particularly evident in well 5, where mineralogical composition data has the smallest sampling interval (1 m). There are no clear geographic or burial-depth dependent trends in BI_{min} values in the study area (Fig. 3.15). There is no consistent difference in BI_{min} values between the Upper and Lower Montney, which can be higher in the Upper Member (wells 1, 6, 3), Lower Member (wells 2, 7), or similar in both (well 5).

3.4.6 Dynamic elastic moduli and sonic brittleness index

Vertical profiles for dynamic Young's Modulus, dynamic Poisson's Ratio, and hardness for all wells are presented in Fig. 3.6 - 3.12. A summary of the elastic moduli for all wells can be found in Fig. 3.15. Dynamic Young's Modulus values for the study wells range from 21 to 83 GPa [3.05×10^6 - 12×10^6 psi], and values generally increase from well to well with increasing burial depth, although the trend is not entirely consistent (Fig. 3.15). In individual well profiles, dynamic Young's Modulus values generally decrease with depth (Fig. 3.6 - 3.12). Proximal wells have the lowest Young's Modulus values with median of 25.6 and 41.4 GPa for well 7 and well 4, respectively, while the middle wells have the highest Young's Modulus values with median of 66, 60, and 59.1 GPa for wells 3, 5, and 6, respectively (Fig. 3.15). The distal wells have intermediate Young's Modulus values with median of 52.1 GPa for well 1 and 47.1 GPa for well 2.

Dynamic Poisson's Ratio values for the study wells change between 0.16 and 0.31. Values decrease with increasing burial depth (Fig. 3.6 - 3.12) and are consistently higher in the Lower Montney Member than in the Upper Member (Fig. 3.15). Proximal wells have the highest dynamic Poisson's Ratio values with median of 0.25 and 0.26 for well 7 and well 4,

respectively. All other wells have median dynamic Poisson's Ratio values of 0.19 to 0.22 (Fig. 3.15). Dynamic Poisson's Ratio values fluctuate with depth, and do not have a systematic, consistent relationship with dynamic Young's Modulus curves (Fig. 3.6 - 3.12). In some of the well profiles, dynamic Poisson's Ratio slightly increases with depth (wells 1, 3, and 4), but in others it slightly decreases with depth (well 2, 5, 6, and 7).

The relationship between dynamic Young's Modulus and dynamic Poisson's Ratio varies between wells and can be either positive or negative (Fig. 3.16 and Fig. 3.6 - 3.12), but in all cases the correlation is weak (R <0.5). The same correlation (positive or negative) exists for both Montney Members individually within each well. In wells that show a positive correlation between dynamic Young's Modulus and dynamic Poisson's Ratio, there is little difference between the Upper and Lower Members. However, in wells that show a negative correlation, the Upper Montney Member usually exhibits higher dynamic Young's Modulus and lower dynamic Poisson's Ratio values than the Lower Montney Members (Fig. 3.16).

Sonic brittleness index (BI_{sonic}) values fluctuate between 0.1 and 0.92 and decrease with depth in all wells (Fig. 3.6 - 3.12). BI_{sonic} curves are similar to hardness curves and to a lesser extent to the Mineral Brittleness Index (BI_{min}). No clear trend of BI_{sonic} values exists from east to west (proximal to distal setting), but values systematically increase with increasing burial depth (Fig. 3.15). Sonic brittleness index values in the Upper Montney are mostly higher than those of the Lower Montney (wells 2, 3, 5, and 7), but can also show the reverse trend (wells 1 and 6).
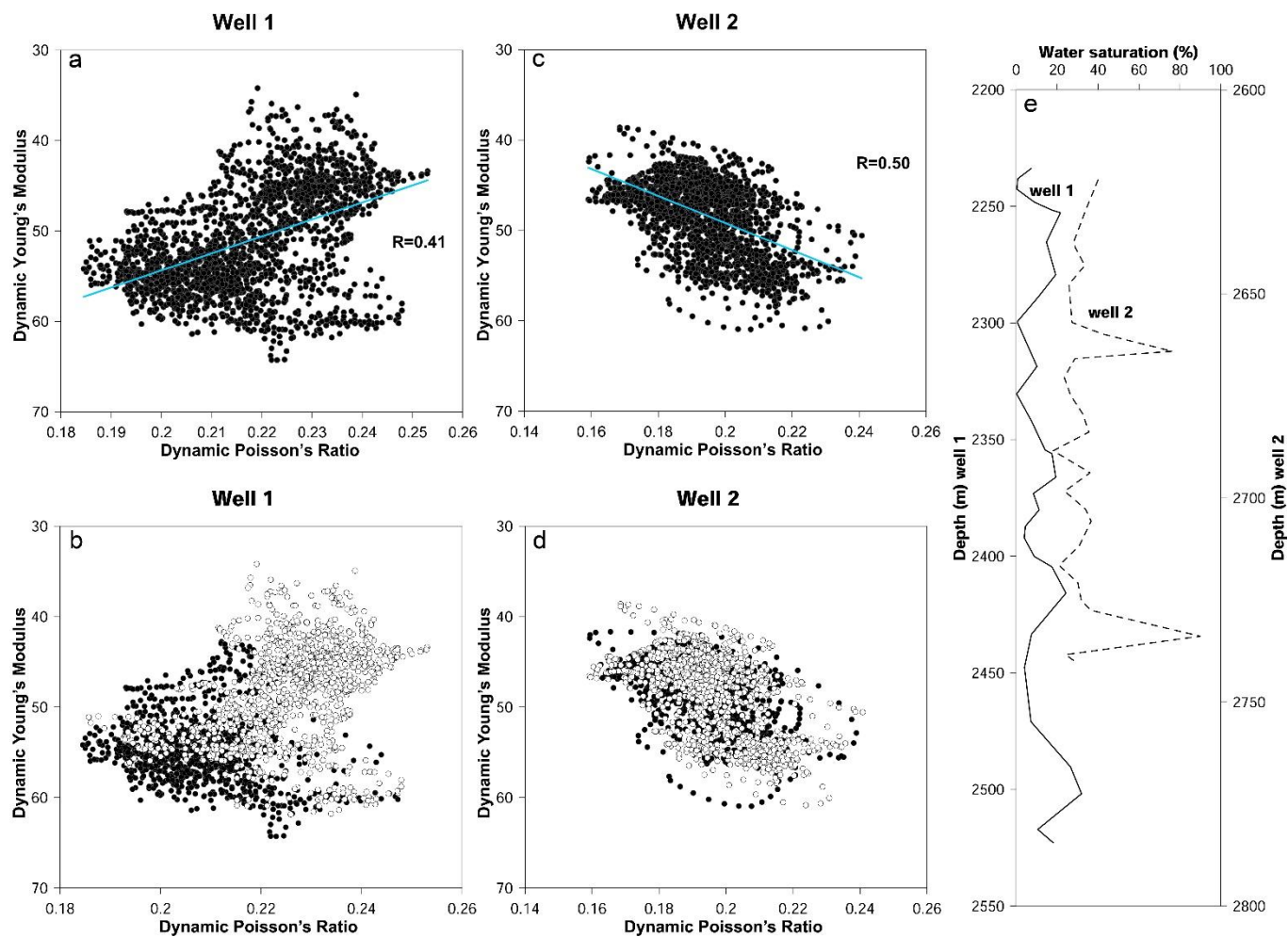
Fig. 3.16: Dynamic Young's Modulus versus dynamic Poisson's ratio from downhole logs. In well 1 there is a negative correlation between dynamic Young's Modulus and dynamic Poisson's ratio (a), and Upper Montney wells show higher dynamic Young's Modulus and Lower Poisson's ratio values than the Lower Montney (b). In well 2 there is a positive correlation between dynamic Young's Modulus and dynamic Poisson's ratio (c), and there is no clear difference between Upper and Lower Montney values of dynamic Young's Modulus or Poisson's ratio (d). Water saturation data for wells 1 and 2 (e) showing higher water saturation for well 2.

124

3.4.7 Hydraulic stimulation modeling results

To inspect the impact of lithofacies on the dominant physics of fluid flow and fracture propagation in the Montney Formation, the model initially included only one discrete fracture from one stage of a horizontal well. By injecting the fracturing fluid, the fracture opens, aperture increases, and fluid pressure travels toward model boundaries. The results of the two simulation runs are presented in Fig. 3.17. After 24 minutes of injection (0.4 m3/sec) pore pressure, as well as fracture geometry and the magnitude of the aperture in the two simulation runs, are similar.

Additional modeling tested the dependency of fracture development on the location of the injection point. Results after 24 minutes of injection are presented in Fig. 3.18 and show that once the location of injection was moved from the center of the section, both fracture geometry and pore pressure distribution significantly changed. Injecting at a shallower depth enhanced the stimulated reservoir volume, but achieved a lower pore pressure, and smaller aperture, whereas aperture, pore pressure, and induced conductivity were higher when injection occurs at a deeper location.
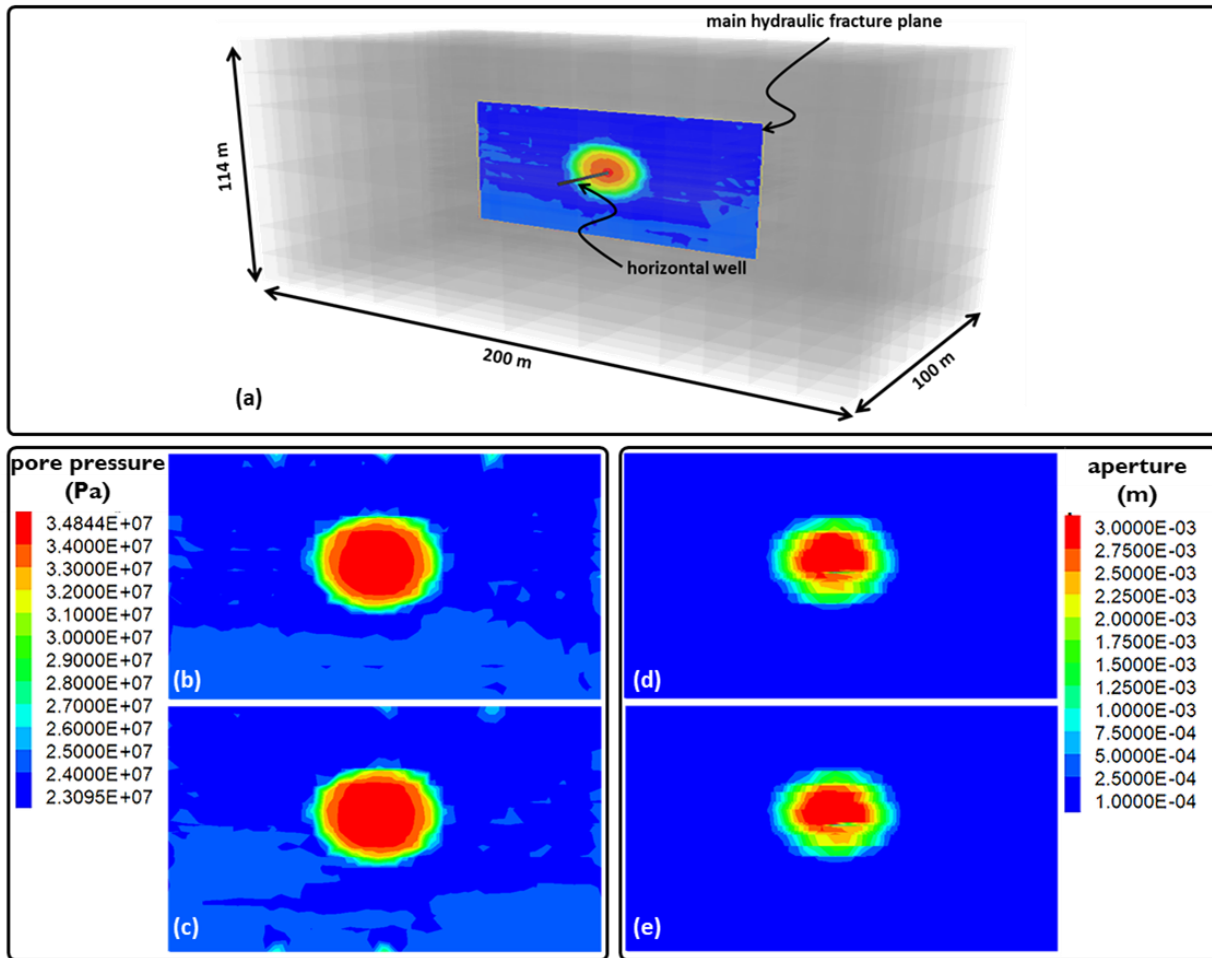
Fig. 3.17: The impact of lithology on the extent of fracture geometry during hydraulic fracturing treatment; (a) 3DEC model of hydraulic fracturing treatment, and across-section perpendicular to hydraulic fracture plane. The fracture plane is represented as a pipe as the model assumes an isotropic stress regime. The simulated pore pressures after 24 minutes of injection at a rate of 0.4 m^3/second are shown when lithofacies are included in the model (b) and when all the beds are given the same values (c). The associated apertures are shown when geological facies included and, with no facies in (d) and (e), respectively.
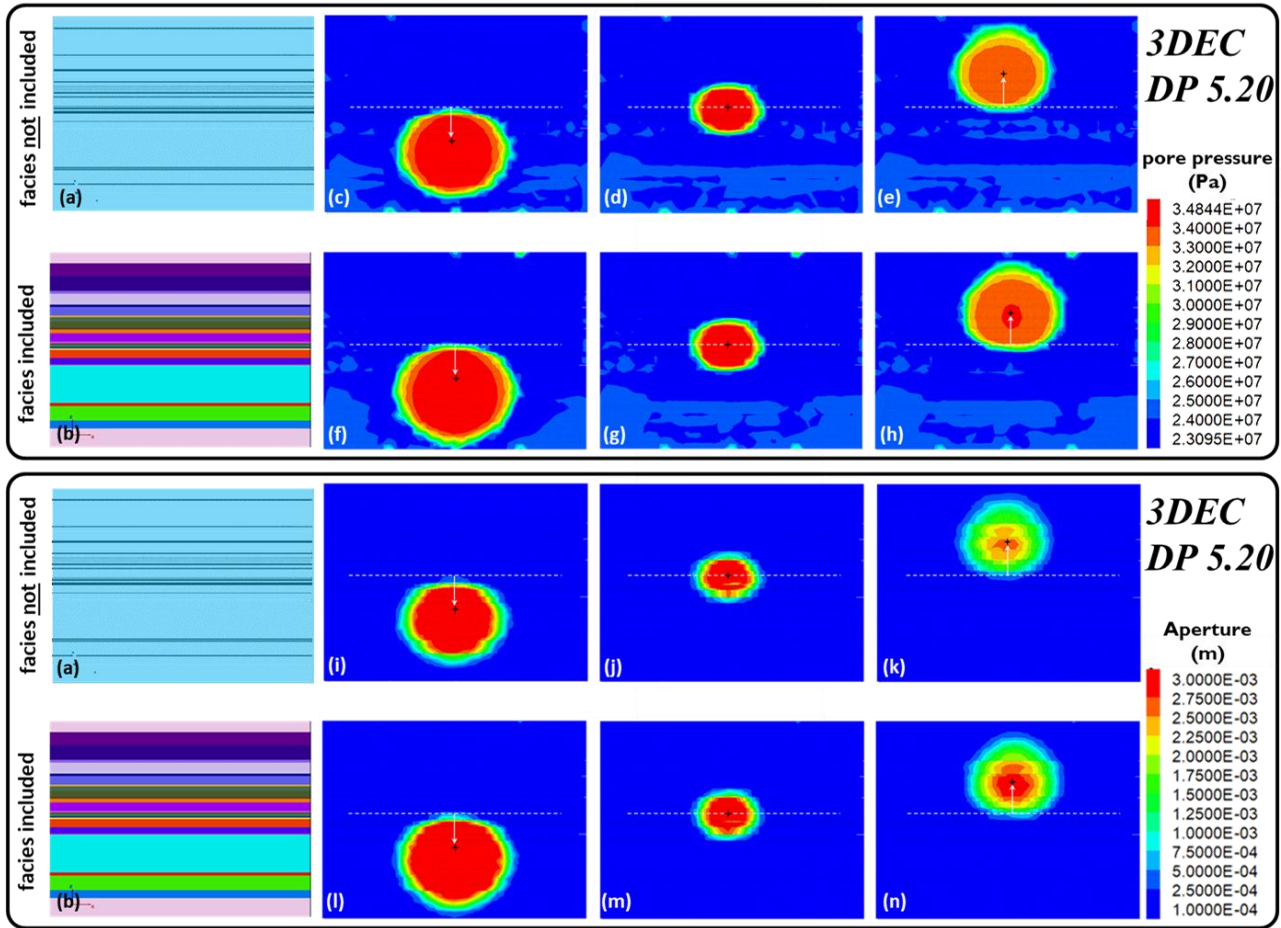
Fig. 3.18: Impact of vertical location of injection point on fracture geometry is more significant than geological facies. A vertical cross-section of pressure, along main hydraulic fracture plane, is shown when fluid injection occurs at (d) middle of formation as the base case, (c) 15 m below, (e) 15 m above while no facies included, and in (g) middle of formation, (f) 15 m below, (h) 15 m above while facies included. Also, a vertical cross-section of aperture, along main hydraulic fracture plane, is shown when fluid injection occurs at (j) middle of formation as the base case, (i) 15 m below, (k) 15 m above while no facies included, and in (m) middle of formation, (l) 15 m below, (n) 15 m above while facies included. All figures show model response after 24 minutes of injection at a rate of 0.4 m^3/second.

3.5 Discussion

3.5.1 Log-derived parameters

Dynamic Young's Modulus and BI$_{sonic}$ decrease toward the base of the Montney in all wells (Fig. 3.6 - 3.12). We suggest this decrease is related in part to an increase in clay content with depth in our study wells. Although clay minerals in the Montney (mostly MLIS) have similar density to quartz and feldspars, they also contain abundant microporosity, which in the Montney is filled with either fluids or organic matter (Wood, 2015; Vaisblat et al., 2017). This reduces the density of the rock, leading to lower P wave velocities and lower values of dynamic Young's Modulus.

The presence of different fluids in the rock can also retard sonic waves to different degrees. Zhang and Bentley (2005) demonstrated via modeling that Poisson's Ratio of water-saturated rocks is higher than that of dry (gas-saturated) samples. Wood (2013) reported higher water saturation in the Upper Montney and higher gas saturation in the Lower Montney. We propose that such fluid distribution contributes to the reduced compressional velocities in the Lower Montney, resulting in higher calculated dynamic Young's Modulus and BI$_{sonic}$.

Higher water saturation in the Upper Member can also reduce the stiffness of the rock, known as the water-weakening effect (Lai et al., 2015). Water-weakening will lead to a relative decrease in Young's Modulus and BI$_{sonic}$ (Lai et al., 2015; Nei et al., 2017; Han, 2018) and an increase in dynamic Poisson's Ratio (Castagna et al., 1985) in the upper part of the formation. A clear negative correlation between Young's Modulus and neutron porosity data in all wells (Fig. 3.19a) suggests that increase in porosity (saturated with water and/or hydrocarbons) or solid bitumen (Harris et al., 2019) in the Montney Formation acts to reduce Young's Modulus values.
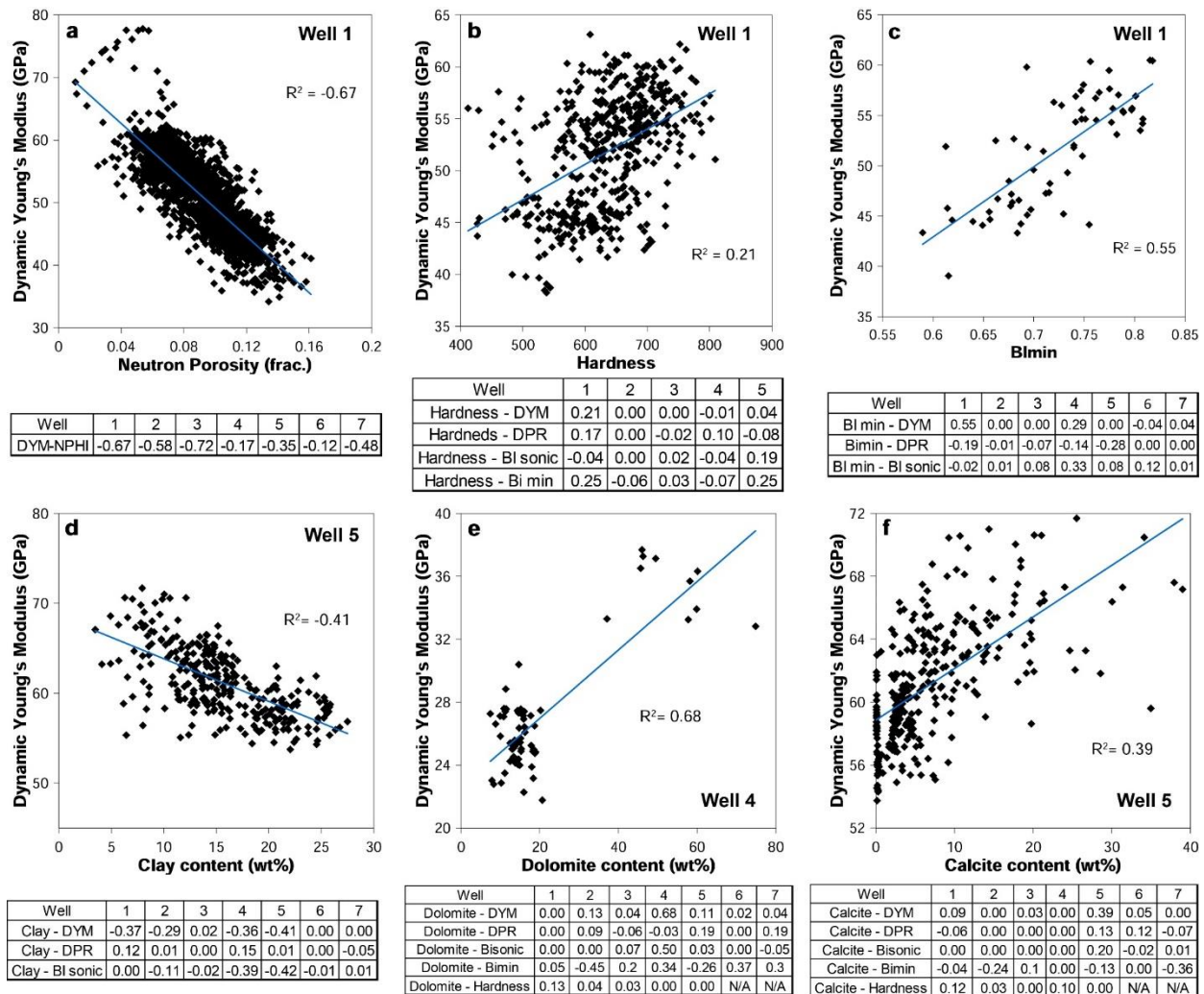
Fig. 3.19: Correlations in the dataset. Tables bellow the graphs show coefficient of determination values (R^2) for all wells. The (-) symbol identifies a negative trend. No symbol identifies a positive trend.
(a) Dynamic Young's Modulus Versus Neutron Porosity data from downhole log, well 1. (b) Dynamic Young's Modulus versus hardness measurements for well 1. Note moderate to low R^2 values for all variable pairs. (c) Dynamic Young's Modulus versus Bi_{min} for well 1. Note moderate to low R^2 values for all variable pairs. (d) Negative trend between dynamic Young's Modulus and clay content for well 1. Coefficient of determination (R^2) is 0.41. (e) Dynamic Young's Modulus Versus dolomite content for well 4. R^2 values is highly influenced by presence of heavily dolomitized facies at the top of the section. (f) Dynamic Young's Modulus Versus calcite content for well 5. Note that in most wells there is no correlation between dynamic moduli or brittleness coefficients and calcite.

Tables:

Well	1	2	3	4	5	6	7
DYM-NPHI	-0.67	-0.58	-0.72	-0.17	-0.35	-0.12	-0.48

Well	1	2	3	4	5
Hardness - DYM	0.21	0.00	0.00	-0.01	0.04
Hardneds - DPR	0.17	0.00	-0.02	0.10	-0.08
Hardness - BI sonic	-0.04	0.00	0.02	-0.04	0.19
Hardness - Bi min	0.25	-0.06	0.03	-0.07	0.25

Well	1	2	3	4	5	6	7
BI min - DYM	0.55	0.00	0.00	0.29	0.00	-0.04	0.04
Bimin - DPR	-0.19	-0.01	-0.07	-0.14	-0.28	0.00	0.00
BI min - BI sonic	-0.02	0.01	0.08	0.33	0.08	0.12	0.01

Well	1	2	3	4	5	6	7
Clay - DYM	-0.37	-0.29	0.02	-0.36	-0.41	0.00	0.00
Clay - DPR	0.12	0.01	0.00	0.15	0.01	0.00	-0.05
Clay - BI sonic	0.00	-0.11	-0.02	-0.39	-0.42	-0.01	0.01

Well	1	2	3	4	5	6	7
Dolomite - DYM	0.00	0.13	0.04	0.68	0.11	0.02	0.04
Dolomite - DPR	0.00	0.09	-0.06	-0.03	0.19	0.00	0.19
Dolomite - Bisonic	0.00	0.00	0.07	0.50	0.03	0.00	-0.05
Dolomite - Bimin	0.05	-0.45	0.2	0.34	-0.26	0.37	0.3
Dolomite - Hardness	0.13	0.04	0.03	0.00	0.00	N/A	N/A

Well	1	2	3	4	5	6	7
Calcite - DYM	0.09	0.00	0.03	0.00	0.39	0.05	0.00
Calcite - DPR	-0.06	0.00	0.00	0.00	0.13	0.12	-0.07
Calcite - Bisonic	0.00	0.00	0.00	0.00	0.20	-0.02	0.01
Calcite - Bimin	-0.04	-0.24	0.1	0.00	-0.13	0.00	-0.36
Calcite - Hardness	0.12	0.03	0.00	0.10	0.00	N/A	N/A

Bedding planes act as planes of weakness. Thus, the degree of lamination in a rock can significantly affect rock strength, (Dewhurst et al., 2011; Slatt and Abousleiman, 2011). The presence of multiple bedding planes also acts to slow sonic waves velocities (Lai et al., 2015 and reference therein; Ramos et al., 2019), reducing dynamic Young's Modulus. For well 1, the average bed thickness in the Upper Montney is 1.4 m, while the average bed thickness in the Lower Montney is 3.9 m (Fig. 3.6). In addition, the Upper Montney in this well contains 95 beds, while the Lower Montney contains only 33 beds (Fig. 3.6). Variation in beds thickness and number can explain why dynamic Young's Modulus values of well 1 are higher for the Upper Montney Member. In well 2, the distribution of bed thickness is similar between the Montney Members (0.6 m and 0.7 m for the Upper and Lower Members, respectively), but the number of beds in the lower Montney member is 60% fewer than that of the Upper member (Fig. 3.7), which can explain why dynamic Young's Modulus in well 2 are slightly higher in the Lower Montney Member.

The relationship between dynamic Young's Modulus and dynamic Poisson's Ratio in Montney wells is inconsistent (Fig. 3.16). Correlation between Young's Modulus and Poisson's Ratio in mudrocks has been reported to be either negative (Rickman et al., 2008; Dong et al., 2017; Labani and Rezaee,2015) or positive (Harris et al., 2011; Huo et al., 2018). Zhang and Bentley (2005) demonstrated that Poisson's Ratio increases with increasing water saturation and with the presence of fractures within the sample (as opposed to spherical pores, which have negligible influence on Poisson's Ratio). They suggested that positive correlation between Young's Modulus and Poisson's Ratio exists for dry (gas-saturated), intact rock, while a negative correlation develops when the rock is fractured and saturated with water because of the elevated Poisson's Ratio values.

Many faults penetrate the Montney (Fig. 3.1) and natural fractures occur throughout the Formation (Ouenes et al., 2014; Rogers and McLellan, 2014; Vishkai and Gates, 2018). Water saturation data (publicly available through the British Columbia Oil and Gas Commission) for

wells 1 and 2 point to a much higher water saturation through the entire Montney interval in well 2 (average water saturation of 12% and 34% for well 1 and 2 respectively, Fig. 3.16e). This indicates that water saturation is an important parameter controlling the stiffness of the Montney siltstone, and the relationship between dynamic Young's Modulus and dynamic Poisson's Ratio in the formation.

3.5.2 Core derived parameters (Hardness and BI_{min})

The application of hardness testers to geological materials was developed as a non-destructive, and cost and time-effective substitute for unconfined compressive stress (UCS) tests to estimate the strength of a rock (Verwaal and Mulder, 1993; Aoki and Matsukura, 2008). However, in recent years, studies suggested that hardness measurements should only be used as a qualitative strength index rather than a quantitative parameter for rock strength (Germay et al., 2018), particularly in clay-rich formations (Corkum et al., 2018).

In the study of unconventional reservoirs hardness measurements are often correlated to Young's Modulus and BI_{sonic} curves and used as a proxy for rock brittleness (Yang et al., 2015; Dong et al., 2017, 2017; Wang and Grammer, 2018; Moghadam et al., 2019). Hardness vertical profiles in our study wells appear to follow a similar trend as do the dynamic Young's Modulus and BI_{sonic} curves (Fig. 3.6 - 3.12). However, quantitative correlations between hardness and the dynamic elastic parameters are moderate at best (Fig. 3.19b).

Inconsistency between log-derived parameters and hardness measurements of core can be attributed to small-scale inaccuracies in the core-log depth shift or to changes in the hardness of core material resulting from handling and sampling over time. Inconsistencies can also arise from differences in sampling volume between well-logs and the hardness tester; whereas a log signal may average several beds, (depending on the logging tool resolution), the hardness tester samples a much smaller volume (<1mm), and is more sensitive to small-scale changes in the rock. Finally, it is worth noting that since the cores we examined are dry,

hardness measurements represent a property of the solid rock mass alone and does not account for fluids that can considerably affect log-derived (dynamic) elastic parameters.

Unlike hardness measurements that are conducted on a wide variety of rocks (e.g. Aoki and Matsukura, 2008; Coombes et al., 2013), composition-based brittleness index (BI_{min}) is primarily utilized for assessing the fraction of brittle minerals in mudrocks (Jin et al., 2015; Zhang et al., 2016; Dong et al., 2017). Good correlation is commonly observed between BI_{min} and dynamic Young's Modulus or BI_{sonic} (Dong et al., 2017; Moghadam et al., 2019).

In our study wells, no significant correlation was found between BI_{min} values and any of the log-derived parameters (with an exception of a positive correlation between BI_{min} and dynamic Young's Modulus for well 1) (Fig. 3.19c). Because BI_{min} is based on the mineralogical analysis of core samples, the lack of correlation between BI_{min} and log-derived parameters may be partially associated with locally imprecise core depth shift, sampling volume issues, or the absence of formation fluids as was described for the hardness measurements. Compositional data for wells 6 and 7 was obtained from cuttings samples. For these wells, the accurate depth of the samples is unknown, and it is possible that some mixing took place in the well bore during drilling, shifting rock fragments from their original position and further reducing the correlation between BI_{sonic} and log-derived parameters.

As for the lack of correlation between hardness measurements and BI_{min}, it is possible that the samples taken for mineralogical analysis are not representative of the rock interval from which they were retrieved. However, other composition-based brittleness indicators (Wang and Gale, 2009; Jin et al., 2014) did not yield better correlations with either the hardness measurements or the log-derived elastic parameters (appendix 3). We suggest that changes in mineralogical composition are not manifested in BI_{min} or hardness measurements because the total fraction of hard minerals (quartz, feldspars, and carbonates) and soft minerals (clays and micas) in the formation exhibits little variation. Although the proportions of any single mineral in any set of samples might vary significantly (samples may contain more dolomite

while others contain more quartz, for example; Fig. 3.13) the total fraction of hard and minerals changes over a very narrow range in each well (Fig. 3.6 - 3.12).

3.5.3 Compositional effect on geomechanical properties

3.5.3.1 Organic matter

To determine the effects of rock composition on geomechanical properties, we examine the relationships between Young's Modulus, Poisson's Ratio, BI_{sonic}, organic and inorganic components, and porosity in the Montney siltstone.

Organic carbon is a low-density material that lowers rock bulk density and transmits sonic waves through the rock at lower velocity than minerals (Ahmadovet al., 2009; Vernik and Milovac, 2011; Harris et al., 2019). Equations 1 and 2 indicate that a rock with higher TOC content should have lower dynamic Young's Modulus and potentially a higher dynamic Poisson's Ratio values. Labani and Rezaee (2015) report a significant negative correlation between TOC and Young's Modulus and a significant positive correlation between TOC and Poisson's Ratio (R^2 of 0.55 and 0.54, respectively) for rocks with TOC content of 0-12 wt%. However, these relationships become less significant (R^2 <0.28) or are absent altogether when the maximum TOC content in the shale is below 8 wt. % (Aoudia et al., 2010; Perez Altamar and Marfurt, 2014; Labani and Rezaee, 2015; Dong et al., 2017).

In the 7 Montney wells studied here, TOC had a negative relationship with dynamic Young's Modulus and BI_{sonic}, and an inconsistent relationship with dynamic Poisson's Ratio. In all cases the correlation was extremely weak (R^2<0.17), implying that the organic matter in the Montney does not contribute significantly to elastic behavior of the formation in response to stress. Organic matter in the Montney Formation is primarily in the form of bitumen and pyrobitumen (Chalmers and Bustin, 2012; Akai and Wood, 2014; Sanei et al., 2015; Wood et al., 2015; Wood et al., 2018; this study, chapter 2). Flow structures identified in the organic phase (Wood et al., 2015) suggest that liquid hydrocarbons were introduced into the

formation following consolidation. These observations strengthen our conclusion that the organic matter in the Montney carries no structural load.

No primary organic matter (kerogen) was identified in any of our samples, but other studies have proposed that at least some of the organic carbon in the Montney is of primary origin, particularly in deeply buried sections of the Montney (Ness, 2001; Ibrahimbas and Riediger, 2004; Ejezie, 2007; Chalmers and Bustin, 2012; Feng et al., 2016; Chatellier et al., 2018; Feng, personal communication). Under these circumstances, some of the organic matter (kerogen) was deposited as part of the rock fabric and should be load-bearing.

In the distal Montney wells (wells 1, and 2), the absence of a clear relationship between TOC and the elastic parameters is attributed to the high thermal maturity of the organic matter. At low thermal maturity, kerogen is a relatively soft component, with Young Modulus <10 GPa (Zargari et al., 2013; Eliyahu et al., 2015; Emmanuel et al., 2016). With increasing thermal maturation rock stiffness increases, in part because the amount of total organic matter in the rock decreases (Prasad et al., 2011; Zargari et al., 2013), but also because the residual kerogen itself becomes stiffer, and can reach 15-30 GPa (Kumar, et al., 2012; Emmanuel et al., 2016).

In addition to stiffer kerogen, pyrobitumen is also present in high maturity Montney wells (Wood et al., 2015; Wood et al., 2018). Young's Modulus values of pyrobitumen are similar to those of mature kerogen and can reach up to 19 GPa (Eliyahu et al., 2015; Emmanuel et al., 2016). The high Young's Modulus values of pyrobitumen and mature kerogen makes it difficult to distinguish the influence of the organic matter on the rock from that of micas and clay minerals, which have similar Young's Modulus values (Wang et al., 1998; Prasad et al., 2002; Prasad et al., 2005; Mondol et al., 2008; Wei, 2009).

3.5.3.2 Clay minerals

Clay minerals consist mostly of illite and low-expandability mixed layer illite smectite (MLIS) and smaller amount of kaolinite (Table 3.5). Clays are ductile minerals that have a

negative affect on rock brittleness (Rickman et al., 2008; Aoudia et al., 2010; Herwanger et al., 2015; Dong et al., 2015; Katz et al., 2016; Yu et al., 2016; Wand and Grammer, 2018; Moghadam et al., 2019). For most of our study wells, clay content has a negative correlation with dynamic Young's Modulus (Fig. 3.19d). However, for three wells in the study (5, 6, and 7) clay content do not correlate with Young's Modulus at all. The absence of correlation in wells 6 and 7 (Fig. 3.19d) may originate from inaccurate depth of the cutting samples and errors associated with Vs prediction. Clay content in well 3 is atypically low for the Montney (1 to 15 wt%, with a median of 5 wt%) possibly because the core retrieved from this well is missing the Lower section of the formation, which is usually more clay rich. The anomalous clay concentration may explain why Young's Modulus do not correlate with clays in well 3.

Both detrital and authigenic clay minerals are present in the Montney Formation. Detrital clays appear as grain coats (inherited clays; Wilson, 1992), and clay clumps (Vaisblat et al., 2017; this study, chapter 2). These clays are part of the grain framework and are responsible for the negative correlation between clay content and Young's Modulus. Authigenic clays are pore-filling or pore-lining (Davies et al., 1997; Nassichuk, 2000; Barber, 2002; Vaisblat et al., 2017, this study, chapter 2) and do not carry structural load. In addition, much of the clay is found together with pore-filling organic matter (Lan et al., 2015; Wood et al., 2015; Vaisblat et al., 2017, this study, chapter 2) (Fig. 3.14a, b), and it is not clear whether this clay fraction is detrital or authigenic. Regardless of its origin, the clay associated with organic matter will have negligible influence on the structural strength of the siltstone. The spatial distribution of clay minerals within the rock explains the low correlation between elastic moduli and clay content in the Montney Formation.

3.5.3.3 Quartz

Quartz is one of the major brittle minerals in the Montney Formation (Table 3.5). Aoudia et al. (2010) found that in the Woodford Shale, quartz content had a slight negative relationship with Poisson's Ratio and was unrelated to Young's Modulus. Wang and Grammer

(2018) reported a positive correlation between quartz content and hardness measurements. Dong et al. (2018) observed a negative relationship between detrital quartz and rock hardness in the Duvernay Formation, and suggested this negative trend is related to an association of detrital quartz with clay minerals. In our study wells, no correlation between quartz content and geomechanical properties was identified.

Dong et al. (2015, 2018) reported that quartz cement led to an increase in rock hardness in the Horn River and Duvernay Formations. Quartz cement in the Duvernay (Dong et al., 2018) as in other black shales like the Bakken Formation (Fishman et al., 2015), the Mowry Formation (Milliken and Olson, 2017) and the Woodford Formation (Harris et al., 2013) is mostly derived from recrystallization of biogenic silica. Biogenic silica goes through a temperature dependent transformation from opal-A to opal CT to quartz (Keller and Isaacs, 1985; Bohrmann et al., 1994). This recrystallization forms a rigid framework in an otherwise soft matrix (Slatt and Rodriguez, 2012), strengthens the rock and increases its brittleness.

Quartz cement is pervasive in the Montney Formation (Davies et al., 1997; Vaisblat et al., 2017, this study, chapter 2), and it is probable that some of the quartz cement is of biogenic origin (Wüst et al., 2018; Zelazny et al., 2018, this study, chapter 2), although other sources have also been proposed (this study, chapter 2). However, it is difficult to isolate the influence of quartz cement on geomechanical properties of the Montney siltstone, in part because quartz cement is not restricted to a single interval or lithofacies and in part because it is difficult to destinguish the influence of quartz cement from the influence of other cements (carbonates and feldspars) on the geomechanical properties of the siltstone.

3.5.3.4 Other minerals

Carbonate minerals present in the Montney Formation include calcite, dolomite, and Fe-rich dolomite. In well 4, where a dolomitic interval exists at the top of the well, a good positive correlation was found between dolomite and dynamic Young's Modulus (Fig. 3.19e; R^2=0.68). Dynamic Young's Modulus also has a weak, positive correlation with calcite concentration in

well 5 (Fig. 3.19f; R^2=0.39). In other wells, neither of the carbonate minerals correlates with any of the mechanical properties of the siltstone. Similarly, Dong et al. (2017) and Moghadam et al. (2019) found no correlation between brittleness coefficients and carbonate mineral concentrations in their studies of the Horn River Formation.

Potassium feldspar content shows a negative correlation with dynamic Young's Modulus in well 4 (R^2=0.55) but did not correlate with any elastic parameter in the other wells. Other minerals (Na-feldspar, micas, pyrite and apatite) also did not correlate with geomechanical properties. Aoudia et al. (2010) and Labani and Rezaee (2015) concluded that no single mineralogical phase can be individually considered as a strong control on Young's Modulus or Poisson's Ratio in the Woodford and the Perth Basin shale Formations, respectively. With the exception of clay minerals, this conclusion holds true for the Montney Formation as well.

3.5.4 Lithofacies and geomechanical properties

Studies of several mudstones demonstrated that different lithofacies can exhibit distinct mechanical behavior (Dong et al., 2017; Moghadam et al., 2019). Lithofacies are manifestations of the energy level of the medium in which sediments were deposited, and may have significantly different mineralogical composition, grain size distributions, and bioturbation fabrics. Those physical and compositional differences between lithofacies can lead to unique geomechanical behaviors in various sections of the same formation.

In the Montney Formation, however, there is no clear geomechanical distinction between different lithofacies. Calculated dynamic Young's Modulus and dynamic Poisson's Ratio for all lithofacies in wells 1 to 4 are presented in Fig. 3.20a. Two important observations can be made: (1) with one exception in well 4, it is impossible to distinguish lithofacies from each other based on their Young's Modulus and Poisson's Ratio values; and (2) the same lithofacies may exhibit a very different range of Young's Modulus and Poisson's Ratio values in different wells. Variations in dynamic Young's Modulus and dynamic Poisson's Ratio are more a function of well location in the basin than the lithofacies present in the rock. This is further emphasized

by the hydraulic fracturing simulations, in which a detailed lithofacies description in the simulation run had no effect on the results of a hydraulic fracturing treatment (Fig. 3.17, 3.18).

Similar geomechanical behavior of different lithofacies in the same well can be explained by comparing the mineralogical composition and grain size distribution of those lithofacies. Fig. 3.20b shows that little variation in detrital quartz grain size exists between lithofacies in our samples. Different lithofacies in the Montney Formation also have similar mineralogical composition (Fig. 3.13). Similarities in mineralogical and rock fabric between the lithofacies suggest that depositional environment in the Montney exerted little control over grain size distribution and mineralogical composition of most lithofacies and thus do not strongly influence the geomechanical properties of the rock. We attribute the weak influence of depositional environments on the sediment to the size and compositional homogeneity of detrital material that entered the basin (Davies et al., 1997; this work, chapter 2). A pervasive, shallow burial diagenetic overprint further homogenized the rock, and eliminated residual compositional (and thus geomechanical) differences in between lithofacies (this work, chapter 2).

Similar results of the hydraulic fracturing simulations with and without detailed lithofacies consideration shows that fracturing pressure propagation and stimulated aperture evolution for both simulations are not controlled by lithology. The results further show that the vertical location of the injection point has a stronger impact on fracture geometry and pressure magnitude than inclusion of detailed lithological description (Fig. 3.18). This demonstrates that the combined effects of in-situ stress and pressure gradients affect the stimulated reservoir volume of the Montney siltstone much more than lithological variation does.
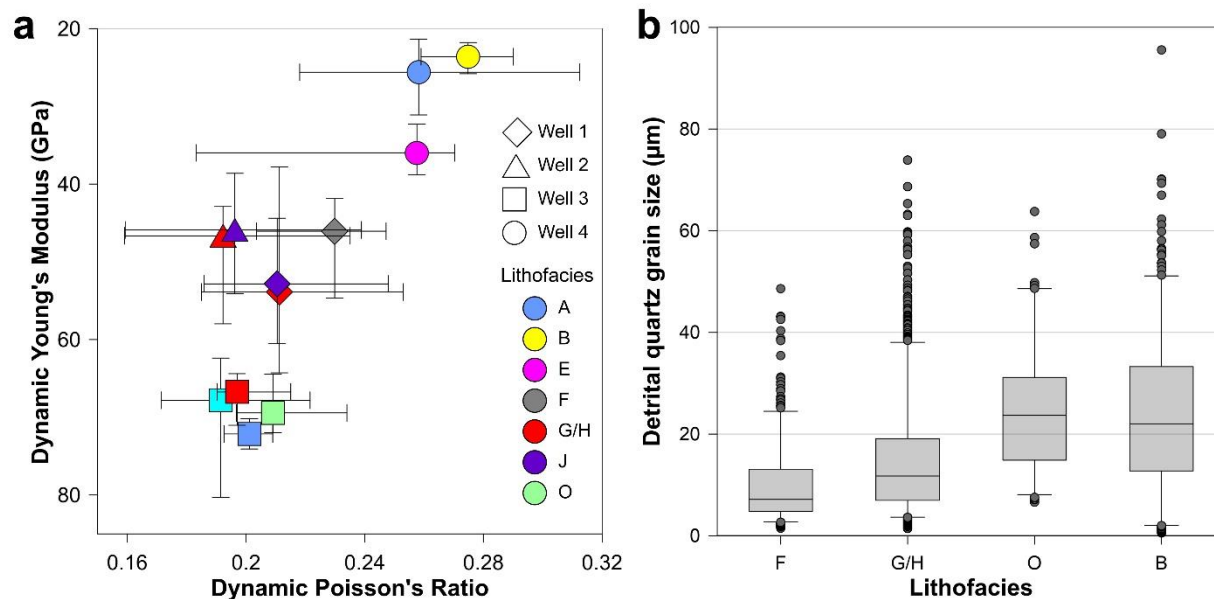
Fig. 3.20: Lithofacies-dependent properties (a) Median value and range of calculated dynamic Young's Modulus and dynamic Poisson's Ratio for all major facies in wells 1-4. Note that with one exceptions in well 4, it is impossible to distinguish one lithofacies from another based on their Young's Modulus and Poisson's ratio values, and that the same lithofacies may exhibit a very different range of Young's Modulus and Poisson's ratio values in different wells (for example lithofacies H in wells 1-3). (b) detrital quartz grain size range for five lithofacies in the study area. Range of values is 5-95 percentile. Outliers (dots) are upper and lower 5%. Although there are little variation in grain size total range, two grain size groups are notable (1) facies F, G, and H with a slightly smaller median grain size, and (2), facies O and B with a slightly larger median grain size.

Is the Montney siltstone a mudstone equivalent?

The Montney Formation is sometimes referred to as a mudstone (shale) (Chalmers and Bustin 2012; Davey, 2012; Feiyu et al., 2013; Nieto et al., 2013; Ouenes et al., 2014), although the predominant grain size in the formation is generally silt (Barber, 2002; Krause et al., 2012; Vaisblat et al., 2017; this work, chapter 2), and all lithofacies investigated in this study are silt-rich or silt-dominated (Table 3.4). However, the majority of hydrocarbon production from the Montney Formation is conducted through multi-stage hydraulic fracturing in horizontal wells, as in shale (mudrock) plays. To test whether the geomchanical behavior

139

of the Montney Formation is similar to a shale, we compare the geomechanical properties of the Montney Formation to other shale reservoirs for which similar information was available.

In Fig. 3.21a we compare the average mineralogical composition of the seven Montney wells with the average mineralogical composition of the Eagle Ford shale (Hernandez-Uribe et al., 2017; Gupta et al., 2018), the Horn River shale (Dong et al., 2017), and the Kockatea and Carynginia shales from the Perth Basin in Australia (Labani and Rezaee, 2015). The formations were selected to represent (1) a shale with mineralogical composition similar to the Montney Formation (Horn River shale), (2) a shale with higher carbonate minerals content than the Montney (Eagle Ford), and (3) a shale with higher clay mineral content than the Montney Formation (Perth Basin shales). Next, we examined how dynamic Young's Modulus values and dynamic Poisson's Ratio values compare between the study wells and the three shale formations (Fig. 3.21b). It is evident that although some overlap exists, the three shale formations exhibit lower dynamic Young's Modulus than most Montney wells, and a larger range in dynamic Poisson's Ratio values. Compositional effect of the geomechanical properties of the rock have been studied in all formations. A comparison between all formations is summarized in Table 3. 6, and discussed below.

In the Montney Formation, clay mineral content was found to be the most significant factor affecting the dynamic moduli of the rock (increasing Young's Modulus and Decreasing Poisson's Ratio).
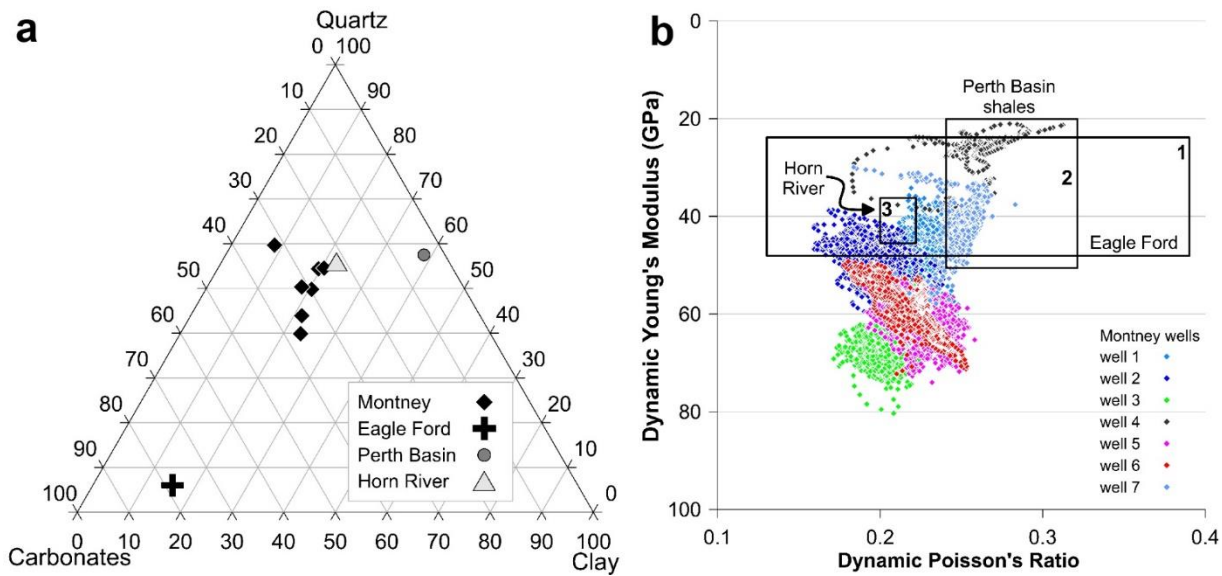
Fig. 3.21: (a) Average mineralogical composition for the Montney Formation (this study), the Eagle Ford Formation (Hernandez-Uribe et al., 2017; Gupta et al., 2018), The Horn River Formation (Dong et al., 2017), and Shales from the Perth Basin (Labani and Rezaee, 2015). (b) Dynamic Poisson's Ratio and dynamic Young's Modulus for the seven Montney wells. Frames are ranges of dynamic Poisson's Ratio and dynamic Young's Modulus for the (1) Eagle Ford Formation (Alqahtani et al., 2013; Mokhtari et al., 2016; Hernandez-Uribe et al., 2017), (2) Perth Basin shales (Labani and Rezaee, 2015), and (3) the Horn River Formation (Dong et al., 2017).

Similar conclusions were derived for the Horn River shale (Dong et al., 2017), the Perth basin shales (Labani and Rezaee, 2015) and the Eagle Ford Formation (Alqahtani et al., 2013; Tinnin et al., 2015). This may explain why wells 1 and 2 of the Montney, which have the highest clay content of all the study wells (Table 3.5), partly overlap with the dynamic Young's Modulus and dynamic Poisson's Ratio values of the shale formations.

Quartz content was not found to be significant in determining the elastic moduli in our study well. Similarly, quartz content does not play an important role in determining the geomechanical properties of the Eagle Ford (Hernandez-Uribe et al., 2017). Detrital quartz content also did not correlate with rock brittleness in the Horn River Formation, although biogenic quartz did increase hardness measurements of the shale (Dong et al., 2017). Only for the Perth Basin shales was a positive correlation observed

Table 3.6: Relationship between Young's Modulus and Poisson's ration, and rock components for the Montney Formation, the Horn River shale, the Eagle ford shale and Perth Basin shales shale Formations.

Red color indicates a negative trend, green color indicates a positive trend, and white indicates no trend. Note that the only variable that consistently affect Young's Modulus and Poisson's Ratio in all formation is clay minerals content.

Variables / Formation	YM Clay	PR Clay	YM Quartz	PR Quartz	YM Carb[a]	PR Carb	YM TOC	PR TOC	YM Matur.[f]
Montney	(red)	(green)			2/7 wells[c] (green)				
Horn River	(red)	(green)	Biogenic[b] / Detrital[a] (green)						N/A[g]
Eagle Ford	(red)	(green)			Dolomite[d] (green)	Calcite (green)	(red)		?[h] (green)
Perth Basin	(red)	(green)		(green)			TOC >8[e] (red) / TOC <8[e]	TOC >8[e] (green) / TOC <8[e]	?[h] (green)

[a] Carbonate minerals.
[b] Correlation between biogenic/ detrital quartz content and hardness measurements. Hardness is well correlated with Young's Modulus (dong et al, 2017).
[c] One montney well showed positive correlation between Young's Modulus and dolomite content, and another well showed positive correlation between Young's Modulus and calcite content.
[d] Correlation between Brittleness and dolomite content.
[e] TOC in wt%.
[e] Organic matter maturity.
[f] Organic matter maturity does not change in the horn River Formation.
[g] qualitative correlation; never quantified.

between quartz content and the dynamic Young's Modulus and a negative correlation between quartz content and the dynamic Poisson's Ratio (Labani and Rezaee, 2015).

The presence of carbonate minerals affects the elastic properties of the Montney siltstone only locally. No correlation was identified between brittleness coefficients and carbonate minerals concentrations in the Horn River shale (Dong et al., 2017); in the Eagle Ford shale, the presence of dolomite is shown to increases brittleness (Hernandez-Uribe et al., 2017), and the presence of calcite is positively correlated with Poisson's Ratio (Breyer et al., 2013).

The effect of carbonate minerals on the geomechanical properties of the Perth Basin shales was not examined.

Total organic carbon in Montney is commonly < 4 wt. %. Other shales have similar (Horn River) or much higher (Eagle Ford, Perth Basin shale) average TOC concentration. No significant correlation was found between organic matter content and the geomechanical properties in the Montney and the Horn River shale (Dong et al., 2017). However, organic matter was found to have a positive correlation with Poisson's Ratio and a negative correlation with Young's Modulus for the Perth Basin Shale (Labani and Rezaee, 2015), and the Eagle Ford Formation (Alqahtani et al., 2013; Hernandez-Uribe et al., 2017; Gupta et al., 2018).

Increasing maturity of the organic matter seems to somewhat increase Young's Modulus for the Perth Basin shales (Labani and Rezaee, 2015) and the Eagle Ford shale (Alqahtani et al., 2013), but the trends were never quantified. This is potentially because the organic matter in the Perth Basin shales and the Eagle Ford Formation are both of primary origin (kerogen) that was deposited as part of the rock matrix (Cooper et al., 2015; Chalmers and Bustin, 2017). In the Woodford Formation of the Permian Basin, Texas, Young's Modulus increases by approximately 300% from the early oil to the wet gas window (Harris et al., 2019). For the Montney Formation, no trend was identified that relates thermal maturity to any geomechanical properties, probably because the organic matter is of secondary origin and is not load bearing. The maturity of the organic matter in the Horn River shale is high (dry gas window) across the basin and therefore cannot be used for comparison to elastic moduli (Dong et al., 2017).

From this comparison, the only consistent relationship between the Montney and the other three shale formations is the negative effect of clay minerals on rock brittleness, related to increasing Poisson's Ratio and decreasing Young's Modulus. All other rock components, including minerals and organic matter, have either no effect at all or inconsistent influences on the geomechanical properties of some or all formations.

The fundamental difference between many mudrocks formations (shale) and the Montney siltstone lies in the fabric of the rock. Mudrocks are for the most part soft and ductile rocks because they are matrix-supported, with silt grains 'floating' within a clay-rich matrix (Fig. 3.22a). Where pervasive quartz cement, commonly from biogenic origin, is present in the mudrock (Fig. 3.22b) it creates a rigid framework that supports the soft matrix, and the cemented interval becomes more brittle. Unlike mudrocks, the Montney siltstone has a hard, grain and cement-supported framework (Fig. 3.22b) which makes it more brittle than other
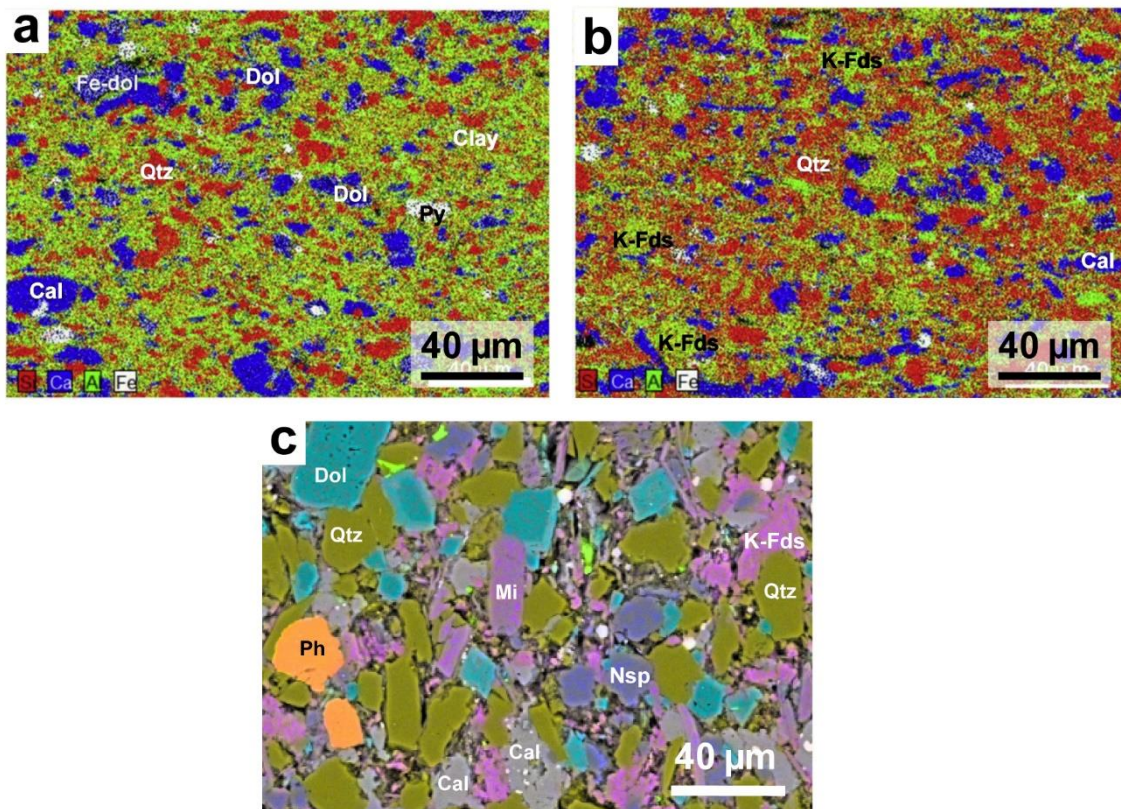
Fig. 3.22: Rock fabric differences between mudrocks (shales) and the Montney siltstone. (a) example for a clay rich (green) matrix-supported mudrock. Horn River shale (image from Dong et al., 2017). (b) biogenic quartz cement (red) creates a rigid framework in otherwise soft and ductile matrix (image from Dong et al., 2017). (c) hard, grain and cement-supported framework of the Montney Formation siltstone. Because of the grain and cement supported matrix the siltstone is more brittle than the Horn River Shale, although both formations have comparable mineralogy.

mudrocks with comparable mineralogy like the Horn River Formation. Rock fabric rather than mineralogy is the main control over rock brittleness.

3.6 Conclusions

In this study we examine spatial and vertical variations of the geomechanical properties of the Montney Formation, and their correlation to mineralogy, lithology, and rock fabric. We demonstrated that:

(1) Hardness measurements are a poor proxy for rock brittleness in the Montney Formation, in contrast to observations of several shale formations. We suggest that this is because the siltstone framework of the Montney is generally grain-supported, in contrast to the fabric of shale formations that are more typically matrix-supported by either clay minerals or organic matter.

(2) Clay content is the most significant parameter affecting the mechanical properties of the Montney Formation, an observation consistent with several other fine-grained reservoirs. An increase in clay content leads to an increase in dynamic Poisson's Ratio and a decrease in dynamic Young's Modulus values in all the formations examined in this study.

(3) In many fine-grained formations, differences between depositional lithofacies in geomechanical properties are generally associated with differences in rock fabric: composition, grain size and sorting. In the Montney Formation, where detrital sediment entering the basin was homogeneous and the rock fabrics of different lithofacies are indistinguishable, lithofacies show no significant or systematic differences in geomechanical properties. Geomechanical contrasts, in-situ stress, and pressure gradients are the major controlling factors on the propagation of hydraulic fractures in the Montney siltstone.

(4) The fundamental difference between mudrocks (shale) and the siltstone is the fabric of the rock. Whereas mudrocks clay-rich, matrix-supported rocks, siltstone has a hard,

grain-and cement-supported framework. Rock fabric rather than mineralogy is the main control over rock brittleness.

(5) Water saturation and the number of bedding planes are positively correlated with a decrease in rock brittleness in the Montney Formation.

Acknowledgments

3.7 Reference

Ahmadov, R., Vanorio, T., and Mavko, G., 2009. Confocal laser scanning and atomic-force microscopy in estimation of elastic properties of the organic-rich Bazhenov Formation. Leading Edge, 28(1), 18-23. https://doi.org/10.1190/1.3064141.

Akai, T., and Wood, J.M., 2014, Petrophysical analysis of a tight siltstone reservoir: Montney Formation, Western Canada. the 20th Formation Evaluation Symposium of Japan, P. 1-4.

Al-Awadi, M., Clark, W.J., Moore, W.R., Herron, M., Zhang, T., Zhao, W. Hurley, N. Kho, D. Montaron, B., and Sadooni, F., 2009. Dolomite: Perspectives on a Perplexing Mineral. Oilfield Review 21(3): 3-45.

Alqahtani, A.A., Mokhtari, M., Tutuncu, A.N., and Sonnenberg, S., 2013. Effect of mineralogy and petrophysical characteristics on acoustic and mechanical properties of organic rich shale. In Unconventional Resources Technology Conference (pp. 399-411). Society of Exploration Geophysicists, American Association of Petroleum Geologists, Society of Petroleum Engineers. https://doi.org/10.1190/urtec2013-045.

Aoki, H. and Matsukura, Y., 2008. Estimating the unconfined compressive strength of intact rocks from Equotip hardness. Bulletin of Engineering Geology and the Environment, 67(1), 23-29. https://doi.org/10.1007/s10064-007-0116-z.

Aoudia, K., Miskimins, J.L., Harris, N.B., and Minch, C.A., 2010. Statistical analysis of the effects of mineralogy on rock mechanical properties of the Woodford Shale and the associated impacts for hydraulic fracture treatment design. 44th US Rock Mechanics

Symposium and 5th U.S.-Canada Rock Mechanics Symposium. Salt Lake City, Utah, U.S.A., 27-30 June. ARMA 10-303.

Barber, L.M., 2002. Sedimentology, Diagenesis and reservoir characterization of the Montney Formation at Sturgeon Lake South 'F' Pool West-Central Alberta, M.Sc. thesis, Department of geology and geophysics, University of Calgary, Calgary, Alberta, Canada.

BC oil and gas commission, 2012. Montney Formation play atlas for NEBC.

Beranek, L.P., Mortensen, J.K., Orchard, M.J., and Ullrich, T., 2010. Provenance of North American Triassic strata from west-central and southeastern Yukon: correlations with coeval strata in the Western Canada Sedimentary Basin and Canadian Arctic Islands. Canadian Journal of Earth Sciences 47, 53-73. https://doi.org/10.1139/E09-065.

Blakey, R.C., 2014. Mesozoic paleogeography and tectonic history - western North America: Triassic tectonics and paleogeography, 245 Ma. http://deeptimemaps.com/north-american-key-time-slices-series. Last accessed july 20, 2019.

Bohrmann, G., Abelmann, A., Gersonde, R., Hubberten, H., and Kuhn, G., 1994. Pure siliceous ooze, a diagenetic environment for early chert formation. Geology, 22(3), 207-210. https://doi.org/10.1130/0091-7613(1994)022<0207:PSOADE>2.3.CO;2.

Breyer, J.A., Denne, R., Kosanke, T., Spaw, J.M., Funk, J.E., Christianson, P., Bush, D.A. and Nelson, R., 2013. Facies, Fractures, Pressure and Production in the Eagle Ford Shale (Cretaceous) between the Maverick Basin and the San Marcos Arch, Texas, USA. Unconventional Resources Technology Conference, Denver, Colorado, U.S.A., 12-14 August https://doi.org/10.1190/urtec2013-159.

Castagna, J.P., Batzle, M.L., and Eastwood, R.L., 1985. Relationships between compressional-wave and shear-wave velocities in clastic silicate rocks. Geophysics, 50(4), 571-581. https://doi.org/10.1190/1.1441933.

Chalmers, G.R., and Bustin, M.R., 2017. A multidisciplinary approach in determining the maceral (kerogen type) and mineralogical composition of Upper Cretaceous Eagle Ford Formation: Impact on pore development and pore size distribution. International Journal of Coal Geology, 171, 93-110.

Chalmers, G.R., and Bustin, M.R., 2012. Geological evaluation of Halfway–Doig–Montney hybrid gas shale–tight gas reservoir, northeastern British Columbia. Journal of Marine and Petroleum Geology, 38(1), 53-72.

Chatellier, J.Y., Simpson,K., Perez, R., and Tribobillard, N., 2018. Geochemically focused integrated approach to reveal reservoir characteristics linked to better Montney productivity potential. Bulletin of Canadian Petroleum Geology, 66(2), 516-551.

Coney, P.J., Jones, D.L., and Monger, J.W.H., 1980. Cordilleran suspect terranes. Nature,

288(5789), 329-333. https://doi.org/10.1038/288329a0.

Coombes, M.A., Feal-Pérez, A., Naylor, L.A., and Wilhwlm, K. .,2013. A non-destructive tool for detecting changes in the hardness of engineering materials: Application of the Equotip durometer in the coastal zone. Engineering Geology, 167, 14-19. https://doi.org/10.1016/j.enggeo.2013.10.003.

Cooper, G., Xiang, R., Agnew, N., Ward, P., Fabian, M., and Tupper, N., 2015. A systematic approach to unconventional play analysis: the oil and gas potential of the Kockatea Shale and Carynginia Formation, north Perth Basin, Western Australia. The Australian Petroleum Production and Exploration Association Journal, 55(1), 193-214.

Corkum, A.G., Asiri, Y., El Naggar, H., and Kinakin, D., 2018. The Leeb Hardness Test for Rock: An Updated Methodology and UCS Correlation. Rock Mechanics and Rock Engineering. 51 (3), 665-675. https://doi.org/10.1007/s00603-017-1372-2.

Crombez, V., 2016 P´etrofaci`es, s´edimentologie et architecture stratigraphique des roches riches en mati`ere organique: ´etude multi-approches des formations Montney et Doig (Trias inferieur et moyen, Alberta - Colombie Britannique, Canada). PhD. Thesis, Sciences de la Terre. Universit´e Pierre et Marie Curie, Paris, France.

Crombez, V., Baudin, F., Rohais, S., Riquier, L., Euzen, T., Pauthier, S., Ducros, M., Caron, B. and Vaisblat, N., 2017. Basin scale distribution of organic matter in marine fine-grained sedimentary rocks: Insight from sequence stratigraphy and multi-proxies analysis in the Montney and Doig Formations. Marine and Petroleum Geology, 83: 382-401.

Crombez, V., Rohais, S., Baudin, F., and Euzen, T., 2016. Facies, well-log patterns, geometries and sequence stratigraphy of a wave-dominated margin: insight from the Montney Formation (Alberta, British Columbia, Canada). Bulletin of Canadian Petroleum Geology, 64(4), 516-537.

Cundall, P.A., and Hart, R.D., 1992. Numerical modelling of discontinua. Engineering computations, 9 (2), 101-113.

Davey, H., 2012. Geomechanical characterization of the Montney shale, northwest Alberta and northeast British Columbia, Canada. M.Sc. Thesis, Department of Geology and Geological Engineering, Colorado School of Mines, Golden, Colorado, USA.

Davies, G.R., 1997. Aeolian sedimentation and bypass, Triassic of western Canada, Bulletin of Canadian Petroleum Geology 45(4), 624–642.

Davies, G.R., Watson, N., Moslow, T.F., and Maceachern, J.A., 2018. Regional subdivisions, sequences, correlations and facies relationships of the Lower Triassic Montney Formation, west-central Alberta to northeastern British Columbia, Canada - With emphasis on role of paleostructure. Bulletin of Canadian petroleum geology, 66(1), 23-92.

Davies, G.R., and Hume, D., 2016. Lowstand/Slope-onlap wedges in the Montney: Stratigraphic and sequence framework, reservoir significance. GeoConvention 2016, Abstract, 4.

Davies, G.R., Moslow, T.F., and Sherwin, M.D., 1997. The Lower Triassic Montney Formation, west-central Alberta. Bulletin of Canadian Petroleum Geology, 45(4), 474-505.

Derder, O.M., 2012. Characterizing Reservoir Properties for the Lower Triassic Montney Formation (Units C and D) Based on Petrophysical Methods. M.Sc. Thesis, Department of Geosciense, University of Calgary, Calgary, Alberta, Canada.

Dewhurst, D.N., A.F. Siggins, J. Sarout, M.D. Raven, and H.M. Nordgård-Bolås, 2011, Geomechanical and ultrasonic characterization of a Norwegian Sea shale: Geophysics, 76 (3), WA101-WA111. https://doi.org/10.1190/1.3569599.

Dong, T., Harris, N.B., Knapp, L.J., McMillan, J.M., and Bish, D.L., 2018. The effect of thermal maturity on geomechanical properties in shale reservoirs: An example from the Upper Devonian Duvernay Formation, Western Canada Sedimentary Basin. Marine and Petroleum Geology, 97, 137-153.

Dong, T., Harris, N.B., Ayranci, K., Twemlow, C.E., and Nassichuk, B., 2017. The impact of rock composition on geomechanical properties of a shale formation: Middle and Upper Devonian Horn River Group shale, Northeast British Columbia, Canada. American Association of Petroleum Geologists Bulletin, 101(2), 177-204. https://doi.org/10.1306/07251615199.

Dong, T., Harris, N.B., Ayranci, K., Twemlow, C.E., and Nassichuk, B.R., 2015. Porosity characteristics of the Devonian Horn River shale, Canada: Insights from lithofacies classification and shale composition. International Journal of Coal Geology, 141, 74-90.

Ducros, M., Sassi, W., Vially, R., Euzen, T., and Crombez, V., 2017. 2-D Basin modeling of the Western Canada Sedimentary Basin across the Montney-Doig System: Implications for hydrocarbon migration pathways and unconventional resources potential, in: AbuAli, M.A., Moretti, I., and Bolås, H.M.N. (Eds.), Petroleum Systems Analysis-Case Studies: American Association of Petroleum Geologists Bulletin Memoir, 114. pp. 117-134. https://doi.org/10.1306/13602027M1143703.

Ducros, M., Euzen, T., Vially, R., and Sassi, W., 2014. 2-D basin modeling of the WCSB across the Montney-Doig system: implications for hydrocarbon migration pathways and unconventional resources potential, in: Geoconvention, Calgary, AB, Canada, 13-17 May.

Edwards, D.E., Barclay, J.E., Gibson, D.W., Kvill, G.E., and Halton, E., 1994. Triassic strata of the Western Canada Sedimentary Basin, in: Mossop, G.D., and Shetsen, I. (Eds.), Geological Atlas of the Western Canada Sedimentary Basin. Canadian Society of Petroleum

Geologists and Alberta Research Council, Calgary, pp. 259–275.

Ejezie, N., 2007, Triassic oil families and possible source rocks, Peace River Embayment area, Alberta, Canada, Ms.C. Thesis, Department of Geology and Geophysics, University of Calgary, Calgary, Alberta, Canada.

Eliyahu, M., Emmanuel, S., Day-Stirrat, R.J., and Macaulay, C.I., 2015. Mechanical properties of organic matter in shales mapped at the nanometer scale. Journal of Marine and Petroleum Geology, 59, 294-304. https://doi.org/10.1016/j.marpetgeo.2014.09.007.

Emmanuel, S., Eliyahu, M., Day-Stirrat, R.J., Hofmann, R., and Macaulay, C.I., 2016. Impact of thermal maturation on nano-scale elastic properties of organic matter in shales. Journal of Marine and Petroleum Geology, 70, 175-184. https://doi.org/10.1016/j.marpetgeo.2015.12.001.

Euzen, T., Moslow, T.F., Crombez, V., and Rohais, S., 2018. Regional stratigraphic architecture of the spathian deposits in western Canada - Implications for the Montney resource play. Bulletin of Canadian Petroleum Geology. 66(1), 175-192.

Feiyu, W., Jing, G., Weiping, F., and Bao., L., 2013. Evolution of overmature marine shale porosity and implication to the free gas volume. Petroleum Exploration and Development 40(6), 819-824. https://doi.org/10.1016/S1876-3804(13)60111-1.

Feng, W., Chen, Z., and Jiang, C., 2016. Oil and source correlations of Triassic Montney Formation in WCSB: Implication to shale gas resource potential in: GeoConvention. CSPG CSEG CWLS, Calgary, AB, Canada, p. 1.

Fishman, N.S., Egenhoff, S.O., Boehlke, A.R., and Lowers, H.A., 2015. Petrology and diagenetic history of the upper shale member of the Late Devonian - early Mississippian Bakken Formation, Williston Basin, North Dakota. Geological Society of America Special Papers, 515, SPE515-07.

Furlong, C.M., Gingras, M.K., Moslow, T.F., and Zonneveld, J.-P., 2018. The Sunset Prairie Formation: designation of a new Middle Triassic formation between the Lower Triassic Montney Formation and Middle Triassic Doig Formation in the Western Canada Sedimentary Basin, northeast British Columbia. Bulletin of Canadian Petroleum Geology, 66(1), 193-214.

Germay, C., Lhomme, T., McPhee, C., and Daniels, G., 2018. An objective review of non-destructive methods for the direct testing of strength on rock cores. 52nd US Rock Mechanics / Geomechanics Symposium, Seattle, Washington, U.S.A. 24-27 June.

Ghanizadeh, A., Clarkson, C.R., Aquino, S., Ardakani, O.H., and Sanei, H., 2015. Petrophysical and geomechanical characteristics of Canadian tight oil and liquid-rich gas reservoirs : I. Pore network and permeability characterization. Fuel, 153, 664-681.

https://doi.org/10.1016/j.fuel.2015.03.020

Gibson, D.W., and Edwards, D.E., 1990. An overview of Triassic stratigraphy and depositional environments in the Rocky Mountain Foothills and Western Interior Plains , Peace River Arch area , northeastern British Columbia. Bulletin of Canadian Petroleum Geology, 38(1), 146-158.

Golding, M.L., Mortensen, J.K., Ferri, F., Zonneveld, J.-P., and Orchard, M.J., 2016. Determining the provenance of Triassic sedimentary rocks in northeastern British Columbia and western Alberta using detrital zircon geochronology, with implications for regional tectonics. Canadian Journal of Earth Sciences, 53(2), 140-155. https://doi.org/10.1139/cjes-2015-0082.

Golding, M.L., Orchard, M.J., Zonneveld, J.-P., and Wilson, N.S.F., 2015. Determining the age and depositional model of the Doig Phosphate Zone in northeastern British Columbia using conodont biostratigraphy, Bulletin of Canadian Petroleum Geology, 63(2), 143-170.

Golonka, J., Ross, M.I., and Scotese, C.R., 1994. Phanerozoic paleogeographic and paleoclimatic modeling maps, in: Embry, A.F., Beauchamp, B., and Glass, D.J. (Eds.), Pangea, Global Environments and Resources. Canadian Society of Petroleum Geologist, Calgary, 1-47.

Gupta, I., Sondergeld, C., Rai, C., and Hofmann, R., 2018. Water Weakening: Case study from Marcellus, Woodford, Eagle Ford and Wolfcamp. In 52nd US Rock Mechanics/Geomechanics Symposium. American Rock Mechanics Association.

Han, L., 2018. Moisture effects on dynamic elastic properties of shale from deep formations. M.Sc. Thesis, The Newbourne School of Petroleum and Geological Engineering, University of Oklahoma, Norman, Oklahoma, U.S.A.

Harris, N.B., Moghadam, A. and Dong, T., 2019. The effects of organic carbon content and thermal maturity on acoustic parameters in a black shale: Woodford Shale, Permian Basin, West Texas. Geophysics 84(6), D231-D248.

Harris, N.B., Minch, C.A., Selby, D., and Korn, D., 2013. Minor and trace element and Re-Os chemistry of the Upper Devonian Woodford Shale, Permian Basin, west Texas: Insights into metal abundance and basin processes. Chemical Geology, 356, 76-930.

Harris, N.B., Miskimins, J.L., and Mnich, C.A., 2011. Mechanical anisotropy in the Woodford Shale, Permian Basin: Origin, magnitude, and scale. Leading Edge, 30(3), 284-291. https://doi.org/10.1190/1.3567259.

Hernandez-Uribe, L.A., Aman, M., and Espinoza, D.N., 2017. Assessment of Mudrock Brittleness with Micro-scratch Testing. Rock Mechanics and Rock Engineering, 50(11), 2849-2860.

Herwanger, J. V., Bottrill, A.D., and Mildren, S.D., 2015. Uses and Abuses of the Brittleness Index With Applications to Hydraulic Stimulation. Unconventional Resources Technology Conference, San Antonio, Texas, U.S.A., 20-22 July. https://doi.org/10.2118/178678-MS.

Huo, Z., Zhang, J., Li, P., Tang, X., Yang, X., Qiu, Q., Dong, Z., and Li, Z., 2018. An improved evaluation method for the brittleness index of shale and its application - A case study from the southern north China basin. Journal of Natural Gas Science and Engineering, 59, 47-55. https://doi.org/10.1016/j.jngse.2018.08.014.

Ibrahimbas, A., and Riediger, C., 2004. Hydrocarbon source rock potential aAs determined by RockEval 6/TOC pyrolysis, N.E. B.C. and N.W. Alberta. Resource Development and Geoscience Branch, Summary of Activities 2004, 7-18.

Jarvie, D.M., Hill, R.J., Ruble, T.E., and Pollastro, R.M., 2007. Unconventional shale-gas systems: The Mississippian Barnett Shale of north-central Texas as one model for thermogenic shale-gas assessment. American Association of Petroleum Geologists Bulletin, 91(4), 475-499.

Jin, X., Shah, S.N., Roegiers, J.-C., and Zhang, B., 2015. An integrated petrophysics and geomechanics approach for fracability evaluation in shale reservoirs. SPE Journal 20(3), 518-526. https://doi.org/10.2118/168589-PA.

Jin, X., Shah, S.N., Truax, J.A., and Roegiers, J.-C., 2014. A Practical Petrophysical Approach for Brittleness Prediction from Porosity and Sonic Logging in Shale Reservoirs. SPE Annual Technical Conference and Exhibition Amsterdam, The Netherlands, 27-29 October. https://doi.org/10.2118/170972-MS.

Katz, D., Jung, M., Canter, L., Sonnefeld, M. Odegard, M., Daniels, J., Byres, A., Guisinger, M., Jones, K., and Forster, J., 2016. Mineralogy Derived Brittleness from the Qemscan: Niobrara Case Study. SPE Low Perm Symposium, Denver, Colorado, U.S.A., 5-6 May. https://doi.org/10.2118/180251-MS.

Keller, M.A., and Isaacs, C.M., 1985. An evaluation of temperature scales for silica diagenesis in diatomaceous sequences including a new approach based on the Miocene Monterey Formation, California. Geo-Marine Letters, 5(1), 31-35. https://doi.org/10.1007/BF02629794.

Krause, F.F., Wiseman, A.C., Williscroft, K.R., Solano, N., Morris, N.J., Meyer, R., and Marr, R., 2012. Petrographic and petrophysical comparison of the Montney Formation in the Sturgeon Lake South area. In Site, Canadian Well Logging Society Magazine, 31, 6-9.

Kumar, V., Sondergeld, C.H., and Rai, C.S., 2012. Nano to macro mechanical characterization of shale. SPE Annual Technical Conference and Exhibition, San Antonio, Texas, USA, 8-10 October. SPE 159804

Labani, M.M., and Rezaee, R., 2015. The Importance of Geochemical Parameters and Shale Composition on Rock Mechanical Properties of Gas Shale Reservoirs: a Case Study From the Kockatea Shale and Carynginia Formation From the Perth Basin, Western Australia. Rock Mechanics and Rock Engineering, 48(3), 1249-1257. https://doi.org/10.1007/s00603-014-0617-6.

Lai, B., Li, H., Zhang, J., Jacobi, D., and Georgi, D., 2015. Water-Content Effects on Dynamic Elastic Properties of Organic-Rich Shale. SPE Journal 21(2), 635-647. https://doi.org/10.2118/175040-PA.

LaMothe, J.T., 2008. Sedimentology, Ichnology, Stratigraphy and Depositional History of the Contact Between the Triassic Doig and Montney Formations in West-Central Alberta, Canada - Presence of an Unconformity Bound Sand Wedge. M.Sc Thesis, Departmrnt of Earth and Atmospheric Sciences, University of Alberta, Edmonton, Alberta, canada.

Lan, Q., Dehghanpour, H., Wood, J.M., and Sanei, H., 2015. Wettability of the Montney Tight Gas Formation. SPE Reservoir Evaluation & Engineering, 18(3), 417-431. https://doi.org/10.2118/171620-PA.

Macquaker, J.H., and Adams, A.E., 2003. Maximizing information from fine-grained sedimentary rocks: An inclusive nomenclature for mudstones. Journal of Sedimentary Research, 73(5), 735-744.

Miall, A.D., and Blakey, R.C., 2008. The Phanerozoic tectonic and sedimentary evolution of North America, in: Miall, A.D. Sedimentary Basins of United States and Canada, p. 1-29. Amsterdam, Netherlands, Elsevier.

Milliken, K.L., and Olson, T., 2017. Silica diagenesis, porosity evolution, and mechanical behavior in siliceous mudstones, Mowry Shale (Cretaceous), Rocky Mountains, U.S.A.. Journal of Sedimentary Research, 87(4): 366-387. doi: https://doi.org/10.2110/jsr.2017.24.

Moghadam, A., Harris, N.B., Ayranci, K., Gomez, J.S., Angulo, A.A., and Chalaturnyk, R., 2019. Brittleness in the Devonian Horn River shale, British Columbia, Canada. Journal of Natural Gas Science and Engineering, 62, 247-258. https://doi.org/10.1016/j.jngse.2018.12.012.

Mokhtari, M., Honarpour, M.M., Tutuncu, A.N., and Boitnott, G.N., 2016. Characterization of elastic anisotropy in Eagle Ford Shale: Impact of heterogeneity and measurement scale. SPE Reservoir Evaluation & Engineering, 19(3), 429-439.

Mondol, N.H., Jahren, J., Bjørlykke, K., and Brevik, I., 2008. Elastic properties of clay minerals. Leading Edge, 27(6) 758-770. https://doi.org/10.1190/1.2944161.

Monger, J.W, and Price, R.,A. 2002. The Canadian Cordillera: Geology and tectonic evolution.

Canadian Society of Exploration Geophysicists Recorder, 27(2), 17-36.

Monger, J.W., and Price, R.A., 1979. Geodynamic evolution of the Canadian Cordillera - progress and problems. Canadian Journal of Earth Sciences, 16(3), 770-791. https://doi.org/10.1139/e79-069.

Moslow, T.F., 2000. Reservoir architecture of a fine-grained turbidite system: Lower Triassic Montney Formation, Western Canada Sedimentary Basin, in: Weimer, P. (Ed.), Deep-Water Reservoirs of the World. SEPM Society for Sedimentary Geology, Houston, Texas, pp. 686-713. https://doi.org/10.5724/gcs.00.15.0686.

Moslow, T.F., Haverslew, B., and Henderson, C.M., 2018. Sedimentary facies, petrology, reservoir characteristics, conodont biostratigraphy and sequence stratigraphic framework of a continuous (395m) full diameter core of the lower Triassic Montney Fm, northeastern British Columbia. Bulletin of Canadian Petroleum Geology, 66(1), 259-287.

Moslow, T.F., and Davies, G.R., 1997. Turbidite reservoir facies in the Lower Triassic Montney Formation, west-central Alberta. Bulletin of Canadian Petroleum Geology, 45(4), 507-536.

Nagel, N.B., Gil, I., Sanchez-Nagel, M., and Damjanac, B., 2011. Simulating Hydraulic Fracturing in Real Fractured Rocks - Overcoming the Limits of Pseudo 3D Models, Society of Petroleum Engineers Hydraulic Fracturing Technology Conference. doi:10.2118/140480-MS.

Nassichuk, B.R., 2000. Sedimentology, diagenesis and reservoir development of the lower Triassic Montney formation, northeastern British Columbia. , Ms.C. Thesis, Department of Earth and Ocean Sciences, University of British Columbia, Vancouver, British Columbia, Canada.

National energy board, 2013. Canada's energy future 2013 energy supply and demand projections to 2035. https://www.cer-rec.gc.ca/nrg/ntgrtd/ftr/2013/2013nrgftr-eng.pdf. Last accessed March 31, 2020.

Ness, S.M., 2001. The application of basin analysis to the Triassic succession, Alberta Basin: an investigation of burial and thermal history and evolution of hydrocarbons in Triassic rocks. Ms.C. Thesis, Department of Geology and Gepophysics, University of Calgary, Calgary, Alberta, Canada.

Nieto, J., Batlai, B., and Delbecq, F., 2013. Seismic lithology prediction : A Montney Shale Gas case study. CSEG Recorder, 38(2), 34-41.

Orchard, M.J., and Zonneveld, J.-P. 2009. The Lower Triassic Sulphur Mountain Formation in the Wapiti Lake area: lithostratigraphy, conodont biostratigraphy, and a new biozonation for the lower Olenekian (Smithian). Canadian Journal of Earth Sciences, 46(10), 757-790. https://doi.org/10.1139/E09-051.

Ouenes, A., Aimene, Y., and Nairn, J., 2014. Interpretation of Microseismic Using Geomechanical Modeling of Multiple Hydraulic Fractures Interacting with Natural Fractures – Application to Montney Shale. Canadian Society of Exploration Geophysicists Recorder, 39(9), 46-54.

Perez Altamar, R., and Marfurt, K. 2014. Mineralogy-based brittleness prediction from surface seismic data: Application to the Barnett Shale. Interpretation 2(4), T255-T271. https://doi.org/10.1190/INT-2013-0161.1.

Playter, T.L., 2013. Petrographic and x-ray microtomographic analysis of the Upper Montney Formation, Northeastern British Columbia, Canada. Ms.C. Thesis, Department of Earth and Atmospheric Sciences, University of Alberta, Edmonton, Alberta, Canada.

Prasad, M., Kenechukwu C. Mba., McEvoy, T.E., and Batzel, M.L., 2011. Maturity and impedance analysis of organic-rich shales. SPE Reservoir Evaluation & Engineering 14(5), 533-543.

Prasad, M., Hofman, R., Batzel, M., Kopycinska-Muler, M., Rabe, U., Arnold, W., 2005. Values of mineral modulus of clay, in: SEG Annual Meeting, Houston, Texas, U.S.A., 6-11 November. https://doi.org/10.1016/j.jcrc.2012.07.027.

Prasad, M., Kopycinska, M., Rabe, U., and Arnold, W., 2002. Measurement of Young's modulus of clay minerals using atomic force acoustic microscopy. Geophysical Research Letters, 29(8), 13-1-13-4. https://doi.org/10.1029/2001GL014054.

Price, R.A., 1994. Cordilleran tectonics and the evolution of the Western Canada sedimentary basin. In Geological Atlas of Western Canada, Mossop, G.D., and Shetsen, I., pp. 13-24, Calgary, Alberta, Canadian Society of Petroleum Geologists/ Alberta Research Council.

Proverbs, I.P., Bann, K.L., Fratton, C.M., Frostad, C.J., and Juska, A., 2018. Facies architecture and sequence stratigraphy of the Lower Triassic Montney Formation , NE British Columbia : Fundamental controls on the distribution of 'sweet spots' in a world-class unconventional reservoir. Bulletine of Canadian petroleum Geology, 66(1), 237-258.

Ramos, M.J., Espinoza, D.N., Goldfarb, E.J.,Tisato, N., Laubach, S.E., and Torres-Verdin, C., 2019. Microstructural controls on elastic anisotropy of finely laminated Mancos Shale. Geophysical Journal International, 216(2), 991-1004.

Rangriz Shokri, A., Chalaturnyk, R.J., and Bearinger, D., 2019. Deployment of Pressure Hit Catalogues to Optimize MultiStage Hydraulic Stimulation Treatments and Future Re-Fracturing Designs of Horizontal Wells in Horn River Shale Basin, URTEC-196221-MS presented at SPE Annual Technical Conference and Exhibition, Calgary, AB, 29 Sept.-2 Oct.

Rangriz Shokri, A., Chalaturnyk, R.J., Bearinger, D., Virues, C., and Lehmann, J., 2017.

Constraining the Complexity of Stimulated Reservoir Volume during Multi-Stage Hydraulic Fracturing of Horizontal Wells through Inter-Well Pressure Hit Modeling, Society of Petroleum Engineers, doi:10.2118/187188-MS.

Rickman, R., Mullen, M.J., Petre, J.E., Grieser, B., and Kundert, D., 2008. A practical use of shale petrophysics for stimulation design optimization: All shale plays Are not clones of the Barnett Shale. SPE Annual Technical Conference and Exhibition, Denver, Colorado, USA, 21-24 Sptember. https://doi.org/10.2118/115258-MS.

Riediger, C.L., Fowler, M.G., Brooks, P.W., and Snowdon, L.R., 1990. Triassic oils and potential Mesozoic source rocks, Peace River Arch area, Western Canada Basin. Organic Geochemistry, 16(1-3), 295–305. https://doi.org/10.1016/0146-6380(90)90049-6.

Rogers, S., and McLellan, P., 2014. Investigation of the Effects of Natural Fractures and Faults on Hydraulic Fracturing in the Montney Formation , Farrell Creek Gas Field , British Columbia, in: International Discrete Fracture Network Engineering Conference. DFNE, Vancouver, Canada, pp. 1-13.

Rohais, S., Crombez, V., Euzen, T., and Zonneveld, J.-P., 2018. Subsidence dynamics of the Montney Formation (Early Triassic, western Canada sedimentary basin): Insights for its geodynamic setting and wider implications. Bulletin of Canadian Petroleum Geology, 66(1), 128-160.

Rohais, S., Crombez, V., Euzen, T., and Baudin, F., 2016. The Lower and Middle Triassic of Western Canada: Passive margin, Back-Arc or Fore-Arc geodynamic setting?, in: CWLS, C.C. (Ed.), Geoconvention. Calgary, AB, Canada, pp. 1-4.

Rokosh, C.D., Lyster, S., Anderson, S.D.A., Beaton, A.P., Berhane, H., Brazzoni, T., Chen, D., Cheng, Y., Mack, T., Pana, C. and Pawlowicz, J.G., 2012. Summary of Alberta's shale-and siltstone-hosted hydrocarbon resource potential. Energy Resources Conservation Board, ERCB/AGS Open File Report, 6, p.327.

Romero-Sarmiento, M.F., Euzen, T., Rohais, S., Jiang, C., and Littke, R., 2016. Artificial thermal maturation of source rocks at different thermal maturity levels: Application to the Triassic Montney and Doig formations in the Western Canada Sedimentary Basin. Organic Geochemistry, 97, 148-162. https://doi.org/10.1016/j.orggeochem.2016.05.002.

Ross, G.M., Gehrels, G.E., and Patchett, P.J., 1997. Provenance of Triassic strata in the Cordilleran miogeocline , western Canada. Bulletin of Canadian Petroleum Geology, 45(4), 461-473.

Rybacki, E., Meier, T., and Dresen, G., 2016. What controls the mechanical properties of shale rocks? - Part II: Brittleness. Journal of Petroleum Science and Engineering, 144, 39-58. https://doi.org/10.1016/j.petrol.2016.02.022.

Sanders, S., Etienne, C., Gegolic, A., Kelly, D., and Zonneveld, J.-P., 2018. The Middle Montney Altares Member : lithology , depositional setting and significance for horizontal drilling and completion in the Altares field , British Columbia. Bulletin of Canadian Petroleum Geology, 66(1), 318-337.

Sanei, H., Wood, J.M., Ardakani, O.H., Clarkson, C.R., and Jiang, C., 2015. Characterization of organic matter fractions in an unconventional tight gas siltstone reservoir. International Journal of Coal Geology, 150-151, 296-305. https://doi.org/10.1016/j.coal.2015.04.004.

Slatt, R.M., and Rodriguez, N.D., 2012. Comparative sequence stratigraphy and organic geochemistry of gas shales: Commonality or coincidence? Journal of Natural Gas Science and Engineering, 8, 68-84. https://doi.org/10.1016/j.jngse.2012.01.008.

Slatt, R.M., and Abousleiman, Y., 2011. Merging sequence stratigraphy and geomechanics for unconventional gas shales. Leading Edge, 30(3), 274-282. https://doi.org/10.1190/1.3567258.

Tinnin, B., Bello, H., and McChesney, M., 2015. Multi-source data integration: Eagle ford shale sweet spot mapping, in: Unconventional Resources Technology Conference This. Society of Exploration Geophysicists and American Association of Petroleum Geologists, San Antonio, Texas, U.S.A., pp. 1-9. https://doi.org/10.1190/ice2016-6874854.1.

Vaisblat, N., Harris, N.B., DeBhur, C., Euzen, T., Gasparrini, M., Crombez, V., Rohais, S., Krause, F. and Ayranci, K. 2017. Diagenetic model for the deep Montney Formation, Northeastern British Columbia. Geoscience BC Report 2017-1, p. 37-48. http://www.geosciencebc.com/i/pdf/SummaryofActivities2016/SoA2016_Vaisblat.pdf.

Vernik, L., and Milovac, J., 2011. Rock physics of organic shales. Leading Edge, 30(3), 318-323. https://doi.org/10.1190/1.3567263.

Verwaal, W., and Mulder, A., 1993. Estimating rock strength with the equotip hardness tester. International Journal of Rock Mechanics and Mining Sciences & Geomechanics Abstracts, 30(6), 659-662. https://doi.org/10.1016/0148-9062(93)91225-8.

Vishkai, M., and Gates, I.D., 2018. Geomechanical Characterization of Naturally Fractured Formation, Montney, Alberta. 52nd U.S. Rock Mechanics/Geomechanics Symposium, June 17-20, Seattle, Washington.

Wang, Y., and Grammer, G.M., 2018. Rebound hardness: relationship to facies, mineralogy , natural fractures, reservoir quality, and rock mechanical properties, the " Mississippian Limestone " play, North -Central Oklahoma, USA, in: 52nd US Rock Mechanics / Geomechanics Symposium. American Rock Mechanics Association, Seattle, Washington, U.S.A., pp. 1-10.

Wang, F.P., and Gale, J.F.W., 2009. Screening criteria for shale-gas systems. Gulf Coast

Association of Geological Societies, 59, 779-793.

Wang, Z., Wang, H., and Cates, M.E., 1998. Elastic Properties of Solid Clays, 1998. In Proceedings of the AEG Annual International Meeting. Extended abstract. https://doi.org/10.1190/1.1820064.

Wei, Z., 2009. Nanoidentation behavior of clay minerals and claybased nonstructured multilayers. PhD dissertation, The Department of Civil and Environmental Engineering, Louisiana State University and Agricultural and Mechanical College, Baton Rouge, Louisiana, U.S.A.

Wilson, M.D., 1992. Inherited grain-rimming clays in sandstones from eolian and shelf environments: their origin and control on reservoir properties. Origin Diagenesis and Petrophysics of Clay Minerals in Sandstones SEPM Special Publication No. 47, 209-225.

Willett, S.D., Issler, D.R., Beaumont, C., Donelick, R.A., and Grist, A.M., 1997. Inverse modeling of annealing of fission tracks in apatite; 2, Application to the thermal history of the Peace River Arch region, Western Canada sedimentary basin. American Journal of Science, 297(10), 970-1011. https://doi.org/10.2475/ajs.297.10.970.

Wood, J.M., 2015. Crushed-rock versus full-diameter core samples for water-saturation determination in a tight-gas siltstone play, SPE Reservoir Evaluation & Engineering 18(3): 407-416. SPE-174548-PA. http://dx.doi.org/10.2118/174548-PA.

Wood, J.M., 2013. Water Distribution in the Montney Tight Gas Play of the Western Canadian Sedimentary Basin: Significance for Resource Evaluation, in: SPE Canadian Unconventional Resources Conference. Society of Petroleum Engineers, Calgary, AB, Canada, pp. 290–302. https://doi.org/10.2118/161824-MS.

Wood, J.M., Sanei, H., Haeri-Ardakani, O., Curtis, M.E., and Akai, T., 2018. Organic petrography and scanning electron microscopy imaging of a thermal maturity series from the Montney tight-gas and hydrocarbon liquids fairway. Bulletin of Canadian Petroleum Geology, 66(2), 499-515. https://doi.org/10.1038/ncomms13614.

Wood, J.M., and Sanei, H., 2016. Secondary migration and leakage of methane from a major tight-gas system. Nature Communications, 7, 13614.

Wood, J.M., Sanei, H., Curtis, M.E., and Clarkson, C.R., 2015. Solid bitumen as a determinant of reservoir quality in an unconventional tight gas siltstone play. International Journal of Coal Geology, 150-151, 287–295. https://doi.org/10.1016/j.coal.2015.03.015.

Wüst, R.A.J., and Cui, X., 2018. From X-ray Fluorescence (XRF) to Mechanical Profiling for Better Well Completion. Valuable Analytics for the Exploration Toolbox! Recorder 43, 22-28.

Wüst, R.A., Tu, S., Nassichuk, B., Bozarth, T., Tucker, J., and Cui, A., 2018.

Chemostratigraphy, petrography, and SEM investigations of the Lower Triassic Montney Formation in Alberta: Implications for a new and revised diagenetic and depositional model. Bulletin of Canadian Petroleum Geology, 66(2), 436-471.

Yang, S., Harris, N., Dong, T., Wu, W., and Chen, Z., 2015. Mechanical Properties and Natural Fractures in a Horn River Shale Core from Well Logs and Hardness Measurements, in: EUROPEC 2015. Society of Petroleum Engineers, Madrid, Spain, pp. 1-13. https://doi.org/10.2118/174287-MS

Yu, H., Wang, Z., Rezaee, R., Arif, M., and Xiao, L., 2016. Characterization of elastic properties of lacustrine shale reservoir using well logging and core analysis, in: SPE Asia Pacific Oil & Gas Conference and Exhibition. Society of Petroleum Engineers, pp. 1-11. https://doi.org/10.2118/182215-MS.

Zargari, S., Prasad, M., Mba, K.C. and Mattson, E.D., 2013. Organic maturity, elastic properties, and textural characteristics of self resourcing reservoirs. Geophysics, 78(4), D223-D235.

Zelazny, I.V., Gegolick, A., Zonneveld, J.-P., Playter, T., and Moslow, T.F., 2018. Sedimentology, stratigraphy and geochemistry of Sulphur Mountain (Montney equivalent) Formation outcrop in south central Rocky Mountains, Alberta, Canada. Bulletin of Canadian Petroleum Geology, 66(1), 288-317.

Zhang, D., Ranjith, P.G., and Perera, M.S.A., 2016. The brittleness indices used in rock mechanics and their application in shale hydraulic fracturing: A review. Journal of Petroleum Science and Engineering, 143, 158-170. https://doi.org/10.1016/j.petrol.2016.02.011.

Zhang, J.J., and Bentley, L.R., 2005. Factors determining Poisson's ratio. Consortium for Research in Elastic Wave Exploration Seismology, Research Report, 17, 1-15.

Zonneveld, J.-P., 2011. Suspending the rules: unraveling the ichnological signature of the Lower Triassic post-extinction recovery interval. Palaios 26(11), 677–681. https://doi.org/10.2307/41317453.

Zonneveld, J.-P., and Moslow, T.F., 2018. Palaeogeographic setting, lithostratigraphy, and sedimentary framework of the Lower Triassic Montney Formation of western Alberta and northeastern British Columbia. Bulletin of Canadian Petroleum Geology, 66(1), 93-127.

Zonneveld, J.-P., and Moslow, T.F., 2014. Perennial river deltas of the Montney Formation: Alberta and British Columbia subcrop edge, in: Geoconvention. CSPG CSEG CWLS, Calgary, AB, Canada, pp. 1-2.

Zonneveld, J.-P., Golding, M.L., Moslow, T.F., Orchard, M.J., Playter, T.L., and Wilson, N., 2011. Depositional framework of the Lower Triassic Montey Formation, West-central

Alberta and Northeastern British Columbia, in: Geoconvention. CSPG CSEG CWLS, Calgary, AB, Canada, pp. 1-4.

Zonneveld, J.-P., Beatty, T.W., MacNaughton, R.B., Pemberton, S.G., Utting, J., and Henderson, C.M., 2010. Sedimentology and ichnology of the Lower Triassic Montney Formation in the Pedigree-Ring/Border-Kahntah River area, northwestern Alberta and northeastern British Columbia. Bulletin of Canadian Petroleum Geology, 58(2), 115–140. https://doi.org/10.2113/gscpgbull.58.2.115

Chapter 4 - The Petrophysics of a Siltstone - Example from the Montney Formation, Western Canada

Noga Vaisblat, Nicholas B. Harris, Korhan Ayranci, Rick Chalaturnyk Matthew Power, David L. Bish, Corey Twemlow, Nik Minion, (Manuscript in preparation).

Abstract:

The Lower Triassic Montney Formation in western Canada is one of the most important siltstone reservoirs in the world. We examined the controls on the petrophysical properties of the siltstone, focusing on effects of rock fabric and composition on permeability and pore system characteristics.

Compositional control on the petrophysical properties of the siltstone include quartz, clay and organic matter. Quartz content exerts a positive control on both porosity and permeability, related to strengthening of the rock framework and reduced porosity loss due to compaction. Elevated clay content is also associated with higher porosity and permeability, in part because of an association with quartz, and in part because clays may shelter interconnected primary porosity that promotes permeability. Organic matter content is negatively correlated to porosity and permeability despite the presence of organic matter porosity, because relict oil (now pyrobitumen) plugs primary pore space and because other pore types contribute more to the total pore volume of the rock. Lithofacies, characterized in four cores in the siltstone are indistinguishable from one another based on their petrophysical properties due to their similar grain size and composition and the massive overprinting by shallow burial diagenesis.

We compared our finding to main processes identified as controlling pore systems in shale formations and concluded that although the petrophysical properties of the Montney siltstone is similar to many unconventional shale reservoirs, the controls on reservoir quality are

different, and are related to fundamental differences in compaction, chemical diagenesis and the nature of organic matter maturation and migration.

4.1 Introduction

Numerous studies over the last decades have documented the characteristics of pore systems in mudrocks and tight sandstones and identified controls over their petrophysical rock properties. Siltstone formations have received less attention, although many unconventional reservoirs are at least partially composed of siltstone intervals. Prominent examples include the Lucaogou Formation in China (Cao et al., 2017), parts of the Marcellus Formation in the northern Appalachian Basin of North America (Scuderi et al., 2015), the Rurikfjellet Formation in Spitsbergen (Rakocinski et al., 2018), the Snadd and Steinkobbe Formations in the Barents Sea (Abay et al., 2018), and the Middle Bakken Member (Nicolas, 2016).

We focus on the Lower Triassic Montney Formation of the Western Canadian Sedimentary Basin (Fig. 4.1). One of the most important siltstone reservoirs in the world, the Montney holds estimated reserves of 450 TCF of gas, 14,520 MMB of gas liquids, and 1125 MMB of oil (National Energy Board, Government of Canada, 2013). More specifically, we examine the influence of rock composition and fabric over a range of spatial scales from microns to centimeters on the petrophysical properties of the siltstone (porosity, permeability, pore size and pore throat size distribution), identify underlying processes that control pores system evolution, and interpret them in the context of siltstone diagenesis (this study, chapter 2). We further compare our results to some of the more extensive studies of shale petrophysics to highlight the similarities and differences between the two rock types.

4.2 Geological setting

The Montney Formation is a southwestward-dipping wedge of mixed siliciclastic and carbonate siltstones, covering an area of 130,000 km^2, mostly in the subsurface of

northeastern British Columbia and west-central and southwestern Alberta (Fig. 4.1). The Montney Formation

was deposited on the western margin of the supercontinent Pangea during the Early Triassic (Fig. 4.2) (Davies et al., 1997; Utting et al., 2005; Zonneveld et al., 2010; Henderson et al., 2018).
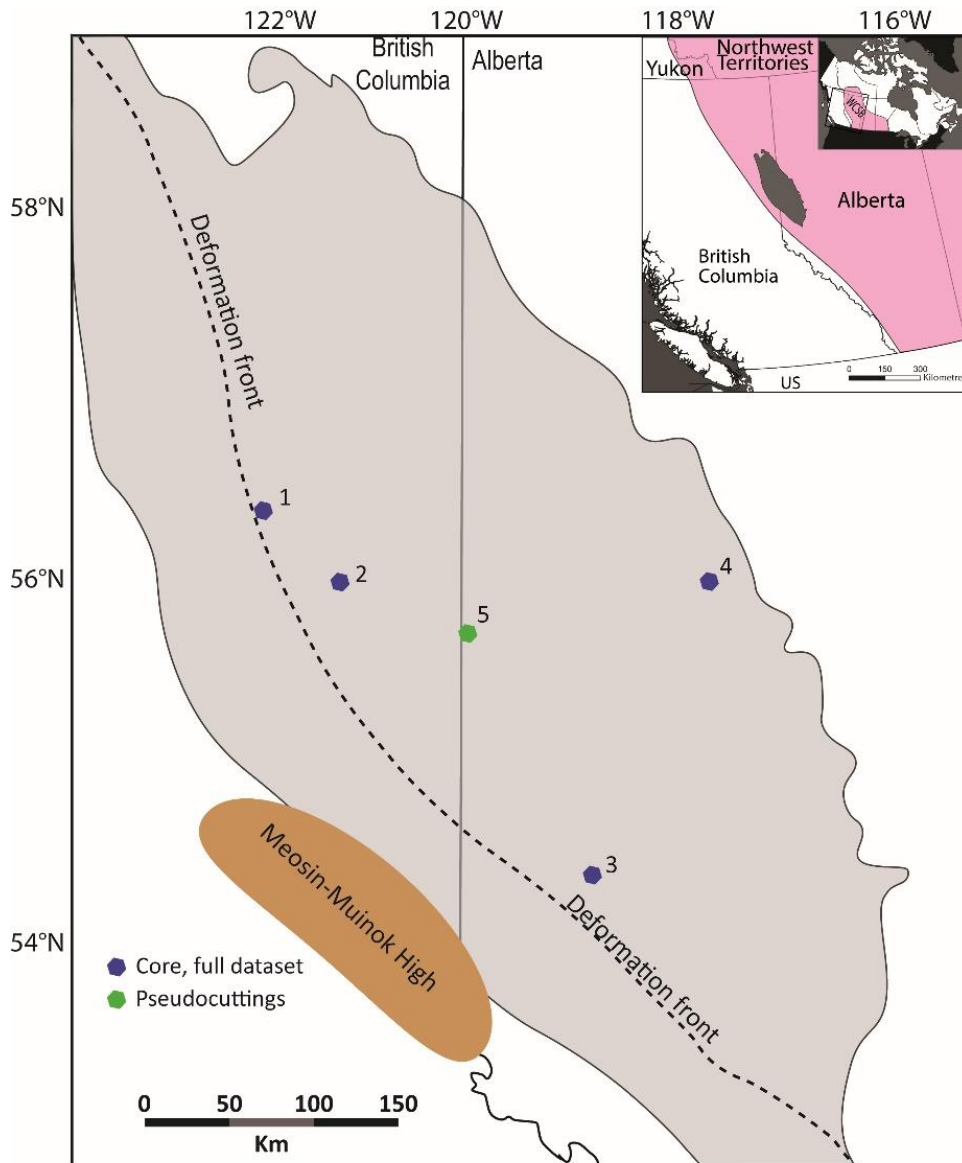
Fig. 4.1: Location of study wells: (1) 16-17-083-25W6 (2) 16-29-079-20W6 (3) 05-24-063-6W6 (4) 103/05-20-079-22W5 (5) 06-03-079-13W6. Insert shows the location of the Montney Formation within the Western Canadian Sedimentary Basin (pink). Map after Zonneveld and Moslow (2018).

Interpretations of the tectonic regime for the western Pangea margin during the Lower Triassic have evolved over the past 30 years (Monger and Price, 1979, 2002; Coney et al., 1980; Edwards et al., 1994; Price, 1994; Miall and Blakey, 2008; Zonneveld et al., 2010), with recent studies proposing a fore-arc to retro-foreland setting (Blakey, 2014; Golding et al., 2016, Rohais et al., 2018).
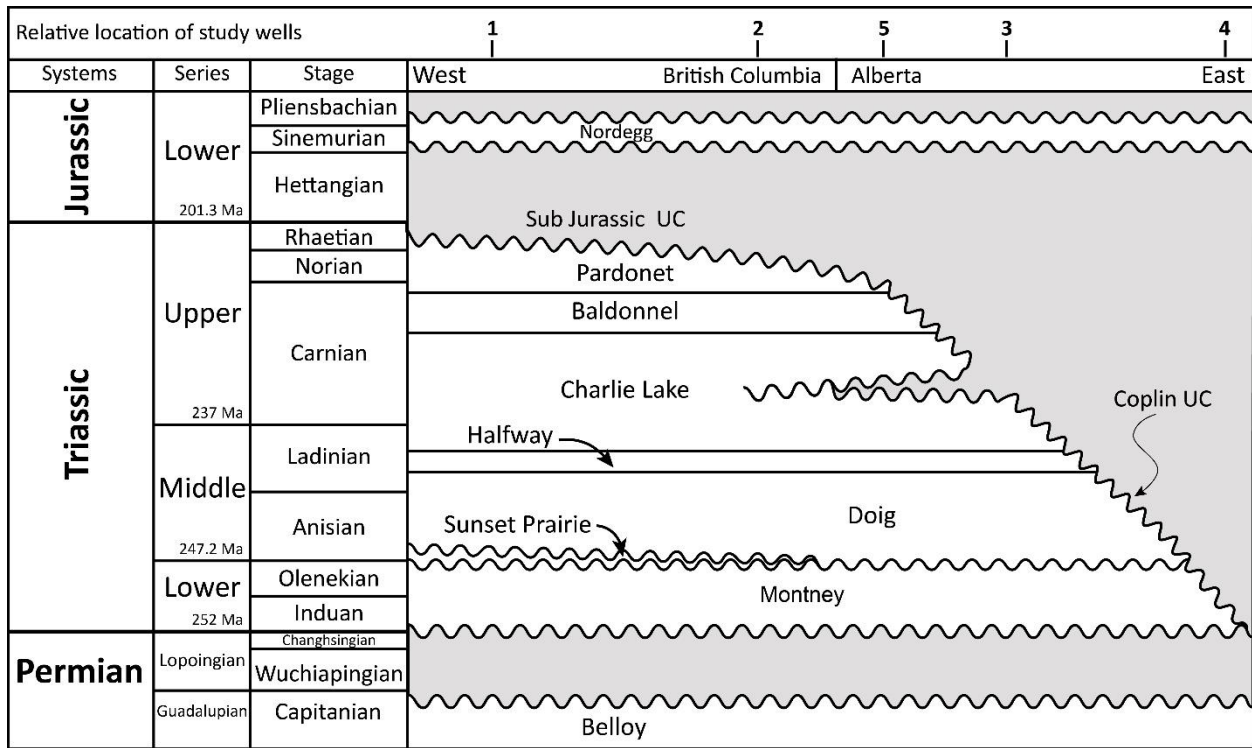
Fig. 4.2: Chronostratigraphic chart for the Triassic and Lower Jurassic of the subsurface in Alberta and British Columbia. The location of the study wells is marked at the top of the chart. UC is unconformity. Ages after Golding et al., 2016.

Studies suggest that during the Early Triassic, the WCSB was located at approximately $30°$ north, and rotated $30°$ clockwise relative to its current position (Golonka et al., 1994; Davies et al., 1997; Blakey, 2014). Paleoclimatic reconstructions indicate conditions were hot and arid with seasonal monsoons (Davies et al., 1997; Golonka and Ford, 2000; Preto et al., 2010, Sun et al., 2012; Zonneveld and Moslow, 2018).

Comprehensive sedimentological research on the Montney Formation identifies a wide array of depositional environments extending from shoreface to off-shore environments, varying with location in the basin (e.g. Davies et al., 1997; 2018; Zonneveld et al., 2011; Playter, 2013; Crombez. et al., 2016; Euzen et al., 2018; Moslow et al., 2018; Zonneveld and Moslow, 2018). The sediments comprising the Montney Formation were sourced mainly from the Laurentian continental margin lying east of the WCSB, while the Innuitian orogenic wedge to the north of the WCSB provided a smaller volume of sediments (Ross et al., 1997; Beranek et al., 2010; Golding et al., 2016). A western volcanic source was also proposed for some Montney sediments (Edwards et al., 1994; Crombez et al., 2017; Rohais et al., 2018) but is not conclusively demonstrated.

The Montney Formation thickens from <1m in the northeast to over 350 m in the southwest and is stratigraphically subdivided into Upper and Lower Members consisting of siltstone and a Dolomitic Coquina Middle Member (Davies et al., 1997; Dixon, 2000; Moslow, 2000; Zonneveld and Moslow, 2018). The Coquina Middle Member is present in the eastern and southeastern area of the formation and thins to the west (Davies et al., 1997; Zonneveld and Moslow, 2018). The Montney Formation is bounded below by the Permian-Triassic unconformity. In the eastern section of the basin, the formation is bounded above by the Coplin and sub-Jurassic unconformities (Fig. 4.2; Gibson and Edwards, 1990; Edwards et al., 1994; Davies et al., 1997; Moslow, 2000). In western parts of the basin where these unconformities cuts through younger formations, the Montney is overlain by the Doig Formation or the Sunset Prairie Formation (Furlong et al., 2018).

Burial depth, thermal maturity, and bottom-hole temperatures also increase along the northeast to southwest trend. Burial depth increases from under <1000 m in the northeast to over 4000 m close near the Rocky Mountains deformation front. Formation temperatures and thermal maturity increase from less than 50°C and a vitrinite reflectance (Ro) of 0.59% in the shallow northeast to more than 100 $^{\circ}$C and R$_{o}$>2% in the southwest (Riediger et al., 1990;

Ibrahimbas and Riediger, 2004; Romero-Sarmiento et al., 2016; Wood and Sanei, 2016; Crombez et al., 2017).

4.3 Methods

4.3.1 Materials and sampling

The data set for this study includes five long cores, retrieved from different locations in the Montney Formation (Fig. 4.1). Cores represent five fields in the Montney Formation and were chosen because they cut through all or most of the formation. Two cores were selected to represent distal and deeply buried section of the basin (wells 1 and 2) one well (well 3) was selected to represent a deeply buried section that is proximal to the Meosin-Muinok high; Fig. 4.1). The last well (well 4) was selected to represent a proximal section of the basin that is buried to a shallow depth (Fig. 4.1).

The data obtained for each well in the study are summarized in Table 4.1. Ten cm long samples were cut at 1 to 3 m intervals from the back of cores 1 to 4. Data for well 5 was received directly from Birchcliff Energy Ltd. A suite of well logs obtained for each well included a minimum of gamma-ray (GR), density (RHOB), and neutron porosity (NPHI). Meticulous depth-matching between core gamma and downhole wireline gamma logs was performed using the stretch and squeeze method.

4.3.2 Core description

We performed detailed (1 cm scale) sedimentological description of cores 1-4 (total length of 583.5 m) to identify lithofacies in the Montney Formation. Information used for lithofacies identification includes (1) lithology, (2) grain size, (3) physical sedimentary structures, (4) trace fossil assemblages, and (5) bioturbation intensity (BI).

166

Table 4.1: summary of analyses

Well #	Well location	core description	sample type	QEMSCAN	TOC	He-pycnometry Crushed rock	Pulse decay	MICP[f]	BET[g]	Well-Logs[f]
1	16-17-083-25w6m	available	Core samples	63[a] (1-16)[b,c]	38 (2-21)[b,d]	31[a] (2-20)[b,d]	0	10	7	GR, RHOB, NPHI, core GR
2	16-29-079-20W6	available	Core samples	67 (1-4)	62 (1-7)[d]	62 (1-7)	44	16	10	GR, RHOB, NPHI, core GR
3	05-24-063-6W6	available	Core samples	40 (2-3)	40 (2-3)[d]	50 (0.5-5)	19	0	8	GR, RHOB, NPHI, core GR
4	103/05-20-079-22W5	available	Core samples	68 (1-2)	24 (1-6)[d]	34 (1-3)	0	0	4	GR, RHOB, NPHI, core GR
5	06-03-079-13W6	Not Available	Pseudocuttings	314 (0.14-1.56)	75 (1-9)[d]	109 (1-6)	110	47	0	GR, RHOB, NPHI, core GR

[a]Number of samples analysed.
[b]sampling interval for the specific analysis, meters.
[c]Large distance between samples due to missing core.
[d]TOC in wt%, obtained from Leco TOC analysis.
[e]TOC in wt%, obtained from RockEval analysis.
[f]Mercury Injection - Capillary Pressure.
[g] Adsorption/desorption BET analysis.
[h]GR=Gamma Ray; RHOB=density; NPHI=neutron porosity.

4.3.3 Mineralogical composition

Quantitative mineralogical composition was obtained through QEMSCAN analysis at SGS Canada laboratories in Burnaby, Canada. For this analysis, a small sub sample ($\sim$ 2 cm^2) was cut perpendicular to bedding from each of the core samples. In addition, a continuous thin sliver was cut along the entire length of core 5. The sliver was then divided into 314 intervals (0.14-1.56 m in length; most $\sim$1 m) and each interval was crushed to generate pseudo-cuttings. A random subsample from each interval ($\sim$50 g) was collected and sent for QEMSCAN analysis. The repeatability of QEMSCAN measurements is very high, with results commonly being over 98% similar between repeated measurements of the same sample (Power, pers. Com.). In QEMSCAN analysis, the minimal grain/mineral size reported is limited by the pixel size selected for analysis, 4.8 μm in this study. However, clay minerals in this study were commonly aggregated into clumps rather than single laths, and we found that a pixel size of 4.8 μm is sufficient for appropriate description of the rock.

Twenty-three samples were subjected to quantitative bulk composition and clay mineral XRD analysis. Three samples were analyzed at the James Hutton Institute, Aberdeen, Scotland. X-ray diffraction patterns were recorded with a Panalytical Xpert Pro instrument using Ni-filtered CuKα radiation and an Xcelerator position-sensitive detector, counting for 100 seconds per 0.0167° step between 3-70°2θ. The clay fraction (<2μm) was separated by timed sedimentation in water, prepared as oriented mounts on glass and scanned between 3-45°2θ in the air-dried state and after glycolation. The remaining 20 samples were analyzed at the Mineralogy Facility at the **Indiana University in** Bloomington with a Bruker D8 Advance X-Ray Powder Diffractometer, using CuKα radiation and a Si(Li) energy-dispersive detector, counting for 2 seconds per 0.02° step between 2-70°2θ. Clay fraction (<2μm) was separated by timed sedimentation in water, and concentrates were prepared as randomly oriented mounts on quartz slides and scanned between 2-20°2θ in the air-dried state and after glycolation.

4.3.4 Organic content

Total organic carbon was measured on all samples using LECO TOC analysis at Geomark Research in Humble, TX. For cores 1 to 4, a split of the sample was crushed and homogenized, and a subsample was randomly selected for testing. Wells 1, 2, and 3 were drilled through an overmature (dry gas) area of the Formation, and all the organic matter in the sample is assumed to be insoluble pyrobitumen. Samples from core 4 were oil-saturated and therefore cleaned prior to analysis by solvent mixture of chloroform (47 wt%), methanol (23 wt%), and acetone (30 wt%). For core 5, a random sample was selected from the 1 m interval pseudocuttings and sent for analysis. A total of 75 pseudocutting samples and 164 core split samples were analyzed for organic carbon content.

4.3.5 Petrography

To examine the morphology and distribution of pores in the siltstone, we used scanning electron microscopy (SEM) imaging. Both polished and non-polished (freshly broken) samples were coated with carbon or gold before imaging. to obtain smooth surfaces samples were mechanically polished and then ion-milled with a Fischione Model 1060 SEM Mill at the University of Alberta, Edmonton. SEM analysis and energy dispersive X-ray spectroscopy (EDS) analysis were performed on a JEOL 6301F Field Emission SEM (FE-SEM) or a Zeiss EVO LS15 EP-SEM, with an accelerating voltage of 20 kV, at the University of Alberta. In addition, we used SEM-Cathodoluminescence (SEM-CL) imaging to study the fabric morphology of the rock and differentiate detrital grains from cements. SEM-CL images were captured with a FEI Quanta 250 FEG with a GATAN MonoCL4 detector (SEM-CL) at the University of Calgary.

4.3.6 Pore volume measurements

Pore volume measurements were obtained with multiple techniques: QEMSCAN analysis, He-pycnometry on crushed rock samples and plugs samples, and mercury injection-capillary pressure analysis (MICP). Porosity reported from QEMSCAN analysis (552 samples) includes

only pores >4.8 µm, and as QEMSCAN cannot distinguish between open pores and pores filled with organic matter, both are reported together. Matrix porosity (He-pycnometry analysis) was measured on samples crushed and sieved to <2 mm particles using a Quantachrome Pentapyc analyzer 5200e. Samples from wells 1, 2, and 4 (134 samples) were analyzed at Trican (now AGAT) laboratories in Calgary, Alberta. Samples from well 3 were analyzed by Terratek, Salt Lake City, Utah (50 samples), and samples from well 5 (109 samples) were analyzed at Core laboratories in Calgary, Alberta.

Porosity of 1'' diameter plug samples from well 3 (64 samples) was measured with a Quantachrome Pentapyc analyzer 5200e at the University of Alberta. Matrix porosity was also measured using MICP technique. All measurements were conducted with a Micromeretics Autopore IV 9000/9510 with analyses running between 0 and 400 MPa. Samples from well 1 (10 samples) were analyzed at the University of Alberta. Samples from well 2 (16 samples) were analyzed at Trican (now AGAT) laboratories in Calgary, Alberta, and samples from well 5 (47 samples) were analyzed at Core Laboratories in Calgary, Alberta.

4.3.7 Permeability measurements

Matrix permeability of crushed samples was acquired at the same time with matrix porosity by measuring pressure decay over time during He-pycnometry analysis. Matrix permeability was obtained for samples from wells 1, 2, 3, and 4. Plug permeability was measured on 1'' diameter horizontal plugs from wells 2, 3, and 5 using the pulse decay method. Samples from well 2 (44 samples) were analyzed at Weatherford Laboratories, Calgary, using a Hassler type bi-axial core holder and confining pressure of 5.5 MPa (800 psi). Samples from well 3 (19) were analyzed at the University of Alberta using an NDP-605 nanodarcy permeameter with a confining stress of 10.3, 20.7, 27.6 MPa (1500, 3000 and 4000 psi). Samples from well 5 (110 samples were analyzed with a CMS - 300 device under confining stress of 5.6 and 13 MPa (800 and 1884 Psi). Klinkenberg correction was applied to all pulse decay permeability measurement results.

4.3.8 Nitrogen adsorption/desorption analysis

Nitrogen adsorption and desorption analysis was conducted using a Quantachrome Autosorb-1 at the nanoFAB Facility at the University of Alberta. The device measures the amount of nitrogen gas adsorbed to the surface of a sample at increasing pressures and then the amount of nitrogen desorpted from the sample at decreasing pressures. Adsorption and desorption data can be used to calculate surface area and pore size distribution of the samples. The results are presented as adsorption/desorption hysteresis loops. The shapes of these hysteresis loops are associated with different pore shapes (De Bore, 1958).

A total of 24 samples from cores 1 to 4 were analyzed, selected to represent all lithofacies and a wide range of rock compositions. Samples were crushed and sieved to 0.5-1 mm particle size, dried overnight and then degassed under high vacuum at 150°C. Adsorption and desorption isotherms were recorded, and sample surface area was calculated using the BET model (Brunauer et al., 1938; Schettler et al., 1989) in P/P_0 range of 0 to 0.3. The BET method can be used to calculate pore volume versus pore size distribution. However, this model generally underestimates the volumes of micropores and small mesopores (Ravikovitch et al., 1998). Therefore, we also applied the Density Functional Theory (DFT) molecular model (Do and Do, 2003) to obtain pore size distributions in our samples, since micropores are common in fine-grained rocks (Kulia and Prasad, 2011; Labani et al., 2013; Dong et al., 2015; Ghanizadeh et al., 2015).

4.4 Results

4.4.1 Core description

We identified 14 lithofacies in cores 1 to 4. Lithofacies are distinguished mainly on the basis of sedimentary structures and ichnological features that were particularly important in the upper section of the formation. Seven of the lithofacies identified (A, B, E, F, G/H, J, and O) compose more than 90% of all cores. The discussion in this manuscript will be limited to those lithofacies. Distribution and characteristics of the major 7 lithofacies are reported in

Table 4.2, and representative images of the seven major lithofacies are presented in Fig. 4.3. Core descriptions and vertical profiles (porosity, permeability and rock composition) are presented in Fig. 4.4 - 4.8.

All the lithofacies are either silt-dominated or are either silt-dominated or silt-rich mudstones (Table 4.2). The most abundant lithofacies in the deeply buried distal wells 1 and 2, are the laminated siltstone (lithofacies G/H) and the massive siliceous clayey siltstone (lithofacies J). Lithofacies F (the faintly laminated calcareous siltstone) is another important lithofacies in wells 1 and 2. The most important lithofacies in the deeply buried proximal well 9 are the massive sandy siltstone (lithofacies B), the massive siliceous clayey siltstone (lithofacies J), and the hummocky to ripple cross-stratified sandy siltstone (lithofacies O). The dominated lithofacies n the shallow buried proximal well 15, is the interlaminated siltstone and sandstone alternation (lithofacies A). The dolomitic siltstone (lithofacies E) is the second most abundant lithofacies in well 15.

4.4.2 Rock composition and framework

Mineralogical compositions as obtained by QEMSCAN analysis for all five wells in the study are reported in Fig. 4.9. Major mineralogical phases include quartz, K-feldspar and Na-feldspar, micas, dolomite, Fe-rich dolomite, and calcite. Minor phases include pyrite, phosphate, anhydrite, and heavy minerals. Excluding outliers, clay mineral content varies between 1 and 30 wt%, QFM (total Quartz-Feldspar-Mica) content ranges from 40 to 80 wt%, and carbonate minerals (dolomite, Fe-rich dolomite, and calcite) show the larges range and vary from 20 to 90 wt% (Fig. 4.9). In vertical profiles, (Fig. 4.4 - 4.8) QFM generally varies antithetically to the total carbonate curve (dolomite, Fe-rich dolomite, and calcite), while total clay content correlates positively with QFM.

Table 4.2: Distribution and characteristics of lithofacies in the study cores

Facies	Lithology	Rock type classification [a]	Sedimentary structures	Trace fossil Assemblage	Bioturbation intensity	Average composition			% core2[c] (261 m)	% core 4 (185 m)	% core 9 (148 m)	% core 15 (51 m)	% all cores
						% Clay	% Silt	% Sand					
A	Interlaminated siltstone and sandstone alternation	Sand bearing, silt rich to sand and clay-bearing, silt rich mudstone	Dominant flaser and lenticular bedding, current ripples, rare climbing ripples, mud rip-up clasts and soft sediment deformation	*Thalassinoides, Conichnus, Planolites*, and escape structures	0-2	11.9 (4.5)[b]	65.0 (10.3)	23.1 (11.1)			10.6	53.1	16.8
B	Massive sandy siltstone	Silt-rich to sand-bearing, silt rich mudstone	Rare soft sediment deformation, flame structures, carbonate nodules, mud rip-up clasts, and high-angle cross bedding	N/A	0	5.1 (2.5)	76.0 (11.0)	19.0 (10.7)			37.7	12.0	13.1
E	Dolomitic siltstone	Dolomite cement-dominated to dolomite cement-rich, silt-dominated to sand and clay-bearing, silt-rich mudstone	Low-high angle bedding, and rare rip-up clasts/ dolomitic breccia	N/A	0	7.2 (3.4)	75.2 (13.3)	17.6 (12.7)				22.4	5.9
F	Faintly laminated calcareous siltstone	Calcite cement-bearing, clay-bearing, silt-rich mudstone	Horizontal parallel lamination, carbonaceous grains, and rare shell debris	Biodeformation structures	0-1	14.6 (4.0)	83.3 (6.8)	2.1 (5.0)	16.5			9.8	6.6
G/H	Laminated siltstone	Silt-dominated to clay-bearing, silt-rich mudstone	Horizontal parallel lamination, rare wavy bedding, current ripples, rare amalgamated current ripples, soft sediment deformation, and presence of dolomite beds	Biodeformation structures, Planolites, laminae disruption and escape structures	0-1	11.8 (3.3)	85.9 (3.2)	2.3 (2.7)	58.4	61.5	10.4		31.1
J	Massive siliceous clayey siltstone	Silica cement-bearing, silt-dominated mudstone to clay-bearing, silt-rich mudstone	Rare dolomite beds	N/A	0	12.5 (3.4)	86.0 (2.9)	1.5 (1.3)	9.2	21.3	20.7		12.6
O	Hummocky to ripple cross-stratificatified sandy siltstone	Silt rich to sand-bearing, clay-bearing, silt-rich mudstone	Hummocky cross-stratification, current ripples, climbing ripples, mud rip-up clasts, rare loading structures and soft sediment deformation	Rare *Planolithes*	0-1	6.0 (2.8)	82.0 (2.3)	12.0 (3.5)			20.5		5.4

[a] After Macquaker and Adams, 2003.
[b] Standard deviation 1σ.
[c] Facies % of core, normalize to exclude missing core sections.

Fig. 4.3: Representative photographs of the major Montney Formation lithofacies: (a) lithofacies A, interlaminated siltstone and sandstone alternation. (b) Lithofacies B, massive sandy siltstone with carbonate concentration (in white). (c) lithofacies E, dolomitic siltstone. (d) lithofacies F, faintly laminated calcareous siltstone (arrows point to faint laminations). (e) lithofacies G/H, Laminated siltstone. (f) lithofacies J, massive, siliceous clayey mudstone, and (g) lithofacies O, hummocky to ripple cross-stratified sandy siltstone. CR - current ripple, HCS- Hummocky cross stratification.

174

Fig. 4.4: Well 1. Curves from left to right are core description, gamma ray log, porosity, matrix permeability (He- pycnometry), and rock composition. Grayed area in the permeability curve is the error associated with the measurements (2σ). Error for matrix porosity is smaller than the width of the curve.
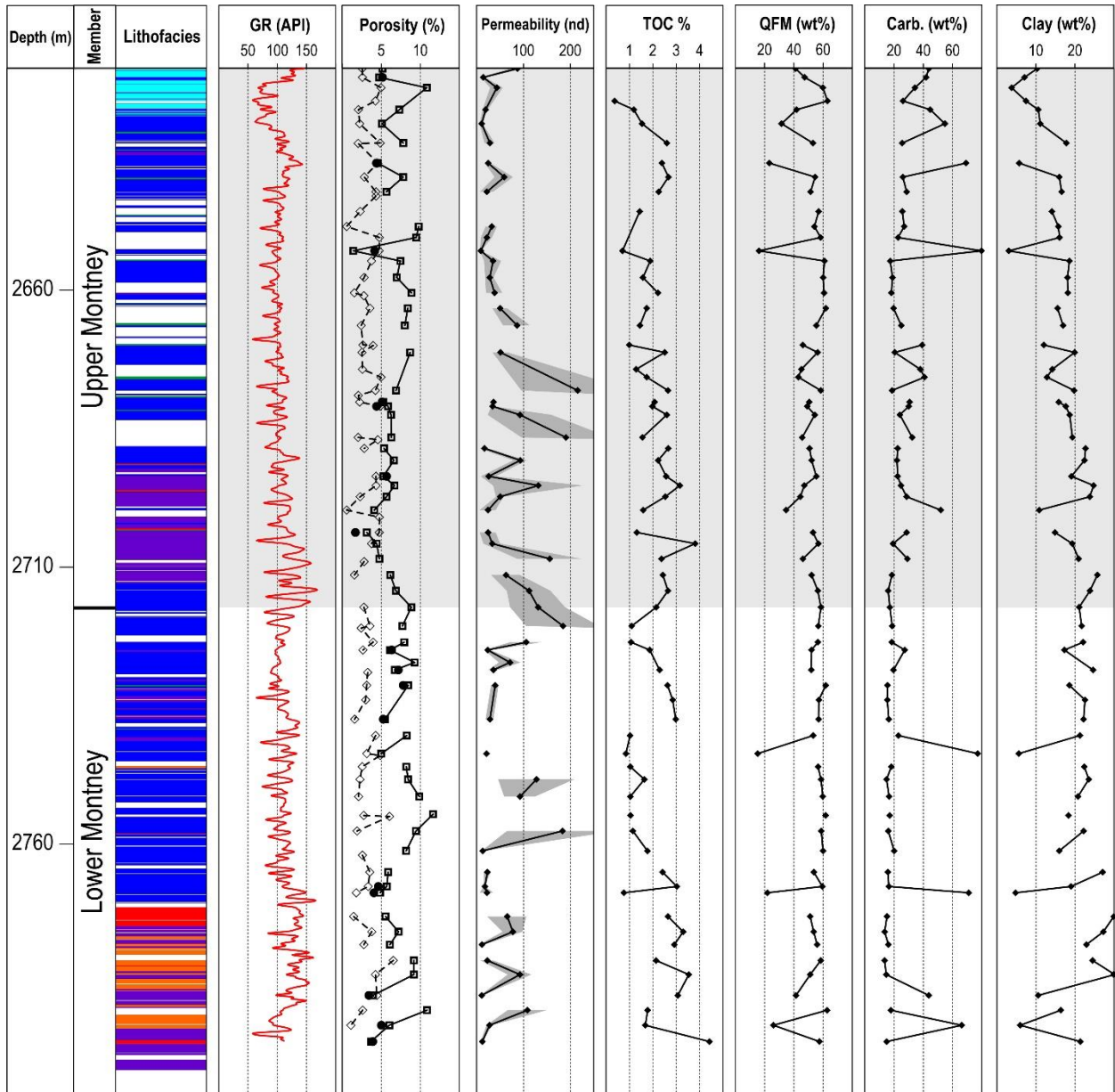
Fig. 4.5: Well 2. Curves from left to right are core description, gamma ray log, porosity, matrix permeability (He- pycnometry), and rock composition. Grayed area in the permeability curve is the error associated with the measurements (2σ). See legend in Fig. 4.4.
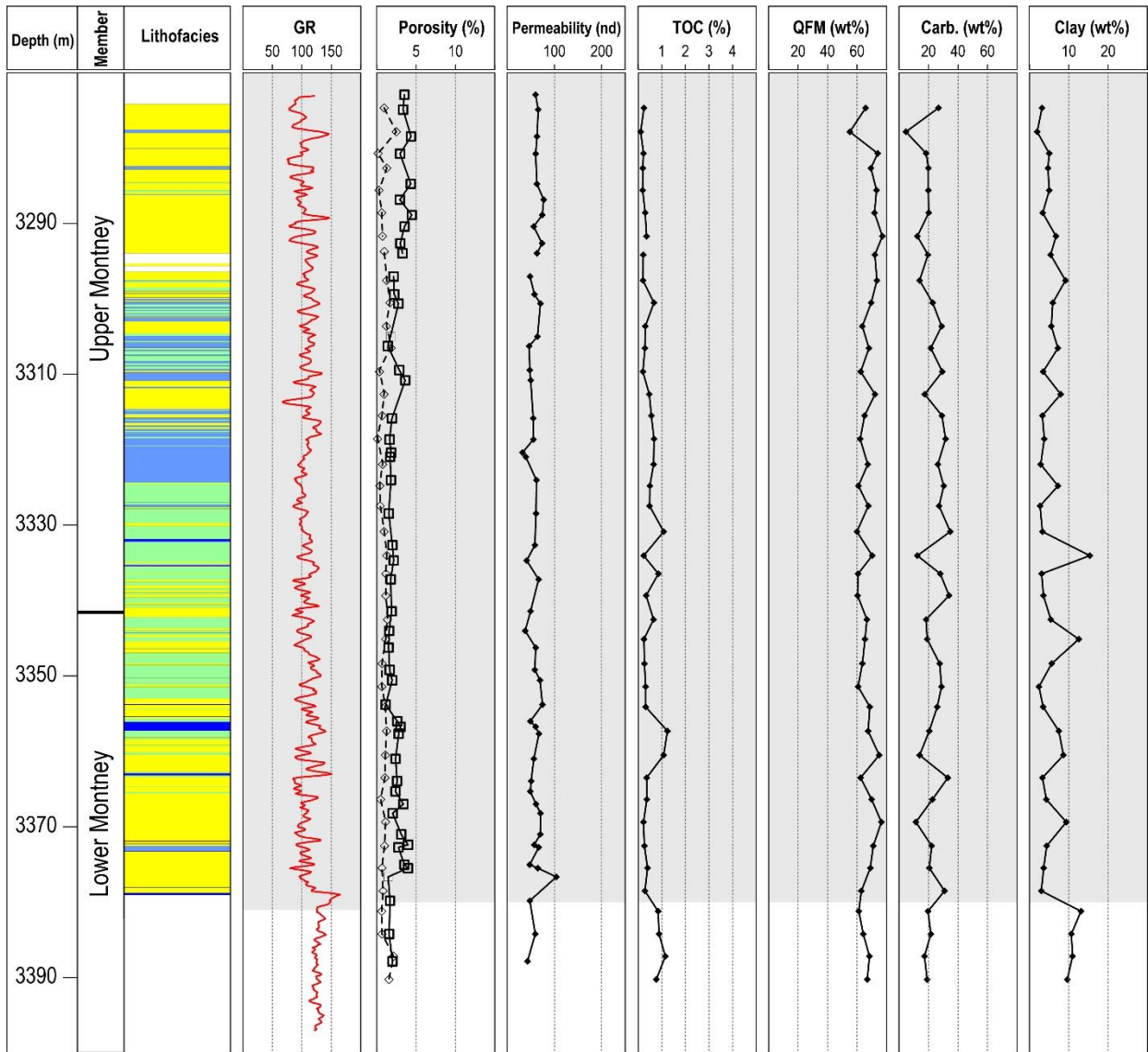
Fig. 4.6: Well 3. Curves from left to right are core description, gamma ray log, porosity, matrix permeability (He- pycnometry), and rock composition. Matrix permeability error was not reported. See legend in Fig. 4.4.
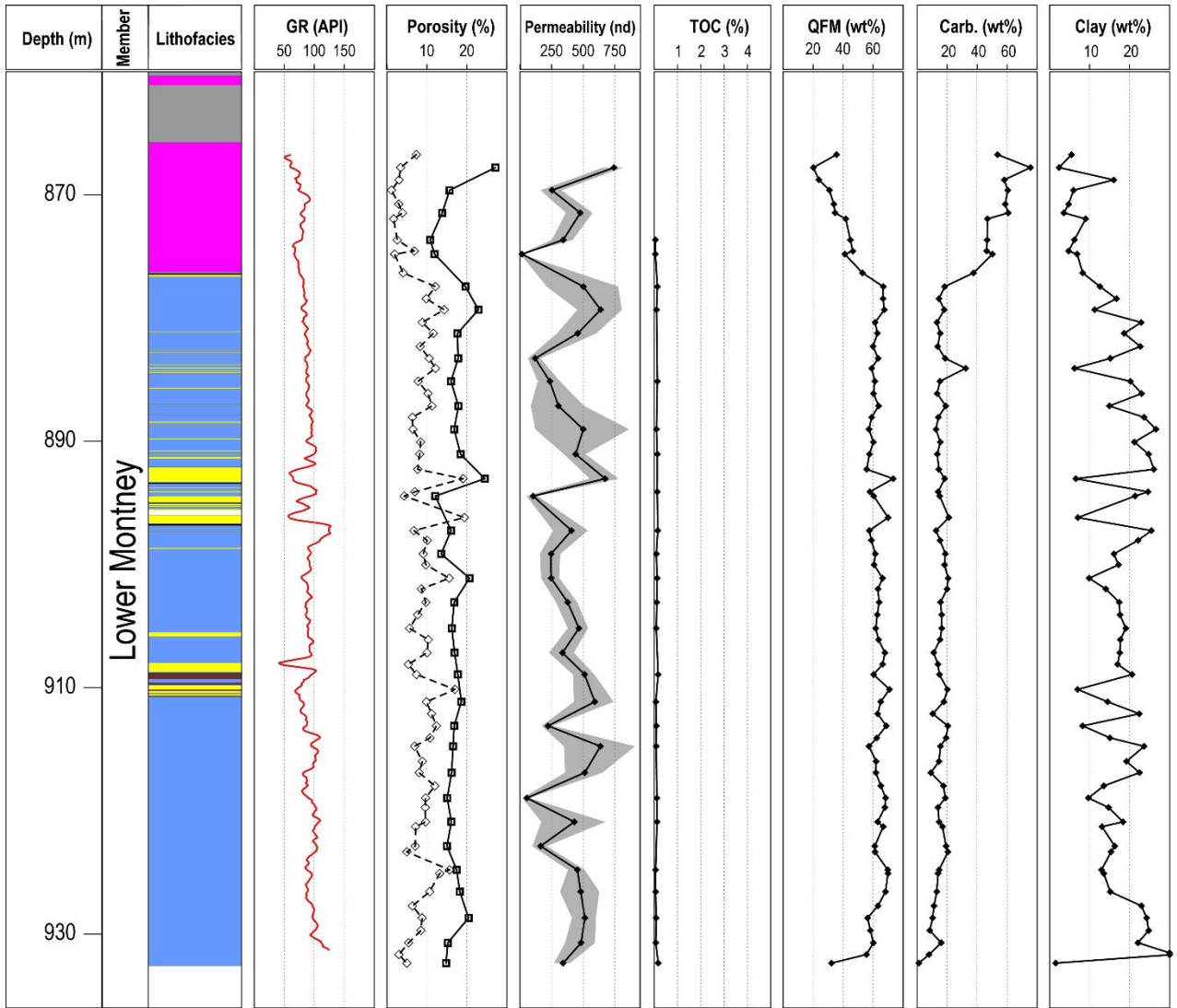
Fig. 4.7: Well 4. Curves from left to right are core description, gamma ray log, porosity, matrix permeability (He- pycnometry), and rock composition. Grayed area in the permeability curve is the error associated with the measurements (2σ). See legend in Fig. 4.4.
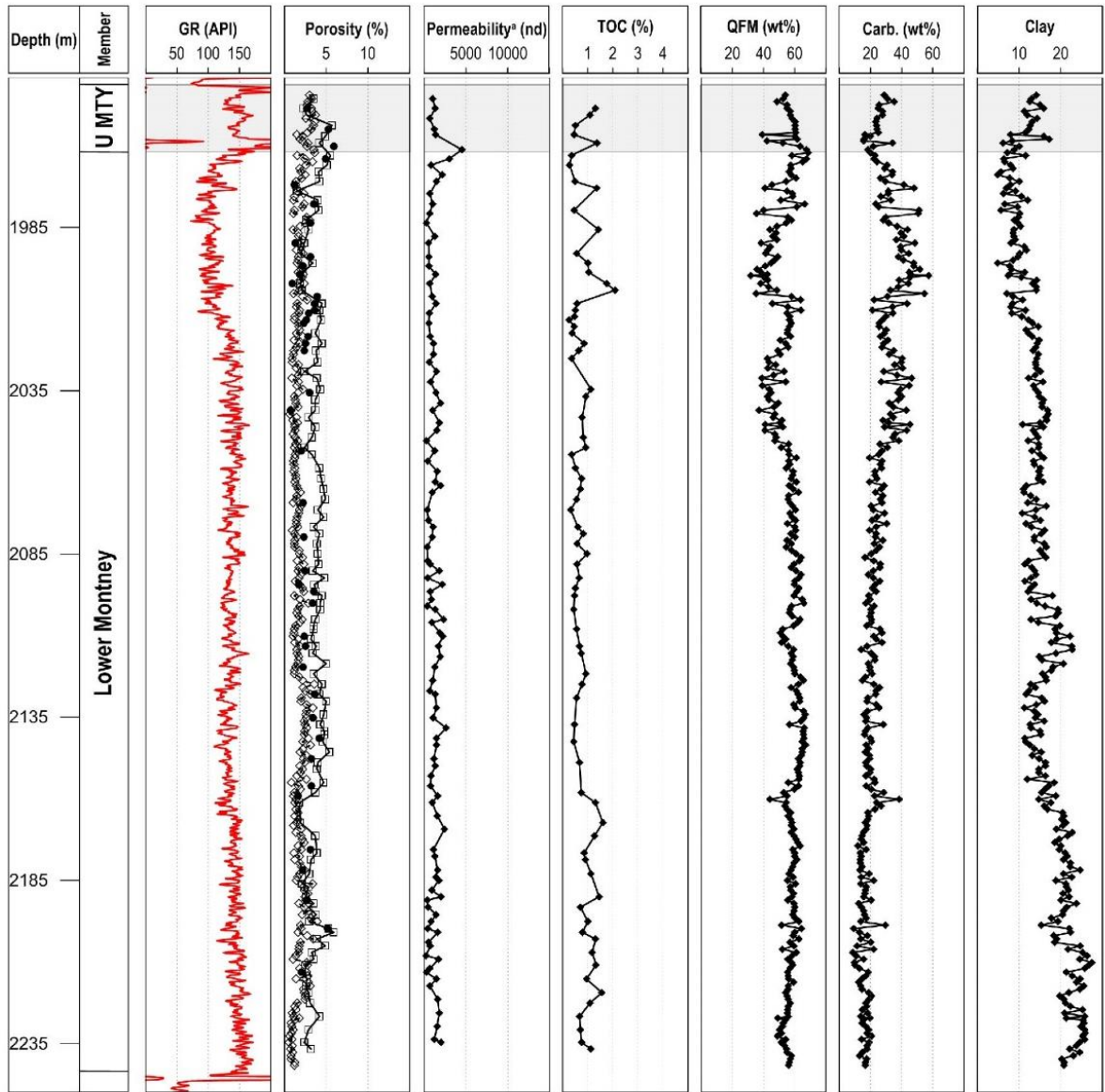
Fig. 4.8: Well 5. Curves from left to right are gamma ray log, porosity, plug permeability (He- pycnometry), and rock composition. Plug permeability error was not reported. See legend in Fig. 4.4.
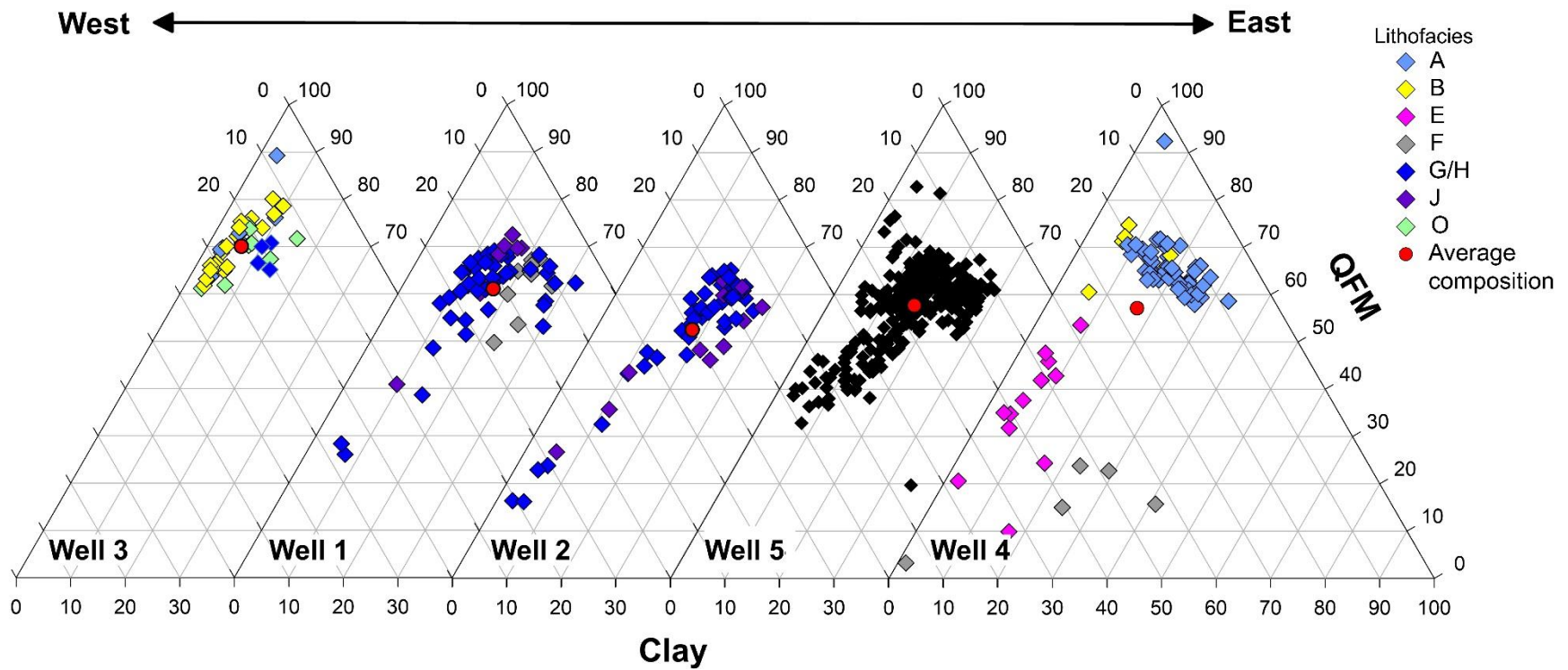
Fig. 4.9: Mineralogical compositions from QEMSCAN analysis for all five study wells. Mineralogical data for wells 1-4 is color coded by lithofacies. Note that with the exception of well 4, there are no significance differences in the mineralogical composition between different lithofacies. QFM is the sum of quartz, feldspars, and micas. Carbonate minerals include calcite, dolomite, and Fe-dolomite. Clay minerals include mixed layer illite-smectite and kaolinite.

Total organic carbon content ranges from <1 wt% to a maximum of 4.4 wt%, with an average of 1.1 wt%. Well 3 has the lowest TOC content (<0.2 wt% for all samples). Average TOC content is higher in the Upper Montney Member than the Lower Montney Member in well 1 (1.8 and 1.0 wt%, respectively), but not in wells 2 and 3. Wells 4 and 5 are missing all or most of the Upper Montney Member, rendering this comparison impossible. Images of ion-milled surfaces reveal hard framework composed of grains and cements, with organic matter and clays filling some of the pores between hard minerals (Fig. 4.7a, b). No depositional organic macerals were identified in SEM imaging analysis.
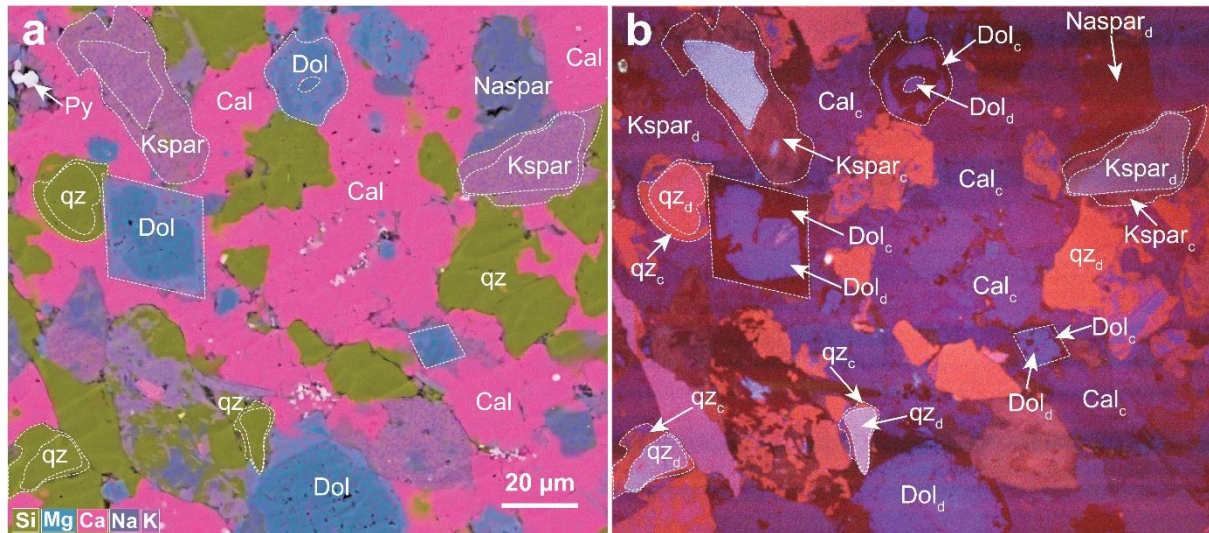
Fig. 4.10: EDS-SEM (a) and SEM-CL (b) images of showing highly cemented framework. Hard detrital grains (d) are surrounded by cement (c). Most contacts are between hard grains or cements. Core 2, sample 3AJ, 2653 m. Dol is dolomite, Cal is calcite, Kspar is K-feldspar, Naspar is Na-feldspar, qz is quartz.

4.4.3 Pore volume

Porosity values obtained by QEMSCAN, He-Pycnometry, and MICP analyses are presented in Fig. 4.4 - 4.8 and Fig. 4.11. Porosity reported from QEMSCAN analysis is macroporosity (> 4.8 μm) and may include organic matter-filled pores as well as open pores. QEMSCAN macroporosity values in our samples range from 0.1 to 22.7%, with an average of 3.1%.

Porosity measured through He-pycnometry represents total porosity, as helium molecules can penetrate pores as small as 140 pm (Anovitz and Cole, 2015). Porosity measured through He-pycnometry is measured on crushed samples and is thus considered as the matrix porosity (excluding fracture porosity). The error on measured porosity is <6% of the measured value. Matrix porosity is almost always larger than QEMSCAN porosity and ranges between 1.4 and 27.1%, with an average of 6.7% and a median value of 5%. Well 4 has significantly higher He-pycnometry values than all other wells (average of 17.1%). When excluding well 4 from the calculation, the average total porosity in our Montney samples decreases to 5.1%.

The smallest pore diameter identifiable by MICP analysis is 3 nm. MICP porosity measurements were available for wells 1, 2, and 5 and range from 0.7 to 7.1% with an average of 3.2%. With all methods, the average porosities of the Upper and Lower Members of the Montney Formation are within 1% of one other with the exception of well 1, where QEMSCAN porosity in the Upper Member samples has almost double the average porosity of the Lower Member (4.0% and 2.1%, respectively). Excluding the shallow well 4, matrix porosity generally increases with increasing burial depth (Fig. 4.11).

4.4.4 Pores morphology and size distribution

We identified seven pore types in our samples through thin section analysis and SEM imaging of both polished and ion-milled surfaces. Primary interparticle pores are present in all samples and are commonly <2 μm in diameter (Fig. 4.12a). In well 4, primary interparticle pores are abundant, and in some intervals, pores can reach over hundred micrometers (Fig. 4.12b). Nanometer-scale spaces between minerals are common in SEM images of all our samples (Fig. 4.12c), although it is unclear whether these spaces are a true feature of the rock or an artifact of associated with pressure release during core retrieval (Clarkson et al., 2015). (2) Dissolution pores do not appear in all samples but are important locally, particularly in well 4. Dissolution pores are usually <1 μm and appear at boundaries between organic

matter and dolomite (Fig. 4.12d), within detrital feldspar or dolomite grains (Fig. 4.9e), or within biotite and mica-like chlorite grains (Fig. 4.12f) but are rare in muscovite.

In well 4, large (>5μm) dissolution derived pores are common in dolomite and feldspars (Fig. 4.12g). Pores related to grain deformation occur mainly mica and dolomite grains. Micropores (Fig. 4.12h) developed as a result of mica layers splitting along cleavage planes are common and were identified in most samples. Pores generated by deformation of dolomite grains appear as fractures along cleavage planes (Fig. 4.12i), identified in a small number of samples. Pores developed within organic matter are common, but not all organic matter is porous, and frequently porous and non-porous organic matter are found in very close proximity (Fig. 4.12c, j). Pores were also identified between crystals of pyrite framboids (Fig. 4.12k) in all our samples. In some cases, pores within the framboids are filled with organic matter, which can be either porous or non-porous. Finally, pores are developed between clay particles. Not all samples are clay-rich, but in most samples, porosity within clay particles is substantial (Fig. 4.12l).

Information about pores morphology is also obtained from the shape of nitrogen adsorption and desorption hysteresis loop. Adsorption-desorption hysteresis loops of representative samples are presented in Fig. 4.13a-c. Hysteresis loops of all samples have shapes that are consistent with Type B loops and are associated with slit-shape porosity (De Bore, 1958). Our observations are consistent with previously reported results for Montney samples (Ghanizadeh et al., 2015, 2018).

nternal surface areas of samples, calculated from nitrogen adsorption data with the BET model vary between 1.4 m^2/gr and 21.6 m^2/gr, with an average of 8.3 m^2/gr. The average surface area in well 3 (3.8 m^2/gr) is significantly less than average surface area of samples from all other wells (7.9 to 11.5 m^2/gr). Our results are similar to previously reported surface area values for the Montney (Chalmers and Bustin, 2012; Ghanizadeh et al., 2018), although Ghanizadeh et al. (2015) reported lower surface area values, ranging from 0.3 to 2.1 m^2/g. The volume of mesopores is positively correlated with surface area (R^2 = 0.71), indicating

that macropores make a smaller contribution to the surface area of the sample, also noted by

Chalmers and Bustin (2012).
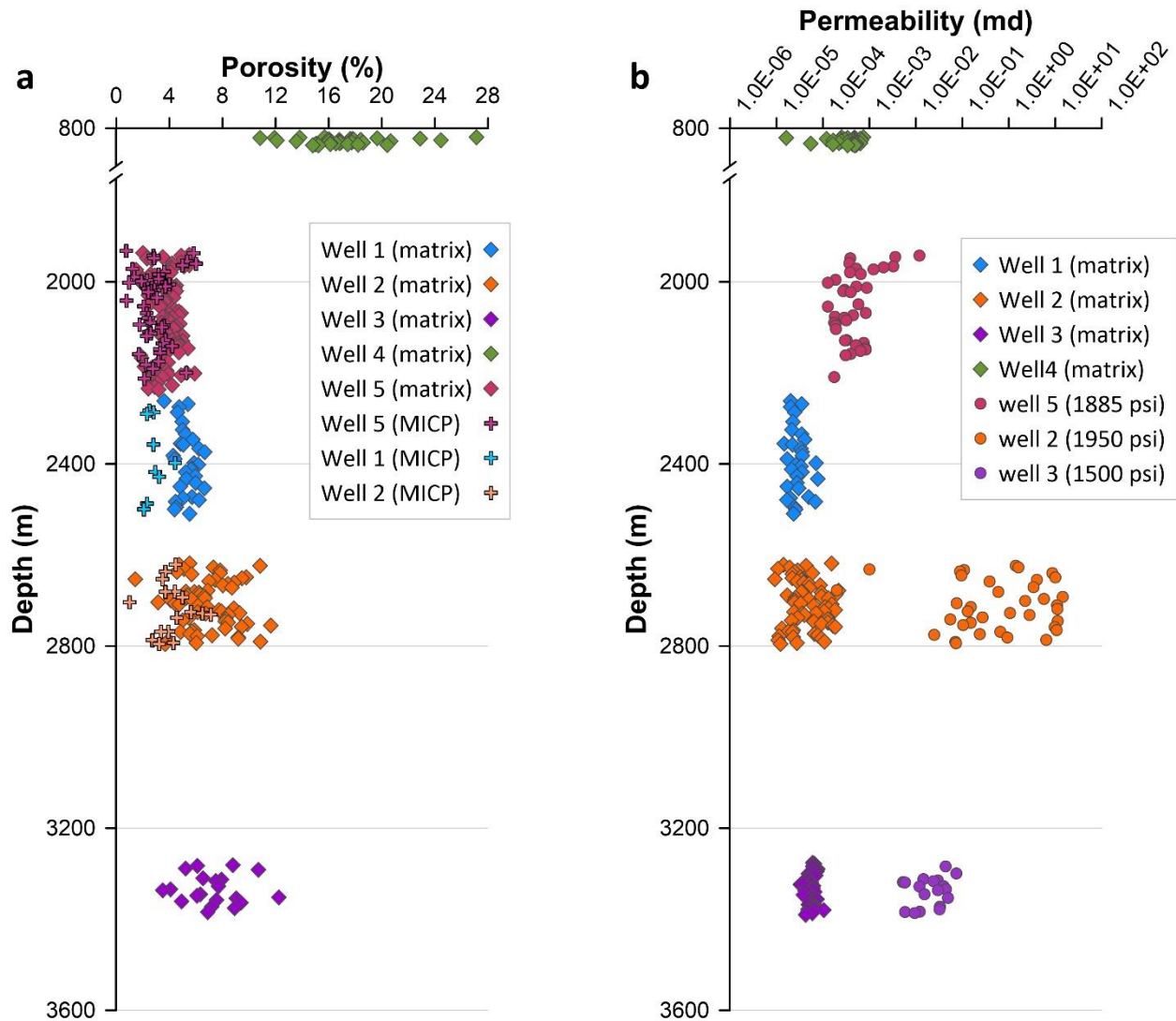
Fig. 4.11: Porosity and permeability of all 5 study wells. Matrix porosity and permeability refers to permeability obtained by obtained by He-pycnometry on crushed rock. (a) Porosity. With the exception of well 4, there is a general trend of increasing matrix porosity (diamonds) with depth between wells. MICP porosity (plus symbols) is always lower than matrix porosity. (b) Permeability. Pulse decay plug permeability (circles) is always larger than matrix permeability (diamonds) in the same well.
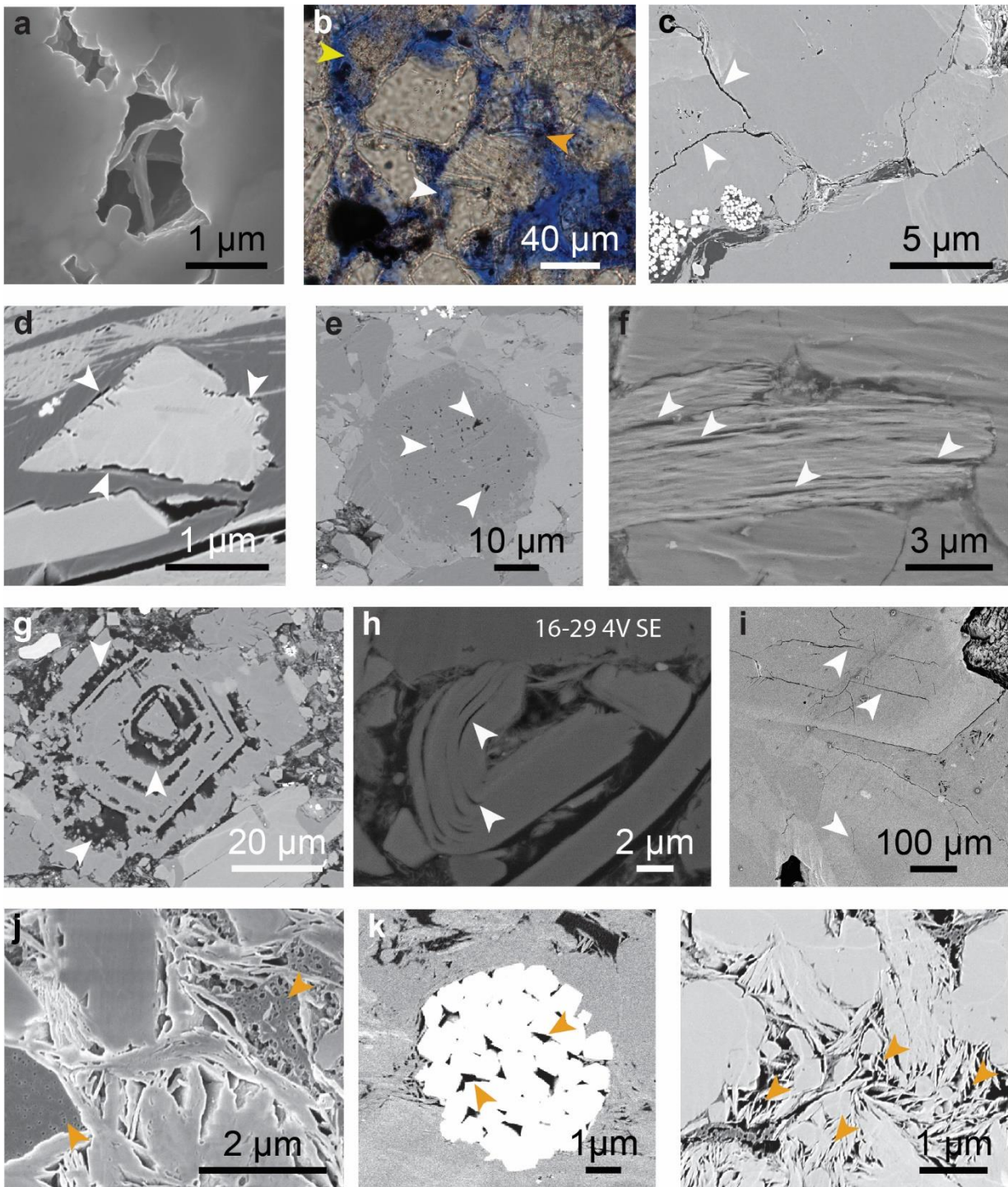
Fig. 4.12: Pore types in the Montney Formation. (a) SEM-SE image of a primary interparticle pore. Note clay strands bridging the pore. Well 3, Sample 1C, 3278 m. (b) Thin section micrograph showing primary interparticle porosity (white arrow) and secondary porosity generated by the dissolution of dolomite (yellow arrow) and mica (orange arrow). Well 4, sample 1AC, 867 m. (c) Gaps between grains (arrows). It is not clear whether these gaps a true feature of the rock or whether they were generated through pressure relive during core retrieval. Well 1, sample 3A, 2285

(d) Dissolution derived porosity at the boundary between organic matter and dolomite (arrows). Well 1, sample 9P, 2366.2 m. (e) Dissolution derived porosity in a detrital dolomite grain, (arrows). Well 2, sample 3AJ, 2653 m. (f) Dissolution derived porosity in a mica grain (arrows). Well 3, sample 1C, 3278 m. (g) Large dissolution generated pores (arrows) in dolomite. Well 4, sample 1AE, 864.9 m. (h) Microporosity (arrows) generated through grain deformation in a mica. Well 2, sample 4V, 2703 m. (i) Microfractures (arrows) developed along cleavage planes in a dolomite grain. Well 1, sample 16I, 2487 m. (j) Porosity developed within organic matter (dark grey). Note the differences in porosity between two patches of organic matter (arrows) that are less than 5 μm apart. Well 1, sample 11H, 2410 m. (k) Porosity between crystals of pyrite framboids (arrows). Well 1, sample 11H, 2410 m. (l) Porosity in between clay particles (arrows). Well 1, sample 17O, 2499 m.

Three pore types were identified, based on the shape of the hysteresis loops. The hysteresis loop of group one samples resembles a hockey stick (Fig. 4.13a). These samples commonly have a low surface area (< 3.4 m^2/g), low TOC (< 1 wt%), low clay content (<13%; commonly < 7.5 wt%), and average matrix porosity of 6.4%. The hysteresis loop of group two samples resembles a feather (Fig. 4.13b). These samples commonly have a moderate to high surface area (commonly 8-14 m^2/g, but can be as high as 21.6 m^2/g), medium to high TOC (commonly 1.5-2.5 wt%, but up to 4.4 wt%), low to moderate clay content (10-26 wt%), and average matrix porosity of 5.7. The hysteresis loop of group three samples resembles a banana (Fig. 4.13c). These samples commonly have moderate surface area (9-10 m^2/g), low to moderate TOC (commonly ~1.5 wt%, but in some cases very low), low to moderate clay content (10-20 wt%), and relatively high average matrix porosity of 10.6%.

Pore size distribution for representative samples calculated by applying the DFT model is presented in Fig. 4.13d-e. In fine-grained rocks, pores are classified into macropores (>50 nm), mesopores (2-50 nm) and micropores (<2 nm). The majority of the pores in all our samples are in the mesoporosity range (89 to 100% of pore volume), with a small portion (0 to 11% of total pore volume) in the macroporosity range. Based on these calculations, none of the samples contains pores smaller than 2 nm, and in three of the samples   the smallest pore diameter identified was 8 nm. However, it is important to note an increase in pore volume in the lower pore diameter size in many of our samples (for example sample 2AC in

Fig. 4.13d and sample 16Q in Fig. 4.13f), suggesting that smaller pores exist in the sample but are unresolved by our analytical approach.

Maximum pore diameters vary between 40 and 180 nm, but for most samples, the largest pore diameter is around 45 or 75 nm. Plots of pore volume versus pore diameter (Fig. 4.13d-e) show that the dominant pore size in most samples is at 5 nm, with a secondary peak around 3.5 nm, regardless of the total pore volume. However, a small number of the samples have dominant pore diameter of approximately 20 nm, and in one of the samples, the main peak is at 3.5 nm (Fig. 4.13f).

Ghanizadeh et al. (2015, 2018) and Chalmers and Bustin (2012) used the BJH model (rather than the DFT method used in this study) to model pore size distribution. Their results are, for the most part, comparable with our results, although Chalmers and Bustin (2012) reported a much larger portion of macropores in their samples (20 to 56% of pore volume versus <11% in this study).

4.4.5 Pore throats size distribution

In addition to total porosity values, MICP analyses also provides pore throats size distribution. Pore throats size distributions of representative samples are presented in Fig. 4.14. In all samples, the major pore throat size is between 7 and 9 nm. Many of the samples have a secondary peak at either 13 nm or 32 nm. The presence of pore throats > 10 μm was documented in most samples, but for the most part, they appear in low frequency. In four samples, the highest peak is associated with pore throats of 7 to 10 μm. The smallest pore throat size identified through MICP analysis in any of the samples is 3 nm, which is the smallest pore diameter identifiable by MICP analysis under these experimental conditions. Similar results were reported by Chalmers and Bustin (2012) and Yang (2018).
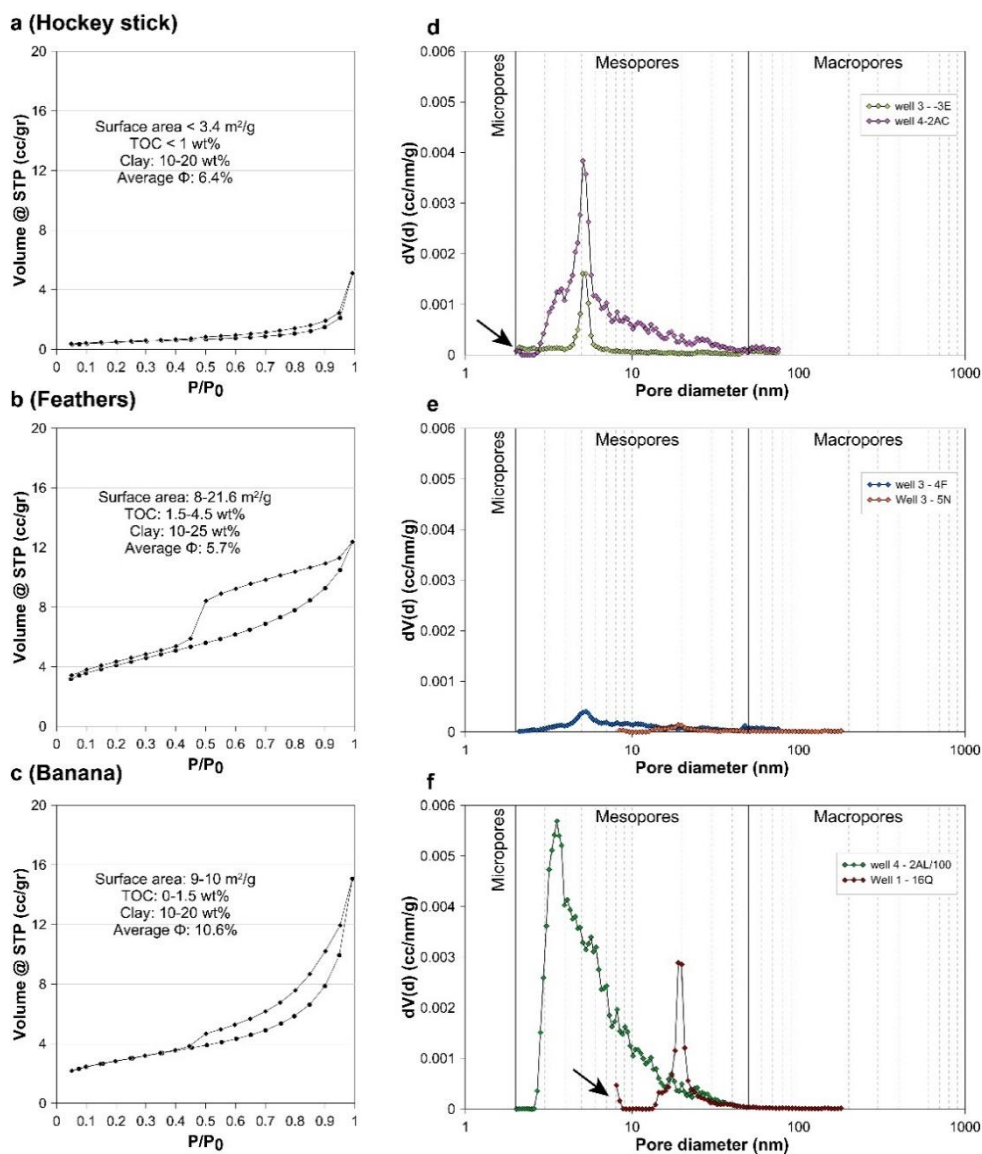
Fig. 4.13: Representative nitrogen adsorption-desorption analysis results. Three groups were identified based on BET hysteresis loops (a) Samples with a hockey stick shape hysteresis loop. Well 3, sample 4F 3366 m. (b) Samples with a feather shaped hysteresis loop. Well 2, sample 2O, 2637 m. (c) Samples with a banana shaped hysteresis loop. Well 2, sample 2AC, 2623. Representative values of surface area, TOC, clay content and porosity are presented for all three groups. Pore size distribution (DFT model) indicates a majority of mesopores and a small fraction of macropores. Note that some samples have increased pore volume in the lower pore diameter size (black arrows e), indicating that smaller pores exist in the sample. (d) Samples in this group has a main peak at 5 nm, and some samples have a secondary peak at ~3.5 nm. Well 3, sample 3E, 3339 m, well 4, sample 2AC, 905 m. (e) Samples in this group have a flat PSD pattern relative to all other samples, indicating very low pore volume. Main peaks are commonly at 3.5 nm and 5 nm but can also be at 20 nm. Well 3, sample 4F, 3366 m, Well 3, sample 5N, 3378.5 m. (f) Outlier samples. One PSD pattern shows the main peak at 20 nm (16Q). The other sample (2AL) has the main peak at 3.5 nm. Note that incremental pore volume is divided by 100, indicating very large pore volume in this sample. Well 4, sample 2AL, 896 m, Well 1, sample 16Q, 2479 m.

188

4.4.6 Permeability

Vertical profiles of matrix permeability are presented in Fig. 4.4 - 4.8. Matrix permeabilities for wells 1, 2, and 3 vary between 9 and 191 nd with an average of 54 nd. For well 4, matrix permeability is usually higher, (16 to 744 nd), with an average of 392 nd. The error on matrix permeability analysis (Fig. 4.4 - 4.8) varies between 2 and 74% and averages 34% (1σ). This error does not change stratigraphic (vertical) permeability trends or the order of magnitude of the permeability for all four wells. No clear depth trend of matrix permeability was identified within wells (Fig. 4.4 - 4.8) or between wells (Fig. 4.11b). Where comparison between stratigraphic units is possible (wells 1 and 2), the average permeability is slightly higher in the Lower Member than in the Upper Member of the Montney Formation.

Plug permeability measured by pulse decay on samples from wells 2, 3, and 5. Permeability measurements on plugs reported as visibly fractured were discarded. Plug permeability values varies over several orders of magnitude, between 1.7 nd and 90 md ($9*10^7$ nd), with an average of 2.9 md ($2.9*10^6$ nd). In well 2, 42 of the 44 plugs taken were reported as fractured. All the fractured plugs have permeability larger than 0.001 md ($1*10^3$ nd). Pulse-decay permeability shows no trend with depth in either of the individual wells and between wells (Fig. 4.11b). Due to the limited number of measurements, it is impossible to compare pulse decay permeability results between the Upper and Lower Members of the formation.
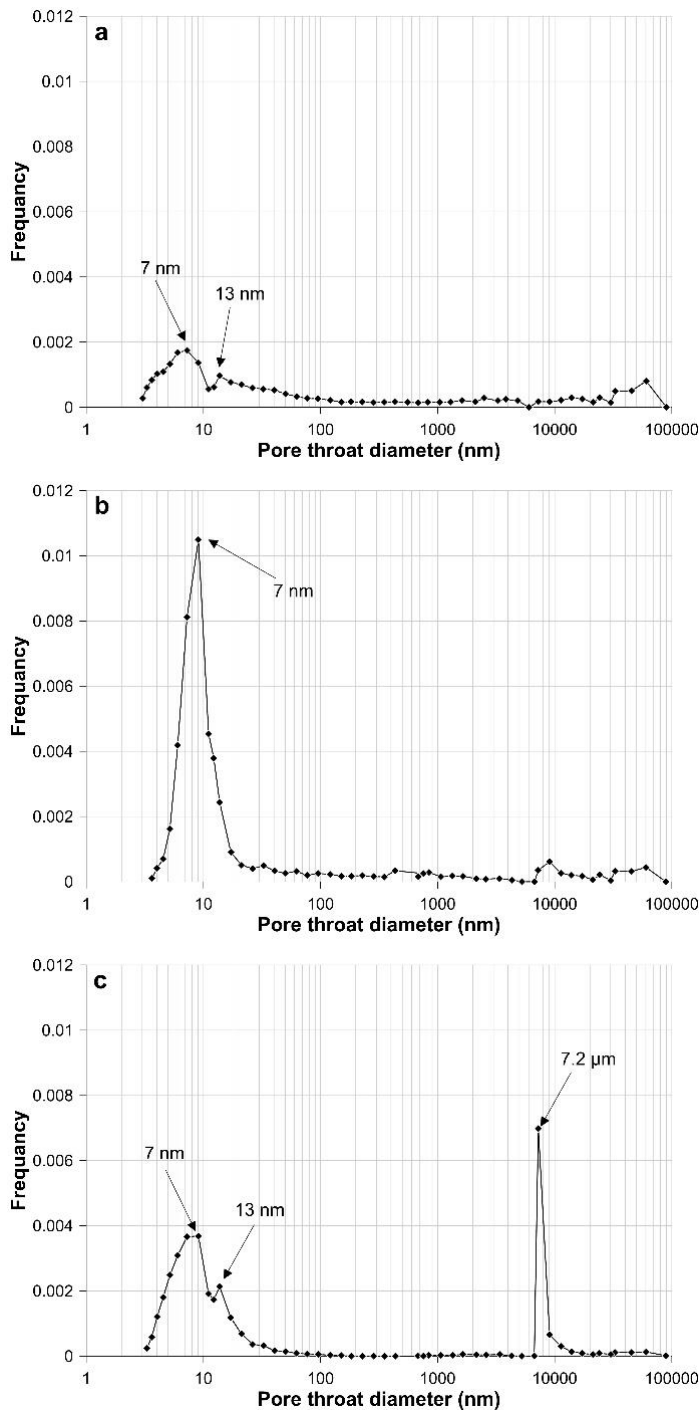
Fig. 4.14: Representative MICP results. In all samples, the major pore throat size is 7-9 nm (a-c), and many of the samples have a smaller peak at 13 nm (a, c). The presence of pore throats > 10 µm was documented in most samples, but for the most part these appear in low frequency. In four samples the largest peak is associated with pore throats of ~10 µm (c). (a) Well 1, sample 4P, 2291 m. (b) Well 2, sample 5X, 2737 m. (c) Well 2, sample 3AJ, 2653 m.

190

4.5 Discussion

In this section, we examine the effect of rock fabric and rock composition on the petrophysical properties of the Montney Formation siltstone. We aim to identify the underlying processes that control pores system characteristics in the siltstone. We then compare the processes affecting pore system development of the siltstone to these affecting shale formations and highlight the similarities and differences between the two rock types.

4.5.1 Porosity and permeability relationship

Many studies report a positive correlation between matrix porosity and matrix permeability in the Montney Formation (Nieto et al., 2009; Wood, 2012, 2013; Akai and wood, 2014; Clarckson et al., 2012; Ghanizadeh et al., 2015; Akai and wood, 2018; Cui and Nassichuk, 2018; Russell, 2018; Yang, 2018). Our study confirms this trend (Fig. 4.15). The relationship between porosity and permeability in fine-grained rocks was shown to be controlled by clay content in organic matter-lean rocks (Dewhurst et al., 1998, 1999; Yang and Aplin, 2007) or by organic matter content in organic matter-rich rocks (Dong et al., 2017). In our data set, neither clay content (Fig. 4.15a) nor organic matter content (Fig. 4.15b) control the relationship between porosity and permeability, although samples with low TOC values (<0.5 wt%) have the largest porosity and permeability values (Fig. 4.15b).

4.5.2 Compositional dependency of petrophysical properties

Numerous studies have evaluated the petrophysical properties of the Montney Formation (for example, Wood, 2013; Akai et al., 2014; Clarckson et al., 2012; Sanei et al., 2016; Akai and Wood, 2018; Cui and Nassichuk, 2018; Ghanizadeh et al., 2015, 2018; Yang, 2018), but few examined relationships between petrophysical properties and rock composition. Of these, most concentrated on the effect of organic matter (Akai and Wood, 2014; Sanei et al., 2015;
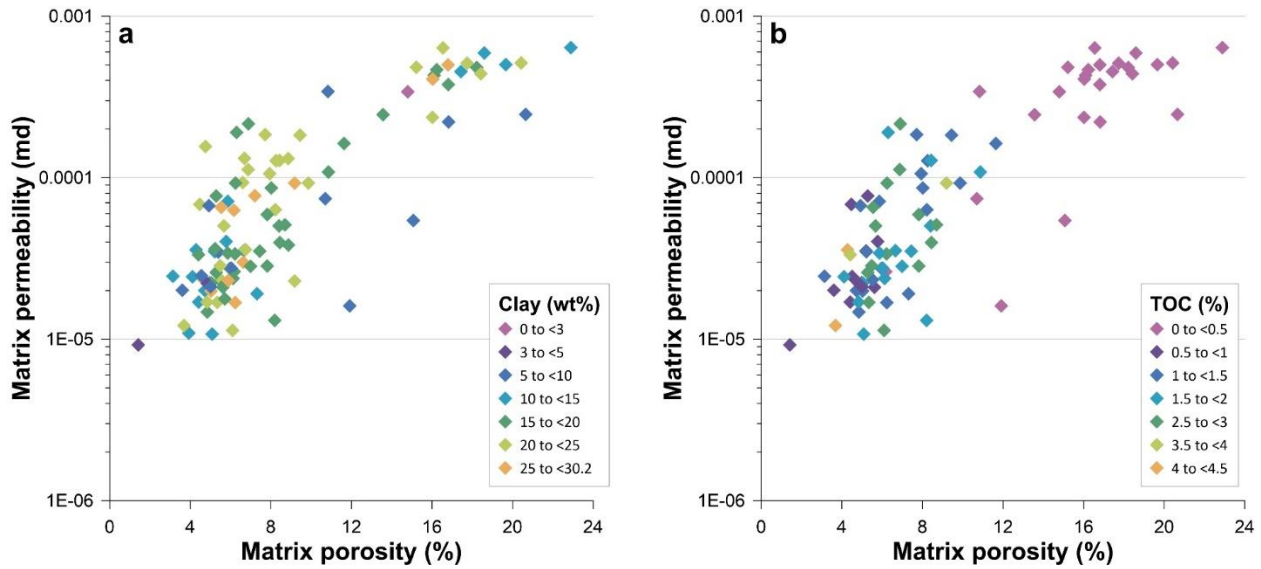
Fig. 4.15: Positive correlation between matrix porosity and matrix permeability in the Montney Formation. Unlike other fine grained rocks, the relationship between porosity and permeability in the siltstone is not controlled by clay content (a) or organic matter content (b), although samples with low TOC values (<0.5 wt%) have the largest porosity and permeability values.

Wood et al., 2015, 2018), or did not focus solely on the Montney Formation (Chalmers and Bustin, 2012); thus, the nature and extent of mineralogical controls on reservoir quality and petrophysical behavior are unclear.

In order to identify the main controls over petrophysical properties in our samples, we performed multiple stepwise regression analyses, which select the smallest subset of independent variables that can best predict a property. We applied this method to test the influence of rock composition on sample surface area, matrix porosity and permeability, and plug permeability. Each of these analyses was performed on the largest possible subsets of data from the five study wells. All regression equations are presented in Table 4.3.

4.5.3 Sample surface area

The subset used for establishing the compositional control on sample surface area included 20 samples. Regression results explain over 90% ($R^2 = 0.92$) of the dataset. The variance in surface area data is explained by TOC content (73.1% of the variance) and to a lesser extent

192

Table 4.3: Regression equations obtained from stepwise regression analysis.

	Petrophysical property	n[a]	Regression equation[b]	R²[c]
(1)	Surface area	20	**Surface Area = -0.4 + 3.3 TOC +0.36 clay** (73.1%) (18.5%)	0.93
(2)	Matrix porosity	192	$\boldsymbol{\varphi_{matrix}}$ **= 1.27 - 1.41 TOC +0.24 quartz - 1.15 mica + 0.33 clay** (5.8%) (39.0%) (7.7%) (7.4%)	0.60
(3)	Matrix permeability	107	$\mathbf{K_{matrix}}$ **= 5.0E-5 - 7.9E-5 TOC + 5.0E-6 quartz - 4.40E-5 mica + 1.40E-5 clay** (33%) (7.7%) (11.2%) (3.6%)	0.57
(4)	Plug permeability	68	$\mathbf{K_{plug}}$ **= -0.037 + 9.8E-4 quartz + 5.1E-4 dolomite** (44.0%) (14.0%)	0.58

[a] Number of samples in the regression analysis .

[b] Percentage below each variable is the variance in the data set explained by the variable.

[c] R^2 is the coefficient of multiple determination .

clay content (18.5%) (eq. 1, Table 4.3). Increased TOC and clay concentrations both lead to increased surface area in samples. Chalmers and Bustin (2012) observed a similar trend and attributed the increase in surface area to the decrease in grain size with increasing clay content and to the increase in organic matter porosity with increased TOC.

Organic matter porosity in the Montney Formation is interpreted to form through secondary cracking of oil to gas (Wood et al., 2015, 2018) and should increase with increasing burial depth and thermal maturity. Thus, the volume of porosity in the organic matter and internal sample surface area should increase with depth and thermal maturity. It is worth noting, however, that the specific thresholds for development of organic porosity depends on the type of organic matter present in the rocks; for example, cracking kinetics of a bitumen phase to oil or gas are very different from those of an oil undergoing secondary cracking to gas.

All the samples we analyzed for nitrogen adsorption-desorption are from the dry gas window (wells 1 to 3; BC Oil and Gal Commission, 2012), or have negligible organic matte content (<0.2 wt%, well 4). Therefore, examination of surface area with increasing thermal maturity in our samples is impossible. However, the strong positive correlation of surface area with TOC content (R^2=0.73) indicate that organic matter porosity is significant to the internal surface area of the samples.

4.5.4 Matrix porosity and permeability

Data sets used in stepwise linear regression analysis to explain variation in matrix porosity and matrix permeability contained 191 and 107 samples, respectively. Regression equations explain 60% of the variance in the matrix porosity dataset ($R^2 = 0.60$), and 57% of the variance for matrix permeability dataset ($R^2 = 0.57$). The variance of matrix porosity and matrix permeability are controlled by the same variables (TOC, quartz, mica, and clay), but the relative contribution of each variable to the variance in the two datasets is different (eq. 2 and 3, Table 4.3).

Total organic carbon has a negative correlation with both porosity and permeability. This trend is well documented in the Montney Formation (Jarvie, 2012; Akai and wood, 2014; Wood et al., 2015) and is attributed to the presence of migrabitumen and pyrobitumen in the pore system (Chalmers and Bustin, 2012; Akai and Wood, 2014; Sanei et al., 2015; Wood et al., 2015, 2018; chapter 2 this study).

Total organic carbon concentration explains 33% of the variance in permeability values (eq. 3, Table 4.3), and 5.8% of the variance in porosity values (eq. 2, Table 4.3), indicating that organic matter content affects permeability more than porosity. Surface area analysis and SEM imaging demonstrate that micropores have developed in some portion of the organic matter (Fig. 4.12j). These pores, however, appear to occupy only a small portion of the total pore volume, explaining why TOC content has a marginal effect on matrix porosity.

The negative relationship between TOC and permeability and the large influence of TOC on permeability values can be explained by narrowing of pore throats due to the presence of bitumen, either because bitumen coats pores or because small connected pores are developed within the organic matter itself. Our interpretation is supported by negative correlation between peak pore throat size and TOC content, and a positive correlation between peak pore throat size and permeability Akai and Wood (2018), suggesting that bitumen is coating pore throats, reducing pore throat size and restricting flow.

In addition to TOC, mica grains are also associated with porosity and permeability reduction. Mica content explains 7.7% and 11.2% of the variance in porosity and permeability values, respectively (eq. 2 and 3, Table 4.3). Micas are flat and soft (ductile) grains. As such, mica grains can either stack or deform around detrital grains, creating a tightly packed rock and reducing porosity and permeability. In addition, the presence of micas promotes pressure solution in silicate minerals (Walderhaug, 2004; Meyer et al., 2006), which is common in the Montney Formation (Nassichuk, 2000; Vaisblat et al., 2017, chapter 2 this study). Pressure solution is a process that involves chemical dissolution of minerals at grain contacts, which reduces porosity by creating a more tightly compacted rock. In addition, the dissolved

material is commonly precipitated as cement in nearby open pore space (McBride, 1989 and reference therein). Both pressure solution and quartz cementation are documented for the Montney Formation (Fig. 4.10 and 4.16) (Vaisblat et al., 2017; chapter 2 this study).

Dissolution porosity (Fig. 4.12f) and deformation porosity (Fig.4.12h) were identified in micas in our samples. Yet our analysis suggests that micas have a negative influence on both porosity and permeability. To this end, it is important to note that total mica comprises <10 wt% of the rock volume, and that dissolution porosity is mostly associated with biotite and mica-like chlorite grains, and is rare in muscovite, which is the major micaceous mineral in the formation (commonly > 60% of total mica). In addition, much of the porosity in micas generated through dissolution and deformation is now filled by organic matter. Thus, mica dissolution and deformation processes are responsible for a very small fraction of the total porosity and the total effect of micas on porosity and permeability is negative.

Regression analysis suggests a positive correlation between quartz concentration and both porosity and permeability. Quartz explains the majority of the variance in our porosity datasets, and accounts for 39% of the variance in in porosity values, and 7.7% of the variance in permeability values (eq. 2 and 3, Table 4.3). A positive correlation between quartz and porosity and between quartz and matrix permeability was previously reported by Chalmers and Bustin (2012), who also noted that samples containing over 65% quartz plus feldspar have high permeabilities, whereas those containing less than 65% quartz plus feldspar have permeability values ranging from low to high. In our dataset, neither porosity nor permeability correlate with high concentrations of quartz plus feldspar, although only 7 of our 238 samples contained > 65 wt% quartz plus feldspar. However, we were able to confirm a positive trend between quartz content and matrix porosity (R^2=0.42), and a weak positive trend between quartz content and matrix permeability (R^2=0.28).
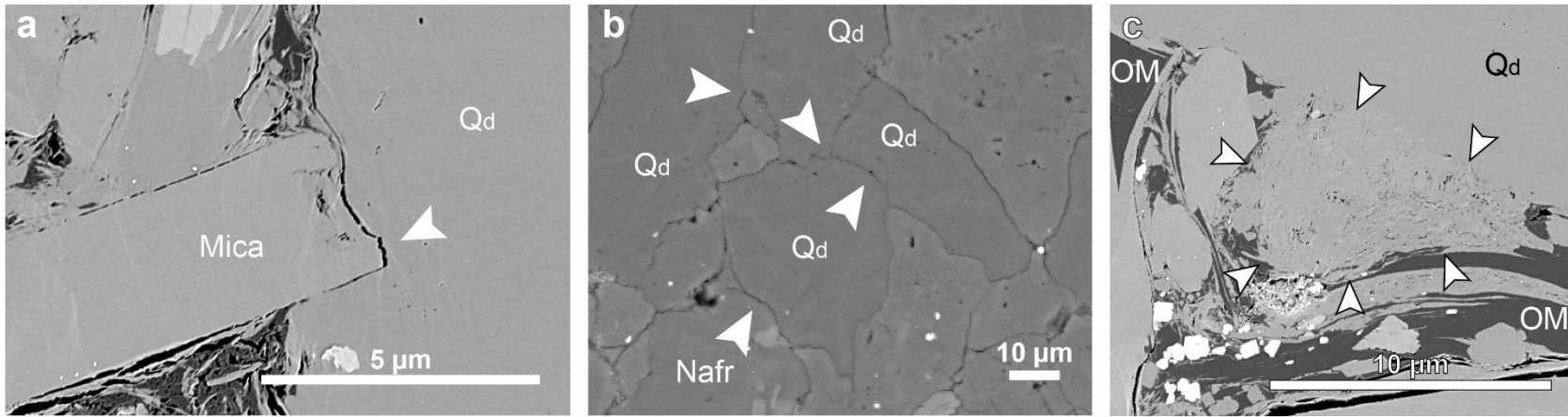
Fig. 4.16: Pressure solution and clay floccules in Montney samples. (a) SEM-BS showing a mica penetrating a quartz (white arrow), sample 12 E, well 1, 2431 m. (b) SEM-BS of concave-convex contacts indicative of pressure solution (white arrows) between detrital quartz grains (Qd) and Na-feldspar (Nafr), sample 5N, well 3, 3376 m. (c) SEM-BS image of a clay clump (white arrows) between detrital grains. White minerals are pyrite; sample 9P, well 2, 2366.25 m.

Our interpretation is similar to that presented by Chalmers and Bustin (2012), who suggested that intergranular porosity is better preserved in the presence of abundant hard grains. However, it is difficult to deconvolve this relationship from the negative correlations between carbonate mineral abundance and porosity and permeability, given the negative relationship that exists between QFM (quartz, feldspar and mica) and carbonate minerals (dolomite, Fe-rich dolomite and calcite) (Fig. 4.17) because these two groups of minerals together comprise 75% of the rock on average in the Montney Formation.
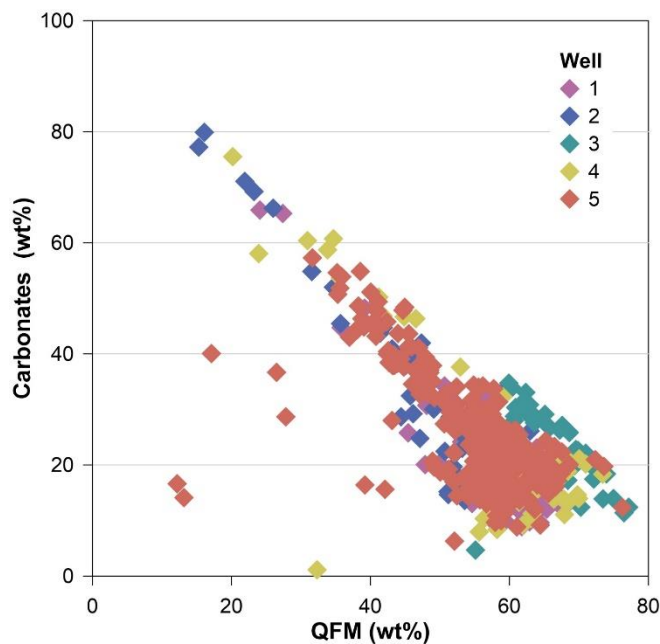
Fig. 4.17: Relationship between QFM and carbonate minerals. (a) Negative correlation between QFM (quartz, feldspars, and micas) and carbonate minerals (calcite, dolomite, and Fe-dolomite). QFM is the sum of quartz, feldspars, and micas.

Finally, regression analysis suggests that porosity and permeability increase with increasing clay content. Clays are soft, easily deformable minerals and are documented to reduce matrix

porosity and permeability in shales (Dewhurst et al., 1998, 1999; Yang and Aplin, 2007), where they are the dominant component of the matrix. In contrast, clay content has a positive relationship, albeit small, with porosity and permeability in the Montney Formation. According to the regression equations (eq. 2 and 3, Table 4.3), clay is the variable least affecting both petrophysical properties, accounting for 7.4% of the variance in porosity values, and 3.6% of

the variance in permeability values. We suggest that the positive relationship between clay and permeability is a reflection of the positive effect quartz has on porosity and permeability. Most of the quartz in the Montney is of detrital origin (>75 %, chapter 2, this study), and so are the majority of the clays. Thus, an increase in quartz concentrations is associated with an increase in clay concentration.

Examining the framework of the siltstone provides additional explanation to the contrasting effect clay has on porosity and permeability in siltstones and shales. In shales, isolated silt grains float within the clay matrix that constitutes the bulk of the rock (Dewhurst et al., 1998). Following compaction, clay floccules tend to be compacted and flattened (Schieber et al., 2007). In contrast, the Montney Formation is primarily composed of hard framework silt-size grains. Based on SEM imaging, clay minerals in the Montney Formation rarely form distinct beds and are mostly found as coatings on detrital grains, floccules between hard minerals or mixed with organic matter that fills paleopores (chapter 2 this study). The hard mineral framework protects clay floccules from compacting and preserves their original porosity (Fig. 4.16c), thus explaining the positive correlation between clay content, and porosity and permeability.

4.5.5 Plug permeability

The data set used for generating the regression equation for plug permeability contained 66 samples from wells 3 and 5. Samples from well 2 were excluded from the analysis since all plugs were reported to have visible fractures, and permeability values of these plugs were significantly higher than in all other cores (Fig. 4.11b). The regression equation obtained for plug permeability explains 58% of the variance in dataset ($R^2 = 0.58$) and relates increased plug permeability to increased quartz concentration (44% of the variance) and dolomite concentration (14 % of the variance).

Our SEM investigation revealed that large pores (10 to 100 µm) exist as microfractures within dolomite grains (Fig. 4.12i), or as elongated voids between hard minerals (quartz,

feldspar and dolomite) (Fig. 4.12c). Nitrogen adsorption-desorption analysis suggest these slit-shaped pores are the main type of porosity in our samples. It is unclear whether microfractures and elongated voids exist in the subsurface or are artifacts of pressure relief during core retrieval or handling. Regardless, these can explain the positive correlation between plug permeability and quartz and dolomite concentrations due to enhanced rock brittleness.

Plug permeability is consistently higher than matrix permeability (regardless of the confining pressure applied; Fig. 4.11b). One possibility is that crushing the sample in preparation for matrix permeability measurements eliminates the largest pore throats that contribute to the higher plug permeability values. Alternatively, plugs may contain internal cracks that increase the measured permeability in plugs. These cracks may not visible to the naked eye but can be detected by a CT scan (Akai and wood, 2014) if they are wider than the scan resolution (usually several tens of micrometers). However smaller microfractures affecting permeability may never be detected (Cui and Nassichuk, 2018; Russell, 2018).

4.5.6 Diagenetic control on porosity and permeability

Negative correlations between carbonate minerals and porosity and carbonate minerals permeability were noted in several studies and were attributed to pore filling carbonate cement (Chalmers and Bustin, 2012; Ghanizadeh et al., 2015; Sanei et al., 2016). Chalmers and Bustin (2012) proposed that calcite, rather than dolomite is responsible for occluding pore systems. Their observations were strengthened by the conclusions of Vaisblat et al. (2017) and chapter 2 (this study), who suggested that dolomite cement crystallized at shallow burial depth, before major compaction took place, whereas calcite cement precipitated in the pores following further compaction and thus has a greater effect on occluding pores and restricting pore throats.

In this study, we documented a negative relationship between calcite content and porosity. Calcite-porosity ratio depends greatly on the wells (Fig. 4.18), confirming the large
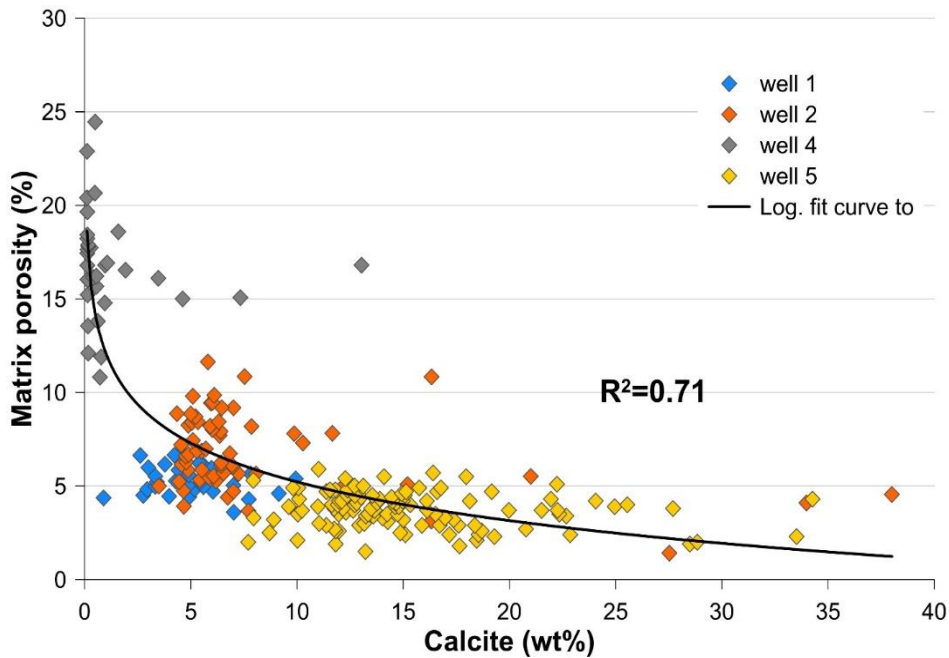
Fig. 4.18: Negative relationship between calcite content and porosity. calcite-porosity ratio depends greatly on the well from which the samples were taken. Fit line is logarithmic. The change in porosity with increasing calcite concentration is more pronounced for low cement values (up to ~7 wt%), and less pronounce for higher cement volumes.

spatial variations of calcite cementation. The best fit trend line to the porosity-calcite concentration dataset is logarithmic (R^2 = 0.71), with a more pronounced change in porosity with increasing calcite concentration at low cement values (up to ~7 wt%). Samples with low carbonate content and thus high quartz plus feldspar content have higher porosity and permeability values.

4.5.7 Lithofacies dependence of petrophysical properties

In sandstone reservoirs and some shale formations, different lithofacies can have significantly distinctive mineralogical composition, grain size distributions, bioturbation fabric, and sedimentary structures, related to varying depositional energy levels. As a result, different lithofacies may have unique petrophysical characteristics (see Dong et al., 2015 for an example of facies control in a shale reservoir). However, in our Montney data set, no clear petrophysical differences emerge between the lithofacies. Fig. 4.19 shows the distribution of

porosity and permeability values for all seven major lithofacies in wells 1 to 4. Two important observations arise from Fig. 4.19: (1) Ranges of matrix porosity and permeability values of the different lithofacies largely overlap. This is most noticeable when comparing lithofacies within the same well, and (2) a particular lithofacies may exhibit significantly different porosity and permeability values in different wells. This is most noticeable in comparing wells 3 and 4 (lithofacies A-E). In addition, neither pore size distribution (BJH) nor pore throat size distribution (MICP) show distinctly different results in samples taken from different lithofacies (appendix 3). These observations demonstrate that no lithofacies in the four wells examined has a unique petrophysical character. Similar observations were made by Chalmers and Bustin (2012).

We examine the similar ranges of petrophysical properties in the different lithofacies by comparing detrital grain size distribution and mineralogical compositions. Average detrital quartz was calculated for all the major eight lithofacies in wells 1 to 4 using equation 1 (chapter 2 this study). Results are presented in Fig. 4.19c. Qz_d is detrital quartz grain size and Qz_{min} is quartz mineral size from QEMSCAN analysis.

$$[1] \quad Qz_d = \frac{Qz_{min}+7.5}{1.93}$$

All calculated detrital quartz grain sizes are in the silt size grange, varying between 15 and 40 μm. The facies can be separated into two groups based on average grain size: medium silt and finer grain size (facies F, G/H, and J) and medium silt and coarser grain size (facies A, B, E, and O). These results are consistent with detrital quartz grain size measurements of samples from the same wells (chapter 2 this study), although the lower end of detrital grain sizes (<10 μm) is missing due to the scanning resolution selected for QEMSCAN analysis (4.8 μm/pixel).
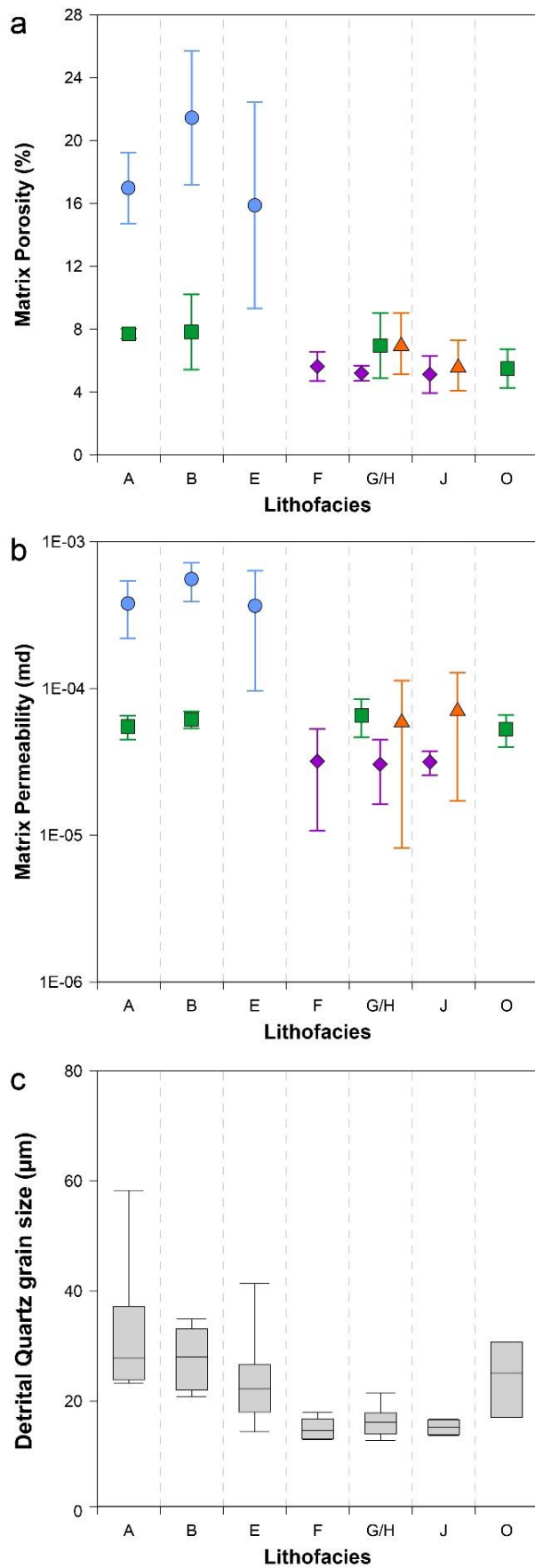
Fig. 4.19: Average and standard deviation (2σ) of matrix porosity (a) and permeability (b) for the major eight lithofacies in cores 1-4. Note that different lithofacies may have similar range of porosity and permeability (for example porosity of lithofacies F-O in wells 1-3). In addition, the same lithofacies may exhibit different ranges of porosity and permeability in different cores (for example facies A in wells 3 and 4). (c) Detrital quartz grain size calculated from QEMSCAN mineral grain size (appendix 4). All calculated detrital quartz grain sizes range from 15 to 40 μm. Two grain size groups are notable (1) facies F, G, H, and J, all with grain size of <20 μm, and (2) facies A, B, E, and O, with a slightly larger median grain size.

203

Similarities in calculated detrital grain size for all eight major lithofacies indicate a restricted range of grain sizes in the detrital sediment composing Montney Formation siltstone (Davies et al., 1997, chapter 2 this study), but also suggest that the different energy levels at different depositional environment had only a minor effect on the accumulating sediment.

In addition, there is no clear distinctions in mineralogical composition between different lithofacies in wells 1 to 4 (Fig. 4.9). The compositional homogeneity is attributed in part to the ineffectiveness of different depositional environments at segregating minerals based on their size and density, and in part to a pervasive shallow burial cementation event (chapter 2, this study). For the first 100 Ma following deposition the Montney Formation was buried to a shallow depth of ~1Km (Ness, 2001; Ducrous et al., 2017). During this time massive amount of quartz, feldspars and dolomite cements were precipitated, accounting for >30% of today's rock volume chapter 2, this study). Vaisblat (chapter 2, this study) reported no significant distinctions in the type and magnitude of diagenetic processes between lithofacies. This cementation homogenized the composition of the siltstone and erased any small variability that still existed between the different lithofacies.

4.5.8 Are siltstones and shales equivalent?

The Montney Formation is composed predominantly of silt-size material (Barber, 2002; Krause et al., 2012; Vaisblat et al., 2017, chapter 2 this study), although it is frequently referred to as a shale (Chalmers and Bustin, 2012; Davey, 2012; Feiyu et al., 2013; Nieto et al., 2013; Ouenes et al., 2014). A comparison between the petrophysical properties the Montney siltstone and these of several clay-rich mudstone (shale) formations reveals many similarities. Pore types in shales are similar to those described in this study for the Montney Formation siltstone (Jarvie et al., 2007; Loucks et al., 2012; Slatt and O'Brian, 2011; Chalmers et al., 2012; Labani et al., 2013; Milliken et al., 2013; Dong et al. 2015; Chen et al., 2016; Dong et al. 2017), and porosity and permeability values of Montney samples are similar to these of several other shale formations (Fig. 4.20). In addition, shale studies that
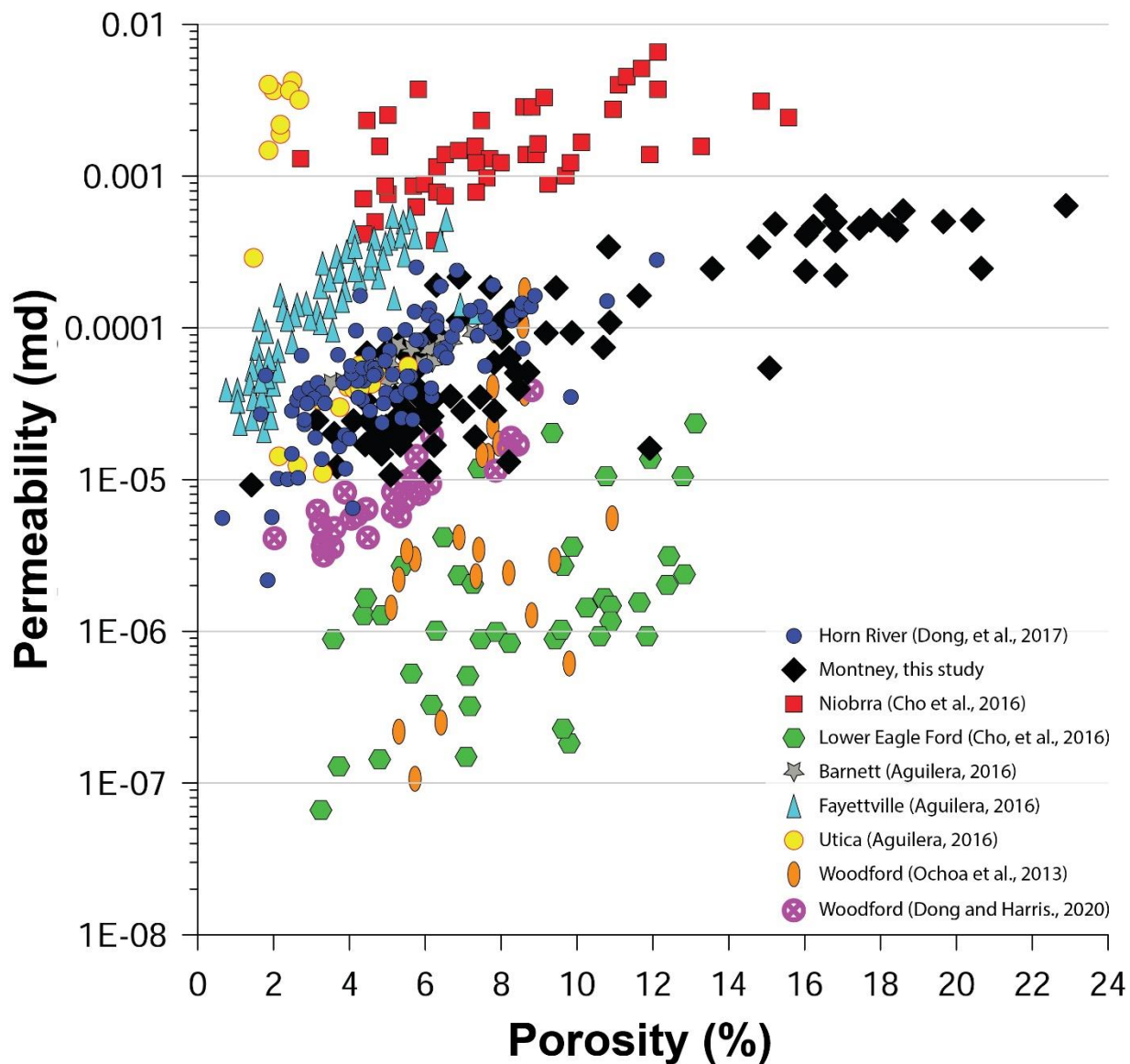
Fig. 4.20: Porosity and permeability values for the Montney Formation siltstone and other shale formations. Noe that samples from the Montney Formation have similar porosity and permeability ranges to several shale formations.

apply nitrogen adsorption and desorption analysis report slit-shaped pores and sample surface areas similar to the values we report in this study (Labani et al., 2013; Dong et al., 2015; Chen et al., 2016). Finally, pore size distributions of shale samples have similar patterns to Montney samples, with mesopores (2 to 100 nm) accounting for most of the pore volume (Fig. 4.13) (Chalmers et al., 2012; Labani et al., 2013; Saidian and Prasad, 2015). This

comparison shows that the petrophysical properties of the Montney Formation siltstone are not intrinsically different from these of many shale formations.

One major difference between siltstones and shales, however, lies in the processes that control the petrophysical properties. The major process that reduces porosity and permeability in all sedimentary rocks is compaction. Given a similar composition and a similar burial and effective stress histories, the rate of compaction is dictated by the grain size of the sediment (Morad et al., 2010). Depositional porosity of muds ranges between 80 and 90% (Muller, 1967; Aplin and Macquaker, 2011), but initial compaction rate is very high, and the sediment loses up to 50% of its initial porosity within several hundred meters of burial (Hedberg, 1936; Müller, 1967; Velde, 1996).

Depositional porosity of silty sediments is lower than that of muds, estimated to be 40 to 80% (Kominz et al., 2011), but the initial compaction rate of silts is lower; thus, porosity remains much higher than that of shale at equivalent depth (Camp, 2019). Compaction is effective at reducing porosity and permeability in shales and siltstones, but while is it detrimental to reservoir quality of shales, other processes may be more effective in controlling porosity and permeability of siltstone at shallow depth.

Chemical diagenesis also affects the pore systems of sedimentary rocks, decreasing porosity and permeability through precipitation of cement and increasing porosity and permeability through dissolution. Mineral dissolution in the Montney siltstone is not extensive (chapter 2, this study). In shales, dissolution may involve large volumes of the rock (particularly K-feldspar dissolution), but since it is associated with elevated temperatures at large burial depth matrix collaps due to the overburden pressure can eliminate any textural evidence for dissolution (Milliken, 1992).

Chemical diagenesis taking place in clay-rich mudrocks (shales) at shallow burial depths is generally thought to be dominated by the recrystallization of silica from biogenic sources that can account for up to 40% of the rock volume (Milliken and Olson, 2017). Recrystallization of biogenic silica is an isochemical reaction that does not require addition of

silica from sources external to formation. Dong et al. (2015) reported a positive relationship between quartz content and porosity and suggested that biogenic silica in the Horn River shale preserved porosity by providing a rigid framework that prevented the matrix from collapsing.

Quartz cement in the Montney siltstone is also thought to be largely isochemical, derived from several internal sources and it is possible that some of the quartz cement is of biogenic origin (chapter 2, this study). Our study also identified a positive relationship between porosity and quartz content (Table 4.3) suggesting that intergranular porosity is better preserved in the presence of abundant hard grains. Despite these similarities, we note that the volume of quartz cement in our samples is commonly <10% (chapter two, this study), much lower than quartz cement volumes recorded for shales (Milliken and Olson, 2017). Other cements are present in the siltstone, and it is impossible to isolate the effect of any particular cement on the rock framework.

Organic matter maturation and/or migration also affects the petrophysical properties in fine-grained rocks. Organic matter in shales is ultimately of primary origin, although secondary forms exist (migrabitumen or pyrobitumen, depending on thermal maturity). Porosity may develop within the organic matter due to hydrocarbons expulsion or secondary cracking increases the total porosity of the rock and is the main contributor to total pore volume in the rock (Dong et al., 2015; Dong and Harris, 2020). This explains the positive correlation between TOC and porosity in many organic rich shales (Passey et al., 2010; Jarvie, 2012; Milliken et al., 2012; Milliken et al., 2013; Dong et al., 2015).

In contrast to shales, TOC content is negatively correlated with porosity in the Montney siltstone and is responsible for only 5.8% of the variance in porosity values (eq. 2, Table 4.3). The origin of the organic matter in the Montney Formation is debated and may, in part, be of primary origin (deposited with the sediment) (Ibrahimbas and Riediger, 2004; Ejezie, 2007; Chalmers and Bustin 2012; Feng et al., 2016) or be entirely externally sourced and migrated into the formation as liquid hydrocarbons (Akai and Wood 2014; Sanei et al 2015; Wood et al., 2015, 2018). Migration of liquid hydrocarbons into the Montney Formation suggests that

the porosity and permeability of the siltstone at the time of hydrocarbons migration were high enough to allow fluid flow. This model suggests that bituminization of hydrocarbons in the siltstone (Sanei et al 2015; Wood et al., 2015, 2018) plugged much of the paleoporosity, explaining the negative influence of TOC on the petrophysical properties. Porosity generated through secondary cracking exists in the Montney Formation but, unlike shales where organic matter porosity is the main contributor to total porosity, other pore types are more prevalent in the siltstone and have larger contribution to the total pore volume and the permeability of the siltstone.

4.6 Conclusions

We examined controls the petrophysical properties in a siltstone hydrocarbon reservoir, specifically considering the effects of rock fabric and composition on pores system characteristics in the Lower Triassic Montney Formation that control. In this study, we have demonstrated:

1. Porosity and permeability values and pore dimensions are similar to those reported in shale reservoirs, in spite of the coarser grain size of the siltstone.

2. Quartz content exerts a positive control on both porosity and permeability, related to strengthening of the rock framework and reduced porosity loss due to compaction. Elevated clay content is also associated with higher porosity and permeability, possibly in part because of an association with quartz, but also because clays may shelter interconnected primary porosity that promotes permeability.

3. Organic matter content is negatively correlated to porosity despite the presence of organic matter porosity. We suggest that this relationship reflects two controls: (1) relict oil (now pyrobitumen) fills primary pore space, and (2) organic porosity contributes less to total porosity than other pore types.

4. Organic matter content is the most significant factor reducing permeability in the siltstone. We associate this negative relationship with the pyrobitumen that narrows

pore throats and limits flow. Clay has a positive relationship with permeability due to micropores preserved in clay aggregates.

5. Lithofacies in the siltstone are indistinguishable from one another based on their petrophysical properties due to their similar grain size and composition and the massive overprinting by shallow burial diagenesis.

6. Although petrophysical properties of this siltstone is similar to many unconventional shale reservoirs, the controls on reservoir quality are different, related to fundamental differences in compaction, chemical diagenesis and the nature of organic matter maturation and migration.

4.7 Reference

Abay, T.B., Karlsen, D.A., Pedersen, J.H., Olaussen, S. and Backer-Owe, K., 2018. Thermal maturity, hydrocarbon potential and kerogen type of some Triassic–Lower Cretaceous sediments from the SW Barents Sea and Svalbard. Petroleum Geoscience, 24(3), 349-373. doi: https://doi.org/10.1144/petgeo2017-035.

Aguilera, R., 2016. Shale gas reservoirs: Theoretical, practical and research issues. Petroleum Research, 1(1), 10-26.

Akai, T, Takakuwa, Y., Sato, K, and Wood, J.M., 2014. Pressure dependent permeability of tight rocks, SPE Low Perm Symposium, Denver, Colorado, USA, May 5-6. SPE-180262-MS.

Akai, T., and Wood, J.M., 2014, Petrophysical analysis of a tight siltstone reservoir: Montney Formation, Western Canada, The 20th Formation Evaluation Symposium of Japan, P. 1-4

Akai, T., and Wood, J.M., 2018. Application of pore throat size distribution data to petrophysical characterization of Montney tight-gas siltstones, Bulletin of Canadian Petroleum Geology, 66, 425-435.

Anovitz, L.M., and D R. Cole, 2015. Characterization and analysis of porosity and pore structures. Reviews in Mineralogy and Geochemistry, 80(1), 61-164, doi: 10.2138/rmg.2015.80.04.

Aplin, A.C., and Macquaker, J. H., 2011. Mudstone diversity: Origin and implications for source, seal, and reservoir properties in petroleum systems. American Association of Petroleum Geologists Bulletin, 95(12), 2031-2059. https://doi.org/10.1306/03281110162.

Barber, L.M., 2002, Sedimentology, Diagenesis and Reservoir Characterization of the Montney Formation at Sturgeon Lake South 'F' Pool West-Central Alberta, M.Sc. thesis, University of Calgary, Department of Geology and Geophysics, Calgary, Alberta.

BC oil and gas commission, 2012. Montney Formation play atlas for NEBC.

Beranek, L.P., Mortensen, J.K., Orchard, M.J., and Ullrich, T., 2010. Provenance of North American Triassic strata from west-central and southeastern Yukon: correlations with coeval strata in the Western Canada Sedimentary Basin and Canadian Arctic Islands. Canadian Journal of Earth Sciences 47, 53-73. https://doi.org/10.1139/E09-065.

Blakey, R.C., 2014. Mesozoic paleogeography and tectonic history - western North America: Triassic tectonics and paleogeography, 245 Ma. http://deeptimemaps.com/north-american-key-time-slices-series. Last accessed july 20, 2019.

Brunauer, S., Emmett, P.H., and Teller, E., 1938. Adsorption of Gases in Multimolecular Layers. Journal of the American Chemical Society, 60 (2), 309-319.

Camp, W.K., 2019. A New Method to Predict Organic Matter Porosity in Unconventional Shale Reservoirs. William C. CSPG Gussow Geoscience Conference, Banff, Alberta, Canada, 15-17 October.

Cao, Z., Liu, G., Zhan, H. Gao, J. Zhang, J., Li, C., and Xiang, B., 2017. Geological roles of siltstones in tight oil play. Journal of Marine and Petroleum Geology, 88, 333-344.

Chalmers, G.R., and Bustin, M.R., 2012. Geological evaluation of Halfway–Doig–Montney hybrid gas shale–tight gas reservoir, northeastern British Columbia. Journal of Marine and Petroleum Geology, 38(1), 53-72.

Chalmers, G.R., Bustin, R.M. and Power, I.M., 2012. Characterization of gas shale pore systems by porosimetry, pycnometry, surface area, and field emission scanning electron microscopy/transmission electron microscopy image analyses: Examples from the Barnett, Woodford, Haynesville, Marcellus, and Doig units. American Association of Petroleum Geologists bulletin, 96(6), 1099-1119.

Chen, Q., Zhang, J., Tang, X., Wei, D., Li, Z., Liu, C., and Zhang, X., 2016. Pore Structure Characterization of the Lower Permian Marine Continental Transitional Black Shale in the Southern North China Basin, Central China. Energy and Fuel, 30(12), 1092-10105. https://doi.org/10.1021/acs.energyfuels.6b01475.

Cho, Y., Eker, E., Uzun, I., Yin, X. and Kazemi, H., 2016. Rock characterization in unconventional reservoirs: a comparative study of Bakken, Eagle Ford, and Niobrara Formations. SPE Low Perm Symposium, Denver, Colorado, USA, 5-6 May.

Clarkson, C.R., Wood, J., Burgis, S., Aquino, S. and Freeman, M., 2012. Nanopore-structure analysis and permeability predictions for a tight gas siltstone reservoir by use of low-

pressure adsorption and mercury-intrusion techniques. SPE Reservoir Evaluation and Engineering, 15(6), 648-661.

Coney, P.J., Jones, D.L., and Monger, J.W.H., 1980. Cordilleran suspect terranes. Nature, 288(5789), 329-333. https://doi.org/10.1038/288329a0.

Crombez, V., Rohais, S., Baudin, F., and Euzen, T., 2016. Facies, well-log patterns, geometries and sequence stratigraphy of a wave-dominated margin: insight from the Montney Formation (Alberta, British Columbia, Canada). Bulletin of Canadian Petroleum Geology, 64(4), 516-537.

Crombez, V., Baudin, F., Rohais, S., Riquier, L., Euzen, T., Pauthier, S., Ducros, M., Caron, B. and Vaisblat, N., 2017. Basin scale distribution of organic matter in marine fine-grained sedimentary rocks: Insight from sequence stratigraphy and multi-proxies analysis in the Montney and Doig Formations. Marine and Petroleum Geology, 83: 382-401.

Cui. X., and Nassichuk, B., 2018. Permeability of the Montney Formation in the Western Canada Sedimentary Basin: insights from different laboratory measurements. Bulletin of Canadian Petroleum Geology, 66, 394-424.

Davey, H., 2012. Geomechanical characterization of the Montney shale, northwest Alberta and northeast British Columbia, Canada. M.Sc. Thesis, Department of Geology and Geological Engineering, Colorado School of Mines, Golden, Colorado, USA.

Davies, G.R., Moslow, T.F., and Sherwin, M.D., 1997. The Lower Triassic Montney Formation, west-central Alberta. Bulletin of Canadian Petroleum Geology, 45(4), 474-505.

Davies, G.R., Watson, N., Moslow, T.F., and Maceachern, J.A., 2018. Regional subdivisions, sequences, correlations and facies relationships of the Lower Triassic Montney Formation, west-central Alberta to northeastern British Columbia, Canada - With emphasis on role of paleostructure. Bulletin of Canadian petroleum geology, 66(1), 23-92.

De Bore, J.H., 1958. The shapes of capillaries, in the structure and properties of porous materials, Butterworth, London, 68-94.

Dewhurst, D.N., Aplin, A.C., Sarda, J.-P., and Yang, Y., 1998. Compaction-driven evolution of porosity and permeability in natural mudstones: An experimental study. Journal of Geophysical Research: Solid Earth 103(B1), 651-661.

Dewhurst, D.N., Yang, Y.L., and Aplin, A.C., 1999. Permeability and fluid flow in natural mudstones. In: Aplin, A.C., et al. (Eds.), Muds and Mudstones: Physical and Fluid Flow Properties, 158. Geological Society Special Publication, p. 23-43.

Dixon, J., 2000. Regional lithostratigraphic units in the Triassic Montney formation of Western Canada. Bulletin of Canadian Petroleum Geology, 48(1), 80–83.

Do, D.D., and Do, D.H., 2003. Pore Characterization of Carbonaceous Materials by DFT and GCMC Simulations: A Review. Adsorption Science and Technology 21(5) 389-423. https://doi.org/10.1260/026361703769645753.

Dong, T., and Harris, N.B., 2020. The effect of thermal maturity on porosity development in the Upper Devonian–Lower Mississippian Woodford Shale, Permian Basin, US: Insights into the role of silica nanospheres and microcrystalline quartz on porosity preservation. International Journal of Coal Geology, 217, 103346.

Dong, T., Harris, N.B., Ayranci, K., Twemlow, C.E., and Nassichuk, B., 2017. The impact of rock composition on geomechanical properties of a shale formation: Middle and Upper Devonian Horn River Group shale, Northeast British Columbia, Canada. American Association of Petroleum Geologists Bulletin, 101(2), 177-204. https://doi.org/10.1306/07251615199.

Dong, T., Harris, N.B., Ayranci, K., Twemlow, C.E., and Nassichuk, B.R., 2015. Porosity characteristics of the Devonian Horn River shale, Canada: Insights from lithofacies classification and shale composition. International Journal of Coal Geology, 141, 74-90.

Ducros, M., Sassi, W., Vially, R., Euzen, T., and Crombez, V., 2017. 2-D Basin modeling of the Western Canada Sedimentary Basin across the Montney-Doig System: Implications for hydrocarbon migration pathways and unconventional resources potential, in: AbuAli, M.A., Moretti, I., and Bolås, H.M.N. (Eds.), Petroleum Systems Analysis-Case Studies: American Association of Petroleum Geologists Bulletin Memoir, 114. pp. 117-134. https://doi.org/10.1306/13602027M1143703.

Edwards, D.E., Barclay, J.E., Gibson, D.W., Kvill, G.E., and Halton, E., 1994. Triassic strata of the Western Canada Sedimentary Basin, in: Mossop, G.D., and Shetsen, I. (Eds.), Geological Atlas of the Western Canada Sedimentary Basin. Canadian Society of Petroleum Geologists and Alberta Research Council, Calgary, pp. 259–275.

Ejezie, N., 2007, Triassic oil families and possible source rocks, Peace River Embayment area, Alberta, Canada, Ms.C. Thesis, Department of Geology and Geophysics, University of Calgary, Calgary, Alberta, Canada.

Euzen, T., Moslow, T.F., Crombez, V., and Rohais, S., 2018. Regional stratigraphic architecture of the spathian deposits in western Canada - Implications for the Montney resource play. Bulletin of Canadian Petroleum Geology. 66(1), 175-192.

Feiyu, W., Jing, G., Weiping, F., and Bao., L., 2013. Evolution of overmature marine shale porosity and implication to the free gas volume. Petroleum Exploration and Development 40(6), 819-824. https://doi.org/10.1016/S1876-3804(13)60111-1.

Feng, W., Chen, Z., and Jiang, C., 2016. Oil and source correlations of Triassic Montney Formation in WCSB: Implication to shale gas resource potential in: GeoConvention. CSPG CSEG CWLS, Calgary, AB, Canada, p. 1.

Furlong, C.M., Gingras, M.K., Moslow, T.F., and Zonneveld, J.-P., 2018. The Sunset Prairie Formation: designation of a new Middle Triassic formation between the Lower Triassic Montney Formation and Middle Triassic Doig Formation in the Western Canada Sedimentary Basin, northeast British Columbia. Bulletin of Canadian Petroleum Geology, 66(1), 193-214.

Ghanizadeh, A., Rashidi, B. Clarkson, C.R., Sidhu, N., Hobbs, J.J., Yang, Z., and Song, C., 2018. Characterization of reservoir quality in tight rock using drill cuttings: Examples from the Montney Formation, Alberta, Canada. SDPE Canada Unconventional Resources Conference, Calgary, Alberta, Canada, March 13-14. SPE-189807-MS.

Ghanizadeh, A., Clarkson, C.R., Aquino, S., Ardakani, O.H., and Sanei, H., 2015. Petrophysical and geomechanical characteristics of Canadian tight oil and liquid-rich gas reservoirs : I. Pore network and permeability characterization. Fuel, 153, 664-681. https://doi.org/10.1016/j.fuel.2015.03.020

Gibson, D.W., and Edwards, D.E., 1990. An overview of Triassic stratigraphy and depositional environments in the Rocky Mountain Foothills and Western Interior Plains , Peace River Arch area , northeastern British Columbia. Bulletin of Canadian Petroleum Geology, 38(1), 146-158.

Golding, M.L., Mortensen, J.K., Ferri, F., Zonneveld, J.-P., and Orchard, M.J., 2016. Determining the provenance of Triassic sedimentary rocks in northeastern British Columbia and western Alberta using detrital zircon geochronology, with implications for regional tectonics. Canadian Journal of Earth Sciences, 53(2), 140-155. https://doi.org/10.1139/cjes-2015-0082.

Golonka, J., and Ford, D., 2000. Pangean (Late Carboniferous–Middle Jurassic) paleoenvironment and lithofacies. Palaeogeography, Palaeoclimatology, Palaeoecology, 161(1-2), 1-34. https://doi.org/10.1016/S0031-0182(00)00115-2.

Golonka, J., Ross, M.I., and Scotese, C.R., 1994. Phanerozoic paleogeographic and paleoclimatic modeling maps, in: Embry, A.F., Beauchamp, B., and Glass, D.J. (Eds.), Pangea, Global Environments and Resources. Canadian Society of Petroleum Geologist, Calgary, 1-47.

Hedberg, H.D., 1936. Gravitational compaction of clays and shales. American Journal of Sciense, 31, 241-287. https://doi.org/10.2475/ajs.s5-31.184.241.

Henderson, C.M., Golding, M.L., and Orchard, M.J., 2018. Conodont sequence biostratigraphy of the Lower Triassic Montney Formation, Bulletin of Canadian Petroleum Geology, 66(1), 7-22.

Ibrahimbas, A., and Riediger, C., 2004. Hydrocarbon source rock potential aAs determined by RockEval 6/TOC pyrolysis, N.E. B.C. and N.W. Alberta. Resource Development and Geoscience Branch, Summary of Activities 2004, 7-18.

Jarvie, D. M., 2012, Shale resource systems for oil and gas: Part 1-Shale-gas resource systems, in J. A. Breyer, ed., Shale reservoirs - Giant resources for the 21st century: American Association of Petroleum Geologists Memoir 97, 69-87.

Jarvie, D.M., Hill, R.J., Ruble, T.E., and Pollastro, R.M., 2007. Unconventional shale-gas systems: The Mississippian Barnett Shale of north-central Texas as one model for thermogenic shale-gas assessment. American Association of Petroleum Geologists Bulletin, 91(4), 475-499.

Kominz, M.A., Patterson, K., and Odette, D., 2011. Lithology dependence of porosity in slope and deep marine sediments. Journal of Sedimentary Research, 81(10), 730-742.

Krause, F.F., Wiseman, A.C., Williscroft, K.R., Solano, N., Morris, N.J., Meyer, R., and Marr, R., 2012. Petrographic and petrophysical comparison of the Montney Formation in the Sturgeon Lake South area. In Site, Canadian Well Logging Society Magazine, 31, 6-9.

Kulia, U., and Prasad, M., 2011. Surface area and pore size distribution in clays and shales, SPE annual technical conference and exhibition, Denver, Colorado, USA, October 30-November 2.

Labani, M.M., Rezaee, R., Saeedi, A., and Al Hinai, A., 2013. Evaluation of pore size spectrum of gas shale reservoirs using low pressure nitrogen adsorption, gas expansion and mercury porosimetry: A case study from the Perth and Canning Basins, Western Australia, Journal of Petroleum Science and Engineering, 112, 7-16.

Loucks, R.G., Reed, R.M., Ruppel, S.C., and Hammes, U., 2012. Spectrum of pore types and networks in mudrocks and a descriptive classification for matrix-related mudrock pores. American Association of Petroleum Geologists Bulletin, 96, 1071-1098.

Macquaker, J.H., and Adams, A.E., 2003. Maximizing information from fine-grained sedimentary rocks: An inclusive nomenclature for mudstones. Journal of Sedimentary Research, 73(5), 735-744.

McBride, E.F., 1989. Quartz cement in sandstones: A review. Earth-Science Reviews, 26(1-3), 69-112.

Meyer, E.E., Green, G.W., Alcantar, N.A., Israelachvili, J.N., and Boles, J.R., 2006. Experimental investigation of the dissolution of quartz by a muscovite mica surface:

Implications for pressure solution, Journal of Geophysics Research, 111 B08202, doi: 10.1029/2005JB004010.

Miall, A.D., and Blakey, R.C., 2008. The Phanerozoic tectonic and sedimentary evolution of North America, in: Miall, A.D. Sedimentary Basins of United States and Canada, p. 1–29. Amsterdam, Netherlands, Elsevier.

Milliken, K., 1992. Chemical behavior of detrital feldspars in mudrocks versus sandstones, Frio Formation (Oligocene), South Texas. Journal of Sedimentary Research, 62 (5), 790-801. https://doi.org/10.1306/D42679DD-2B26-11D7-8648000102C1865D.

Milliken, K.L., and Olson, T., 2017. Silica diagenesis, porosity evolution, and mechanical behavior in siliceous mudstones, Mowry Shale (Cretaceous), Rocky Mountains, U.S.A.. Journal of Sedimentary Research, 87(4): 366-387. doi: https://doi.org/10.2110/jsr.2017.24.

Milliken, K.L., Rudnicki, M., Awwiller, D.N., and Zhang, T.W., 2013. Organic matter hosted pore system, Marcellus Formation (Devonian), Pennsylvania. American Association of Petroleum Geologists Bulletin, 97, 177-200.

Milliken, K.L., Esch, W.L., Reed, R.M., and Zhang, T., 2012. Grain assemblages and strong diagenetic overprinting in siliceous mudrocks, Barnett Shale (Mississippian), Fort Worth Basin, Texas. American Association of Petroleum Geologists Bulletin, 96(8), 1553-1578.

Monger, J.W, and Price, R.,A. 2002. The Canadian Cordillera: Geology and tectonic evolution. Canadian Society of Exploration Geophysicists Recorder, 27(2), 17-36.

Monger, J.W., and Price, R.A., 1979. Geodynamic evolution of the Canadian Cordillera - progress and problems. Canadian Journal of Earth Sciences, 16(3), 770-791. https://doi.org/10.1139/e79-069.

Morad, S., Al-Ramadan, K., Ketzer, J.M., and De Ros, L.F., 2010. The impact of diagenesis on the heterogeneity of sandstone reservoirs: A review of the role of depositional facies and sequence stratigraphy. American Association of Petroleum Geologists Bulletin, 94(8), 1267–1309. https://doi.org/10.1306/04211009178.

Moslow, T.F., 2000. Reservoir architecture of a fine-grained turbidite system: Lower Triassic Montney Formation, Western Canada Sedimentary Basin, in: Weimer, P. (Ed.), Deep-Water Reservoirs of the World. SEPM Society for Sedimentary Geology, Houston, Texas, pp. 686-713. https://doi.org/10.5724/gcs.00.15.0686.

Moslow, T.F., Haverslew, B., and Henderson, C.M., 2018. Sedimentary facies, petrology, reservoir characteristics, conodont biostratigraphy and sequence stratigraphic framework of a continuous (395m) full diameter core of the lower Triassic Montney Fm, northeastern British Columbia. Bulletin of Canadian Petroleum Geology, 66(1), 259-287.

Müller, G., 1967. Diagenesis in argillaceous sediments, in: Larsen, G., and Chilingar, G. V. (Eds.), Developments in Sedimentology. Elsevier, pp. 127-177. https://doi.org/10.1016/S0070-4571(08)70843-4.

Nassichuk, B.R., 2000. Sedimentology, diagenesis and reservoir development of the lower Triassic Montney formation, northeastern British Columbia. , Ms.C. Thesis, Department of Earth and Ocean Sciences, University of British Columbia, Vancouver, British Columbia, Canada.

National energy board, 2013. Canada's energy future 2013 energy supply and demand projections to 2035. https://www.cer-rec.gc.ca/nrg/ntgrtd/ftr/2013/2013nrgftr-eng.pdf. Last accessed March 31, 2020.

National energy board, 2013. Canada's energy future 2013 energy supply and demand projections to 2035. https://www.cer-rec.gc.ca/nrg/ntgrtd/ftr/2013/2013nrgftr-eng.pdf. Last accessed March 31, 2020.

Ness, S.M., 2001. The application of basin analysis to the Triassic succession, Alberta Basin: an investigation of burial and thermal history and evolution of hydrocarbons in Triassic rocks. Ms.C. Thesis, Department of Geology and Gepophysics, University of Calgary, Calgary, Alberta, Canada.

Nicolas, M., 2006. Petroleum geology of the Devonian Three Forks Formation, Sinclair Field and surrounding area, southwestern Manitoba; in E.H. Nickel (Eds.), Saskatchewan and Northern Plains oil and gas symposium core workshop volume, Saskatchewan geological society special publication 20, p.32-49.

Nieto, J., Batlai, B., and Delbecq, F., 2013. Seismic lithology prediction : A Montney Shale Gas case study. CSEG Recorder, 38, 34-41.

Nieto, J., Bercha, R., and Chan, J., 2009. Shale Gas Petrophysics - Montney and Muskwa, Are They Barnett Look-Alikes?. SPWLA 50th Annual Logging Symposium. The Woodlands, Texas, 21-24 June.

Ochoa, J., Wolak, J., and Gardner, M.H., 2013. Recognition criteria for distinguishing between hemipelagic and pelagic mudrocks in the characterization of deep-water reservoir heterogeneity. American Association of Petroleum Geologists Bulletin, 97(10), 1785-1803.

Ouenes, A., Aimene, Y., and Nairn, J., 2014. Interpretation of Microseismic Using Geomechanical Modeling of Multiple Hydraulic Fractures Interacting with Natural Fractures – Application to Montney Shale. Canadian Society of Exploration Geophysicists Recorder, 39(9), 46-54.

Passey, Q.R., Bohacs, K.M., Esch, W.L., Klimentidis, R., and Sinha, S., 2010. From oil-prone source rock to gas-producing shale reservoir-geologic and petrophysical characterization

of unconventional shale-gas reservoirs. SPE Paper 131350, 2010. In: CPS/SPE International Oil and Gas Conference and Exhibition. Beijing, China, p. 29.

Playter, T.L., 2013. Petrographic and x-ray microtomographic analysis of the Upper Montney Formation, Northeastern British Columbia, Canada. Ms.C. Thesis, Department of Earth and Atmospheric Sciences, University of Alberta, Edmonton, Alberta, Canada.

Preto, N., Kustatscher, E., and Wignall, P.B., 2010. Triassic climates - State of the art and perspectives. Palaeogeography, Palaeoclimatology, Palaeoecology, 290(1-4), 1-10. https://doi.org/10.1016/j.palaeo.2010.03.015.

Price, R.A., 1994. Cordilleran tectonics and the evolution of the Western Canada sedimentary basin. In Geological Atlas of Western Canada, Mossop, G.D., and Shetsen, I., pp. 13-24, Calgary, Alberta, Canadian Society of Petroleum Geologists/ Alberta Research Council.

Rakociński, M., Zatoń, M., Marynowski, L., Gedl, P., and Lehmann, J., 2018. Redox conditions, productivity, and volcanic input during deposition of uppermost Jurassic and Lower Cretaceous organic-rich siltstones in Spitsbergen, Norway. Cretaceous Research, 89, 126-147.

Ravikovitch, P.I., Haller, G.L., and Neimark, A.V., 1998. Density functional theory model for calculating pore size distributions: pore structure of nanoporous catalysts. Advances in Colloid Interface Science, 76-77, 203-226.

Riediger, C.L., Fowler, M.G., Brooks, P.W., and Snowdon, L.R., 1990. Triassic oils and potential Mesozoic source rocks, Peace River Arch area, Western Canada Basin. Organic Geochemistry, 16(1-3), 295–305. https://doi.org/10.1016/0146-6380(90)90049-6.

Rohais, S., Crombez, V., Euzen, T., and Zonneveld, J.-P., 2018. Subsidence dynamics of the Montney Formation (Early Triassic, western Canada sedimentary basin): Insights for its geodynamic setting and wider implications. Bulletin of Canadian Petroleum Geology, 66(1), 128-160.

Romero-Sarmiento, M.F., Euzen, T., Rohais, S., Jiang, C., and Littke, R., 2016. Artificial thermal maturation of source rocks at different thermal maturity levels: Application to the Triassic Montney and Doig formations in the Western Canada Sedimentary Basin. Organic Geochemistry, 97, 148-162. https://doi.org/10.1016/j.orggeochem.2016.05.002.

Ross, G.M., Gehrels, G.E., and Patchett, P.J., 1997. Provenance of Triassic strata in the Cordilleran miogeocline , western Canada. Bulletin of Canadian Petroleum Geology, 45(4), 461-473.

Russell, P., 2018. Recent advances in routine core analysis on the Montney Formation. Bulletin of Canadian Petroleum Geology, 66, 363-393.

Saidian, M., and Prasad, M., 2015. Effect of mineralogy on nuclear magnetic resonance surface relaxivity: A case study of Middle Bakken and Three Forks formations. Fuel, 161, 197-206.

Sanei, H., Haeri-Ardakani, O., Ghanizadeh, A., Clarkson, C.R., and Wood, J.M., 2016. Simple petrographic grain size analysis of siltstone reservoir rocks: An example from the Montney tight gas reservoir (Western Canada). Fuel 166, 253-257. https://doi.org/10.1016/j.fuel.2015.10.103.

Sanei, H., Wood, J.M., Ardakani, O.H., Clarkson, C.R., and Jiang, C., 2015. Characterization of organic matter fractions in an unconventional tight gas siltstone reservoir. International Journal of Coal Geology, 150-151, 296-305. https://doi.org/10.1016/j.coal.2015.04.004.

Schettler, P.D., Parmely, C.R., and Lee, W.J., 1989. Gas Storage and Transport in Devonian Shales, SPE Formation Evaluation, 3(3), 371-376. http://doi.org/10.2118/17070-PA.

Schieber, J., Southard, J., and Thaisen, K., 2007. Accretion of Mudstone Beds from Migrating Floccule Ripples. Science, 318, 1760-1763.

Scuderi, M.M., Kitajima, H., Carpenter, B.M., Saffer, D.M., and Marone, C., 2015. Evolution of permeability across the transition from brittle failure to cataclastic flow in porous siltstone. Geochemistry, Geophysics, Geosystems, 16(9), 2980-2993.

Slatt, R.M., and O'Brien, N.R., 2011. Pore types in the Barnett and Woodford gas shales: contribution to understanding gas storage and migration pathways in fine grained rocks. American Association of Petroleum Geologists Bulletin, 95, 2017-2030.

Sun, Y., Joachimski, M.M., Wignall, P.B., Chunbo, Y., Chen, Y., Jiang, H., Wang, L., Lai, X., and Yan, C., 2012. Lethally hot temperatures during the Early Triassic greenhouse. Science, 338, 366-370. https://doi.org/10.1126/science.1224126.

Utting, J., Zonneveld, J.P., MacNaughton, R.B., and Fallas, K.M., 2005. Palynostratigraphy, lithostratigraphy and thermal maturity of the Lower Triassic Toad and Grayling, and Montney formations of western Canada, and comparisons with coeval rocks of the Sverdrup Basin, Nunavut. Bulletin of Canadian Petroleum Geology, 53(1), 5-24. https://doi.org/10.2113/53.1.5.

Vaisblat, N., Harris, N.B., DeBhur, C., Euzen, T., Gasparrini, M., Crombez, V., Rohais, S., Krause, F. and Ayranci, K. 2017. Diagenetic model for the deep Montney Formation, Northeastern British Columbia. Geoscience BC Report 2017-1, p. 37-48. http://www.geosciencebc.com/i/pdf/SummaryofActivities2016/SoA2016_Vaisblat.pdf.

Velde, B., 1996. Compaction trends of clay-rich deep sea sediments. Marine Geology, 133(3-4), 193-201.

Walderhaug, O., Oelkers, E.H. and Bjørkum, P.A., 2004. An analysis of the roles of stress, temperature, and pH in chemical compaction of sandstones: discussion. Journal of Sedimentary Research, 74(3), 447-449.

Wood, J.M., 2013. Water Distribution in the Montney Tight Gas Play of the Western Canadian Sedimentary Basin: Significance for Resource Evaluation, in: SPE Canadian Unconventional Resources Conference. Society of Petroleum Engineers, Calgary, AB, Canada, pp. 290–302. https://doi.org/10.2118/161824-MS.

Wood, J.M., Sanei, H., Haeri-Ardakani, O., Curtis, M.E., and Akai, T., 2018. Organic petrography and scanning electron microscopy imaging of a thermal maturity series from the Montney tight-gas and hydrocarbon liquids fairway. Bulletin of Canadian Petroleum Geology, 66(2), 499-515. https://doi.org/10.1038/ncomms13614.

Wood, J.M., and Sanei, H., 2016. Secondary migration and leakage of methane from a major tight-gas system. Nature Communications, 7, 13614.

Wood, J.M., Sanei, H., Curtis, M.E., and Clarkson, C.R., 2015. Solid bitumen as a determinant of reservoir quality in an unconventional tight gas siltstone play. International Journal of Coal Geology, 150-151, 287–295. https://doi.org/10.1016/j.coal.2015.03.015.

Yang, B., 2018. Geological characteristics and reservoir properties in the unconventional Montney Formation, southwestern Alberta, Canada. Geoscience Journal, 22 (2), 313-325.

Yang, Y.L., and Aplin, A.C., 2007. Permeability and petrophysical properties of 30 natural mudstones. Journal of Geophysical Research, 112, B03206.

Zonneveld, J.-P., and Moslow, T.F., 2018. Palaeogeographic setting, lithostratigraphy, and sedimentary framework of the Lower Triassic Montney Formation of western Alberta and northeastern British Columbia. Bulletin of Canadian Petroleum Geology, 66(1), 93-127.

Zonneveld, J.-P., Golding, M.L., Moslow, T.F., Orchard, M.J., Playter, T.L., and Wilson, N., 2011. Depositional framework of the Lower Triassic Montey Formation, West-central Alberta and Northeastern British Columbia, in: Geoconvention. CSPG CSEG CWLS, Calgary, AB, Canada, pp. 1-4.

Zonneveld, J.-P., Beatty, T.W., MacNaughton, R.B., Pemberton, S.G., Utting, J., and Henderson, C.M., 2010. Sedimentology and ichnology of the Lower Triassic Montney Formation in the Pedigree-Ring/Border-Kahntah River area, northwestern Alberta and northeastern British Columbia. Bulletin of Canadian Petroleum Geology, 58(2), 115–140. https://doi.org/10.2113/gscpgbull.58.2.115.

Chapter 5 - A probabilistic approach for calculating permeability and water saturation in a tight reservoir; An example from the Montney Formation in Western Canada

Noga Vaisblat, Eric V. Eslinger, Nicholas B. Harris, Rick Chalaturnyk (Manuscript in preparation).

Abstract

Accurate determination of water saturation (S_w) is important for: (1) understanding water distribution in an unconventional reservoir, (2) calculating hydrocarbons reserves and (3) estimating relative permeabilities of formation fluids. Water saturation is typically measured directly on core samples or calculated indirectly using different methods (well-logs analysis or mercury injection data) for a single well, with limited ability to propagate results across a producing field.

We present a novel method for calculating S_w through matrix and fluids mass-balance, accounting for fluids properties and rock composition. Our model is computed in the software GAMLS$^©$ that uses a probabilistic multi-variate cluster analysis of well-logs to identify rock types endmembers (electroclasses). During clustering, each sample (depth step) is probabilistically assigned to one or more endmembers. Through the MFBG module (Matrix-Fluid mass Balance in GAMLS), each endmember is assigned fluid properties and an average mineral composition, and log-scale fluids and mineralogical abundances curves for the model well are generated. Water saturation for the model well can then be computed through matrix-fluid mass-balance. This mass-balance relies on matrix and pore fluid hydrogen content, and the readings of the neutron-porosity well-log. This probabilistic assignment permits a refined calibration of the model to downhole well logs and core analysis data.

We apply this method to the Montney Formation in the Pouce Coupe Field of western Canada. The data set includes eight wells in the Pouce Coupe area. The model well is cored

through the entire Montney Formation section, with core analyses (QEMSCAN mineralogy, porosity, permeability measurements, total organic carbon) taken in 1 m intervals. A second well, used for verification of model results, is cored through the top section of the formation. Water saturation data are available for both cores. Our model was calibrated to core analysis and well logs and tested with the verification well.

Results show that modeled mineralogy and computed total water saturation fit core measurements in the model well and the validation well, and are consistent with previously published data for the Montney Formation. The probabilistic model allows for better estimations of hydrocarbons reserves and permits more credible decision-making when targeting low S_w reservoir zones.

5.1 Introduction

Water saturation (Sw) is the fraction of pore volume occupied by water and is composed of free water, capillary-bound irreducible water, and water that is bound to clay minerals if those exist in the formation (Eslinger and Everett, 2012). Water saturation is important both because of its role in calculating hydrocarbons reserves and because it influences relative permeabilities of the reservoir rock to different fluids. However, water saturation is one of the most difficult petrophysical parameters to obtain.

In this paper we briefly review methods used for determining Sw from core samples and standard suites of downhole well logs. We then discuss the disadvantages of these methods with emphasis on Sw estimation for unconventional reservoirs and propose a new approach for calculating Sw that overcomes these shortcomings. Finally, we present a test case demonstrating the application of our approach for calculating water saturation on a dataset of the western Canadian Montney Formation in the Pouce Coupe area.

5.2 Review of water saturation measurement methods

Direct measurement of water saturation on core samples requires that the core is drilled using oil-based mud to ensure that drilling do not introduce water into the rock. Once retrieved, the core is sealed to prevent water loss. At the laboratory, water is extracted from the core and that volume, together with sample porosity are used to calculate Sw as a fraction of the total pore volume. Although routinely executed, direct measurement of Sw is not free of problems. Inappropriate preservation or sample preparation, sample size and measurement conditions can all affect the final results (Hurst, 1987 and reference therein, Wood, 2015).

Several methods exist for estimating Sw from downhole well logs, most relying the Archie equation (equation 1, Archie, 1942) that relates water saturation (Sw) to formation resistivity (R_t), formation water resistivity at formation temperature (R_w) and porosity (Ø), where a is the tortuosity factor, m is the cementation exponent, and n is the saturation exponent.

(1) $S_w = \left(\frac{a * R_w}{R_t * Ø^m} \right)^{\frac{1}{n}}$

Porosity is estimated through one or more of the porosity logs and can be calibrated to core measurements when these are available, although using a single matrix density value for heterogeneous sedimentary rocks to obtain porosity from the density-porosity equation (equation 2) may introduce uncertainties to the calculated porosity.

(2) $Ø_t = \frac{(\rho_m - \rho_b)}{(\rho_m - \rho_f)}$

Where $Ø_t$ is total porosity, ρ_m is matrix density, ρ_b is bulk rock density, and ρ_f is the fluid density. Additional uncertainties may be introduced in fine-grained rocks if bed thickness is below well-log resolution, for example by variation in grain density between beds (for example interbedded clastic- and carbonate-rich beds), complicating the extraction of meaningful porosities from well-logs.

Archie (1942) proposed using a value of 2 for m and n, and a value of 1 for a. Later, a range of values for m and a was suggested that depend on lithology (Asquith and Krygowski,

2004 and references therein). Single values for m, n, and a are usually selected for the entire reservoir interval. This is possibly suitable for homogeneous conventional reservoirs, but perhaps not adequate for describing the frequent variation in mineralogy (grain density) encountered in heterogeneous unconventional reservoirs (Eslinger and Everett, 2012).

Many fine-grained rocks also contain substantial amounts of clay minerals that may be important for water saturation calculations because their negative surface charge. This results in adsorbed water and cations that neutralize the unbalanced charge around each clay crystal. Ions neutralizing the negatively charged surface area of clay minerals exchange easily with ions in formation water. It is possible to measure this Cation Exchange Capacity (CEC) of the clays. Formations containing clay with high CEC will have high bulk rock conductivity and lower resistivity.

Water bound to clay minerals occupy pore space and reduce total porosity($\emptyset_t$) and reduce it to effective porosity ($\emptyset_e$), which is the sum of free porosity ($\emptyset_{free}$) and porosity occupied by irreducible fluids ($\emptyset_{irr}$). Several methods attempt to account for the effect of clay minerals on total porosity and bulk-rock resistivity (and thus S$_w$) by estimating the volume of clay (V$_{shale}$) from either gamma ray (GR) log, spontaneous potential log or neutron-density cross plot (Asquith and Krygowski, 2004).

V$_{shale}$ is commonly estimated from the GR log. In this method, GR reading is normalized and then empirically related to the volume of shale (for example Larinov, 1969; Steiber, 1970) and less commonly to the actual volume of clay minerals (David et al., 2015). The calculated shale volume is then subtracted from total porosity to obtain the effective porosity. Two main complications arise in this application.

First, since shale volume and clay volume are commonly used interchangeably (see Spooner, 2014 for discussion), the higher radioactivity of shale is entirely attributed to clay minerals. The gamma ray log measures the natural radioactivity of the rock, emitted mainly through the decay of U, Th, and K isotopes. Potassium and, to a lesser extent, thorium are associated with clays. Thus, in cases where U and possibly when Th contribute to the total

223

gamma ray reading, attributing the entire increase in the GR reading of shaley intervals to clay minerals results in an underestimation of effective porosity, and an overestimation of water saturation.

Second, the correlation between the GR log and shale volume is based on empirical measurements that were derived for specific data sets, introducing errors into $\emptyset_e$ and S_w calculations (Larinov, 1969; Steiber, 1970; Clavier et al, 1971; David et al., 2015). In addition, the V_{shale} method was established for conventional reservoirs (shaley sandstones). In unconventional reservoirs, the basic process of identifying a 'clean' zone in the GR log within the boundaries of the formation is problematic.

Other models investigate the influence of water bound to clays on the total porosity by addressing the volume of clay minerals and their direct control on resistivity (see review by Herrick and Kennedy, 2009). Two such models are the Waxman-Smits-Thomas (WST) (Waxman and Smits, 1968; Waxman and Thomas, 1974) and the dual-water model (Clavier, et al., 1984). If the salinity of formation water is similar to the salinity of the bound water, the two models will generate similar results for S_w. The dual-water model (Clavier, et al., 1984) (equation 3) is an expansion of the WST model that accounts for differences in salinity (and hence conductivity) between formation water (FW in equation 3) and clay bound water BW in equation 3).

(3) $C_t = \frac{S^n_{WT}}{F_0}\left[C_{FW} + \frac{v_Q Q_V}{S_{WT}}(C_{BW} - C_{FW})\right]$

Where:

C_t - formation conductivity (1/formation resistivity)

S^n_{WT} - Total water saturation (n is the saturation exponent)

F_o - Formation factor

C_{FW} - Formation water conductivity

C_{BW} - Clay bound water conductivity

v_Q - volume of clay-water per counterion (charge) in [ml/ meq]

Q_v - concentration of clay counterions (charge) per unit pore volume in [meq/ml]

In the dual-water model, the cation exchange capacity of the clays per unit of pore volume (Qv in equation 3) controls the conductivity of water bound to clay minerals. The operator is required to know the type of clay minerals present in the rock, know or estimate the CEC of those clays, and know or estimate total pore volume.

5.3 Probabilistic clustering to identify rock types endmembers

In this section, we present a method for calculating water saturation that overcomes the three issues highlighted above, namely: (1) using a single value for matrix density (2) using single values for a, m, and n in the Archie equation, and (3) using Vshale to estimate clay mineral content. The method is termed MFBG (Matrix Fluid Balance modeling using GAMLS) and is built into the software GAMLS$^{©}$. A flow chart of the entire procedure is presented in Fig. 5.1. MFBG is an iterative forward-modeling procedure that applies probabilistic clustering of well-logs combined with a database of mineral and organic matter properties and tool-response. The MFBG module allows variables such as a, n, m and matrix density to vary through the reservoir rather than using a single value for the interval. Because the dual-water equation is implemented in the code, there is no need to estimate V_{shale}. The first step for modeling rock properties in GMALS$^{©}$ is a probabilistic (soft / fuzzy) cluster analysis to identify rock-type endmembers (electroclasses), in which each sample is assigned to one or more groups with a probability between 0 and 1 (fig. 5.2).

Probabilistic cluster analysis in GAMLS$^{©}$ is accomplished using the Probabilistic Clustering and Prediction (PCP) module (Eslinger and Boyle, 2011; 2013) and Eslinger et al. (2014), which uses well log data as clustering variables where each digitized depth step is a sample. Bulk density, neutron porosity and gamma ray logs are required for the analysis, but other well-logs can be added. It is possible to cluster one or more wells and run either a supervised or a non-supervised probabilistic clustering. The number of electroclasses is defined by the user. Each sample in each well in the clustering run is assigned to each electroclass with a

fractional (fuzzy) probability. Samples assigned to the same electroclass will have similar well-logs response.

Preparation

1. Import logs (LAS) for all wells to GAMLS.

2. Select tops.

3. Perform core to log depth match.

4. QC logs and Normalized GR logs for all wells.

5. Normalize NPHI logs if needed.

Move to PCP module

Probibilistic Clustering & Predictions

1. Import RHOB, NPHI, GR (other logs are optional).

2. Select clustering method (supervise/ non supervise).

4. Select the number of desired electroclasses.

5. Run clustering analysis.

Move model well to MFBG module

Matrix-Fluid Balance

1. Select input parameters:

temp. gradient, reference depth assign fluid properties (table 3).

2. Assign individual values to each electroclass:

values for a, m, n, initial Sw and clay permeability factor (table 3).

4. Import core analysis:

mineralogy, TOC, porosity, permeability and Sw.

5. Change/ add mineral properties (table 1) if needed.

6. Calibration:

- Adjust mineralogy for each mode until a good fit is achieved between

measured and computed mineralogy and TOC curves,

measured and computed gran density curves,

and measured and computed NPHI curves.

Fig. 5.1: Workflow for calculating water saturation in GAMLS
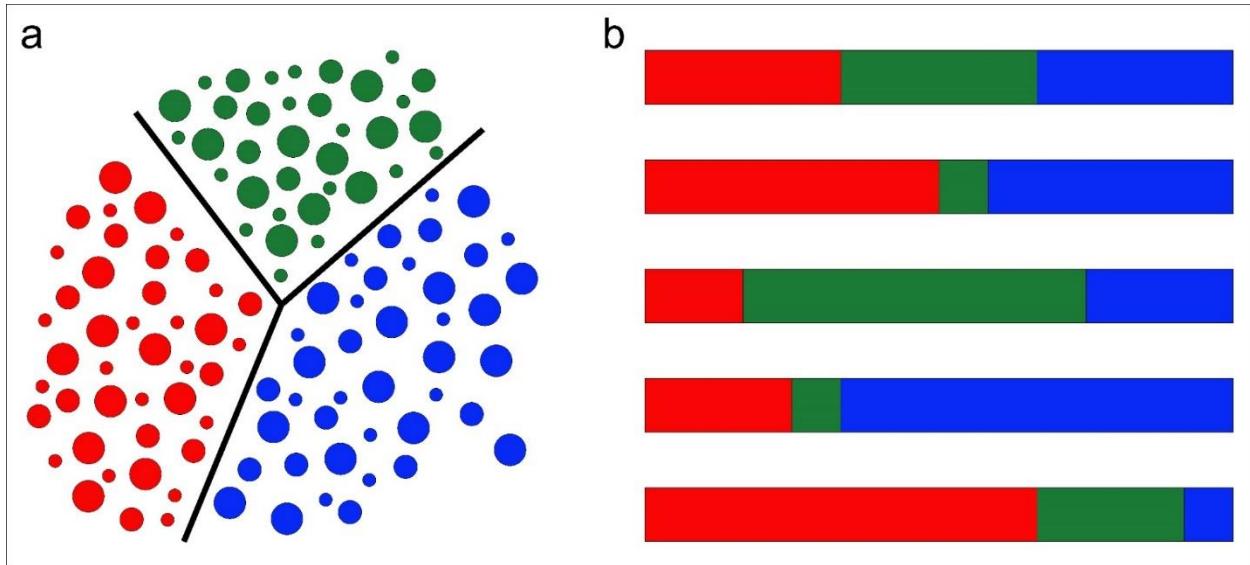
Fig. 5.2: Cluster analysis is a method used for grouping samples based on similarity, such that samples in each group are more similar to one another than to samples in other groups. (a) Hard clustering. Each sample is assigned only to one group. (b) probabilistic (soft / fuzzy) clustering. Each sample is assigned to one or more groups with a probability between 0 and 1.

Following the clustering run, all electroclasses are assigned a lithology (rock type) based on their average GR signal (for sandstone, siltstone and shale) and apparent grain density (for carbonates and evaporites). Density and GR cut-off values are selected by the operator. Fig. 5.3 demonstrates the methodology for determining apparent grain density for each electroclass in the PCP module. Multiple electroclasses can be assigned the same rock type. In addition to lithology, an average mineralogy and organic matter composition (from core data) are assigned to each electroclass, and the average grain density is computed from these parameters for each of the electroclasses.

In the next step, specific parameters (for example: a, n, m in the Archie equation), or petrophysical property (for example: composition, grain density, porosity, Qv, CEC, Sw) are calculated for each sample (depth step) using equation 4:

(4) $X_{sample} = \sum X_i * P_i$

Where X is the computed petrophysical property, X_i is the average value of the property for electroclass i, and P_i the fractional probability assigned to electroclass i in the sample. The probabilistic electroclasses assignment enables the user to generate a unique set of parameters and properties for each depth step in the bulk-rock box model.
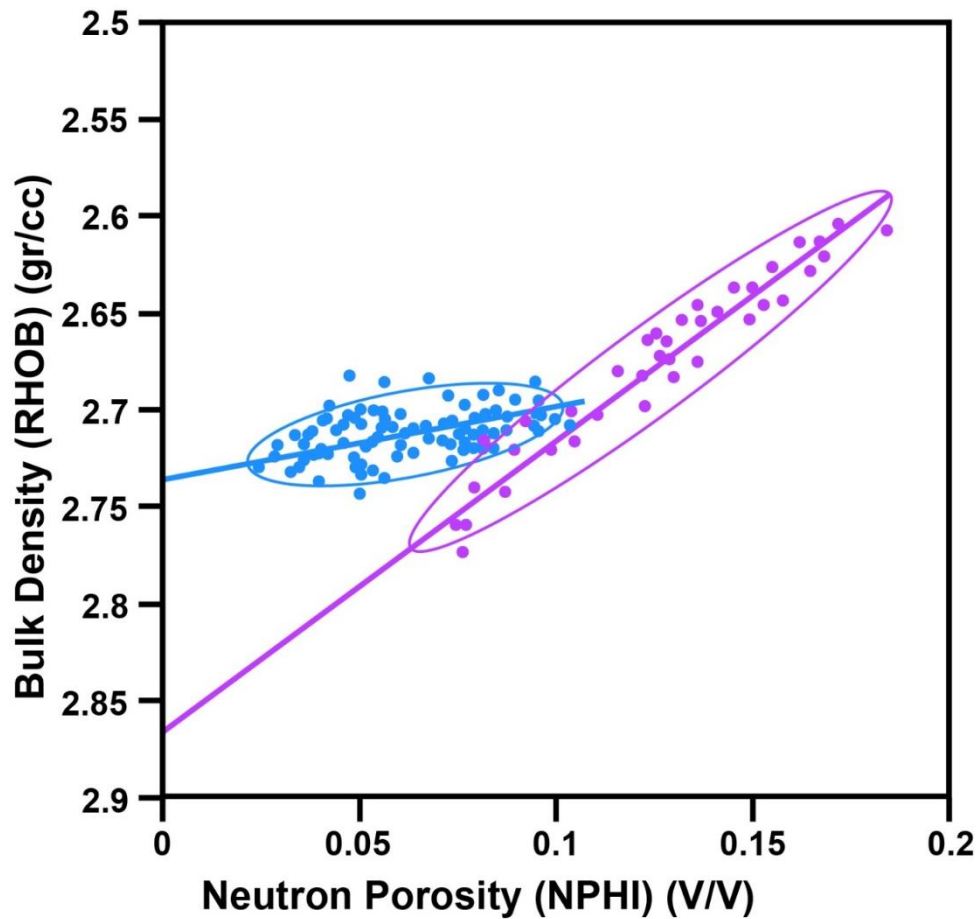
Fig. 5.3: Apparent grain density computation. Apparent grain density is computed from a standard bulk density - neutron porosity cross plot. An ellipse is drawn for each electroclass at 2 standard deviations from the mean NPHI and RHOB values. The ellipse is a projection of n-dimensional ellipsoid onto the 2-dimentional NPHI-RHOB plane. The number of dimensions (n) is the number of variables (well-logs) used for clustering. A line is drawn through the long axis of the ellipse and is extrapolated to NPHI=0. When porosity = 0, bulk density equals mean grain (matrix) density. Samples that are assigned to a given electroclass with very high probabilities should provide the best estimate of grain density.

5.4. Bulk-rock box model

The full modeling procedure, including the equations in the section that follows, is described in Eslinger and Everett (2012). Here we present a conceptual explanation of porosity and Sw calculations using the bulk-rock box model in MFBG. The following calculations are performed for each electroclass, and then for each depth step based on the probabilistic assignment of electroclasses to any particular sample.

The bulk rock in MFBG consists of matrix components and pore-filling components (fig. 5.4). Matrix components include organic matter, clay minerals and non-clay minerals. Pore filling components include hydrocarbons, free water, clay mineral-bound water and capillary-held irreducible water. If an analysis of rock composition is available, the fractions of three of the box model components (organic matter, clay minerals and non-clay minerals) are known.

Fluid density calculations account for the invading fluid volume and density as well as for temperature-dependent fluid resistivities. If hydrocarbons exist in the rock, it is necessary to know (or estimate) their density. If both gas and oil are present, it is necessary to know (or estimate) the fractional gas to oil volumetric ratio (termed GOF in MFBG).

Total porosity ($\emptyset_t$) is calculated with the density-porosity (equation 2) using the unique matrix and fluid densities of each sample. Total porosity ($\emptyset_t$) is the sum of bound water porosity ($\emptyset_{bw}$), irreducible fluids porosity ($\emptyset_{irr}$) and free fluids porosity ($\emptyset_{free}$). The sum of free porosity ($\emptyset_{free}$) and irreducible fluids porosity ($\emptyset_{irr}$) is the effective porosity ($\emptyset_e$) (equation 5):

(5) $\emptyset_t = \emptyset_{bw} + \emptyset_{irr} + \emptyset_{free} = \emptyset_{bw} + \emptyset_e$

The average matrix composition (minerals and organic matter) is next calculated for each electroclass from all samples assigned to this electroclass with a probability ≥ 0.8. Then, using the probabilistic electroclasses assignment, the matrix composition is calculated for each sample. Together with mineralogy, sample surface area and cation exchange capacity are computed for all samples using minerals' specific surface area (Table 5.1).
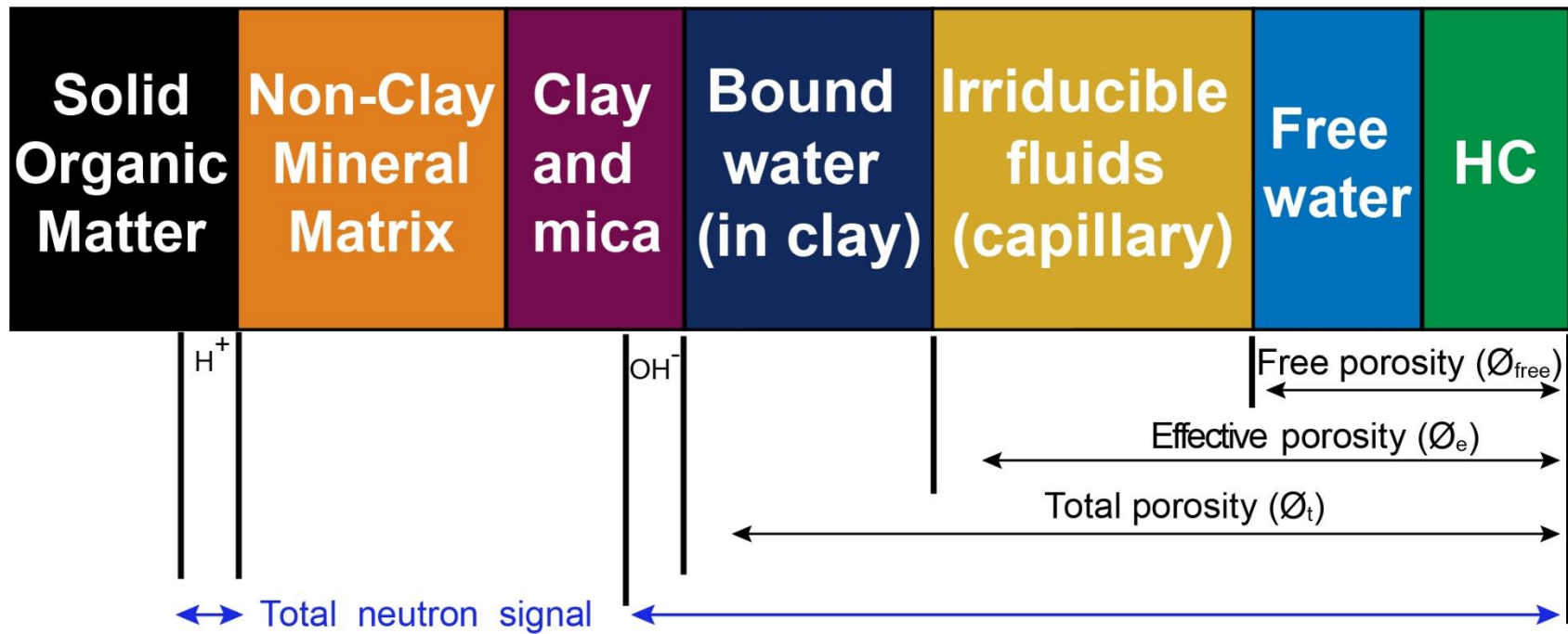
Fig. 5.4: Matrix-fluid box model describes bulk rock composition. Matrix components are organic matter, clay minerals and non-clay minerals. Pore filling components are hydrocarbons, free water, clay minerals bound water and capillary-held irreducible water. Total neutron signal includes total porosity and hydrogen in the organic matter and in clay and mica minerals.

Table 5.1: Minerals calibration parameters.

mineral	Density (gr/cc)	Specific surface area[1] (m^2/gr)	CEC[2] (meq/100 gr)	NPHI[3] (p.u.)
quartz[4]	2.65	1.20	0.00	-1.80
K-feldspar	2.66	0.30	0.00	-0.60
Na-feldspar	2.67	0.30	0.00	-0.50
muscovite	2.84	2.00	0.00	20.80
biotite	3.22	2.00	0.00	11.00
calcite	2.71	0.60	0.00	0.20
dolomite	2.84	0.50	0.00	1.50
Fe-dolomite	2.89	2.00	0.00	5.70
kaolinite	2.62	15.00	2.50	45.00
MLIS[5]	2.77	100.00	28.75	15.00
chlorite	3.42	15.00	2.00	48.20
pyrite	5.01	0.30	0.00	-1.90
siderite	3.96	2.00	0.00	18.40
barite	4.48	1.00	0.00	0.20
anhydrite	2.97	1.00	0.00	-0.70
apatite	3.21	1.00	0.00	-2.00
bitumen	1.3	25.00	25.00	30

[1] Data from Herron et al., 1998.

[2] Data from Grim, 1968 and Van Olphen and Fripiat, 1979.

[3] Neutron porosity tool response; data from Herron and Matteson (1993).

[4] Silt size; data from Herron et al., 1998.

[5] Mixed layer illite-smectite (5% swelling potential).

In the next step, matrix permeability is estimated using a modified Kozeny-Carman equation Carman, 1956) that relates surface area (rather than porosity) to permeability (Herron et al., 1998). The rationale behind this equation is that the ratio of surface area to pore volume can be used as a measure for pore system connectivity, assuming that pore throat radius is the main control on permeability. The Herron et al. (1998) method is appropriate here since it is based on rock composition, and in particular on the surface area of clay minerals, which is also the basis for our modeling of Sw. The general form of the Herron et al. (1998) equation is:

(6) $k_\Lambda = \dfrac{Z*\emptyset^{\alpha(m^*+2)}}{\rho_M{}^\beta(1-\phi)^\beta(\sum m_i v_i S_{0_i})^\beta}$

Where Z is a proportionality constant relating porosity and k_Λ

ϕ is total porosity

m* is an empirically derived modified cementation factor: $m^* = 1.653 + 0.0818 * (S_o\rho_{mM})^{0.5}$

ρ_M is matrix density

m_i is mass fraction of mineral i

S_{oi} is the specific surface area for mineral i in (length^2/mass)

v_i is the clay permeability factor. This parameter accounts for the fraction of the total surface area of a given mineral that affects fluid flow. For detrital clays v_i = 0.1. For authigenic (where more of the surface area participates is available for restricting flow), v_i = 0.2. For non clay minerals v_i = 1.

α and β are constants. If k> 100 md, α=1 and β=2. If k< 100 md, α=1.7 and β=3.4.

Effective porosity ($\emptyset_e$) is calculated by deducting the volume of water bound to clay minerals ($\emptyset_{BW}$) from the previously calculated total porosity. Bound water saturation is computed using bulk rock CEC, grain density and pore water salinity (Clavier, 1984). In MFBG, bulk rock CEC is computed from mineralogical CEC data (Table 5.1) and mineral concentrations. This step requires accurate knowledge of clay type and in the case of smectite clays, swelling potential is also required.

Free porosity ($\emptyset_f$) may be directly estimated from a Nuclear Magnetic Resonance (NMR) log. If that is not available, we use equation 7 (Herron et al., 1998; Eslinger and Everett, 2012) to compute porosity occupied by free (movable) fluids:

(7) $\emptyset_f = \emptyset_t - (\emptyset_{BW} + \emptyset_{irr}) = \emptyset_t - \left[\emptyset_t / \left(\dfrac{K^{0.25}}{10*\emptyset_t{}^{0.5}} + 1\right)\right]$

where K is permeability in md, estimated through equation 6.

Finally, Sw can be computed using the dual-water equation (equation 3). As mentioned, a reliable characterization of minerals allows the assignment of the appropriate CEC value (related to the Qv parameter in the dual water equation) to the matrix. Calculated matrix CEC

values can then be compared with laboratory measurements. Cation exchange capacity values used in our modeling are average values obtained from standard clay samples analyses (Table 5.1).

5.5. Calibrating the model: matrix - fluids mass balance

Checks exist throughout the computation process to confirm internal consistency of the matrix - fluid mass balance (see Eslinger and Everett, 2012 for details) but are not used for model calibration. The calibration is achieved by adjusting input parameters so that output (modeled) parameters fit the following measurements:

(1) Modeled rock composition (mineralogy and organic matter content) is calibrated against core measurements.

(2) Modeled matrix density (grain density) is calibrated against core measurements.

(3) Modeled bulk rock density (matrix + fluids) is calibrated against bulk rock density well-log (RHOB).

(4) Modeled total porosity is calibrated against core measurements.

(5) Modeled bulk rock neutron response is calibrated against neutron porosity well- log (NPHI).

(6) It is possible to calibrate modeled bulk rock response to GR (Gamma ray), PEF (Photoelectric absorption Factor), and DTS (P wave travel time) with downhole well logs, if response values of individual rock components to these measurements are known (Eslinger and Everett, 2012).

Neutron porosity response of the bulk rock is computed solely for calibration purposes and is calibrated against the downhole neutron well log (NPHI). The NPHI tool responds to the hydrogen in the rock. Water and hydrocarbons carry hydrogen, but so do organic matter (kerogen and/or bitumen), and several other minerals including clays, micas, and water bearing minerals like opal and gypsum.

Bulk-rock neutron response is a combined effect of the neutron response of the fluids (water, hydrocarbons and mud filtrate) and the matrix (minerals and organic matter). Values for the neutron response of the fluids are inserted as inputs for the model. These values need to be assessed based on fluids composition and reservoir temperature (Serra, 1984; Schlumberger, 2009, Fig. Gen-8 p. 10). Neutron response accounts for mud filtrates by setting the degree of drilling mud invasion. If both oil and gas exist in the reservoir, the model should account for both fluids. This is done by assigning each electroclass with a Gas to Oil Fraction (GOF) value, which is the volumetric ratio of gas to oil at reservoir condition. The GOF value dictates how much of the neutron signal is contributed by the oil and how much is contributed by the gas. If only gas exists in the reservoir, GOF is zero.

Neutron responses of matrix components are taken from the literature and are provided in Table 5.1. Matrix neutron response is calculated for each electroclass based on its average composition. Finally, the neutron response of the fluids and the matrix are combined and computed for each sample based on the probabilistic assignment of electroclasses for each sample

5.6. An example from the Montney Formation:

5.6.1. General/ Background

We demonstrate the application of the MFBG method to obtaining water saturation in the Montney Formation, a world-class unconventional gas and light oil reservoir in western Canada that is predominantly produced through horizontal drilling with hydraulic fracturing. As of 2013, estimated reserves were 450 TCF of gas, 14,520 MMB of gas liquids, and 1125 MMB of oil (National Energy Board, Government of Canada, 2013). The Montney Formation was deposited in the Lower Triassic (Davies et al., 1997; Utting et al., 2005; Henderson et al., 2018) and it currently subcrops over 130,000 km^2 in central and southwestern Alberta and northeastern British Columbia (Fig. 5.5 a). The rock is composed of mixed siliciclastics and carbonates siltstone (Davies et al., 1997; Barber, 2002; chapter 2 this study).

Obtaining robust estimates of water saturation in the Montney Formation is particularly important for reserve estimates but has proved to be problematic. Water saturation in the Montney Formation has been related to rock fabric (bioturbated sediments typically retain more water), rock composition (mainly clay minerals) and the efficiency of water displacement during hydrocarbon charging (Wood, 2013). Water saturation in the Montney Formation varies widely from close to zero (irreducible water saturation) to over 50% (Wood, 2013). The upper section of the formation typically has higher water saturation than the lower part, but higher water saturations are not constrained to a certain interval, and multiple hydrocarbon/water contacts exists within the siltstone reservoir (Wood 2013). With abundant publically available data, and the need to better constraint water saturation the Montney Formation is appropriate test case for modeling with the GAMLS MFBG module.

5.6.2 Dataset

Our dataset includes 8 wells in the Pouce Coupe field, drilled through the entire thickness of the Montney Formation (fig. 5.5 b). The database comprises publically available data, obtained from the Alberta Energy Regulator (AER) and the British-Columbia Oil and Gas Commission (BC-OGC), with additional data provided by Birchcliff Energy. All wells in our dataset have at minimum gamma ray, density, and neutron porosity well-logs. Two wells (06-03-079-13W6 and 01-25-079-14W6) have additional petrophysical data (mineralogy, organic matter content, porosity, permeability, grain density, and water saturation). The core retrieved from well 01-25-079-14W6 was drilled with oil-base mud, while the core retrieved from well 06-03-079-13W6 was drilled with water-base mud. All the data was acquired by the operators with analyses performed by different service companies. Analyses information is summarized in Table 5.2.
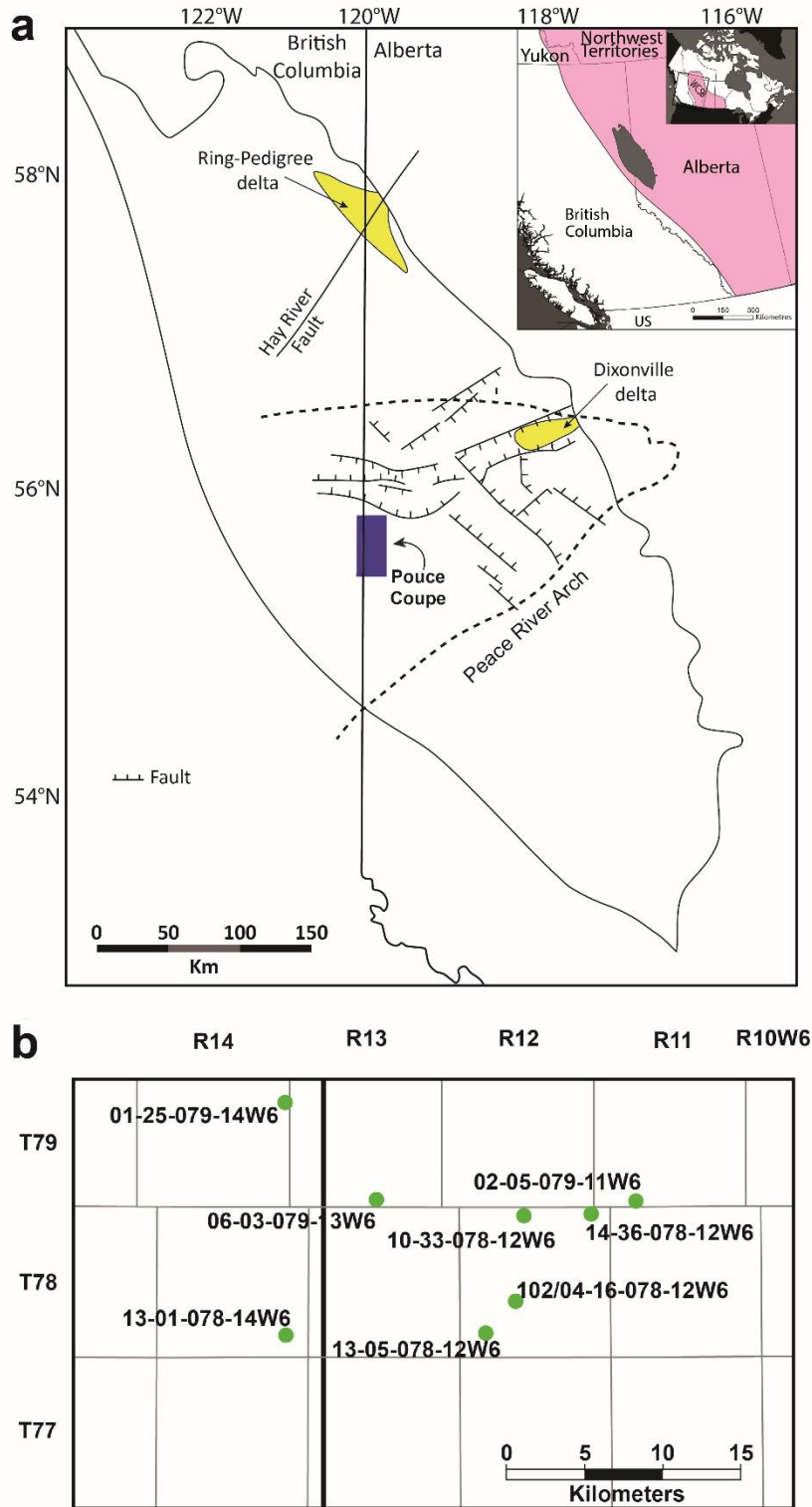
Fig. 5.5: Research area map. (a) The Montney Formation in western Canada (Alberta and British Columbia), highlighting the Pouce-Coupe field. Insert shows the location of the Montney Formation within the Western Canadian Sedimentary Basin (pink). Map modified from Zonneveld and Moslow (2018) (b) Location of study wells in the Pouce Coupe field.

236

Table 5.2: Number of samples and analysis information for the calibration and verification wells.

Well	QEMSCAN	TOC	Porosity	permeability	grain density	Sw
06-03-079-13W6	295	295[a]/ 77[b]	108[c]	108[c]	108[d]	107[e]
01-25-079-14W6	28	4[f]	42[d]	33[g]	49[d]	42[e]

[a] TOC on pseudocutting samples, LECO
[b] TOC on plug samples, LECO
[c] CMS-300 (Core Measurement System),
  pulse decay and porosimetery on plugs.

[d] He-pycnometry
[e] Dean stark, full diameter core
[f] Rock-Eval
[g] Pulse decay, unspecified

Sampling in our analysis was identical in both cores. A continuous sliver was cut along the entire length of each core and divided into 1-meter intervals. Each interval was then crushed to generate pseudo-cuttings. A ~50 gr subsample from each section was sent for QEMSCAN analysis. Mineralogy data was determined by QEMSCAN analysis at SGS Canada laboratories in Burnaby, BC, Canada. A second subsample of the pseudo cuttings was sent for total organic carbon (TOC) analysis. The pseudo cuttings method allows for better calibration with well-logs than a plug analysis would, as it provides information with similar continuity and at a similar resolution to the well-logs (~ 1 meter).

In addition to pseudo cuttings, plug samples were analyzed for TOC content (LECO), grain density (He pycnometry), porosity and permeability (nitrogen pycnometry and pulse decay at reservoir pressure) analyses. Water saturation was obtained by Dean Stark analysis on full diameter core samples.

5.6.3 Clustering and calibration

Three well-logs were selected for clustering: bulk density (RHOB), neutron porosity (NPHI) and gamma ray (GR). Following picks for the tops of stratigraphic units and meticulous core-to-log depth shift, GR logs from all wells were normalized to the gamma log of well 06-03-079-13W6 and one neutron porosity log (well 1-25-79-14W6) was normalized to the neutron log of well 06-03-079-13W6. Well-logs of all eight wells were imported into the PCP module

in GAMLS© and a non-supervised probabilistic clustering run was initiated with instructions to identify 15 electroclasses. The cluster run included the entire interval of the Montney Formation, between the top of the Montney Formation (termed Basal Doig in Alberta) and the Belloy Formation that underlies the Montney. The results of the clustering run is presented in Fig. 5.6.

Since well 06-03-079-13W6 has the most data, it was selected as the model well and transferred into the MFBG module. Input parameters used for generating matrix-fluid mass balance are presented in Table 5.3. Calibration of the model was performed against downhole neutron (NPHI) and photoelectric absorption factor (PEF) well-logs, as well as plugs porosity and grain density measurements, where available.

5.6.4 Results

The calibrated model of rock composition and petrophysical properties is presented in Fig. 5.7 together with measured values from core. The calibrated model shows a good fit to the measured data, except for computed permeability which is two to three orders of magnitude lower than the measured permeability (discussed below). The computed (synthetic) neutron log shows a very good fit to the measured (original) neutron log, and most importantly, computed water saturation fits the measured data.

Measured water saturations for the calibration well range between 3 and 33%, with an average of 14%. Throughout most of the Montney Formation interval Sw is lower than 10%, but several sections show higher water content (Fig. 5.7). Modeled water saturations vary from 1 to 100% with an average of 9%. A modeled water saturation of 100% for the Montney Formation is unrealistic; however, only 2% of the data points (40 of 1955) have values that differ more than 2 standard deviations (2σ) from the average water saturation value. Qualitatively, water saturation is grossly overestimated only six depth steps (Fig. 5.7).

The model generated for well 06-03-079-13W6 was saved and used to model a second well in the cluster run (well 1-25-79-14W6) for verification (Fig. 5.8). Minimal core data is available for the upper part of the verification well, making it difficult to evaluate the fit between the log-based computed mineral curves and the core data. However, Sw curve shows very good fit to the Sw curve calculated from Wood (2013).
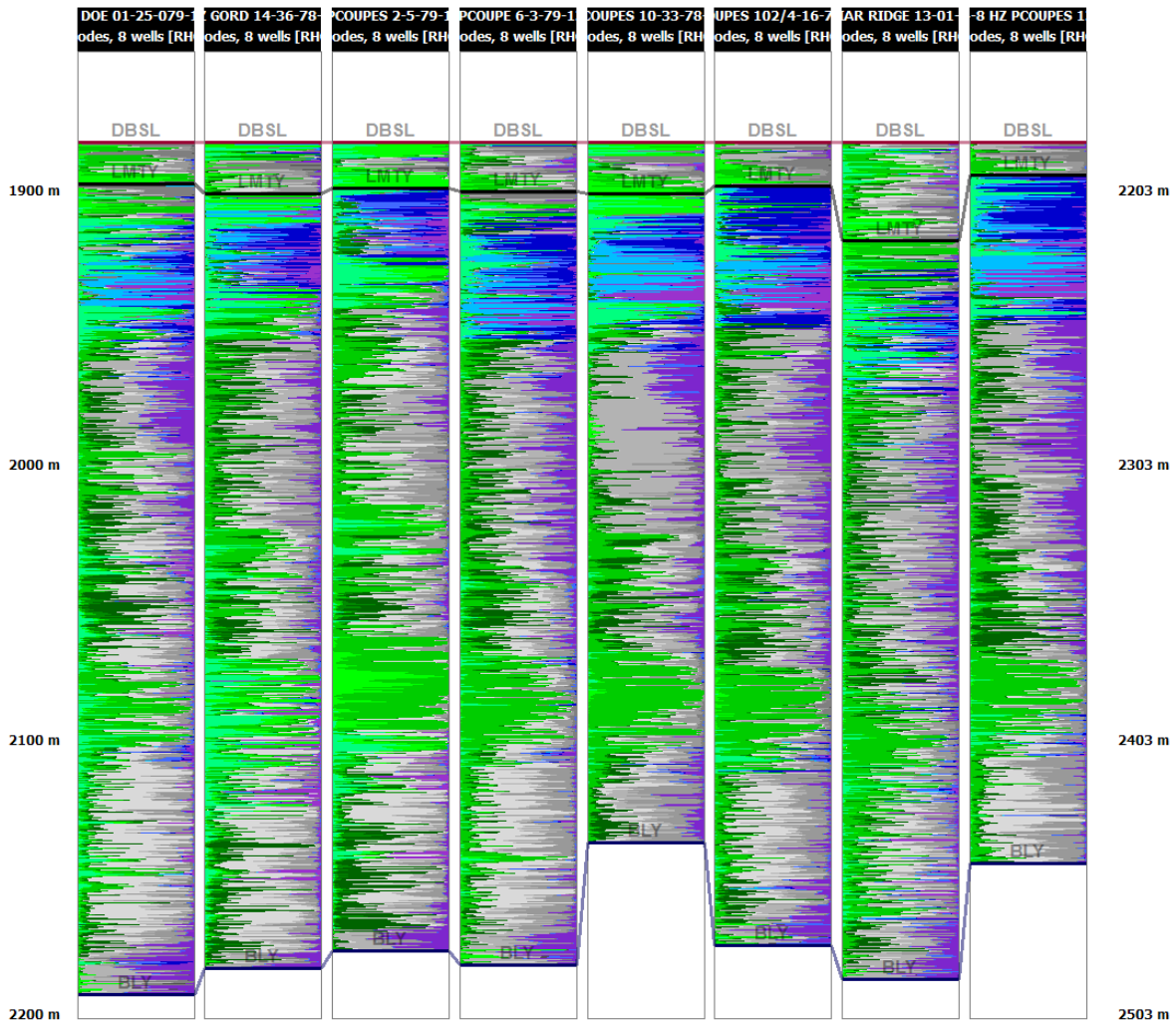
Fig. 5.6: Non supervised clustering run results showing probabilistic assignment of 12 electroclasses. All wells are aligned to the top of the clustered section. Depth (on the left) are for 13-05-078-12W6 well. Depths are different for every well, but the thickness of the interval is similar at ~200 m.

DBSL - top of the Basal Doig (Upper Montney Member); LMTY - top of the Lower Montney Member; BLY - Top of the Belloy Formation.

239

Table 5.3: Input parameters used for MFBG model calibration

Temperature:					Archie[b]	
Surface temperature	17 ^{o}C				a	1
BHT	75.3 ^{o}C				m	1.83
Temp. gradient	25.45 ^{o}C/km				n	1.3
Reference depth	2091.08 m					
Reference depth emperature	58.06 ^{o}C					

Fluids properties					Others	
	Density	**HI**	**Initial Rw**[a]	**API**	v_i [c]	0.1
Water	1.083	0.9	0.04			
Gas	0.185	0.4				
oil	0.83	1.04		42		
Mud filtrate	1.1	0.9	0.03			

[a] Fluid resistivity at reference depth.

[b] Values from Wood, 2013

[c] Clay permeability factor, equation 6.

Fig. 5.7: Calibrated MFBG model for the 06-03-079-13W6 well. Black curves are core measurements. Curves with the initial (M_) are modeled curves.

Track 1: Probabilistic model with assigned electroclasses for the model well. Track 2: modeled and calibrated grain density. Track 3: measured and modeled porosity. Track 4: Measured neutron log and modeled bulk rock neutron log response. Track 5: Measured and modeled TOC content. Track 5: Measured and modeled permeability. Red curve is permeability calculated from the equations proposed by Wood (2013). Track 7: measured and modeled water saturation. Red curve is Sw calculated from the equations proposed by Wood (2013). Track 8 - 21: measured and modeled mineralogical composition. K-feld is K-feldspar; Na-feld. Is Na-feldspar; MLIS is mixed layer illite-smectite clays; musc. is muscovite; chlor. Is chlorite; kaolin. Is kaolinite; Fe-dol is Fe-rich dolomite; and anhyd. is anhydrite. DBSL is the top of the Basal Doig (Upper Montney Member), LMTY is the top of the Lower Montney Member, and BLY is Top of the Belloy Formation.
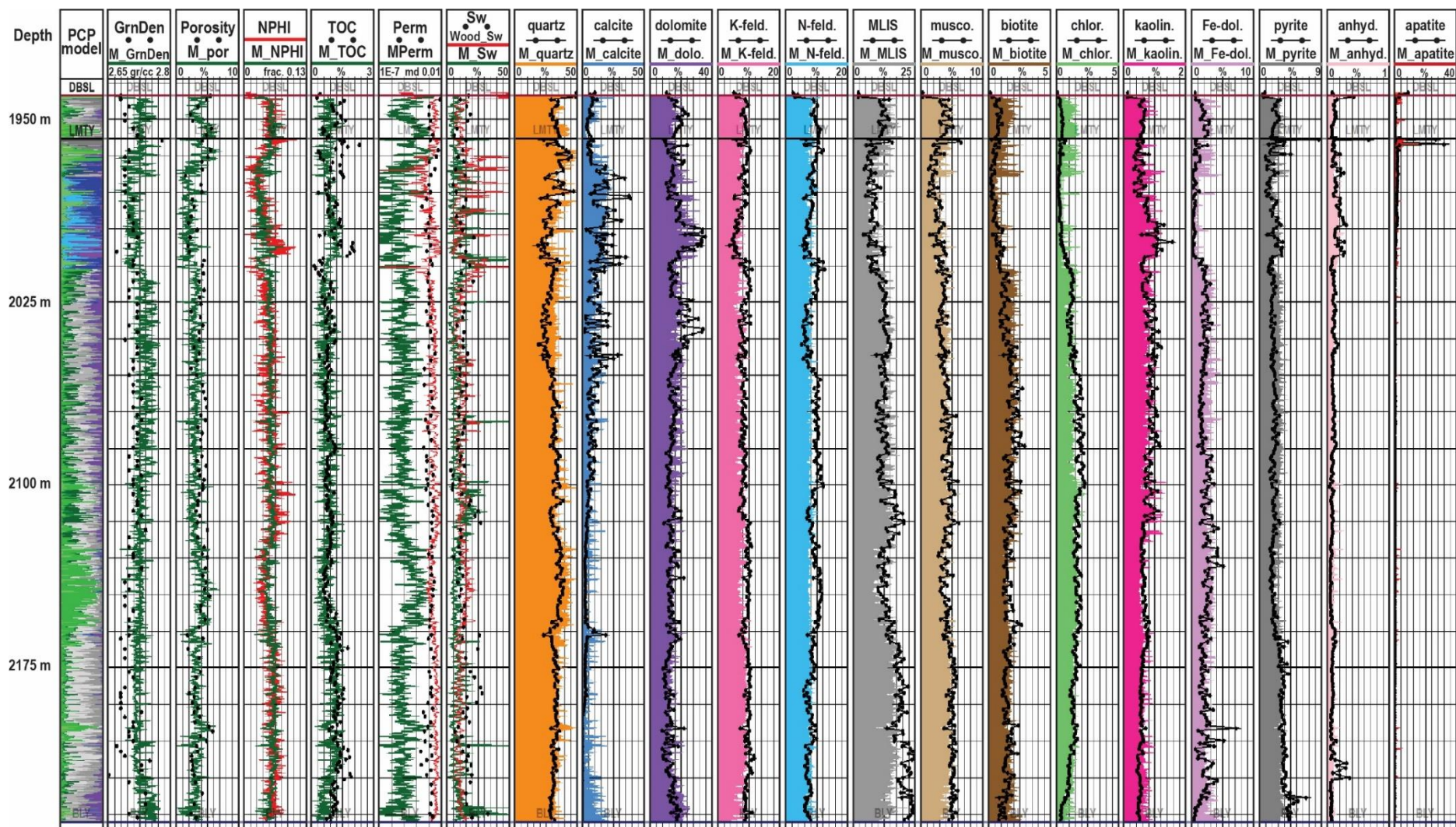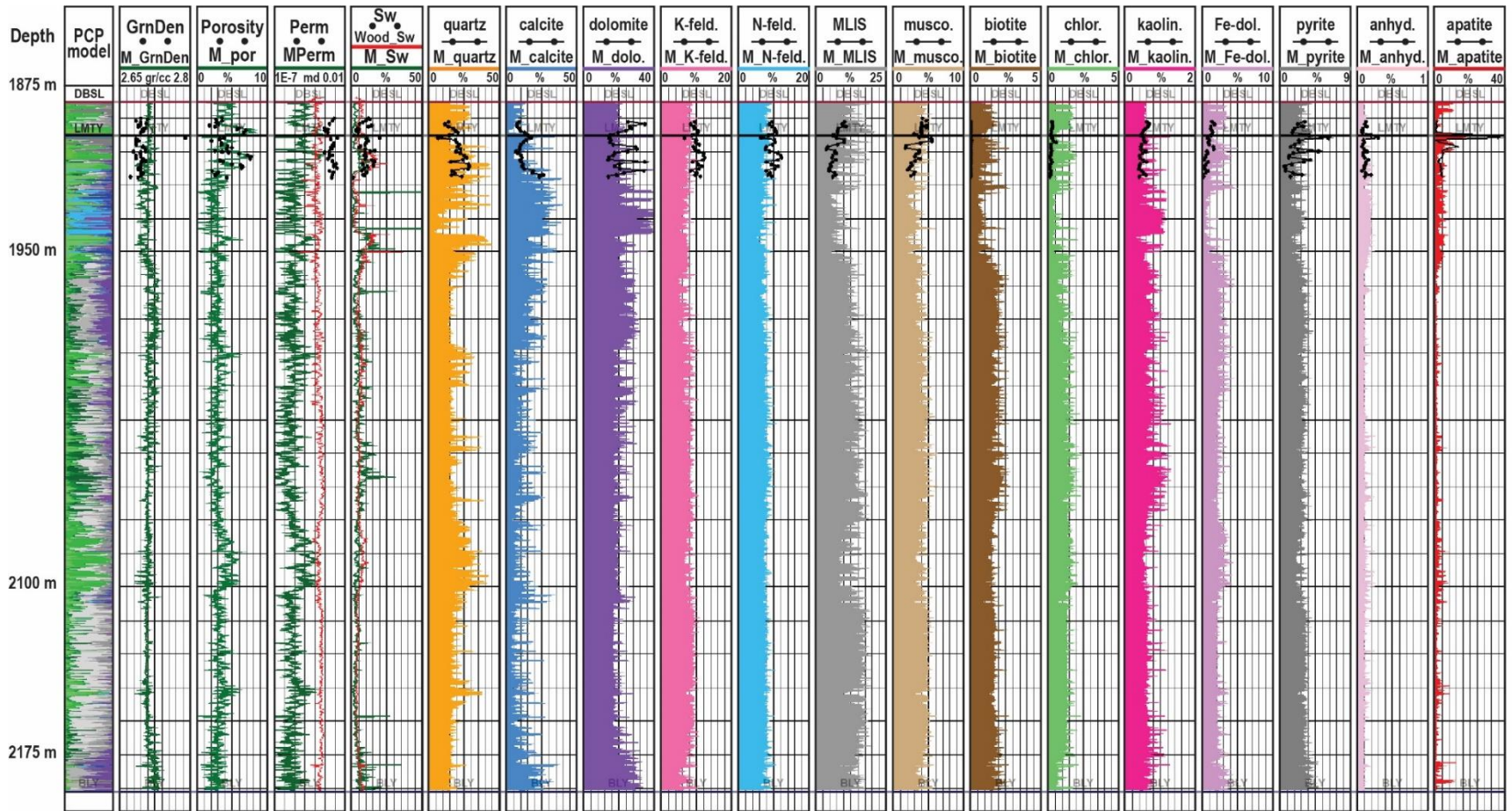
Fig. 5.8: Verification well (01-25-079-14W6) for the MFBG model. Black curves are core measurements.
Red curve in tracks 4 and 5 are permeability and Sw calculated from the equations proposed by Wood (2013). Scarcity of core data makes it difficult to evaluate how well computed mineral curves fit the data. However, Sw curve shows very good fit to the Sw curve calculated from Wood (2013). DBSL is the top of the Basal Doig (Upper Montney Member), LMTY is the top of the Lower Montney Member, and BLY is Top of the Belloy Formation.

242

5.6. Discussion

5.6.5 Sampling and upscaling

In most cases, information on mineralogy, TOC content, and grain density are obtained from analyses of core samples (plugs) or cuttings samples. In the case of cuttings, sample composition is representative of the sampled interval, but sample depth is not accurately known. In the case of plug sampling, the depth from which the sample was taken is accurately known, but sample composition is only representative of that point, potentially problematic in formations of variable composition. This can lead to skewed results, particularly where nodules (phosphate) or patchy cement (carbonate) are present.

One difficulty in petrophysical studies is upscaling core data to the well-log scale. Different well-logs have different vertical resolution. Standard logging tools have vertical resolution of 0.5 to 1.5 m (1.5 to 5 ft). In Canada, cuttings are usually collected at 5 to 10 m intervals. Core samples for routine core analysis are commonly taken at intervals of 0.25 - 1 m, but fewer samples are collected for more expensive analyses. Sampling resolution is therefore another obstacle in upscaling the data obtained from the samples and comparing it to downhole well-logs signal.

The pseudocutting method implemented for sampling both cores used in this study overcomes these drawbacks. Samples are representative of intervals rather than points (similar to cuttings samples) but the accurate sampling depth is known (as in plugs samples), making the comparison of pseudo cutting analysis results to down-hole well-log signals more robust.

5.6.6 CEC

Cation exchange capacity is controlled by clay abundance, type and distribution in the rock. QEMSCAN mineralogical results indicate that the Montney Formation contains over 25% clay minerals, mainly mixed layer illite/smectite (MLIS) clays. Vaisblat (chapter 2 this study) reported that MLIS have a composition of 95% illite and 5% smectite (low expandability).

Bulk rock cation exchange capacity data for the Montney Formation is scarce, and none are reported for clay separates. Owen (2017) reported CEC values of 9.3 to 20.4 for 15 miliequivalent/100 gr Montney bulk rock samples. The exact location in the formation from which the samples were taken is not reported. In our model, calculated bulk rock CEC values range between 1 and 7 miliequivalent/100 gr, lower than the measured values (Owen, 2017). One possibility is that the values used for calculating CEC (Table 5.1) are inappropriate for the Montney siltstone. Another possibility, however, is that a large fraction of the clays in the Pouce Coupe area of the Montney Formation are isolated from pore water and therefore have negligible effect on formation water conductivity. Several studies report the presence of bitumen plugging pores in the formation (Wood et al., 2015; 2018; chapter 2 this study). Migrabitumen is commonly found in association with clay minerals, in many instances completely engulfing the clays and isolating them from formation water.

5.6.7 Permeability

Because permeability is used in calculating Sw (equation 7), the computed permeability and core permeability measurements are presented in Fig. 5.7. Computed permeability is two to three orders of magnitude lower than the measured permeability. This discrepancy arises because the MFBG module computes matrix permeability, whereas core data was obtained from permeability measurements on core plugs. Akai and Wood (2014) and Vaisblat (chapter 4, this thesis) showed that plug permeability measurements of Montney plug samples yield values up to three orders of magnitude higher than matrix permeability (0.1-100 md for plugs and 0.00001-0.001 md for matrix permeability). These differences were attributed to the presence of microcracks in plug samples. Vaisblat (chapter 4, this thesis) reported matrix permeability values for Montney wells that are within a similar range to the computed matrix permeability (0.1 - 0.00001 md). We thus consider modeled matrix permeability for well 06-03-079-13W6 reasonable.

5.6.8 Comparison to other methods

Wood (2013) derived a relationship between total water saturation, bound water saturation, porosity and deep resistivity for the Montney Formation (equation 8 and 9), and a relationship between porosity and absolute permeability (equation 10).

(8) $BVW = 6.7627 * (R_t)^{-0.507}$

(9) $S_w = 100 * \left(\frac{BVW}{\emptyset}\right)$

(9) $K_{abs} = 0.000027 * (\emptyset)^{2.71913}$

Where BVW is bound water saturation in percent, R_t is deep resistivity from well log in ($\Omega*$m) units, Φ is porosity from the neutron well log in percent, and K_{abs} is absolute permeability in md. Equations 8 and 9 were developed from water saturation data from full diameter core analysis and are inconsistent with water saturation data obtained from plugs or cutting samples. Water saturation and absolute permeability curves calculated from equation 8 -10 (using neutron porosity log) for the calibration and verification wells are presented in Fig. 5.7 and 5.8.

The model developed by Wood (2013) fits measured total water saturation in both wells. Permeability calculated from equation 9 is consistent with the core data for the calibration well, but underestimates core permeability for the verification well. This overestimation may be a result of the different methods used for permeability measurements in the two wells (Table 5.2), but it is more probable that permeability values of the verification wells are high due to the presence of fractures in the plugs (Akai and Wood, 2014; Vaisblat, chapter 4, this thesis).

Water saturation values computed from the MFBG model are very similar to the those computed from the model of Wood (2013). Permeability values computed by the MFBG model are several orders of magnitude lower than those calculated by equation 9. However, the model of Wood (2013) was calibrated against plug permeability measurements whereas the

MFBG model computes matrix permeability; thus, this discrepancy does not invalidate the MFBG model.

The equations developed by Wood (2013) were empirically derived from a Montney Formation dataset in a constrained area that includes the Pouce Coupe field, and their applicability to predict permeability and water saturation outside of the study area or in different formations has not been demonstrated. The MFBG model did equally well at predicting water saturation as the Wood (2013) equations and was able to compute reasonable values for matrix permeability. In addition, the model provides a complete set of compositional curves (mineralogy and TOC) and other petrophysical properties (total porosity and grain density) that can be successfully transferred to other wells in the cluster run. As the MFBG method is mineralogy-dependent, it is applicable to any reservoir worldwide, providing there is sufficient rock data for calibration. New wells can be added to the cluster run and their petrophysical properties could be plotted without the need to obtain further core data.

5.7 Conclusion

We demonstrate a method for calculation of water saturation in an unconventional reservoir that applies probabilistic cluster analysis of well logs to generate a framework for an upscaled realization of compositionally complex reservoirs. Within the probabilistic framework, electroclass are determined and are associated with different lithologies, each with a unique composition and a unique set of petrophysical properties. Pseudocutting sampling method produce log-scale compositional data and enable better calibration of the model.

Other methods that use proxies for clay content (gamma ray log) to evaluate the influence of clay mineralogy on water saturation. The MFBG (Matrix-Fluid mass Balance in GAMLS) method presented in this paper uses the dual water saturation and can account for specific clay mineralogies to accurately calculate water saturation. Because a probabilistic model is

used, a variable grain density and CEC depth curves are used rather than the constant grain density commonly used in petrophysical analyses. that allow for accurate calibration. The probabilistic clustering also allows for flexible calibration of the model to produce accurate profiles of water saturation

5.8 Reference

Akai, T. and Wood, J.M., 2014. Petrophysical analysis of a tight siltstone reservoir: Montney formation, Western Canada, The 20th Formation Evaluation Symposium of Japan, 1-2 October, Chiba, Japan.

Archie, G. E., 1942. The electrical resistivity log as an aid in determining some reservoir characteristics, Transactions, AIME, 146, 54-67.

Asquith, G., and Krygowski, D., 2004. Basic well log analysis (Second Edition), AAPG Methods in Exploration Series, 16, AAPG, Tulsa.

Barber, L.M., 2002, Sedimentology, Diagenesis and Reservoir Characterization of the Montney Formation at Sturgeon Lake South 'F' Pool West-Central Alberta, M.Sc. thesis, University of Calgary, Department of Geology and Geophysics, Calgary, Alberta.

Carman, P. C., 1956. Flow of gases through porous media, New York, Academic Press, 396 p.

Clavier, C., Coates, G., and Dumanoir, J., 1984. The theoretical and experimental bases for the dual water model for the interpretation of shaly sand, Society of Petroleum Engineers 52nd Annual Fall Meeting, October 9-12, Denver, Colorado.

Clavier, C., Hoyle, W., and Meunier, D., 1971. Quantitative Interpretation of Thermal Neutron Decay Time Logs: Part I. Fundamentals and Techniques. Society of Petroleum Engineers. doi:10.2118/2658-A-PA.

David, S.O., Rodolfo, S.B., Jonathan, S.O., Pasquel, O., and Arteaga, D., 2015. A universal equation to calculate shale volume for shaly-sands and carbonate reservoirs. Society of petroleum engineers. doi:10.2118/177224-MS.

Davies, G.R., Moslow, T.F., and Sherwin, M.D., 1997. The Lower Triassic Montney Formation, west-central Alberta. Bulletin of Canadian Petroleum Geology, 45(4), 474-505.

Eslinger, E., Pachon, Z., Cantisano, M.T., Marfisi, N., and Slatt, R., 2014. Probabilistic Facies Assignments in the La Luna Formation, Middle Magdalena Basin, Colombia, from Standard Well Logs Using Whole Core CT Scan Data as Initialization Input. Unconventional Resources Technology Conference. 25-27 August, Denver, Colorado. doi:10.15530/URTEC-2014-1934648.

Eslinger, E., and Boyle, F., 2013. Building a Multi-Well Model for Partitioning Spectroscopy Log Elements into Minerals Using Core Mineralogy for Calibration, Society of Petrophysicists and Well-Log Analysts, 54[th]Annual Logging Symposium, June 22-26, New Orleans, Louisiana.

Eslinger, E., and Everett, R.V., 2012. Petrophysics in gas shales, in J. A. Breyer, ed., Shale reservoirs - Giant resources for the 21st century: AAPG Memoir 97, 419-451.

Eslinger, E., and Boyle, F., 2011. Mineral and Well Log Balance for Computing Porosity in Argillaceous Rocks - Application in Gas Shales, the International Unconventional Oil-Gas Conference at the China, University of Petroleum, July 4-5, Qingdao, China.

Grim, R.E., 1968. Clay mineralogy (second edition), McGraw-Hill, New York.

Henderson, C.M., Golding, M.L., and Orchard, M.J., 2018. Conodont sequence biostratigraphy of the Lower Triassic Montney Formation, Bulletin of Canadian Petroleum Geology, 66(1), 7-22.

Herrick, D.C., and Kennedy, W.D., 2009. On the Quagmire of Shaly Sand Saturation Equations. Society of Petrophysicists and Well-Log Analysts. 50th Annual Logging Symposium, 21-24 June, The Woodlands, Texas.

Herron, M. M., Johnson, D. L., and Schwartz, L. M., 1998. A robust permeability estimator for siliciclastics. Society of Petroleum Engineers Annual Technical Conference and Exhibition, September 27-30, New Orleans, Louisiana, 11 p.

Herron, M. M., and Matteson, A., 1993. Elemental composition and nuclear parameters of some common sedimentary minerals, Nuclear Geophysics, 7 (3), 383-406.

Hurst, A., 1987. Mineralogical analysis and the evaluation of the petrophysical parameter Vshale for reservoir description, Journal of Marine and Petroleum Geology, 4, 82-91.

Larionov, V.V., 1969. Radiometry of boreholes, NEDRA, Moscow.

National energy board, 2013. Canada's energy future 2013 energy supply and demand projections to 2035. https://www.cer-rec.gc.ca/nrg/ntgrtd/ftr/2013/2013nrgftr-eng.pdf. Last accessed March 31, 2020.

Owen, J.N., 2017. An investigation into the controls and variability of the flowback water inorganic geochemistry of the Montney Formation, Northeastern British Columbia and Northwestern Alberta, Canada, M.Sc. Thesis, The University of British Columbia, Department of Geological Sciences.

Sanders, S., Etienne, C., Gegolic, A., Kelly, D., and Zonneveld, J.-P., 2018. The Middle Montney Altares Member : lithology , depositional setting and significance for horizontal drilling and completion in the Altares field , British Columbia. Bulletin of Canadian Petroleum Geology, 66(1), 318-337.

Schlumberger, Log Interpretation Charts, 2009, figure Gen-8 p. 10. URL: https://connect.slb.com/~/media/Files/resources/books/log_charts/toc1.pdf (last access March 26, 2020).

Serra, O., 1984, Fundamentals of well-log interpretation: New York, Elsevier, 423 p.

Spooner, P., 2014. Lifting the Fog of Confusion Surrounding Clay and Shale in Petrophysics. Society of Petrophysicists and Well-Log Analysts. 55th Annual Logging Symposium, 18-22 May, Abu Dhabi, United Arab Emirates.

Stieber, S. J., 1970. Pulsed Neutron Capture Log Evaluation - Louisiana Gulf Coast, Fall Meeting of the Society of Petroleum Engineers of AIME, 4-7 October, Houston, Texas. doi:10.2118/2961-MS.

Utting, J., Zonneveld, J.-P., MacNaughton, R.B., and Fallas, K.M., 2005. Palynostratigraphy, lithostratigraphy and thermal maturity of the Lower Triassic Toad and Grayling, and Montney formations of western Canada, and comparisons with coeval rocks of the Sverdrup Basin, Nunavut. Bulletin of Canadian Petroleum Geology, 53(1), 5-24. https://doi.org/10.2113/53.1.5.

Vaisblat, N., Harris, N.B., DeBhur, C., Euzen, T., Gasparrini, M., Crombez, V., Rohais, S., Krause, F. and Ayranci, K. 2017. Diagenetic model for the deep Montney Formation, Northeastern British Columbia. Geoscience BC Report 2017-1, p. 37-48. http://www.geosciencebc.com/i/pdf/SummaryofActivities2016/SoA2016_Vaisblat.pdf.

Van Olphen, H., and Fripiat, J.J., 1979. Data handbook for clay materials and other non-metallic minerals, Pergamon Press, Oxford.

Waxman, M.H., and Thomas, E.C., 1974. Electrical conductivities in oil-bearing shaly sands, I. The relation between hydrocarbon saturation and resistivity index; II. The temperature coefficient of electrical conductivity: Society of Petroleum Engineers Journal, 14, 213-225.

Waxman, M.H., and Smits, L.J.M., 1968. Electrical conductivities in oil-bearing shaly sands, Society of Petroleum Engineers Journal, 8 (2) 107-122.

Wood, J.M., 2015. Crushed-rock versus full-diameter core samples for water-saturation determination in a tight-gas siltstone play, SPE Reservoir Evaluation & Engineering 18(3): 407-416. SPE-174548-PA. http://dx.doi.org/10.2118/174548-PA.

Wood, J.M., 2013. Water Distribution in the Montney Tight Gas Play of the Western Canadian Sedimentary Basin: Significance for Resource Evaluation, in: SPE Canadian Unconventional Resources Conference. Society of Petroleum Engineers, Calgary, AB, Canada, pp. 290–302. https://doi.org/10.2118/161824-MS.

Wood, J.M., Sanei, H., Haeri-Ardakani, O., Curtis, M.E., and Akai, T., 2018. Organic petrography and scanning electron microscopy imaging of a thermal maturity series from

the Montney tight-gas and hydrocarbon liquids fairway. Bulletin of Canadian Petroleum Geology, 66(2), 499-515. https://doi.org/10.1038/ncomms13614.

Chapter 6 - Summary and Conclusions

The work presented in this thesis investigates the controls over reservoir quality of the Lower Triassic Montney Formation silt-rich mudstone (siltstone) through a multidisciplinary analysis that includes sedimentology, mineralogy, petrophysics, geomechanics, and well-logs analysis. This study was set to identify:

(1) What diagenetic processes were/are active in the Montney Formation and how did they affect the mineralogical composition of the siltstone?

(2) What is the relationship between rock fabric, rock composition, and diagenesis and how do they affect reservoir quality (porosity, permeability and the geomechanical properties of the rock) in the siltstones?

(3) How are silt-rich mudstone (siltstone) similar and how so they differ from clay-rich mudstone (shale) reservoirs?

(4) Can water saturation be predicted for the Montney siltstone using matrix-fluid mass balance approach (GAMLS MFBG), if rock composition and fluids composition is known?

6.1 Diagenesis, rock composition and rock fabric:

Chapter 2 investigates the diagenetic history of the Montney siltstone. Both shallow and deep burial diagenetic processes are identified and a paragenetic sequence established. Little compositional variation in the detrital sediment, together with prolonged shallow burial and extensive cementation at shallow depth (300-1100 m) led to compositional homogeneity of different lithofacies in the siltstone. Shallow diagenesis cements accounts for more than 30% of present-day rock volume. Deep burial diagenesis plays only a minor role in the compositional evolution of the rock.

6.2 Controls on reservoir quality

Chapters 3 and 4 examine relationships between rock composition and fabric and reservoir quality parameters in the Montney siltstone (porosity, permeability and the mechanical

properties of the rock). Quartz content exerts a positive control on both porosity and permeability, related to strengthening of the rock framework and reduced porosity loss due to compaction. Elevated clay content is also associated with higher porosity and permeability, possibly in part because of an association with detrital quartz, but also because clays may shelter interconnected primary porosity that promotes permeability. Organic matter content is negatively correlated to porosity and permeability despite the presence of organic matter porosity, because relict oil (now pyrobitumen) plugs primary pore space and because other pore types contribute more to the total pore volume of the rock.

Clay content is the most significant parameter affecting the mechanical properties of the Montney Formation, an observation consistent with the behavior of several other fine-grained reservoirs. Increased clay content leads to an increase in dynamic Poisson's Ratio and a decrease in dynamic Young's Modulus values in the Montney, similar to other formations. In addition, water saturation and the number of observable bedding planes are positively correlated with a decrease in rock brittleness in the Montney Formation.

In fine-grained formations, individual depositional lithofacies are commonly associated with distinctive rock fabric, composition, grain size and sorting, and thus different reservoir quality. In the Montney Formation siltstone, no significant or systematic differences in petrophysical or geomechanical properties were identified between the different lithofacies. We attribute this in part to the homogeneous composition and grain size of detrital sediment entering the basin, and in part to the shallow burial cementation event. Rather than lithology, in-situ stress and pressure gradients are the controlling factors on the propagation of hydraulic fractures in the Montney siltstone.

6.3 Are all mudrocks the same?

Chapters 2 to 5 compare the Montney siltstone (silt-rich mudrock) to several clay-rich mudrock reservoirs to identify key similarities and differences between the two rock types.

Rock composition, porosity and permeability values, pore dimensions and the geomechanical properties of the siltstone are generally consistent with those of shale formations, in spite of the coarser grain size of the siltstone. However, the controls on reservoir quality are different for clay and silt rich mudrocks and are related to fundamental differences in the microscale rock fabric. Whereas mudrocks clay rich, matrix supported rocks, siltstone has a hard, grain and cement-supported framework. Rock fabric rather than mineralogy is the main control over rock brittleness. Other, smaller scale controls on reservoir quality include differences in compaction rates, chemical diagenesis and the nature of organic matter emplacement.

6.4 Water saturation

Chapter 5 presents a model designed to calculate water saturation in fine grained rocks. This model is based on a probabilistic cluster analysis of well logs that identifies rock type endmembers with a unique composition and a unique set of petrophysical properties. Water saturation is calculated using matrix-fluid balance. This model is proven successful at computing water saturation for a model well and a test well in the Montney siltstone.

Reference

Aagaard, P., Egeberg, P.K., Saigal, G.C., Morad, S., and Bjorlykke, K., 1990. Diagenetic albitization of detrital K-feldspars in Jurassic, Lower Cretaceous and Tertiary clastic reservoir rocks from offshore Norway; II, Formation water chemistry and kinetic considerations. Journal of Sedimentary Research, 60(4), 575-581.

Aase, N.E., Bjørkum, P.A., and Nadeau, P.H., 1996. The Effect of grain-coating microquartz on preservation of reservoir porosity. American Association of Petroleum Geologists Bulletin, 80(10), 1654-1673.

Abay, T.B., Karlsen, D.A., Pedersen, J.H., Olaussen, S. and Backer-Owe, K., 2018. Thermal maturity, hydrocarbon potential and kerogen type of some Triassic–Lower Cretaceous sediments from the SW Barents Sea and Svalbard. Petroleum Geoscience, 24(3), 349-373. doi: https://doi.org/10.1144/petgeo2017-035.

Adams, J.E. and Rhodes, M.L., 1960. Dolomitization by Seepage Refluxion. American Association of Petroleum Geologists Bulletin, 44(12), 1912-1920.

Aguilera, R., 2016. Shale gas reservoirs: Theoretical, practical and research issues. Petroleum Research, 1(1), 10-26.

Ahmadov, R., Vanorio, T., and Mavko, G., 2009. Confocal laser scanning and atomic-force microscopy in estimation of elastic properties of the organic-rich Bazhenov Formation. Leading Edge, 28(1), 18-23. https://doi.org/10.1190/1.3064141.

Akai, T, Takakuwa, Y., Sato, K, and Wood, J.M., 2014. Pressure dependent permeability of tight rocks, SPE Low Perm Symposium, Denver, Colorado, USA, May 5-6. SPE-180262-MS.

Akai, T. and Wood, J.M., 2014. Petrophysical analysis of a tight siltstone reservoir: Montney formation, Western Canada, The 20th Formation Evaluation Symposium of Japan, 1-2 October, Chiba, Japan.

Akai, T., and Wood, J.M., 2018. Application of pore throat size distribution data to petrophysical characterization of Montney tight-gas siltstones, Bulletin of Canadian Petroleum Geology, 66, 425-435.

Al Rajaibi, I.M., Hollis, C., and Macquaker, J.H., 2015. Origin and variability of a terminal Proterozoic primary silica precipitate, Athel Silicilyte, South Oman Salt Basin, Sultanate of Oman. Sedimentology, 62(3), 793-825. https://doi.org/10.1111/sed.12173.

Al-Awadi, M., Clark, W.J., Moore, W.R., Herron, M., Zhang, T., Zhao, W. Hurley, N. Kho, D. Montaron, B., and Sadooni, F., 2009. Dolomite: Perspectives on a Perplexing Mineral. Oilfield Review 21(3): 3-45.

Alqahtani, A.A., Mokhtari, M., Tutuncu, A.N., and Sonnenberg, S., 2013. Effect of mineralogy and petrophysical characteristics on acoustic and mechanical properties of organic rich

shale. In Unconventional Resources Technology Conference (pp. 399-411). Society of Exploration Geophysicists, American Association of Petroleum Geologists, Society of Petroleum Engineers. https://doi.org/10.1190/urtec2013-045.

Anovitz, L.M., and D R. Cole, 2015. Characterization and analysis of porosity and pore structures. Reviews in Mineralogy and Geochemistry, 80(1), 61-164, doi: 10.2138/rmg.2015.80.04.

Aoki, H. and Matsukura, Y., 2008. Estimating the unconfined compressive strength of intact rocks from Equotip hardness. Bulletin of Engineering Geology and the Environment, 67(1), 23-29. https://doi.org/10.1007/s10064-007-0116-z.

Aoudia, K., Miskimins, J.L., Harris, N.B., and Minch, C.A., 2010. Statistical analysis of the effects of mineralogy on rock mechanical properties of the Woodford Shale and the associated impacts for hydraulic fracture treatment design. 44th US Rock Mechanics Symposium and 5th U.S.-Canada Rock Mechanics Symposium. Salt Lake City, Utah, U.S.A., 27-30 June. ARMA 10-303.

Aplin, A.C., and Macquaker, J.H., 2011. Mudstone diversity: Origin and implications for source, seal, and reservoir properties in petroleum systems. American Association of Petroleum Geologists Bulletin, 95(12), 2031-2059. https://doi.org/10.1306/03281110162.

Aplin, A.C., Fleet, A.J. and Macquaker, J.H,1999. Muds and mudstones: Physical and fluid-flow properties, Geological Society of London, Special Publications 158, 1-8.

Archie, G. E., 1942. The electrical resistivity log as an aid in determining some reservoir characteristics, Transactions, AIME, 146, 54-67.

Asquith, G., and Krygowski, D., 2004. Basic well log analysis (Second Edition), AAPG Methods in Exploration Series, 16, AAPG, Tulsa.

Barber, L.M., 2002. Sedimentology, Diagenesis and reservoir characterization of the Montney Formation at Sturgeon Lake South 'F' Pool West-Central Alberta, M.Sc. thesis, Department of geology and geophysics, University of Calgary, Calgary, Alberta, Canada.

BC oil and gas commission, 2012. Montney Formation play atlas for NEBC.

Ben Baccar, M., Fritz, B., and Made, B., 1993. Diagenetic albitization of K-feldspar and plagioclase in sandstone reservoirs: thermodynamic and kinetic modeling. Journal of Sedimentary Research, 63(6), 1100-1109. https://doi.org/10.1306/D4267CB2-2B26-11D7-8648000102C1865D.

Beranek, L.P., Mortensen, J.K., Orchard, M.J., and Ullrich, T., 2010. Provenance of North American Triassic strata from west-central and southeastern Yukon: correlations with

coeval strata in the Western Canada Sedimentary Basin and Canadian Arctic Islands. Canadian Journal of Earth Sciences 47, 53-73. https://doi.org/10.1139/E09-065.

Berner, R.A., 1984. Sedimentary pyrite formation: An update. Geochimica et Cosmochimica Acta, 48(4), 605-615. https://doi.org/10.1016/0016-7037(84)90089-9.

Blakey, R.C., 2014. Mesozoic paleogeography and tectonic history - western North America: Triassic tectonics and paleogeography, 245 Ma. http://deeptimemaps.com/north-american-key-time-slices-series. Last accessed july 20, 2019.

Bloch, S., Lander, R.H., and Bonnell, L., 2002. Anomalously high porosity and permeability in deeply buried sandstone reservoirs: Origin and predictability. American Association of Petroleum Geologists Bulletin, 86(2), 301-328.

Bohrmann, G., Abelmann, A., Gersonde, R., Hubberten, H., and Kuhn, G., 1994. Pure siliceous ooze, a diagenetic environment for early chert formation. Geology, 22(3), 207-210. https://doi.org/10.1130/0091-7613(1994)022<0207:PSOADE>2.3.CO;2.

Boles, J.R., and Franks, S.G., 1979. Clay diagenesis in Wilcox sandstones of Southwest Texas; implications of smectite diagenesis on sandstone cementation. Journal of Sedimentary Research, 49(1), 55-70.

Breyer, J.A., Denne, R., Kosanke, T., Spaw, J.M., Funk, J.E., Christianson, P., Bush, D.A. and Nelson, R., 2013. Facies, Fractures, Pressure and Production in the Eagle Ford Shale (Cretaceous) between the Maverick Basin and the San Marcos Arch, Texas, USA. Unconventional Resources Technology Conference, Denver, Colorado, U.S.A., 12-14 August https://doi.org/10.1190/urtec2013-159.

Brunauer, S., Emmett, P.H., and Teller, E., 1938. Adsorption of Gases in Multimolecular Layers. Journal of the American Chemical Society, 60 (2), 309-319.

Buatier, M.D., 1992. Smectite-Illite transition in Barbados accretionary wedge sediments: TEM and AEM evidence for dissolution/crystallization at low temperature. Clays and Clay Minerals, 40(1), 65-80. https://doi.org/10.1346/CCMN.1992.0400108.

Camp, W.K., 2019. A New Method to Predict Organic Matter Porosity in Unconventional Shale Reservoirs. William C. CSPG Gussow Geoscience Conference, Banff, Alberta, Canada, 15-17 October.

Cao, Z., Liu, G., Zhan, H. Gao, J. Zhang, J., Li, C., and Xiang, B., 2017. Geological roles of siltstones in tight oil play. Journal of Marine and Petroleum Geology, 88, 333-344.

Caracciolo, L., Arribas, J., Ingersoll, R.V., and Critelli, S., 2014. The diagenetic destruction of porosity in plutoniclastic petrofacies: The Miocene Diligencia and Eocene Maniobra formations, Orocopia Mountains, southern California, USA. Geological Scoiety of London speciasl publication, 386, 49–62. https://doi.org/10.1144/SP386.9.

Carman, P. C., 1956. Flow of gases through porous media, New York, Academic Press, 396 p.

Castagna, J.P., Batzle, M.L., and Eastwood, R.L., 1985. Relationships between compressional-wave and shear-wave velocities in clastic silicate rocks. Geophysics, 50(4), 571-581. https://doi.org/10.1190/1.1441933.

Cecil, C.B., 2004. Eolian dust and the origin of sedimentary chert. Open-File Report 2004-1098: US Geological Survey, 2004. Last accessed March 31, 2020.

Chalmers, G.R., and Bustin, M.R., 2017. A multidisciplinary approach in determining the maceral (kerogen type) and mineralogical composition of Upper Cretaceous Eagle Ford Formation: Impact on pore development and pore size distribution. International Journal of Coal Geology, 171, 93-110.

Chalmers, G.R., Bustin, R.M. and Power, I.M., 2012. Characterization of gas shale pore systems by porosimetry, pycnometry, surface area, and field emission scanning electron microscopy/transmission electron microscopy image analyses: Examples from the Barnett, Woodford, Haynesville, Marcellus, and Doig units. American Association of Petroleum Geologists bulletin, 96(6), 1099-1119.

Chalmers, G.R., and Bustin, M.R., 2012. Geological evaluation of Halfway–Doig–Montney hybrid gas shale–tight gas reservoir, northeastern British Columbia. Journal of Marine and Petroleum Geology, 38(1), 53-72.

Chatellier, J.Y., Simpson,K., Perez, R., and Tribobillard, N., 2018. Geochemically focused integrated approach to reveal reservoir characteristics linked to better Montney productivity potential. Bulletin of Canadian Petroleum Geology, 66(2), 516-551.

Chen, Q., Zhang, J., Tang, X., Wei, D., Li, Z., Liu, C., and Zhang, X., 2016. Pore Structure Characterization of the Lower Permian Marine Continental Transitional Black Shale in the Southern North China Basin, Central China. Energy and Fuel, 30(12), 1092-10105. https://doi.org/10.1021/acs.energyfuels.6b01475.

Cho, Y., Eker, E., Uzun, I., Yin, X. and Kazemi, H., 2016. Rock characterization in unconventional reservoirs: a comparative study of Bakken, Eagle Ford, and Niobrara Formations. SPE Low Perm Symposium, Denver, Colorado, USA, 5-6 May.

Chilingarian G.V., 1983. Compactional Diagenesis. In: Parker A., Sellwood B.W. (Eds.), Sediment diagenesis. NATO ASI Series (Series C: Mathematical and Physical Sciences), vol 115. Springer, Dordrecht.

Clarkson, M.O., Kasemann, S.A., Wood, R.A., Lenton, T.M., Daines, S.J., Richoz, S., Ohnemueller, F., Meixner, A., Poulton, S.W., and Tipper, E.T., 2015. Ocean acidification and the Permo-Triassic mass extinction. Science, 348(6231), 229-232. https://doi.org/10.1126/science.aaa0193.

Clarkson, C.R., Wood, J., Burgis, S., Aquino, S. and Freeman, M., 2012. Nanopore-structure analysis and permeability predictions for a tight gas siltstone reservoir by use of low-pressure adsorption and mercury-intrusion techniques. SPE Reservoir Evaluation and Engineering, 15(6), 648-661.

Clavier, C., Coates, G., and Dumanoir, J., 1984. The theoretical and experimental bases for the dual water model for the interpretation of shaly sand, Society of Petroleum Engineers 52nd Annual Fall Meeting, October 9-12, Denver, Colorado.

Clavier, C., Hoyle, W., and Meunier, D., 1971. Quantitative Interpretation of Thermal Neutron Decay Time Logs: Part I. Fundamentals and Techniques. Society of Petroleum Engineers. doi:10.2118/2658-A-PA.

Coney, P.J., Jones, D.L., and Monger, J.W.H., 1980. Cordilleran suspect terranes. Nature, 288(5789), 329-333. https://doi.org/10.1038/288329a0.

Coombes, M.A., Feal-Pérez, A., Naylor, L.A., and Wilhwlm, K. .,2013. A non-destructive tool for detecting changes in the hardness of engineering materials: Application of the Equotip durometer in the coastal zone. Engineering Geology, 167, 14-19. https://doi.org/10.1016/j.enggeo.2013.10.003.

Cooper, G., Xiang, R., Agnew, N., Ward, P., Fabian, M., and Tupper, N., 2015. A systematic approach to unconventional play analysis: the oil and gas potential of the Kockatea Shale and Carynginia Formation, north Perth Basin, Western Australia. The Australian Petroleum Production and Exploration Association Journal, 55(1), 193-214.

Corkum, A.G., Asiri, Y., El Naggar, H., and Kinakin, D., 2018. The Leeb Hardness Test for Rock: An Updated Methodology and UCS Correlation. Rock Mechanics and Rock Engineering. 51 (3), 665-675. https://doi.org/10.1007/s00603-017-1372-2.

Crombez, V., 2016 P´etrofaci`es, s´edimentologie et architecture stratigraphique des roches riches en mati`ere organique: ´etude multi-approches des formations Montney et Doig (Trias inferieur et moyen, Alberta - Colombie Britannique, Canada). PhD. Thesis, Sciences de la Terre. Universit´e Pierre et Marie Curie, Paris, France.

Crombez, V., Baudin, F., Rohais, S., Riquier, L., Euzen, T., Pauthier, S., Ducros, M., Caron, B. and Vaisblat, N., 2017. Basin scale distribution of organic matter in marine fine-grained sedimentary rocks: Insight from sequence stratigraphy and multi-proxies analysis in the Montney and Doig Formations. Marine and Petroleum Geology, 83: 382-401.

Crombez, V., Rohais, S., Baudin, F., and Euzen, T., 2016. Facies, well-log patterns, geometries and sequence stratigraphy of a wave-dominated margin: insight from the Montney Formation (Alberta, British Columbia, Canada). Bulletin of Canadian Petroleum Geology, 64(4), 516-537.

Cui. X., and Nassichuk, B., 2018. Permeability of the Montney Formation in the Western Canada Sedimentary Basin: insights from different laboratory measurements. Bulletin of Canadian Petroleum Geology, 66, 394-424.

Cundall, P.A., and Hart, R.D., 1992. Numerical modelling of discontinua. Engineering computations, 9 (2), 101-113.

Davey, H., 2012. Geomechanical characterization of the Montney shale, northwest Alberta and northeast British Columbia, Canada. M.Sc. Thesis, Department of Geology and Geological Engineering, Colorado School of Mines, Golden, Colorado, USA.

David, S.O., Rodolfo, S.B., Jonathan, S.O., Pasquel, O., and Arteaga, D., 2015. A universal equation to calculate shale volume for shaly-sands and carbonate reservoirs. Society of petroleum engineers. doi:10.2118/177224-MS.

Davies, G.R., 1997. Aeolian sedimentation and bypass, Triassic of western Canada, Bulletin of Canadian Petroleum Geology 45(4), 624–642.

Davies, G.R., Watson, N., Moslow, T.F., and Maceachern, J.A., 2018. Regional subdivisions, sequences, correlations and facies relationships of the Lower Triassic Montney Formation, west-central Alberta to northeastern British Columbia, Canada - With emphasis on role of paleostructure. Bulletin of Canadian petroleum geology, 66(1), 23-92.

Davies, G.R., and Hume, D., 2016. Lowstand/Slope-onlap wedges in the Montney: Stratigraphic and sequence framework, reservoir significance. GeoConvention 2016, Abstract, 4.

Davies, G.R., Moslow, T.F., and Sherwin, M.D., 1997. The Lower Triassic Montney Formation, west-central Alberta. Bulletin of Canadian Petroleum Geology, 45(4), 474-505.

De Bore, J.H., 1958. The shapes of capillaries, in the structure and properties of porous materials, Butterworth, London, 68-94.

Derder, O.M., 2012. Characterizing Reservoir Properties for the Lower Triassic Montney Formation (Units C and D) Based on Petrophysical Methods. M.Sc. Thesis, Department of Geosciense, University of Calgary, Calgary, Alberta, Canada.

Dewhurst, D.N., A.F. Siggins, J. Sarout, M.D. Raven, and H.M. Nordgård-Bolås, 2011, Geomechanical and ultrasonic characterization of a Norwegian Sea shale: Geophysics, 76 (3), WA101-WA111. https://doi.org/10.1190/1.3569599.

Dewhurst, D.N., Yang, Y.L., and Aplin, A.C., 1999. Permeability and fluid flow in natural mudstones. In: Aplin, A.C., et al. (Eds.), Muds and Mudstones: Physical and Fluid Flow Properties, 158. Geological Society Special Publication, p. 23-43.

Dewhurst, D.N., Aplin, A.C., Sarda, J.-P., and Yang, Y., 1998. Compaction-driven evolution of porosity and permeability in natural mudstones: An experimental study. Journal of Geophysical Research: Solid Earth 103(B1), 651-661.

Dixon, J., 2000. Regional lithostratigraphic units in the Triassic Montney formation of Western Canada. Bulletin of Canadian Petroleum Geology, 48(1), 80–83.

Do, D.D., and Do, D.H., 2003. Pore Characterization of Carbonaceous Materials by DFT and GCMC Simulations: A Review. Adsorption Science and Technology 21(5) 389-423. https://doi.org/10.1260/026361703769645753.

Dong, T., and Harris, N.B., 2020. The effect of thermal maturity on porosity development in the Upper Devonian–Lower Mississippian Woodford Shale, Permian Basin, US: Insights into the role of silica nanospheres and microcrystalline quartz on porosity preservation. International Journal of Coal Geology, 217, 103346.

Dong, T., Harris, N.B., Knapp, L.J., McMillan, J.M., and Bish, D.L., 2018. The effect of thermal maturity on geomechanical properties in shale reservoirs: An example from the Upper Devonian Duvernay Formation, Western Canada Sedimentary Basin. Marine and Petroleum Geology, 97, 137-153.

Dong, T., Harris, N.B., Ayranci, K., Twemlow, C.E., and Nassichuk, B., 2017. The impact of rock composition on geomechanical properties of a shale formation: Middle and Upper Devonian Horn River Group shale, Northeast British Columbia, Canada. American Association of Petroleum Geologists Bulletin, 101(2), 177-204. https://doi.org/10.1306/07251615199.

Dong, T., Harris, N.B., Ayranci, K., Twemlow, C.E., and Nassichuk, B.R., 2015. Porosity characteristics of the Devonian Horn River shale, Canada: Insights from lithofacies classification and shale composition. International Journal of Coal Geology, 141, 74-90.

Ducros, M., Sassi, W., Vially, R., Euzen, T., and Crombez, V., 2017. 2-D Basin modeling of the Western Canada Sedimentary Basin across the Montney-Doig System: Implications for hydrocarbon migration pathways and unconventional resources potential, in: AbuAli, M.A., Moretti, I., and Bolås, H.M.N. (Eds.), Petroleum Systems Analysis-Case Studies: American Association of Petroleum Geologists Bulletin Memoir, 114. pp. 117-134. https://doi.org/10.1306/13602027M1143703.

Ducros, M., Euzen, T., Vially, R., and Sassi, W., 2014. 2-D basin modeling of the WCSB across the Montney-Doig system : implications for hydrocarbon migration pathways and unconventional resources potential, in: Geoconvention, Calgary, AB, Canada, 13-17 May.

Edwards, D.E., Barclay, J.E., Gibson, D.W., Kvill, G.E., and Halton, E., 1994. Triassic strata of the Western Canada Sedimentary Basin, in: Mossop, G.D., and Shetsen, I. (Eds.),

Geological Atlas of the Western Canada Sedimentary Basin. Canadian Society of Petroleum Geologists and Alberta Research Council, Calgary, pp. 259–275.

Ehrenberg, S.N., 1989. Assessing the relative importance of compaction processes and cementation to reduction of porosity in sandstones: Reply. American Association of Petroleum Geologists Bulletin, 73(10), 1274-1276. https://doi.org/10.1306/44b4aa23-170a-11d7-8645000102c1865d.

Ejezie, N., 2007, Triassic oil families and possible source rocks, Peace River Embayment area, Alberta, Canada, Ms.C. Thesis, Department of Geology and Geophysics, University of Calgary, Calgary, Alberta, Canada.

Eliyahu, M., Emmanuel, S., Day-Stirrat, R.J., and Macaulay, C.I., 2015. Mechanical properties of organic matter in shales mapped at the nanometer scale. Journal of Marine and Petroleum Geology, 59, 294-304. https://doi.org/10.1016/j.marpetgeo.2014.09.007.

Elphinstone, R. and Gorter, J.D., 1991. As the worm turns: implications of bioturbation on source rocks of the Horn Valley Siltstone. Bureau of Mineral Resources, Geology and Geophysics, Bulletin 236(3), 17-332.

Emmanuel, S., Eliyahu, M., Day-Stirrat, R.J., Hofmann, R., and Macaulay, C.I., 2016. Impact of thermal maturation on nano-scale elastic properties of organic matter in shales. Journal of Marine and Petroleum Geology, 70, 175-184. https://doi.org/10.1016/j.marpetgeo.2015.12.001.

Eslinger, E., Pachon, Z., Cantisano, M.T., Marfisi, N., and Slatt, R., 2014. Probabilistic Facies Assignments in the La Luna Formation, Middle Magdalena Basin, Colombia, from Standard Well Logs Using Whole Core CT Scan Data as Initialization Input. Unconventional Resources Technology Conference. 25-27 August, Denver, Colorado. doi:10.15530/URTEC-2014-1934648.

Eslinger, E., and Boyle, F., 2013. Building a Multi-Well Model for Partitioning Spectroscopy Log Elements into Minerals Using Core Mineralogy for Calibration, Society of Petrophysicists and Well-Log Analysts, 54th Annual Logging Symposium, June 22-26, New Orleans, Louisiana.

Eslinger, E., and Everett, R.V., 2012. Petrophysics in gas shales, in J. A. Breyer, ed., Shale reservoirs - Giant resources for the 21st century: AAPG Memoir 97, 419-451.

Eslinger, E., and Boyle, F., 2011. Mineral and Well Log Balance for Computing Porosity in Argillaceous Rocks - Application in Gas Shales, the International Unconventional Oil-Gas Conference at the China, University of Petroleum, July 4-5, Qingdao, China.

Euzen, T., Moslow, T.F., Crombez, V., and Rohais, S., 2018. Regional stratigraphic architecture of the spathian deposits in western Canada - Implications for the Montney

resource play. Bulletin of Canadian Petroleum Geology. 66(1), 175-192.

Feiyu, W., Jing, G., Weiping, F., and Bao., L., 2013. Evolution of overmature marine shale porosity and implication to the free gas volume. Petroleum Exploration and Development 40(6), 819-824. https://doi.org/10.1016/S1876-3804(13)60111-1.

Feng, W., Chen, Z., and Jiang, C., 2016. Oil and source correlations of Triassic Montney Formation in WCSB: Implication to shale gas resource potential in: GeoConvention. CSPG CSEG CWLS, Calgary, AB, Canada, p. 1.

Ferri, F., and Zonneveld, J.-P., 2008. Were Triassic rocks of the Western Canada Sedimentary Basin deposited in a foreland. Canadian Society of Petroleum Geologists Reservoir, 35(10), 12-14.

Fisher, Q.J., Knipe, R.J., and Worden, R.H., 2000. Microstructures of deformed and non-deformed sandstones from the North Sea: implications for the origins of quartz cement in sandstones. Special Publication-International Association of Sedimentologists, 29, 129-146.

Fishman, N.S., Egenhoff, S.O., Boehlke, A.R., and Lowers, H.A., 2015. Petrology and diagenetic history of the upper shale member of the Late Devonian - early Mississippian Bakken Formation, Williston Basin, North Dakota. Geological Society of America Special Papers, 515, SPE515-07.

Furlong, C.M., Gingras, M.K., Moslow, T.F., and Zonneveld, J.-P., 2018. The Sunset Prairie Formation: designation of a new Middle Triassic formation between the Lower Triassic Montney Formation and Middle Triassic Doig Formation in the Western Canada Sedimentary Basin, northeast British Columbia. Bulletin of Canadian Petroleum Geology, 66(1), 193-214.

Flemming, B.W., 2000. A revised textural classification of gravel-free muddy sediments on the basis of ternary diagrams. Continental shelf research, 20(10-11), 1125-1137.

Folk, R.L., and Ward, W.C., 1957. Brazos River bar [Texas]; a study in the significance of grain size parameters. Journal of Sedimentary Research, 27(1), 3-26.

Furlong, C.M., Gingras, M.K., Moslow, T.F., and Zonneveld, J.-P., 2018. The Sunset Prairie Formation: designation of a new Middle Triassic formation between the Lower Triassic Montney Formation and Middle Triassic Doig Formation in the Western Canada Sedimentary Basin, northeast British Columbia. Bulletin of Canadian Petroleum Geology, 66(1), 193-214.

Germay, C., Lhomme, T., McPhee, C., and Daniels, G., 2018. An objective review of non-destructive methods for the direct testing of strength on rock cores. 52nd US Rock Mechanics / Geomechanics Symposium, Seattle, Washington, U.S.A. 24-27 June.

Ghanizadeh, A., Rashidi, B. Clarkson, C.R., Sidhu, N., Hobbs, J.J., Yang, Z., and Song, C., 2018. Characterization of reservoir quality in tight rock using drill cuttings: Examples from the Montney Formation, Alberta, Canada. SDPE Canada Unconventional Resources Conference, Calgary, Alberta, Canada, March 13-14. SPE-189807-MS.

Ghanizadeh, A., Clarkson, C.R., Aquino, S., Ardakani, O.H., and Sanei, H., 2015. Petrophysical and geomechanical characteristics of Canadian tight oil and liquid-rich gas reservoirs : I. Pore network and permeability characterization. Fuel, 153, 664-681. https://doi.org/10.1016/j.fuel.2015.03.020.

Gibson, D.W., and Edwards, D.E., 1990. An overview of Triassic stratigraphy and depositional environments in the Rocky Mountain Foothills and Western Interior Plains, Peace River Arch area, northeastern British Columbia. Bulletin of Canadian Petroleum Geology, 38(1), 146-158.

Giles, M.R., Indrelid, S.L., Beynon, G.V., Amthor, J., Worden, R.H., and Morad, S., 2000. The origin of large-scale quartz cementation: evidence from large data sets and coupled heat-fluid mass transport modelling. Special Publication-International Association of Sedimentologists, 29, 21-38.

Golding, M.L., Mortensen, J.K., Ferri, F., Zonneveld, J.-P., and Orchard, M.J., 2016. Determining the provenance of Triassic sedimentary rocks in northeastern British Columbia and western Alberta using detrital zircon geochronology, with implications for regional tectonics. Canadian Journal of Earth Sciences, 53(2), 140-155. https://doi.org/10.1139/cjes-2015-0082.

Golding, M.L., Orchard, M.J., Zonneveld, J.-P., and Wilson, N.S.F., 2015. Determining the age and depositional model of the Doig Phosphate Zone in northeastern British Columbia using conodont biostratigraphy, Bulletin of Canadian Petroleum Geology, 63(2), 143-170.

Golonka, J., and Ford, D., 2000. Pangean (Late Carboniferous–Middle Jurassic) paleoenvironment and lithofacies. Palaeogeography, Palaeoclimatology, Palaeoecology, 161(1-2), 1-34. https://doi.org/10.1016/S0031-0182(00)00115-2.

Golonka, J., Ross, M.I., and Scotese, C.R., 1994. Phanerozoic paleogeographic and paleoclimatic modeling maps, in: Embry, A.F., Beauchamp, B., and Glass, D.J. (Eds.), Pangea, Global Environments and Resources. Canadian Society of Petroleum Geologist, Calgary, 1-47.

González-Acebrón, L., Arribas, J., and Mas, R., 2010. Role of sandstone provenance in the diagenetic albitization of feldspars: A case study of the Jurassic Tera Group sandstones (Cameros Basin, NE Spain). Sedimentary Geology, 229(1-2), 53-63.

Grim, R.E., 1968. Clay mineralogy (second edition), McGraw-Hill, New York.

Gupta, I., Sondergeld, C., Rai, C., and Hofmann, R., 2018. Water Weakening: Case study from Marcellus, Woodford, Eagle Ford and Wolfcamp. In 52nd US Rock Mechanics/Geomechanics Symposium. American Rock Mechanics Association.

Han, L., 2018. Moisture effects on dynamic elastic properties of shale from deep formations. M.Sc. Thesis, The Newbourne School of Petroleum and Geological Engineering, University of Oklahoma, Norman, Oklahoma, U.S.A.

Hancock, N.J., and Taylor, A.M., 1978. Clay mineral diagenesis and oil generation in the Middle Jurassic Brent Sand Formation, Journal of the Geological Society of London, 135, 69-72.

Harris, N.B., 1989. Diagenetic quartzarenite and destruction of secondary porosity: An example from the Middle Jurassic Brent sandstone of northwest Europe. Geology 17(4), 361. https://doi.org/10.1130/0091-7613(1989)017<0361:DQADOS>2.3.CO;2.

Harris, N.B., Moghadam, A. and Dong, T., 2019. The effects of organic carbon content and thermal maturity on acoustic parameters in a black shale: Woodford Shale, Permian Basin, West Texas. Geophysics 84(6), D231-D248.

Harris, N.B., Minch, C.A., Selby, D., and Korn, D., 2013. Minor and trace element and Re-Os chemistry of the Upper Devonian Woodford Shale, Permian Basin, west Texas: Insights into metal abundance and basin processes. Chemical Geology, 356, 76-930.

Harris, N.B., Miskimins, J.L., and Mnich, C.A., 2011. Mechanical anisotropy in the Woodford Shale, Permian Basin: Origin, magnitude, and scale. Leading Edge, 30(3), 284-291. https://doi.org/10.1190/1.3567259.

Hartmann, B.H., Juhász-Bodnár, K., Ramseyer, K., and Matter, A., 2000. Polyphased quartz cementation and its sources: a case study from the Upper Palaeozoic Haushi Group sandstones, Sultanate of Oman. Special Publication-International Association of Sedimentologists,29, 253-270.

Hattori, I., Umeda, M., and Yamamoto, H., 2003. From chalcedonic chert to quartz chert; diagenesis of chert hosted in a Miocene volcanic-sedimentary succession, central Japan. Journal of Sedimentary Research, 66(1), 163-174.

Heald, M.T., and Larese, R.E., 1974. Influence of coatings on quartz cementation. Journal of Sedimentary Research. 44(4), 1269-1274.

Hedberg, H.D., 1936. Gravitational compaction of clays and shales. American Journal of Sciense, 31, 241-287. https://doi.org/10.2475/ajs.s5-31.184.241.

Hedberg, H.D., 1926. The Effect of gravitational compaction on the structure of sedimentary rocks. American Association of Petroleum Geologists Bulletin, 10(11), 1035-1072.

Henderson, C.M., Golding, M.L., and Orchard, M.J., 2018. Conodont sequence biostratigraphy of the Lower Triassic Montney Formation. Bulletin of Canadian Petroleum Geology, 66(1),

7-22.

Hernandez-Uribe, L.A., Aman, M., and Espinoza, D.N., 2017. Assessment of Mudrock Brittleness with Micro-scratch Testing. Rock Mechanics and Rock Engineering, 50(11), 2849-2860.

Herrick, D.C., and Kennedy, W.D., (2009, January 1). On the Quagmire of Shaly Sand Saturation Equations. Society of Petrophysicists and Well-Log Analysts. 50th Annual Logging Symposium, 21-24 June, The woodlands, Texas.

Herron, M. M., Johnson, D. L., and Schwartz, L. M., 1998. A robust permeability estimator for siliciclastics. Society of Petroleum Engineers Annual Technical Conference and Exhibition, September 27-30, New Orleans, Louisiana, 11 p.

Herron, M.M., and Matteson, A., 1993. Elemental composition and nuclear parameters of some common sedimentary minerals, Nuclear Geophysics, 7 (3), 383-406.

Herwanger, J. V., Bottrill, A.D., and Mildren, S.D., 2015. Uses and Abuses of the Brittleness Index With Applications to Hydraulic Stimulation. Unconventional Resources Technology Conference, San Antonio, Texas, U.S.A., 20-22 July. https://doi.org/10.2118/178678-MS.

Houseknecht, D.W., 1987. Assessing the relative importance of compaction processes and cementation to reduction of porosity in sandstones. American Association of Petroleum Geologists Bulletin, 71(6), 633-642. https://doi.org/10.1306/44B4AA23-170A-11D7-8645000102C1865D.

Hower, J., Eslinger, E.V., Hower, M.E., and Perry, E.A., 1976. Mechanism of burial metamorphism of argillaceous sediment: 1. Mineralogical and chemical evidence. Geological Society of America Bulletin, 87(5), 725.

Huo, Z., Zhang, J., Li, P., Tang, X., Yang, X., Qiu, Q., Dong, Z., and Li, Z., 2018. An improved evaluation method for the brittleness index of shale and its application - A case study from the southern north China basin. Journal of Natural Gas Science and Engineering, 59, 47-55. https://doi.org/10.1016/j.jngse.2018.08.014.

Hurst, A., 1987. Mineralogical analysis and the evaluation of the petrophysical parameter Vshale for reservoir description, Journal of Marine and Petroleum Geology, 4, 82-91.

Ibrahimbas, A., and Riediger, C., 2004. Hydrocarbon source rock potential as determined by RockEval 6/TOC pyrolysis, N.E. B.C. and N.W. Alberta. Resource Development and Geoscience Branch, Summary of Activities 2004, 7-18.

Jarvie, D. M., 2012, Shale resource systems for oil and gas: Part 1-Shale-gas resource systems, in J. A. Breyer, ed., Shale reservoirs - Giant resources for the 21st century: American Association of Petroleum Geologists Memoir 97, 69-87.

Jarvie, D.M., Hill, R.J., Ruble, T.E., and Pollastro, R.M., 2007. Unconventional shale-gas systems: The Mississippian Barnett Shale of north-central Texas as one model for thermogenic shale-gas assessment. American Association of Petroleum Geologists Bulletin, 91(4), 475-499.

Jin, X., Shah, S.N., Roegiers, J.-C., and Zhang, B., 2015. An integrated petrophysics and geomechanics approach for fracability evaluation in shale reservoirs. SPE Journal 20(3), 518-526. https://doi.org/10.2118/168589-PA.

Jin, X., Shah, S.N., Truax, J.A., and Roegiers, J.-C., 2014. A Practical Petrophysical Approach for Brittleness Prediction from Porosity and Sonic Logging in Shale Reservoirs. SPE Annual Technical Conference and Exhibition Amsterdam, The Netherlands, 27-29 October. https://doi.org/10.2118/170972-MS.

Jingli, Y., Xiuqin, D., Yande, Z. Tianyou, H., Meijuan, C., and Jinlian, P., 2013, Characteristics of tight oil in Triassic Yanchang Formation, Ordos Basin. Petroleum Exploration and Development, 40(2), 15-158.

Kalsbeek, F., 1992. Large-scale albitisation of siltstones on Qeqertakavsak island, northeast Disko Bugt, West Greenland. Chemical geology, 95(3-4), 213-233.

Katz, D., Jung, M., Canter, L., Sonnefeld, M. Odegard, M., Daniels, J., Byres, A., Guisinger, M., Jones, K., and Forster, J., 2016. Mineralogy Derived Brittleness from the Qemscan: Niobrara Case Study. SPE Low Perm Symposium, Denver, Colorado, U.S.A., 5-6 May. https://doi.org/10.2118/180251-MS.

Keller, M.A., and Isaacs, C.M., 1985. An evaluation of temperature scales for silica diagenesis in diatomaceous sequences including a new approach based on the Miocene Monterey Formation, California. Geo-Marine Letters, 5(1), 31-35. https://doi.org/10.1007/BF02629794.

Keneti, A., and Wong, R.C.K., 2010. Investigation of anisotropic behavior of Montney shale under indirect tensile strength test, in: Canadian Unconventional Resources and International Petroleum Conference. Society of Petroleum Engineers, Calgary, AB, Canada, p. 9. https://doi.org/10.2118/138104-MS.

Kiehl, J.T., and Shields, C.A., 2005. Climate simulation of the latest Permian: Implications for mass extinction. Geology 33(9), 757. https://doi.org/10.1130/G21654.1.

Kirsimäe, K., Jøgensen, P., and Kalm, V., 1999. Low-temperature diagenetic illite-smectite in Lower Cambrian clays in North Estonia. Clay Minerals, 34(1), 151-163. https://doi.org/10.1180/000985599546000.

Kominz, M.A., Patterson, K., and Odette, D., 2011. Lithology dependence of porosity in slope and deep marine sediments. Journal of Sedimentary Research, 81(10), 730-742.

Krause, F.F., Wiseman, A.C., Williscroft, K.R., Solano, N., Morris, N.J., Meyer, R., and Marr, R., 2012. Petrographic and petrophysical comparison of the Montney Formation in the Sturgeon Lake South area. In Site, Canadian Well Logging Society Magazine, 31, 6-9.

Kulia, U., and Prasad, M., 2011. Surface area and pore size distribution in clays and shales, SPE annual technical conference and exhibition, Denver, Colorado, USA, October 30-November 2.

Kumar, V., Sondergeld, C.H., and Rai, C.S., 2012. Nano to macro mechanical characterization of shale. SPE Annual Technical Conference and Exhibition, San Antonio, Texas, USA, 8-10 October. SPE 159804.

Labani, M.M., and Rezaee, R., 2015. The Importance of Geochemical Parameters and Shale Composition on Rock Mechanical Properties of Gas Shale Reservoirs: a Case Study From the Kockatea Shale and Carynginia Formation From the Perth Basin, Western Australia. Rock Mechanics and Rock Engineering, 48(3), 1249-1257. https://doi.org/10.1007/s00603-014-0617-6.

Labani, M.M., Rezaee, R., Saeedi, A., and Al Hinai, A., 2013. Evaluation of pore size spectrum of gas shale reservoirs using low pressure nitrogen adsorption, gas expansion and mercury porosimetry: A case study from the Perth and Canning Basins, Western Australia, Journal of Petroleum Science and Engineering, 112, 7-16.

Lai, J., Wang, G., Ran, Y., Zhou, Z., and Ciu, Y., 2016. Impact of diagenesis on the reservoir quality of tight oil sandstones: The case of Upper Triassic Yanchang Formation Chang 7 oil layers in Ordos Basin, China. Journal of Petroleum Science and Engineering, 145, 54-65.

Lai, B., Li, H., Zhang, J., Jacobi, D., and Georgi, D., 2015. Water-Content Effects on Dynamic Elastic Properties of Organic-Rich Shale. SPE Journal 21(2), 635-647. https://doi.org/10.2118/175040-PA.

LaMothe, J.T., 2008. Sedimentology, Ichnology, Stratigraphy and Depositional History of the Contact Between the Triassic Doig and Montney Formations in West-Central Alberta, Canada - Presence of an Unconformity Bound Sand Wedge. M.Sc Thesis, Departmrnt of Earth and Atmospheric Sciences, University of Alberta, Edmonton, Alberta, canada.

Lan, Q., Dehghanpour, H., Wood, J.M., and Sanei, H., 2015. Wettability of the Montney Tight Gas Formation. SPE Reservoir Evaluation & Engineering, 18(3), 417-431. https://doi.org/10.2118/171620-PA.

Lander, R.H., Larese, R.E., and Bonnell, L.M., 2008. Toward more accurate quartz cement models: The importance of euhedral versus noneuhedral growth rates. American Association of Petroleum Geologists Bulletin, 92(11), 1537-1563.

Lander, R.H., and Walderhaug, O., 1999. Predicting porosity through simulating sandstone compaction and quartz cementation. American Association of Petroleum Geologists Bulletin, 83(3), 433449. https://doi.org/10.1306/00AA9BC4-1730-11D7-8645000102C1865D.

Larionov, V.V., 1969. Radiometry of boreholes, NEDRA, Moscow.

Laughrey, C.D., Ruble, T.E., Lemmens, H., Kostelnik, J., Butcher, A.R., Walker, G., and Knowles, W., 2011. Black shale diagenesis: insights from integrated high-definition analyses of post-mature Marcellus formation rocks, Northeastern Pennsylvania. *American Association of Petroleum Geologists* Search and Discovery Article #110150. http://www.searchanddiscovery.com/documents/2011/110150laughrey/ndx_laughrey.pdf. Last accessed March 31, 2020.

Lazar, O.R., Bohacs, K.M., Macquaker, J.H., Schieber, J., and Demko, T.M., 2015. Capturing key attributes of fine-grained sedimentary rocks in outcrops, cores, and thin sections: nomenclature and description guidelines. Journal of Sedimentary Research, 85(3), 230-246.

Lewan, M.D. and Kotarba, M.J., 2014. Thermal-maturity limit for primary thermogenic-gas generation from humic coals as determined by hydrous pyrolysis. American Association of Petroleum Geologists Bulletin, 98(12), 2581-2610. DOI: 10.1306/06021413204.

Liseroudi, M.H., Ardakani, O.H., Sanei, H., Pedersen, P.K., Stern, R.A., and Wood, J.M., 2020. Origin of sulfate-rich fluids in the early Triassic Montney Formation, Western Canadian Sedimentary Basin. Marine and Petroleum Geology, 104236. https://doi.org/10.1016/j.marpetgeo.2020.104236

Longman, M.W., Drake, W.R., Milliken, K.L., and Olson, T.M., 2019. A comparison of silica diagenesis in the Devonian Woodford shale (Central Basin Platform, West Texas) and Cretaceous Mowry shale (Powder River Basin, Wyoming), in: W. Camp, Milliken, K., Taylor, K., Fishman, N., Hackley, P., and Macquaker, J. (Eds.), Mudstone Diagenesis: Research Perspectives for Shale Hydrocarbon Reservoirs, Seals, and Source Rocks: American Asociation of Petroleum Geologists Memoir 121, 49-68. https://doi.org/10.1306/13672210M12163.

Loucks, R.G., Reed, R.M., Ruppel, S.C., and Hammes, U., 2012. Spectrum of pore types and networks in mudrocks and a descriptive classification for matrix-related mudrock pores. American Association of Petroleum Geologists Bulletin, 96, 1071-1098.

Lundegard, P.D., 1992. Sandstone porosity loss; a "big picture" view of the importance of compaction, Journal of Sedimentary Research, 62(2), 250-260.

Machel, H.G., 2004. Concepts and models of dolomitization: a critical reappraisal. Geological

Society, London, Special Publications, 235(1), 7-63.

Macquaker, J.H., and Adams, A.E., 2003. Maximizing information from fine-grained sedimentary rocks: An inclusive nomenclature for mudstones. Journal of Sedimentary Research, 73(5), 735-744.

Makowitz, A., and Milliken, K.L., 2003. Quantification of brittle deformation in burial compaction, Frio and Mount Simon Formation sandstones. Journal of Sedimentary Research, 73(6), 1007-1021.

Manger, W.L., 2014. Tripolitic chert development in the Mississippian lime: New insights from SEM. In Mississippian Lime Play Forum. 20 February, Oklahoma City, OK, USA,

McBride, E.F., 1989. Quartz cement in sandstones: A review. Earth-Science Reviews, 26(1-3), 69-112.

Meunier, A., and Velde, B., 2004. Illite: Origins, evolution, and metamorphism. Springer, Berlin.

Meyer, E.E., Green, G.W., Alcantar, N.A., Israelachvili, J.N., and Boles, J.R., 2006. Experimental investigation of the dissolution of quartz by a muscovite mica surface: Implications for pressure solution, Journal of Geophysics Research, 111 B08202, doi: 10.1029/2005JB004010.

Miall, A.D., and Blakey, R.C., 2008. The Phanerozoic tectonic and sedimentary evolution of North America, in: Miall, A.D. Sedimentary Basins of United States and Canada, p. 1-29. Amsterdam, Netherlands, Elsevier.

Milliken, K., 1992. Chemical behavior of detrital feldspars in mudrocks versus sandstones, Frio Formation (Oligocene), South Texas. Journal of Sedimentary Research, 62 (5), 790-801. https://doi.org/10.1306/D42679DD-2B26-11D7-8648000102C1865D.

Milliken, K.L., 1989. Petrography and composition of authigenic feldspars, Oligocene Frio Formation, south Texas. Journal of Sedimentary Research, 59(3), 361-374.

Milliken, K.L., and Olson, T., 2017. Silica diagenesis, porosity evolution, and mechanical behavior in siliceous mudstones, Mowry Shale (Cretaceous), Rocky Mountains, U.S.A.. Journal of Sedimentary Research, 87(4): 366-387. doi: https://doi.org/10.2110/jsr.2017.24.

Milliken, K.L., Rudnicki, M., Awwiller, D.N., and Zhang, T.W., 2013. Organic matter hosted pore system, Marcellus Formation (Devonian), Pennsylvania. American Association of Petroleum Geologists Bulletin, 97, 177-200.

Milliken, K.L., Esch, W.L., Reed, R.M., and Zhang, T., 2012. Grain assemblages and strong diagenetic overprinting in siliceous mudrocks, Barnett Shale (Mississippian), Fort Worth Basin, Texas. American Association of Petroleum Geologists Bulletin, 96(8), 1553-1578.

Milliken, K., Choh, S.J., Papazis, P., and Schieber, J., 2007. "Cherty" stringers in the Barnett Shale are agglutinated foraminifera. Sedimentary Geology, 198(3-4), 221-232.

Moghadam, A., Harris, N.B., Ayranci, K., Gomez, J.S., Angulo, A.A., and Chalaturnyk, R., 2019. Brittleness in the Devonian Horn River shale, British Columbia, Canada. Journal of Natural Gas Science and Engineering, 62, 247-258. https://doi.org/10.1016/j.jngse.2018.12.012.

Mokhtari, M., Honarpour, M.M., Tutuncu, A.N., and Boitnott, G.N., 2016. Characterization of elastic anisotropy in Eagle Ford Shale: Impact of heterogeneity and measurement scale. SPE Reservoir Evaluation & Engineering, 19(3), 429-439.

Mondol, N.H., Jahren, J., Bjørlykke, K., and Brevik, I., 2008. Elastic properties of clay minerals. Leading Edge, 27(6) 758-770. https://doi.org/10.1190/1.2944161.

Monger, J.W, and Price, R.,A. 2002. The Canadian Cordillera: Geology and tectonic evolution. Canadian Society of Exploration Geophysicists Recorder, 27(2), 17-36.

Monger, J.W., and Price, R.A., 1979. Geodynamic evolution of the Canadian Cordillera - progress and problems. Canadian Journal of Earth Sciences, 16(3), 770-791. https://doi.org/10.1139/e79-069.

Moore, D.M., 2000. Diagenesis of the Purington Shale in the Illinois Basin and implications for the diagenetic state of sedimentary rocks of shallow Paleozoic basins. Journal of Geology, 108(5), 553-567. https://doi.org/10.1086/314423.

Morad, S., Al-Ramadan, K., Ketzer, J.M., and De Ros, L.F., 2010. The impact of diagenesis on the heterogeneity of sandstone reservoirs: A review of the role of depositional facies and sequence stratigraphy. American Association of Petroleum Geologists Bulletin, 94(8), 1267–1309. https://doi.org/10.1306/04211009178.

Morad, S., and Aldahan, A.A., 1987. Diagenetic replacement of feldspars by quartz in sandstones. Journal of Sedimentary Research, 57(3), 488-493. https://doi.org/10.1306/212F8B70-2B24-11D7-8648000102C1865D.

Moslow, T.F., 2000. Reservoir architecture of a fine-grained turbidite system: Lower Triassic Montney Formation, Western Canada Sedimentary Basin, in: Weimer, P. (Ed.), Deep-Water Reservoirs of the World. SEPM Society for Sedimentary Geology, Houston, Texas, pp. 686-713. https://doi.org/10.5724/gcs.00.15.0686.

Moslow, T.F., Haverslew, B., and Henderson, C.M., 2018. Sedimentary facies, petrology, reservoir characteristics, conodont biostratigraphy and sequence stratigraphic framework of a continuous (395m) full diameter core of the Lower Triassic Montney Fm, northeastern British Columbia. Bulletin of Canadian Petroleum Geology, 66(1), 259-287.

Moslow, T.F., and Davies, G.R., 1997. Turbidite reservoir facies in the Lower Triassic Montney

Formation, west-central Alberta. Bulletin of Canadian Petroleum Geology, 45(4), 507-536.

Müller, G., 1967. Diagenesis in argillaceous sediments, in: Larsen, G., and Chilingar, G. V. (Eds.), Developments in Sedimentology. Elsevier, pp. 127-177. https://doi.org/10.1016/S0070-4571(08)70843-4.

Nadeau, P.H., Bjørkum, P.A., and Walderhaug, O., 2005. Petroleum system analysis: Impact of shale diagenesis on reservoir fluid pressure, hydrocarbon migration, and biodegradation risks. In Geological Society, London, Petroleum Geology Conference series, 6(1), 1267-1274.

Nagel, N.B., Gil, I., Sanchez-Nagel, M., and Damjanac, B., 2011. Simulating Hydraulic Fracturing in Real Fractured Rocks - Overcoming the Limits of Pseudo 3D Models, Society of Petroleum Engineers Hydraulic Fracturing Technology Conference. doi:10.2118/140480-MS.

Nassichuk, B.R., 2000. Sedimentology, diagenesis and reservoir development of the lower Triassic Montney formation, northeastern British Columbia. , Ms.C. Thesis, Department of Earth and Ocean Sciences, University of British Columbia, Vancouver, British Columbia, Canada.

National energy board, 2013. Canada's energy future 2013 energy supply and demand projections to 2035. https://www.cer-rec.gc.ca/nrg/ntgrtd/ftr/2013/2013nrgftr-eng.pdf. Last accessed March 31, 2020.

Needham, S.J., Worden, R.H., and McIlroy, D., 2005. Experimental production of clay rims by macrobiotic sediment ingestion and excretion processes. Journal of Sedimentary Research, 75(6), 1028-1037.

Ness, S.M., 2001. The application of basin analysis to the Triassic succession, Alberta Basin: an investigation of burial and thermal history and evolution of hydrocarbons in Triassic rocks. Ms.C. Thesis, Department of Geology and Gepophysics, University of Calgary, Calgary, Alberta, Canada.

Nicolas, M., 2006. Petroleum geology of the Devonian Three Forks Formation, Sinclair Field and surrounding area, southwestern Manitoba; in E.H. Nickel (Eds.), Saskatchewan and Northern Plains oil and gas symposium core workshop volume, Saskatchewan geological society special publication 20, p.32-49.

Nieto, J., Batlai, B., and Delbecq, F., 2013. Seismic lithology prediction : A Montney Shale Gas case study. CSEG Recorder, 38(2), 34-41.

Niu, B., and Ishida, H., 2000. Different rates of smectite illitization in mudstones and sandstones from the Niigata Basin, Japan. Clay Minerals, 35(1), 163-173. https://doi.org/10.1180/000985500546558.

Norton, M., Hovdebo, W., Cho, D., Jones, M., and Maxwell, S., 2010. Surface seismic to microseismic : An integrated case study from exploration to completion in the Montney shale of NE British Columbia, Canada, in: Society of Exploration Geophysicists Annual Meeting. Denver, Colorado, p. 5.

Ochoa, J., Wolak, J., and Gardner, M.H., 2013. Recognition criteria for distinguishing between hemipelagic and pelagic mudrocks in the characterization of deep-water reservoir heterogeneity. American Association of Petroleum Geologists Bulletin, 97(10), 1785-1803.

Orchard, M.J., and Zonneveld, J.-P. 2009. The Lower Triassic Sulphur Mountain Formation in the Wapiti Lake area: lithostratigraphy, conodont biostratigraphy, and a new biozonation for the lower Olenekian (Smithian). Canadian Journal of Earth Sciences, 46(10), 757-790. https://doi.org/10.1139/E09-051.

Osborne, M., Haszeldine, R.S., and Fallick, A.E., 1994. Variation in kaolinite morphology with growth temperature in isotopically mixed pore-fluids, Brent Group, UK North Sea. Clay Minerals, 29(4), 591-608. https://doi.org/10.1180/claymin.1994.029.4.15.

Ouenes, A., Aimene, Y., and Nairn, J., 2014. Interpretation of Microseismic Using Geomechanical Modeling of Multiple Hydraulic Fractures Interacting with Natural Fractures – Application to Montney Shale. Canadian Society of Exploration Geophysicists Recorder, 39(9), 46-54.

Owen, J.N., 2017. An investigation into the controls and variability of the flowback water inorganic geochemistry of the Montney Formation, Northeastern British Columbia and Northwestern Alberta, Canada, M.Sc. Thesis, The University of British Columbia, Department of Geological Sciences.

Passey, Q.R., Bohacs, K.M., Esch, W.L., Klimentidis, R., and Sinha, S., 2010. From oil-prone source rock to gas-producing shale reservoir-geologic and petrophysical characterization of unconventional shale-gas reservoirs. SPE Paper 131350, 2010. In: CPS/SPE International Oil and Gas Conference and Exhibition. Beijing, China, p. 29.

Paxton, S.T., Szabo, J.O., Ajdukiewicz, J.M., and Klimentidis, R.E., 2002. Construction of an intergranular volume compaction curve for evaluating and predicting compaction and porosity loss in rigid-grain sandstone reservoirs. American Association of Petroleum Geologists Bulletin, 86(12), 2047-2067.

Pejrup, M., 1988. The triangular diagram used for classification of estuarine sediments: a new approach. In: Boer, P.L., van Gelder, A., and Nio, S.D. (Eds.), Tide-influenced sedimentary environments and facies. Reidel, Dordrech p. 530.

Perez Altamar, R., and Marfurt, K. 2014. Mineralogy-based brittleness prediction from surface seismic data: Application to the Barnett Shale. Interpretation 2(4), T255-T271.

https://doi.org/10.1190/INT-2013-0161.1.

Playter, T.L., 2013. Petrographic and x-ray microtomographic analysis of the Upper Montney Formation, Northeastern British Columbia, Canada. Ms.C. Thesis, Department of Earth and Atmospheric Sciences, University of Alberta, Edmonton, Alberta, Canada.

Polt, R.H., and Krause, F.F., 1997. New discovery in the Montney Formation: "Sturgeon Lake South, Triassic F-Pool", a shoreface sandstone reservoir. Canadian Society of Petroleum Geologists and Society for Sedimentary Geology (SEPM) Joint Convention, Core Conference, pp. 237-255.

Prasad, M., Kenechukwu C. Mba., McEvoy, T.E., and Batzel, M.L., 2011. Maturity and impedance analysis of organic-rich shales. SPE Reservoir Evaluation & Engineering 14(5), 533-543.

Prasad, M., Hofman, R., Batzel, M., Kopycinska-Muler, M., Rabe, U., Arnold, W., 2005. Values of mineral modulus of clay, in: SEG Annual Meeting, Houston, Texas, U.S.A., 6-11 November. https://doi.org/10.1016/j.jcrc.2012.07.027.

Prasad, M., Kopycinska, M., Rabe, U., and Arnold, W., 2002. Measurement of Young's modulus of clay minerals using atomic force acoustic microscopy. Geophysical Research Letters, 29(8), 13-1-13-4. https://doi.org/10.1029/2001GL014054.

Preto, N., Kustatscher, E., and Wignall, P.B., 2010. Triassic climates - State of the art and perspectives. Palaeogeography, Palaeoclimatology, Palaeoecology, 290(1-4), 1-10. https://doi.org/10.1016/j.palaeo.2010.03.015.

Price, R.A., 1994. Cordilleran tectonics and the evolution of the Western Canada sedimentary basin. In Geological Atlas of Western Canada, Mossop, G.D., and Shetsen, I., pp. 13-24, Calgary, Alberta, Canadian Society of Petroleum Geologists/ Alberta Research Council.

Proverbs, I.P., Bann, K.L., Fratton, C.M., Frostad, C.J., and Juska, A., 2018. Facies architecture and sequence stratigraphy of the Lower Triassic Montney Formation , NE British Columbia : Fundamental controls on the distribution of 'sweet spots' in a world-class unconventional reservoir. Bulletine of Canadian petroleum Geology, 66(1), 237-258.

Qiu, Z., Tao, H., Zou, C., Wang, H., Ji, H., and Zhou, S., 2016. Lithofacies and organic geochemistry of the Middle Permian Lucaogou Formation in the Jimusar Sag of the Junggar Basin, NW China. Journal of Petroleum Science and Engineering, 140, 97-107.

Ramos, M.J., Espinoza, D.N., Goldfarb, E.J.,Tisato, N., Laubach, S.E., and Torres-Verdin, C., 2019. Microstructural controls on elastic anisotropy of finely laminated Mancos Shale. Geophysical Journal International, 216(2), 991-1004.

Rangriz Shokri, A., Chalaturnyk, R.J., and Bearinger, D., 2019. Deployment of Pressure Hit Catalogues to Optimize MultiStage Hydraulic Stimulation Treatments and Future Re-

Fracturing Designs of Horizontal Wells in Horn River Shale Basin, URTEC-196221-MS presented at SPE Annual Technical Conference and Exhibition, Calgary, AB, 29 Sept.-2 Oct.

Rangriz Shokri, A., Chalaturnyk, R.J., Bearinger, D., Virues, C., and Lehmann, J., 2017. Constraining the Complexity of Stimulated Reservoir Volume during Multi-Stage Hydraulic Fracturing of Horizontal Wells through Inter-Well Pressure Hit Modeling, Society of Petroleum Engineers, doi:10.2118/187188-MS.

Rakociński, M., Zatoń, M., Marynowski, L., Gedl, P., and Lehmann, J., 2018. Redox conditions, productivity, and volcanic input during deposition of uppermost Jurassic and Lower Cretaceous organic-rich siltstones in Spitsbergen, Norway. Cretaceous Research, 89, 126-147.

Ravikovitch, P.I., Haller, G.L., and Neimark, A.V., 1998. Density functional theory model for calculating pore size distributions: pore structure of nanoporous catalysts. Advances in Colloid Interface Science, 76-77, 203-226.

Rickman, R., Mullen, M.J., Petre, J.E., Grieser, B., and Kundert, D., 2008. A practical use of shale petrophysics for stimulation design optimization: All shale plays Are not clones of the Barnett Shale. SPE Annual Technical Conference and Exhibition, Denver, Colorado, USA, 21-24 Sptember. https://doi.org/10.2118/115258-MS.

Riediger, C.L., Fowler, M.G., Brooks, P.W., and Snowdon, L.R., 1990. Triassic oils and potential Mesozoic source rocks, Peace River Arch area, Western Canada Basin. Organic Geochemistry, 16(1-3), 295–305. https://doi.org/10.1016/0146-6380(90)90049-6.

Roberts, J.M., and Elmore, R.D., 2018. A diagenetic study of the Woodford Shale in the southeastern Anadarko Basin, Oklahoma, USA: Evidence for hydrothermal alteration in mineralized fractures. Interpretation, 6(1), SC1-SC13.

Rogers, S., and McLellan, P., 2014. Investigation of the Effects of Natural Fractures and Faults on Hydraulic Fracturing in the Montney Formation , Farrell Creek Gas Field , British Columbia, in: International Discrete Fracture Network Engineering Conference. DFNE, Vancouver, Canada, pp. 1-13.

Rohais, S., Crombez, V., Euzen, T., and Zonneveld, J.-P., 2018. Subsidence dynamics of the Montney Formation (Early Triassic, western Canada sedimentary basin): Insights for its geodynamic setting and wider implications. Bulletin of Canadian Petroleum Geology, 66(1), 128-160.

Rohais, S., Crombez, V., Euzen, T., and Baudin, F., 2016. The Lower and Middle Triassic of Western Canada: Passive margin, Back-Arc or Fore-Arc geodynamic setting?, in: CWLS, C.C. (Ed.), Geoconvention. Calgary, AB, Canada, pp. 1-4.

Rokosh, C.D., Lyster, S., Anderson, S.D.A., Beaton, A.P., Berhane, H., Brazzoni, T., Chen, D., Cheng, Y., Mack, T., Pana, C. and Pawlowicz, J.G., 2012. Summary of Alberta's shale-and siltstone-hosted hydrocarbon resource potential. Energy Resources Conservation Board, ERCB/AGS Open File Report, 6, p.327.

Romero-Sarmiento, M.F., Euzen, T., Rohais, S., Jiang, C., and Littke, R., 2016. Artificial thermal maturation of source rocks at different thermal maturity levels: Application to the Triassic Montney and Doig formations in the Western Canada Sedimentary Basin. Organic Geochemistry, 97, 148-162. https://doi.org/10.1016/j.orggeochem.2016.05.002.

Ross, G.M., Gehrels, G.E., and Patchett, P.J., 1997. Provenance of Triassic strata in the Cordilleran miogeocline , western Canada. Bulletin of Canadian Petroleum Geology, 45(4), 461-473.

Russell, P., 2018. Recent advances in routine core analysis on the Montney Formation. Bulletin of Canadian Petroleum Geology, 66, 363-393.

Rybacki, E., Meier, T., and Dresen, G., 2016. What controls the mechanical properties of shale rocks? - Part II: Brittleness. Journal of Petroleum Science and Engineering, 144, 39-58. https://doi.org/10.1016/j.petrol.2016.02.022.

Saidian, M., and Prasad, M., 2015. Effect of mineralogy on nuclear magnetic resonance surface relaxivity: A case study of Middle Bakken and Three Forks formations. Fuel, 161, 197-206.

Saigal, G.C., Morad, S., Bjorlykke, K., Egeberg, P.K., and Aagaard, P., 1988. Diagenetic albitization of detrital K-feldspar in Jurassic, Lower Cretaceous, and Tertiary clastic reservoir rocks from offshore Norway, I. Textures and origin. Journal of Sedimentary Research, 58(6), 1003-1013.

Saller, A.H., and Henderson, N., 1998. Distribution of porosity and permeability in platform dolomites: Insight from the Permian of west Texas. American Association of Petroleum Geologists Bulletin, 82(8), 1528-1550.

Sanders, S., Etienne, C., Gegolic, A., Kelly, D., and Zonneveld, J.-P., 2018. The Middle Montney Altares Member : lithology , depositional setting and significance for horizontal drilling and completion in the Altares field , British Columbia. Bulletin of Canadian Petroleum Geology, 66(1), 318-337.

Sanei, H., Haeri-Ardakani, O., Ghanizadeh, A., Clarkson, C.R., and Wood, J.M., 2016. Simple petrographic grain size analysis of siltstone reservoir rocks: An example from the Montney tight gas reservoir (Western Canada). Fuel 166, 253-257. https://doi.org/10.1016/j.fuel.2015.10.103.

Sanei, H., Wood, J.M., Ardakani, O.H., Clarkson, C.R., and Jiang, C., 2015. Characterization of organic matter fractions in an unconventional tight gas siltstone reservoir. International Journal of Coal Geology, 150-151, 296-305. https://doi.org/10.1016/j.coal.2015.04.004.

Saner, S., Cagatay, M.N., and Sanounah, A.A., 1996. Relationships between shale content and grain-size parameters in the Safaniya Sandstone reservoir, NE Saudi Arabia. Journal of Petroleum Geology, 19(3), 305-320.

Schettler, P.D., Parmely, C.R., and Lee, W.J., 1989. Gas Storage and Transport in Devonian Shales, SPE Formation Evaluation, 3(3), 371-376. http://doi.org/10.2118/17070-PA.

Schieber, J., Southard, J., and Thaisen, K., 2007. Accretion of Mudstone Beds from Migrating Floccule Ripples. Science, 318, 1760-1763.

Schlumberger, Log Interpretation Charts, 2009, figure Gen-8 p. 10. URL: https://connect.slb.com/~/media/Files/resources/books/log_charts/toc1.pdf (last access March 26, 2020).

Scuderi, M.M., Kitajima, H., Carpenter, B.M., Saffer, D.M., and Marone, C., 2015. Evolution of permeability across the transition from brittle failure to cataclastic flow in porous siltstone. Geochemistry, Geophysics, Geosystems, 16(9), 2980-2993.

Serra, O., 1984, Fundamentals of well-log interpretation: New York, Elsevier, 423 p.

Shepard, F.P., 1954. Nomenclature based on sand-silt-clay ratios. Journal of sedimentary Research, 24(3), 151-158.

Siebert, R.M., Moncure, G.K., and Lahann, R.W., 1984. A Theory of framework grain dissolution in sandstones, in: McDonald, D.A., and Surdam, R.C. (Eds.), Clastic Diagenesis. The American Association of Petroleum Geologists, Tulsa, pp. 163-176. https://doi.org/10.1306/M37435.

Slatt, R.M., and Rodriguez, N.D., 2012. Comparative sequence stratigraphy and organic geochemistry of gas shales: Commonality or coincidence? Journal of Natural Gas Science and Engineering, 8, 68-84. https://doi.org/10.1016/j.jngse.2012.01.008.

Slatt, R.M., and Abousleiman, Y., 2011. Merging sequence stratigraphy and geomechanics for unconventional gas shales. Leading Edge, 30(3), 274-282. https://doi.org/10.1190/1.3567258.

Slatt, R.M., and O'Brien, N.R., 2011. Pore types in the Barnett and Woodford gas shales: contribution to understanding gas storage and migration pathways in fine grained rocks. American Association of Petroleum Geologists Bulletin, 95, 2017-2030.

Sobolev, S. V., Sobolev, A. V., Kuzmin, D. V., Krivolutskaya, N.A., Petrunin, A.G., Arndt, N.T., Radko, V.A., and Vasiliev, Y.R., 2011. Linking mantle plumes, large igneous provinces and environmental catastrophes. Nature, 477, 312-316.

https://doi.org/10.1038/nature10385.

Spooner, P., 2014. Lifting the Fog of Confusion Surrounding Clay and Shale in Petrophysics. Society of Petrophysicists and Well-Log Analysts. 55th Annual Logging Symposium, 18-22 May, Abu Dhabi, United Arab Emirates.

Stieber, S. J., 1970. Pulsed Neutron Capture Log Evaluation - Louisiana Gulf Coast, Fall Meeting of the Society of Petroleum Engineers of AIME, 4-7 October, Houston, Texas. doi:10.2118/2961-MS.

Sun, Y., Joachimski, M.M., Wignall, P.B., Chunbo, Y., Chen, Y., Jiang, H., Wang, L., Lai, X., and Yan, C., 2012. Lethally hot temperatures during the Early Triassic greenhouse. Science, 338, 366-370. https://doi.org/10.1126/science.1224126.

Tinnin, B., Bello, H., and McChesney, M., 2015. Multi-source data integration: Eagle ford shale sweet spot mapping, in: Unconventional Resources Technology Conference This. Society of Exploration Geophysicists and American Association of Petroleum Geologists, San Antonio, Texas, U.S.A., pp. 1-9. https://doi.org/10.1190/ice2016-6874854.1.

Tribovillard, N., Algeo, T.J., Lyons, T., and Riboulleau, A., 2006. Trace metals as paleoredox and paleoproductivity proxies: An update. Chemical Geology, 232(1-2), 12-32. https://doi.org/10.1016/j.chemgeo.2006.02.012.

U.S. energy Information administration, 2017. Marcellus shale play Geology Review. https://www.eia.gov/maps/pdf/MarcellusPlayUpdate_Jan2017.pdf. Last accessed March 31. 2020.

Utting, J., Zonneveld, J.-P., MacNaughton, R.B., and Fallas, K.M., 2005. Palynostratigraphy, lithostratigraphy and thermal maturity of the Lower Triassic Toad and Grayling, and Montney formations of western Canada, and comparisons with coeval rocks of the Sverdrup Basin, Nunavut. Bulletin of Canadian Petroleum Geology, 53(1), 5-24. https://doi.org/10.2113/53.1.5.

Vaisblat, N., Harris, N.B., DeBhur, C., Euzen, T., Gasparrini, M., Crombez, V., Rohais, S., Krause, F. and Ayranci, K. 2017. Diagenetic model for the deep Montney Formation, Northeastern British Columbia. Geoscience BC Report 2017-1, p. 37-48. http://www.geosciencebc.com/i/pdf/SummaryofActivities2016/SoA2016_Vaisblat.pdf.

Van de Kamp, P.C., 2008. Smectite-illite-muscovite transformations, quartz dissolution, and silica release in shales. Clays and Clay Minerals, 56(1), 66-81.

Van der Plas, L., and Tobi, A.C., 1965. A chart for judging the reliability of point counting results. American Journal of Science, 263(1), 87-90.

Van Olphen, H., and Fripiat, J.J., 1979. Data handbook for clay materials and other non-metallic minerals, Pergamon Press, Oxford.

Vansant, E.F., Van Der Voort, P., and Vrancken, K.C., 1995. Characterization and chemical modification of the silica surface. Amsterdam, Elsevier (chapter 1).

Velde, B., 1996. Compaction trends of clay-rich deep sea sediments. Marine Geology, 133(3-4), 193-201.

Vernik, L., and Milovac, J., 2011. Rock physics of organic shales. Leading Edge, 30(3), 318-323. https://doi.org/10.1190/1.3567263.

Verwaal, W., and Mulder, A., 1993. Estimating rock strength with the equotip hardness tester. International Journal of Rock Mechanics and Mining Sciences & Geomechanics Abstracts, 30(6), 659-662. https://doi.org/10.1016/0148-9062(93)91225-8.

Vishkai, M., and Gates, I.D., 2018. Geomechanical Characterization of Naturally Fractured Formation, Montney, Alberta. 52nd U.S. Rock Mechanics/Geomechanics Symposium, June 17-20, Seattle, Washington.

Walderhaug, O., 1996. Kinetic modeling of quartz cementation and porosity loss in deeply buried sandstone reservoirs. American Association of Petroleum Geologists Bulletin, 80(5), 731-745.

Walderhaug, O., 1994. Temperatures of quartz cementation in Jurassic sandstones from the Norwegian continental shelf; evidence from fluid inclusions. Journal of Sedimentary Research, 64(2a), 311-323. https://doi.org/10.1306/D4267D89-2B26-11D7-8648000102C1865D.

Walderhaug, O., Oelkers, E.H. and Bjørkum, P.A., 2004. An analysis of the roles of stress, temperature, and pH in chemical compaction of sandstones: discussion. Journal of Sedimentary Research, 74(3), 447-449.

Wallmann, K., Aloisi, G., Haeckel, M., Tishchenko, P., Pavlova, G., Greinert, J., Kutterolf, S., and Eisenhauer, A., 2008. Silicate weathering in anoxic marine sediments. Geochimica et Cosmochimica Acta, 72(12), 2895-2918.

Wang, Y., and Grammer, G.M., 2018. Rebound hardness: relationship to facies, mineralogy, natural fractures, reservoir quality, and rock mechanical properties, the "Mississippian Limestone" play, North - Central Oklahoma, USA, in: 52nd US Rock Mechanics / Geomechanics Symposium. American Rock Mechanics Association, Seattle, Washington, U.S.A., pp. 1-10.

Wang, F.P., and Gale, J.F.W., 2009. Screening criteria for shale-gas systems. Gulf Coast Association of Geological Societies, 59, 779-793.

Wang, X., Dong, Z., Zhang, J., Qu, J., and Zhao, A., 2003. Grain size characteristics of dune sands in the central Taklimakan Sand Sea. Sedimentary Geology, 161(1-2), 1-14.

Wang, Z., Wang, H., and Cates, M.E., 1998. Elastic Properties of Solid Clays, 1998. In

Proceedings of the AEG Annual International Meeting. Extended abstract. https://doi.org/10.1190/1.1820064.

Warren, J., 2000. Dolomite: occurrence, evolution and economically important associations. Earth-Science Reviews, 52(1-3), 1-81.

Waxman, M.H., and Thomas, E.C., 1974. Electrical conductivities in oil-bearing shaly sands, I. The relation between hydrocarbon saturation and resistivity index; II. The temperature coefficient of electrical conductivity: Society of Petroleum Engineers Journal, 14, 213-225.

Waxman, M.H., and Smits, L.J.M., 1968. Electrical conductivities in oil-bearing shaly sands, Society of Petroleum Engineers Journal, 8 (2) 107-122.

Wei, Z., 2009. Nanoidentation behavior of clay minerals and claybased nonstructured multilayers. PhD dissertation, The Department of Civil and Environmental Engineering, Louisiana State University and Agricultural and Mechanical College, Baton Rouge, Louisiana, U.S.A.

Wignall, P.B., and Newton, R., 1998. Pyrite framboid diameter as a measure of oxygen deficiency in ancient mudrocks. American Journal of Science, 298(7), 537-552. https://doi.org/10.2475/ajs.298.7.537.

Wilkin, R.T., and Barnes, H.L., 1997. Formation processes of framboidal pyrite. Geochimica et Cosmochimica Acta, 61(2), 323-339. https://doi.org/10.1016/S0016-7037(96)00320-1.

Wilkin, R.T., Barnes, H.L., and Brantley, S.L., 1996. The size distribution of framboidal pyrite in modern sediments: An indicator of redox conditions. Geochimica et Cosmochimica Acta, 60(20), 3897–3912. https://doi.org/10.1016/0016-7037(96)00209-8.

Willett, S.D., Issler, D.R., Beaumont, C., Donelick, R.A., and Grist, A.M., 1997. Inverse modeling of annealing of fission tracks in apatite; 2, Application to the thermal history of the Peace River Arch region, Western Canada sedimentary basin. American Journal of Science, 297(10), 970-1011. https://doi.org/10.2475/ajs.297.10.970.

Williams, L.A., Parks, G.A., and Crerar, D.A., 1985. Silica diagenesis; I, Solubility controls. Journal of Sedimentary Research, 55(3), 301-311.

Wilson, M.D., 1992. Inherited grain-rimming clays in sandstones from eolian and shelf environments: their origin and control on reservoir properties. Origin Diagenesis and Petrophysics of Clay Minerals in Sandstones SEPM Special Publication No. 47, 209-225.

Wilson, J.C., and McBridge, E.F., 1988. Compaction and porosity evolution of Pliocene sandstones, Ventura Basin, California. American Association of Petroleum Geologists Bulletin, 72(6), 664-681.

Wong, T.-F., 1990, Mechanical compaction and brittle–ductile transition in porous sandstones,

in Knipe, R.J., and Rutter, E.H. (Eds.), Deformation Mechanisms, Rheology, and Tectonics: Geological Society of London, Special Publication 54, p. 111–122.

Wood, J.M., 2015. Crushed-rock versus full-diameter core samples for water-saturation determination in a tight-gas siltstone play, SPE Reservoir Evaluation & Engineering 18(3): 407-416. SPE-174548-PA. http://dx.doi.org/10.2118/174548-PA.

Wood, J.M., 2013. Water Distribution in the Montney Tight Gas Play of the Western Canadian Sedimentary Basin: Significance for Resource Evaluation, in: SPE Canadian Unconventional Resources Conference. Society of Petroleum Engineers, Calgary, AB, Canada, pp. 290–302. https://doi.org/10.2118/161824-MS.

Wood, J.M., Sanei, H., Haeri-Ardakani, O., Curtis, M.E., and Akai, T., 2018. Organic petrography and scanning electron microscopy imaging of a thermal maturity series from the Montney tight-gas and hydrocarbon liquids fairway. Bulletin of Canadian Petroleum Geology, 66(2), 499-515. https://doi.org/10.1038/ncomms13614.

Wood, J.M., and Sanei, H., 2016. Secondary migration and leakage of methane from a major tight-gas system. Nature Communications, 7, 13614.

Wood, J.M., Sanei, H., Curtis, M.E., and Clarkson, C.R., 2015. Solid bitumen as a determinant of reservoir quality in an unconventional tight gas siltstone play. International Journal of Coal Geology, 150-151, 287–295. https://doi.org/10.1016/j.coal.2015.03.015.

Worden, R., and Morad, S. (Eds.), 2000. Quartz cementation in sandstones, Malden, MA: Blackwell Science.

Wüst, R.A.J., and Cui, X., 2018. From X-ray Fluorescence (XRF) to Mechanical Profiling for Better Well Completion. Valuable Analytics for the Exploration Toolbox! Recorder 43, 22-28.

Wüst, R.A., Tu, S., Nassichuk, B., Bozarth, T., Tucker, J., and Cui, A., 2018. Chemostratigraphy, petrography, and SEM investigations of the Lower Triassic Montney Formation in Alberta: Implications for a new and revised diagenetic and depositional model. Bulletin of Canadian Petroleum Geology, 66(2), 436-471.

Yang, B., 2018. Geological characteristics and reservoir properties in the unconventional Montney Formation, southwestern Alberta, Canada. Geoscience Journal, 22 (2), 313-325.

Yang, S., Harris, N., Dong, T., Wu, W., and Chen, Z., 2015. Mechanical Properties and Natural Fractures in a Horn River Shale Core from Well Logs and Hardness Measurements, in: EUROPEC 2015. Society of Petroleum Engineers, Madrid, Spain, pp. 1-13. https://doi.org/10.2118/174287-MS.

Yang, Y.L., and Aplin, A.C., 2007. Permeability and petrophysical properties of 30 natural mudstones. Journal of Geophysical Research, 112, B03206.

Yu, H., Wang, Z., Rezaee, R., Arif, M., and Xiao, L., 2016. Characterization of elastic properties of lacustrine shale reservoir using well logging and core analysis, in: SPE Asia Pacific Oil & Gas Conference and Exhibition. Society of Petroleum Engineers, pp. 1-11. https://doi.org/10.2118/182215-MS.

Zargari, S., Prasad, M., Mba, K.C. and Mattson, E.D., 2013. Organic maturity, elastic properties, and textural characteristics of self resourcing reservoirs. Geophysics, 78(4), D223-D235.

Zelazny, I.V., Gegolick, A., Zonneveld, J.-P., Playter, T., and Moslow, T.F., 2018. Sedimentology, stratigraphy and geochemistry of Sulphur Mountain (Montney equivalent) Formation outcrop in south central Rocky Mountains, Alberta, Canada. Bulletin of Canadian Petroleum Geology, 66(1), 288-317.

Zhang, D., Ranjith, P.G., and Perera, M.S.A., 2016. The brittleness indices used in rock mechanics and their application in shale hydraulic fracturing: A review. Journal of Petroleum Science and Engineering, 143, 158-170. https://doi.org/10.1016/j.petrol.2016.02.011.

Zhang, J.J., and Bentley, L.R., 2005. Factors determining Poisson's ratio. Consortium for Research in Elastic Wave Exploration Seismology, Research Report, 17, 1-15.

Zonneveld, J.-P., 2011. Suspending the rules: unraveling the ichnological signature of the Lower Triassic post-extinction recovery interval. Palaios 26(11), 677–681. https://doi.org/10.2307/41317453.

Zonneveld, J.-P., and Moslow, T.F., 2018. Palaeogeographic setting, lithostratigraphy, and sedimentary framework of the Lower Triassic Montney Formation of western Alberta and northeastern British Columbia. Bulletin of Canadian Petroleum Geology, 66(1), 93-127.

Zonneveld, J.-P., and Moslow, T.F., 2014. Perennial river deltas of the Montney Formation : Alberta and British Columbia subcrop edge, in: Geoconvention. CSPG CSEG CWLS, Calgary, AB, Canada, pp. 1-2.

Zonneveld, J.-P., Golding, M.L., Moslow, T.F., Orchard, M.J., Playter, T.L., and Wilson, N., 2011. Depositional framework of the Lower Triassic Montey Formation, West-central Alberta and Northeastern British Columbia, in: Geoconvention. CSPG CSEG CWLS, Calgary, AB, Canada, pp. 1-4.

Zonneveld, J.-P., Beatty, T.W., MacNaughton, R.B., Pemberton, S.G., Utting, J., and Henderson, C.M., 2010. Sedimentology and ichnology of the Lower Triassic Montney Formation in the Pedigree-Ring/Border-Kahntah River area, northwestern Alberta and northeastern British Columbia. Bulletin of Canadian Petroleum Geology, 58(2), 115–140. https://doi.org/10.2113/gscpgbull.58.2.115.

Appendix 1: Core descriptions for the four cored wells.

Lithofacies

A - interlaminated siltstone and sandstone
B - Massive sandy siltstone
C - Bioturbated clay-rich siltstone
D - Mudstone
E - Dolomitic siltstone

F - faintly laminated calcareous siltstone
G/H - laminated siltstone
I - horizontal/irregularly laminated calcareous siltstone
J - massive siliceous clayey siltstone
K - massive calcareous clayey siltstone

L - Siliceous phosphatic siltstone
M/N - bioturbated calcareous sandy siltstone
O - Hommocky to ripple cross startified sandy siltstone
P - interbedded siliceous mudstone and calcareous siltstone
Missing section

Appendix 2: Mass balance calculations for smectite to illite reaction in the Montney Formation. Also included are the amount of K-feldspar albitization and silica liberated during smectite illitization.

		well						
	unit	2	3	4	5	9	11	15
Average MLIS content[a]	gr	15.19	11.18	16.58	11.66	5.71	13.96	14.18
Smectite content [b]	gr	2.28	1.68	2.49	1.75	0.86	2.09	2.13
Smectite content [b]	moles	5.66E-04	4.16E-04	6.17E-04	4.34E-04	2.13E-04	5.20E-04	5.28E-04
Illite generated[b,c]	moles	3.60E-04	2.65E-04	3.93E-04	2.76E-04	1.36E-04	3.31E-04	3.36E-04
K+ needed to create the illite[c]	moles	1.42E-03	1.04E-03	1.55E-03	1.09E-03	5.33E-04	1.30E-03	1.32E-03
Average Na-feldspar concentration[a]	gr	8.87	6.64	8.94	6.65	9.82	3.44	2.33
Albitized K-feldspar[d]	gr	1.12	0.84	1.13	0.84	1.24	0.43	0.29
K+ released by Na-feldspar albitization[e]	moles	4.26E-03	3.19E-03	4.29E-03	3.19E-03	4.72E-03	1.65E-03	1.12E-03
Access of K+ [f]	moles	2.85E-03	2.15E-03	2.75E-03	2.11E-03	4.19E-03	3.52E-04	-2.01E-04
Si released through illitization[c,g]	moles	8.89E-03	6.54E-03	9.70E-03	6.82E-03	3.34E-03	8.16E-03	8.30E-03
SiO_2 precipitated[c]	gr	0.53	0.39	0.58	0.41	0.20	0.49	0.50

All calculations done for 100 gr of rock.

[a]concentration from QEMSCAN analysis.

[b]concentration of detrital smectite assuming original composition of illite (80)/smectite (20) and final composition of illite (95)/ smectite (5).

[c]according to molar ratios from Eq.1.

[d]according to point count analysis albitized Kspar is 12.6% of total Na-feldspar.

[e]K+ released by Na-feldspar albitization is equal to Na^+ consumed by the albitization reaction.

[f]K+ released by Na-feldspar albitization and not consumed by conversion of smectite to illite.

[g] Silica released by smectite to illitization.

Appendix 3: Coefficients of determination (R^2) between core derived and log derived geomechanical properties for all study wells.

well	1	2	3	4	5	6	7
Bimin (W&G) - DYM	0.14	0.17	-0.03	0.38	0.00	-0.01	0.00
Bimin (W&G) - DPR	-0.06	0.00	0.06	0.14	-0.12	-0.07	0.08
Bimin (W&G) - BI sonic	0.00	0.10	0.02	0.40	0.01	0.04	-0.02
Bimin (W&G) - Hardness	0.20	0.06	0.06	-0.05	0.22	N/A	N/A

well	1	2	3	4	5	6	7
Bimin (Jin) - DYM	0.30	0.14	0.00	0.35	0.39	0.00	0.05
Bimin (Jin) - DPR	-0.20	0.00	0.00	-0.17	0.00	0.00	0.00
Bimin (Jin) - BI sonic	-0.01	0.10	0.00	0.40	0.39	0.00	-0.01
Bimin (Jin) - Hardness	0.24	0.12	0.04	-0.05	0.11	N/A	N/A

well	1	2	3	4	5	6	7
Bimin (Jarvie) - DYM	0.20	0.04	-0.03	0.09	-0.05	-0.02	0.00
Bimin (Jarvie) - DPR	-0.07	0.00	-0.07	-0.13	-0.27	-0.10	0.00
Bimin (Jarvie) - BI sonic	0.00	0.03	0.03	0.16	0.00	0.06	0.00
Bimin (Jarvie) - Hardness	0.43	0.00	0.06	-0.07	0.23	N/A	N/A

Appendix 4: Correlation between average quartz mineral size measured through QEMSCAN analysis and average detrital quartz grain size measured from SEM-images.

$$Y=1.93X - 7.54$$
$$R^2=0.96$$